

AN ABSTRACT OF THE THESIS OF

Jeffrey H. Templeton for the degree of Doctor of Philosophy in Geology presented on September 3, 1998. Title: Petrology of the Reversely Zoned Mickey Pass Tuff, West-central Nevada.

Redacted for Privacy

Abstract approved: _____

Anita L. Grunder

The 27.0-Ma Mickey Pass Tuff (MPT) is a voluminous ($>600 \text{ km}^3$) ash-flow deposit at the base of a thick sequence of Oligocene to early Miocene ash-flow tuffs exposed in west-central Nevada. The Guild Mine and Weed Heights Members of the MPT exhibit reverse compositional zoning, that is from more mafic magmatic ejecta at the base of the deposits to more silicic material at the top. The compositional zoning is the stratigraphic reverse of nearly all zoned tuffs. Bulk-tuff compositions from the lower Guild Mine Member grade from dacite to high-silica rhyolite (65.7-78.1 wt. % SiO_2), with a gap between 70 and 73 wt. % SiO_2 . The upper Weed Heights Member displays a narrower compositional range from rhyodacite to high-silica rhyolite (71.5-75.5 wt. % SiO_2).

The range of major and trace element data from bulk tuff can be modelled by a compositionally zoned magma chamber for the Guild Mine Member that was derived primarily by crystal fractionation of an assemblage consisting of plagioclase, biotite, and magnetite with clinopyroxene, sanidine, and/or quartz. The compositional gap, bimodal glass analyses, multiple populations of biotite analyses, the range of estimated Rayleigh numbers, and a pronounced vertical gradient in calculated magma densities support a model that the pre-eruptive MPT chamber consisted of several, stacked compositional

layers that each were internally convecting. The compositional zoning in the MPT is consistent with eruption of a normally zoned chamber with a non-flat roof geometry that was tapped from the deeper, more mafic parts first where a silicic cap was less extensive. During eruption, the less evolved and more evolved compositions in the chamber were mixed to yield compositions in the successively erupted units.

The MPT was erupted at the onset of extensional and transform tectonics in the central Walker Lane, which is a zone of right-lateral, strike-slip faulting in west-central Nevada. The eruption of the MPT and other comparable reversely zoned tuffs occurred in the incipient stages of extension and may be a precursor to rapid rates of extension.

Petrology of the Reversely Zoned Mickey Pass Tuff, West-central Nevada

by

Jeffrey H. Templeton

A THESIS

submitted to

Oregon State University

in partial fulfillment of
the requirements for the
degree of

Doctor of Philosophy

Presented September 3, 1998

Commencement June 1999

Doctor of Philosophy thesis of Jeffrey H. Templeton presented on September 3, 1998

APPROVED:

Redacted for Privacy

11/11/98

Major Professor, representing Geology

Redacted for Privacy

11/11/98

Chair of Department of Geosciences

Redacted for Privacy

Dean of Graduate School

I understand that my thesis will become part of the permanent collection of Oregon State University libraries. My signature below authorizes release of my thesis to any reader upon request.

Redacted for Privacy—

Jeffrey H. Templeton, Author

ACKNOWLEDGEMENTS

I gratefully acknowledge the steadfast support of Anita Grunder throughout the course of this project. Her insights enabled me to develop the focus of this project, and throughout, she was willing to grab the rudder more than once to help me stay on course. John Dilles originally introduced me to the Tertiary ignimbrite sequence in the Yerington district on a ore deposits mapping course to the area in the Spring of 1992. The allure of such uniquely zoned tuffs sparked my curiosity and there was no looking back. I value the geologic experiences that John has provided in western Nevada, central Oregon, and on a phenomenal 10-day field trip to deposits in the Pacific Northwest.

Chris Fridrich greatly assisted me early on with my understanding of compositional zoning in silicic magma chambers. Dick Hardyman helped me pinpoint several key localities in the northern Gillis Range. Roger Nielsen provided his expertise and assistance with the microprobe data collection. Mark Hilyard is also thanked for his help in obtaining the microprobe data. The OSU Radiation Center INAA team of Martin Streck and Erwin Torne ably assisted me with data reduction. My committee, Anita Grunder, John Dilles, Roger Nielsen, Reed Glassman, and Graduate Representative, Martin Fisk, served ably and provided constructive reviews of the dissertation text.

Financial assistance and analytical support is graciously acknowledged from the following: monies from NSF grant EAR-8916645 to John Dilles supported the 1992 field season; Chevron Research Grants in 1994 and 1995 supported field work, as well as provided material support; the OSU Radiation Center provided reactor time and data reduction facilities for INAA analyses; and monies from the Ore Geology fund and the Microprobe fund were instrumental in obtaining the XRF and microprobe analyses,

respectively. A Department of Geosciences Teaching Assistantship, 4 summers of employment at the OSU Geology Field Station in Mitchell, a Laboratory Assistantship at the OSU Radiation Center, the Southwest Research Institute Center for Nuclear Waste Storage, and Willamette Geological Service are acknowledged for the great experiences and the paychecks that each provided.

I thank my fellow travelers for sharing a pint or two of the nectar of the gods'... Black Butte Porter and of course, stimulating conversations whenever possible: Dave Maher, Rene` Laberge, Craig Schneider, Chuck Payne, Christian Brauderick, Peter Powers, Brendan Laurs, Paul Crenna, Ken Bevis, Lisa McNeill, Jim Maclean, Martin Streck, Joe Licciardi, Inchang Riu. R.I.P., Nook and Kaya. The music of the Grateful Dead and Zero were critical to my sanity and probably drove at least a few people insane.

I saved the most important people in my life for last. I am not quite sure how one can thank their partner in life for all of the sacrifices that that person must make in a project of this undertaking. To the love of my life, Lisa, I truly thank you from the bottom of my being for the incredible amount of moral support and everything else you have given me. Quite simply, I would not have been able to complete this project without her amazing support and love through the years. My lovely daughter, Kate, is my inspiration. And of course, Manti, who has provided almost constant companionship through the years.

TABLE OF CONTENTS

	<u>Page</u>
INTRODUCTION.....	1
Purpose and Rationale.....	1
Geologic Framework of the Study Area.....	6
Stratigraphy	6
Tectonic Framework	9
Methods	11
Sample Preparation.....	11
Analytical Techniques.....	12
PHYSICAL AND COMPOSITIONAL ATTRIBUTES OF THE MPT	14
Field Characteristics	14
Field Description of the Guild Mine Member	15
Field Description of the Intermember Ash-flow Tuffs and Sedimentary Rocks.....	19
Field Description of the Weed Heights Member	21
Petrography	25
Bulk-Tuff Composition	31
Major Element Data.....	39
Trace Element Data	39
Glass Analyses	49
Guild Mine Member.....	49
Weed Heights Member.....	52
Mineral Compositions	53
Plagioclase.....	53
Sanidine.....	60
Pyroxene.....	64
Amphibole.....	69
Biotite	70
Fe-Ti Oxides	76

TABLE OF CONTENTS (Continued)

	<u>Page</u>
QUANTITATIVE ANALYSIS OF THE MPT COMPOSITIONAL DATA	81
Estimation of Intensive Parameters	81
Temperature and Oxygen Fugacity using Fe-Ti Oxide Geothermometry	81
Two-feldspar Geothermometry	85
Two-pyroxene Geothermometry	90
Total Pressure	92
Water Content Estimated from Experimental Phase Equilibria	94
Density	97
Viscosity	99
Mechanisms of Differentiation	100
Major Element, Least-Squares Models	100
Trace Element Fractionation Models	105
Magma Mixing Models	110
DISCUSSION: EVOLUTION OF THE MPT MAGMA SYSTEM	114
Configuration of the Pre-eruptive MPT Magma Chamber	114
Origin of Reverse Compositional Zoning	119
Eruption Dynamics of Reversely Zoned Tuffs	123
Tectonic Implications of the Eruption of Reversely Zoned Tuffs	124
Petrogenetic Evolution of the MPT Magma System	129
SUMMARY AND CONCLUSION	136
BIBLIOGRAPHY	141
APPENDICES	153
Appendix A Microprobe analytical conditions	154
Appendix B Geochemical sample locations	156
Appendix C Complete microprobe data for Mickey Pass Tuff	157

LIST OF FIGURES

<u>Figure</u>	<u>Page</u>
1. Generalized distribution map of the MPT.....	4
2. Generalized stratigraphic section of the MPT showing Guild Mine and Weed Heights Members and rhyolite intertuff	5
3a. Modes of select samples of the Guild Mine and Weed Heights Members of the MPT and the rhyolite ash-flow tuff between the two members based on visual estimates	26
3b. Graph showing phenocryst types and abundances for the Guild Mine and Weed Heights Members.....	27
4. Total alkalis versus silica variation diagram for the MPT	38
5. Harker variation diagrams for the MPT.....	40
6. Enrichment factor diagrams	41
7. Variations of select trace elements with volatile-free SiO ₂	44
8. Variations of select trace elements with Ta	45
9. Rare-earth element diagrams for (a) the Guild Mine Member, (b) the Weed Heights Member, and (c) the intermember rhyolite ash-flow tuff.....	48
10. Harker variation diagrams for vitric fiamme and ash shards in the groundmass of select samples from the MPT	51
11. Feldspar compositional data from the MPT plotted on ternary feldspar diagrams	54

LIST OF FIGURES (Continued)

<u>Figure</u>	<u>Page</u>
12. Pyroxene compositional data from the MPT plotted in the system wollastonite (Wo), enstatite (En), and ferrosilite (Fs).....	65
13. Histogram of Mg# (molecular $Mg/(Mg+Fe^*)$) for biotite phenocrysts in the MPT.....	73
14. Plot of log Mg/Mn (molar) ilmenite versus log Mg/Mn (molar) magnetite.....	82
15. Temperature and oxygen fugacity determined for coexisting Fe-Ti oxides from the MPT	82
16. Ternary feldspar diagrams with tie lines connecting equilibrium pairs of plagioclase and sanidine analyses used for two-feldspar geothermometry ...	87
17. Compiled temperature diagram for the MPT	88
18. The results of the density calculations for pre-eruptive MPT.....	98
19. Plots of select trace elements versus Th, which is used as a differentiation index, for the MPT	108
20. Ratio-ratio plot (a) and companion plot (b) for the MPT.....	111
21. Schematic representation of the pre-eruptive MPT magma system	116
22. Schematic representation of the MPT magma system through time	125
23. Relative amounts of faulting and magmatism versus time for the central Walker Lane, NV, the Socorro, NM area, and the Eldorado Mountains in southern NV and northern AZ	127

LIST OF TABLES

<u>Table</u>	<u>Page</u>
1. Survey of reversely zoned tuffs from the literature.....	2
2. Whole-rock compositions of MPT and related samples.....	33
3. Representative glass analyses of the MPT.....	50
4. Representative plagioclase analyses of the MPT.....	57
5. Representative sanidine analyses of the MPT.....	61
6. Representative clinopyroxene and orthopyroxene analyses of the MPT.....	66
7. Representative biotite and amphibole analyses of the MPT.....	71
8. Representative Fe-Ti oxide analyses of the MPT.....	77
9. Water estimates at 2 kbar using the biotite-sanidine-magnetite geobarometer.....	96
10. Results of the major element least squares calculations for the MPT.....	102
11. Partition coefficients used in trace element models.....	106

Petrology of the Reversely Zoned Mickey Pass Tuff, West-central Nevada

INTRODUCTION

Purpose and Rationale

Ash-flow tuffs provide a window into continental silicic batholiths at an instant in time, and, for this reason, they have been used widely to decipher a variety of magmatic processes. Most studies have concentrated on ash-flow tuffs that display a stratigraphic progression from more evolved, silicic material at the base of the deposit to less evolved material at the top. These normally zoned ash-flow tuffs have been interpreted to reflect the downward tapping of a zoned magma chamber with a silicic cap (Lipman, 1967; Smith, 1979). Reversely zoned ash-flow tuffs, on the other hand, display a gradation from more mafic magmatic ejecta at the base of the deposit to more silicic material at the top. Reversely zoned tuffs have been variously interpreted to result from normal tapping of reversely zoned chambers, from reverse tapping of normally zoned chambers, or from the processes of flow in the conduit during withdrawal from a normally zoned magma chamber (Cook, 1968; Eggleston and others, 1983; Elston, 1984; Baker and McBirney, 1985; Blake and Ivey 1986a; 1986b).

Based on a review of the literature, remarkably few tuffs are reversely zoned (Table 1). Four major, middle Tertiary ash-flow tuffs in southwestern New Mexico exhibit reverse compositional zoning (Eggleston and others, 1983; Osburn and Chapin, 1983; Elston, 1984). In the Basin and Range Province, the tuff of Hoover Dam in southeastern Nevada (Mills, 1985; Smith and others, 1990) and the Italian Springs

Table 1: Survey of reversely zoned tuffs from the literature.

<u>Name of Unit</u>	<u>Associated Caldera</u>	<u>Locality</u>	<u>Age (Ma)</u>	<u>Description</u>	<u>References</u>
Guild Mine Member-MPT	-----	west-central Nevada	27.02 ± 0.07	dacite->high SiO ₂ rhyolite	Proffett and Proffett (1976); Ekren and others (1980); McIntosh and others (1992); this study
Weed Heights Member-MPT	-----	west-central Nevada	26.8 ± 0.9	rhyodacite->high SiO ₂ rhyolite	Proffett and Proffett (1976); Ekren and others (1980); this study
Tuff of Hoover Dam	-----	Eldorado Mountains, NV	14.3	andesite->dacite	Mills (1985); Smith and others (1990)
Italian Springs Formation	-----	Hot Creek Range, NV	28-29	rhyodacite-> rhyolite	Cook (1968)
Hells Mesa Tuff	Socorro	Mogollon-Datil volcanic field, NM	32.06 ± 0.10	dacite->rhyolite	Eggleston and others (1983); Osburn and Chapin (1983); Elston (1984); McIntosh and others (1990)
Lemitar Tuff	-----	Mogollon-Datil volcanic field, NM	28.00 ± 0.08	n/a,	ibid.
Bluff Creek Tuff	Tullous	Boot Heel field, southwest NM	$35.09 \pm .04$	n/a,	Elston (1984), and references therein; McIntosh and others (1992)
Tuff of Guadalupe Canyon	Geronimo Trail	southwest NM	27.1 ± 1.5	n/a,	Elston (1984), and references therein
Middle Toba Tuff	Toba	Sumatra, Indonesia	0.501 ± 0.005	rhyolite->high SiO ₂ rhyolite	Chesner and Rose (1991); Chesner (1998)
Whakamaru group ignimbrites	-----	Taupo Volcanic Zone, New Zealand	0.34	rhyolite	Brown and others (1998)

Formation in central Nevada (Cook, 1968) have been identified as reversely zoned. In addition to the western Cordilleran examples, the Middle Toba Tuff exposed in Sumatra, Indonesia also displays mafic-upward zoning (Chesner and Rose, 1991; Chesner, 1998). Aside from the Middle Toba Tuff, scant data are available for the few reversely zoned tuffs mentioned in the literature. Given the available data, though, reversely zoned tuffs appear to span compositional and volumetric ranges comparable to normally zoned tuffs.

The purpose of this study is to describe and interpret the petrologic evolution of the Mickey Pass Tuff (MPT), which is a voluminous, composite ash-flow tuff erupted from a large, silicic volcanic center in west-central Nevada (inset, Fig. 1). The MPT is unique, because it consists of two genetically related ash-flow tuff members that both exhibit reverse compositional zoning. The Guild Mine and Weed Heights Members of the MPT (Fig. 2) provide successive samplings of the same evolving chamber. The genetic relationship is indicated from the following observations: (1) the members are compositionally and mineralogically similar to one another but different from other tuffs in the area, (2) they are geochronologically indistinguishable using the available K-Ar and Ar-Ar age data, (3) they are both paleomagnetic normal, albeit distinct (Geissman and others, 1982), and (4) the stratigraphic section indicates that limited time elapsed between eruptions of the MPT.

This study integrates modal and textural petrographic data, whole-rock chemical analyses, and electron microprobe analyses of minerals and glass to address a series of goals, which are delineated into four main areas:

1. to describe the compositional zoning in the pre-eruptive magma chamber, to provide estimates of the intensive parameters of the magma chamber such as temperature, pressure, oxygen fugacity, and volatile distribution, and to

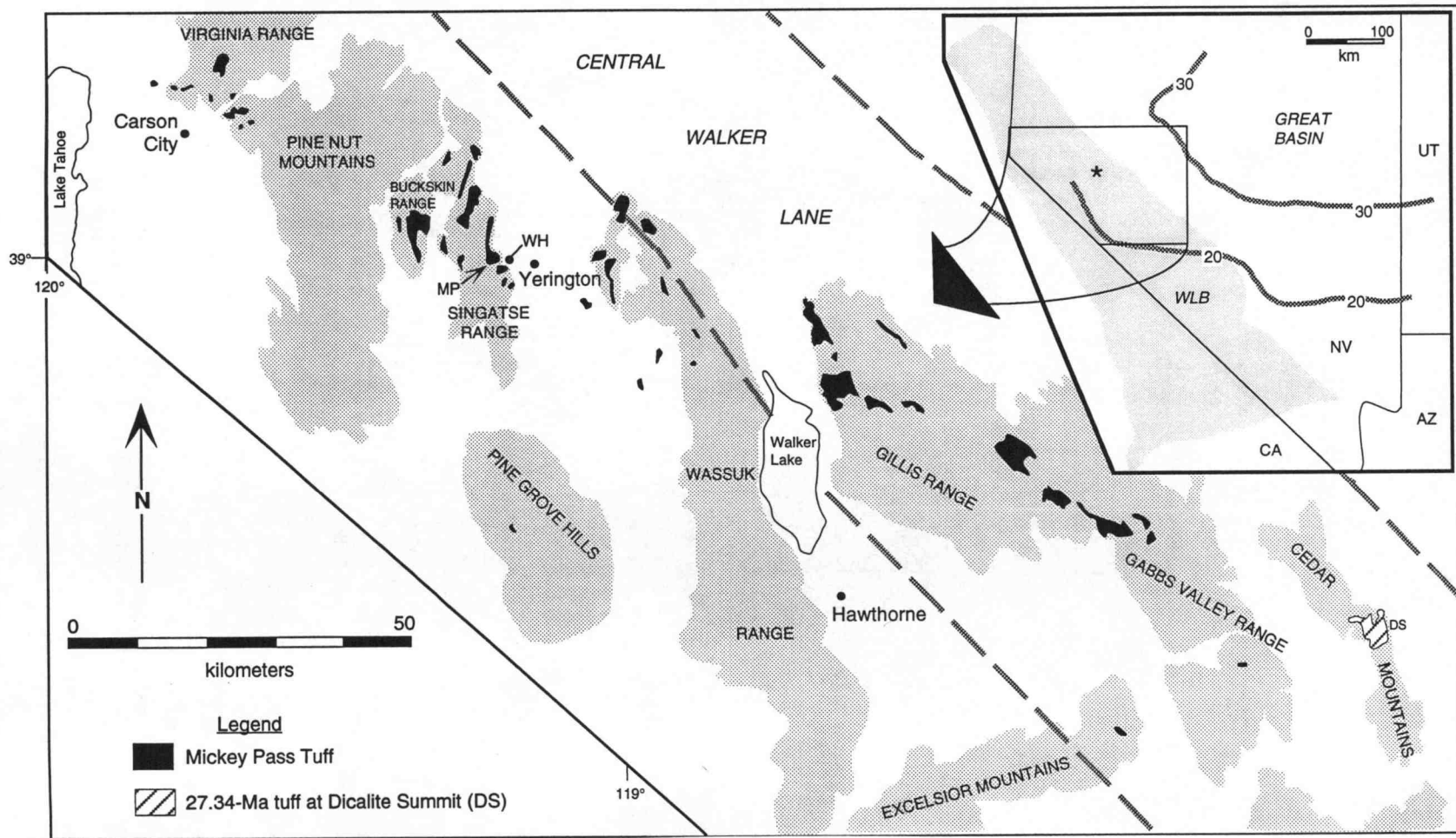


Figure 1: Generalized distribution map of the MPT. Dashed lines show outline of central Walker Lane (after Hardyman and Oldow, 1991). MP=Mickey Pass, MPT type locality (Proffett and Proffett, 1976); WH=Weed Heights. Inset map shows area of the map enclosed by the box, Walker Lane belt in gray (WLB; after Stewart, 1988), limits of caldera-forming eruptions between 30 and 20 Ma (after Best and others, 1989), and inferred source area for MPT by the star (after Ekren and others, 1980).

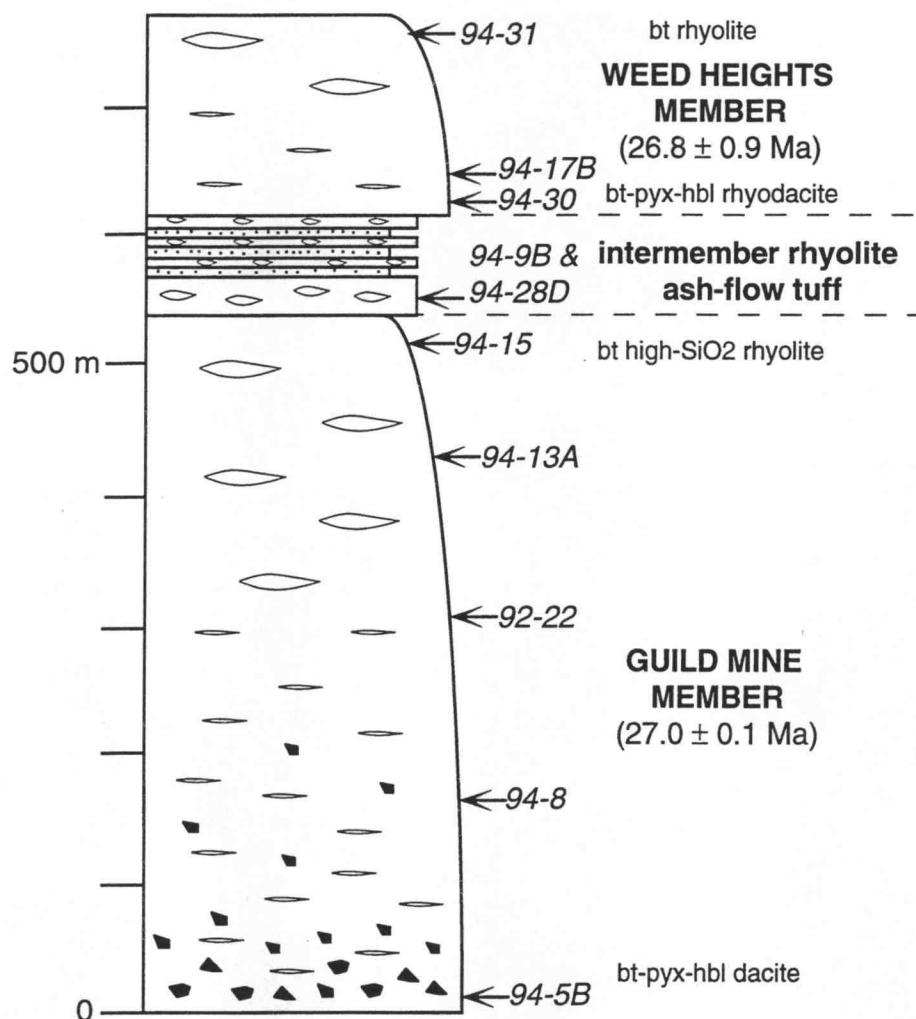


Figure 2: Generalized stratigraphic section of the MPT showing Guild Mine and Weed Heights Members and rhyolite intertuff. The approximate stratigraphic positions of samples used for bulk-tuff geochemistry and mineral content data are indicated by arrows. Lithics are angular-shape and black. Fiamme are oblate-shaped, and the relative size and degree of flattening is shown schematically. Volcaniclastic sedimentary rock is stippled. Abbreviations are as follows: bt = biotite; pyx = pyroxene; hbl = hornblende.

constrain the petrogenesis of the MPT, because the mechanism of zonation is relevant to how the chamber was organized prior to eruption;

2. to explain how the reverse compositional zoning in the MPT originated and to address the origin of reverse compositional zoning in ash-flow tuffs in general;
3. to elucidate the dynamics of the cataclysmic eruptions that formed the two members of the MPT and to compare this model to other studies documenting the eruption dynamics from the upper portions of a silicic magma chamber;
4. to discuss the timing relationships between the eruption of the reversely zoned MPT and the early stages of extensional tectonics in the Central Walker Lane, and to compare the Central Walker Lane to other extensional tectonic regimes, such as Rio Grand Rift and the Colorado River extensional corridor, where reversely zoned tuffs have also been documented.

The MPT is well-suited for this study because geologic mapping has been conducted for a significant portion of its outcrop area at scales of 1:48,000 to 1:24,000; hence, its distribution is quite well known (Fig. 1). Also, well-exposed cross sections of the MPT occur in the tilted fault blocks in the mountain ranges across the region. Nevertheless, no detailed petrological or volcanological studies have been undertaken on the MPT.

Geologic Framework of the Study Area

Stratigraphy

The MPT occurs in the lower part of a thick sequence of Oligocene to lower Miocene ash-flow tuffs, which compose a voluminous, middle Tertiary ash-flow field in western Nevada (Fig. 1). The western Nevada ash-flow field is part of a broad, arcuate band of

predominantly dacitic to rhyolitic ash-flow tuffs that extends from southeastern Utah to eastern California (Stewart and Carlson, 1976; Best and others, 1989). The 30- to 20-Ma ash-flow tuffs in this arc-shaped region (inset, Fig. 1) represent the southward and westward temporal migration of calc-alkaline magmatism through the Great Basin from the Eocene to the Miocene (Cross and Pilger, 1978; Best and others, 1989; Seedorff, 1991).

Descriptions of the stratigraphy of the Oligocene to early Miocene volcanic section in west-central Nevada have been provided by Bingler (1977, 1978a) for the Carson City area, by Proffett and Proffett (1976) and Proffett and Dilles (1984) for the Singatse Range, by Bingler (1978b) and Dilles (1993) for the Wassuk Range, and by Hardyman (1978) and Ekren and others (1980) for the Gillis and Gabbs Valley Ranges. For brevity, only the units pertinent to the MPT are discussed below.

In west-central Nevada, the Oligocene to early Miocene ash-flow tuff sequence rests with marked unconformity upon Mesozoic basement rocks. In most localities throughout the study area, an early Tertiary basal conglomerate marks the base of the sequence and represents a paleovalley system into which the MPT was deposited (Proffett and Proffett, 1976). The lowest part of the Oligocene to early Miocene volcanic sequence locally consists of basaltic andesite and andesite lava flows, flow breccias, and tuff-breccias, and an underlying series of thin rhyolite ash-flow tuffs, representing early Tertiary ash-flow volcanism in west-central Nevada (Proffett and Proffett, 1976).

The first major, voluminous ash-flow tuff deposit in the Oligocene to early Miocene ash-flow tuff sequence in west-central Nevada is the MPT, which consists of two cooling units separated by a thin sequence of tuffs and volcaniclastics (Fig. 2). The Guild Mine Member, which is the lower cooling unit of the MPT, typically has a black vitrophyre at the base and a densely welded, crystal-rich devitrified lower part with

small (<1 cm long), sparse fiamme. The tuff grades up into a moderately welded, crystal-rich devitrified upper part with abundant flattened pumice up to 10 cm long. The Guild Mine Member has yielded an ^{40}Ar - ^{39}Ar date on sanidine of 27.0 ± 0.1 Ma (McIntosh and others, 1992). The eruption of the Guild Mine Member represents a minimum of 600 km^3 of magmatic material (Proffett and Proffett, 1976). Overlying the Guild Mine Member with minor erosional unconformity is an up to 80-m-thick interval of ash-flow tuffs and volcanoclastic sedimentary rocks. The interval contains a rhyolite ash-flow tuff, which is up to 30 m thick (intermember rhyolite ash-flow tuff on Fig. 2). The rhyolite ash-flow tuff, which punctuated the eruption interval between the Guild Mine and Weed Heights Members, has been inferred to represent either a less voluminous eruption of the same system or the distal western edge of an unrelated ash-flow tuff sheet (Proffett and Proffett, 1976). Because this rhyolite ash-flow tuff is compositionally indistinguishable from parts of the Guild Mine and Weed Heights Members, all three tuffs are here interpreted to be from the same magma system (see below). A thin sequence of volcanoclastic sandstone and siltstone and local rhyolite ash-flow tuff interbeds overlie the 30-m-thick rhyolite ash-flow tuff (Fig. 2). The upper cooling unit in the MPT is the Weed Heights Member (Fig. 2), which typically has a thin vitrophyre at the base and a main section of partially welded, moderately crystal rich ash-flow tuff with abundant white pumice up to 7 cm across. The Weed Heights Member has yielded K-Ar age dates on sanidine of 26.8 ± 0.9 Ma (Proffett and Proffett, 1976; recalculated after Dalrymple, 1979) and on biotite of 26.6 ± 0.8 Ma (Bingler and others, 1980).

In most areas across its distribution, the MPT is overlain by the exceptionally voluminous Singatse Tuff (minimum of 3500 km^3), which consists of a compositionally homogeneous cooling unit that is dacitic to rhyodacitic in composition (≈ 68 wt. % SiO_2 ; Proffett and Proffett, 1976).

Tectonic Framework

While the focus of this study is not tectonic, the age and distribution of faulting is important to the regional framework, and more importantly, the timing of eruption of the MPT appears to coincide with the earliest phases of Walker Lane extension. The MPT was erupted and emplaced in an area that lies in and adjacent to the central Walker Lane (Fig. 1), which is a 40-km-wide zone of right-lateral strike-slip faulting in west-central Nevada (Hardyman, 1984). The Walker Lane belt (inset, Fig. 1) is a zone of subparallel north-northwest trending faults that are at an angle of about 40° to the typical north-northeast trending Basin-and-Range faults east of the Walker Lane belt. The Walker Lane faults consist of Basin-and-Range normal faults and right-lateral strike-slip faults slightly oblique to the normal faults (Stewart, 1988). The amount of displacement on the individual strike-slip faults in the central Walker Lane ranges from a few kilometers to 18 km, and cumulative dextral displacement on the northwest-striking faults is estimated at 48-60 km (Nielsen, 1965; Hardyman and others, 1975; Ekren and Byers, 1984; Hardyman, 1984). Cumulative displacements may perhaps be up to 60-75 km (Oldow, 1993).

The MPT was erupted prior to or at the onset of earliest Walker Lane extensional tectonics. In the Singatse Range, in the northern Wassuk Range, and in the Carson City area, the Guild Mine Member is localized in northwest-striking paleovalleys; the origin of the paleovalleys may be directly related to the earliest phases of tectonism. At some localities in the northern Wassuk Range, there is a slight angular discordance between the early Tertiary ash-flow tuffs (28.6 Ma; Dilles and Gans, 1995) and the overlying 27.0-Ma MPT (Dilles, 1993). The structures are ambiguous and poorly understood but indicate that minor faulting was apparently initiated at approximately 28-29 Ma. Although the paleovalleys and the angular unconformity suggest an early phase of

tectonism, the major phase of middle Tertiary faulting in the central Walker Lane was between 26 and 23 Ma. The middle Tertiary phases of tectonism were broadly synchronous with large-volume, silicic, ash-flow tuff volcanism between ≈ 29 and 23 Ma (Dilles, 1993; Dilles and Gans, 1995).

In the Yerington district (Fig. 1), which is located southwest of the dominantly right-slip zone of the central Walker Lane, the MPT is well exposed in a number of steeply west-tilted fault blocks that formed by a series of successively developed normal faults each initiated with an approximate 60° E dip (Proffett, 1977). Using the field relations of Proffett (1977), the normal faults were initiated around 14 to 13 Ma, based on ^{40}Ar - ^{39}Ar age dates on hornblende andesite lavas cut by the faults and dacite dikes that intrude the faults (Dilles, 1993; Dilles and Gans, 1995). In the areas northwest and southeast of Hawthorne (Fig. 1), the Tertiary strata are slightly to strongly tilted, as at Yerington, but, in some cases, the Tertiary rocks, including the MPT, are structurally detached from the Mesozoic basement along low-angle "normal" faults (Hardyman and others, 1975; Hardyman, 1984; Ekren and others, 1980; Ekren and Byers, 1984). The interpreted thin-skinned tectonic features in these areas occur in addition to kinematically related, high-angle, transcurrent strike-slip faults (Hardyman and Oldow, 1991). That this style of deformation was active concurrently with eruption of the Guild Mine Member of the MPT is shown by the Dicalite Summit fault, which is located in the Cedar Mountains southeast of the study area (Fig. 1). The Dicalite Summit fault plane dips shallowly southwest (5° - 10°) and separates an upper plate consisting of Tertiary volcanic rocks from a lower plate consisting of Triassic and Jurassic metasedimentary rocks. The ^{40}Ar - ^{39}Ar radiometric ages from the ash-flow tuffs in the upper plate of the Dicalite Summit fault constrain as much as 50° - 60° of stratal tilt to less than 370,000 years at about 27 Ma (Hardyman and others, 1993).

Methods

Sample Preparation

For each sample, at least 3 kilograms of relatively alteration-free, unfractured rock were collected in the field. To insure that the analytical results are statistically representative of a large volume of rock and to compensate for small-scale heterogeneities within samples, the entire sample was crushed in each case. Strict controls were utilized to prevent contamination during the preparation of samples for geochemical analysis. Large blocks of rock not processed in the field were placed on a steel plate and broken down to fragments of no larger than 2-3 cm diameters using a crack hammer. The steel plate was cleaned using a wire brush between each sample. The particles during this step were examined by hand, and fragments that did not contain any visible lithics and that were not weathered, altered, or highly veined were retained; all other fragments were discarded. Fresh-appearing fragments were further broken into fragments less than 0.5 centimeter using a small-scale ceramic jaw crusher. Between samples, the small jaw crusher was cleaned carefully by brushing and rinsing with acetone, and the crusher was precontaminated by crushing a small aliquot before each sample. The entire quantity of fragments and powder produced in this way was placed on a clean sheet of large paper and was quartered. This was carried out until two statistically representative fractions weighing about 8 grams were obtained. Before further processing, each fraction was studied carefully with a binocular scope to remove any small lithic fragments. One fraction of chips and powder was sent to Washington State University for X-ray fluorescence (XRF) analysis, and the other fraction was reduced to a fine powder for instrumental neutron activation analysis (INAA). A Spex disc mill was used to powder the INAA fraction by running for 15 minutes in a ceramic

alumina grinding vessel. The vessel was cleaned meticulously between each sample using mild chemical glassware soap, water, and acetone. The disc mill was precontaminated with a small portion of sample before grinding each sample.

Analytical Techniques

Major element analyses and select trace element analyses were done by XRF at Washington State University using an automatic Rigaku spectrometer. Analytical precision is estimated from repeat analyses ($n=11$) on two in-house standards (BCR-P and GSP-1) and is compared to replicate analyses ($n=2$) of two samples from this study. One-sigma relative precision estimates for the major elements are better than 1%, except for MnO and P_2O_5 , which are better than 2%, and MgO, which is better than 5%. For XRF trace elements, analytical precision estimates are better than 1% for Sr and Zr, better than 2% for Zn, Rb, and Ba, better than 5% for Y, better than 10% for V, Ni, Ga, and Nb, and better than 20% for Cu and Pb.

The remainder of the trace elements were determined by INAA at the Oregon State University Radiation Center, which houses a 1-MW TRIGA reactor. Analytical precision estimates for the trace elements determined by INAA were supplied by the Radiation Center and were also estimated from replicate analyses of in-house standards. For INAA trace elements, relative precision (one sigma) is better than 3% for Sc, Co, As, Eu, and Tb, better than 5% for Sb, La, Sm, and Th, better than 7% for Cr, Yb, Hf, and U, better than 10% for Ce, Lu, and Ta, and better than 20% for Se and Nd. Cs yields an anomalously high error estimate from one standard (CRB), but otherwise has precision better than 5%.

Mineral compositional data were determined by electron microprobe analyses done at the Oregon State University Microprobe Laboratory, which houses a 4-spectrometer Cameca SX-50 electron microprobe. All analyses were done on polished thin sections. Analytical conditions are provided as footnotes in Tables 3-8 and compiled in Appendix A.

PHYSICAL AND COMPOSITIONAL ATTRIBUTES OF THE MPT

Field Characteristics

The MPT is well exposed in west-central Nevada in a northwest-southeast trending region that extends from the Carson City area through the Yerington district to the mountain ranges beyond Hawthorne (Fig. 1). Of the two members of the MPT, the Guild Mine Member is more widely distributed, extending from the southern Virginia Range to the Excelsior and Pilot Mountains. The Weed Heights Member displays a more limited distribution from the Buckskin Range to the northern Gillis Range. The intermember rhyolite ash-flow tuff is confined to the Singatse and Wassuk Ranges (Fig. 1).

The MPT was erupted into a region that displayed considerable relief (Proffett and Proffett, 1976). One of the key pieces of evidence for this ancient topography is the presence of a conglomerate unit that occurs stratigraphically beneath the MPT at a number of sections throughout its distribution. In outcrop, the early Tertiary basal conglomerate unit consists of round cobbles and boulders dispersed within a medium- to coarse-grained sandstone matrix. In the Carson City area (Fig. 1), the boulders are up to 1 m across, and in the Yerington district, they are smaller with diameters up to 20 cm. The early Tertiary basal conglomerate unit represents an ancient valley system into which the MPT was deposited (Proffett and Proffett, 1976). The distribution of the Guild Mine Member is strongly controlled by this paleotopography. At a locality about 1/2 mile south-southwest of Weed Heights (Fig. 1), the Guild Mine Member and the intermember tuff thin dramatically along strike. The intermember tuff is approximately 7 meters thick and thins rapidly along strike where it pinches out beneath the basal

vitrophyre of the Weed Heights Member. Where the upper part of the Guild Mine Member is missing, the intermember tuff lies directly on the Jurassic basement rocks. This field relation has been interpreted to represent pre-existing topography over which the Tertiary units pinched out against the Jurassic basement rock (Proffett and Proffett, 1976). The strong paleotopographic control of the Guild Mine Member at this locality facilitated the collection of fresh vitrophyric samples for geochemical analysis throughout nearly the entire stratigraphic thickness of the unit.

Field Description of the Guild Mine Member

The base of the Guild Mine Member is marked by a densely welded, moderately lithic-rich, black vitrophyre containing abundant plagioclase and biotite phenocrysts and trace amounts of fresh appearing, green clinopyroxene. A distinguishing feature of the vitrophyre is the presence of black, vitric fiamme. The fiamme are characteristically strongly flattened and small with dimensions usually ranging up to several centimeters long and less than 1 cm wide. Several outsized examples in the northern Gillis Range (Fig. 1) are up to 15 cm long and 2 cm wide in plan view, and in the Singatse Range, strongly flattened fiamme are up to 8 by 11 cm on surfaces parallel to the compaction foliation. The vitrophyre displays a range in thicknesses across its distribution from up to 5 m thick in the Carson City area to 20 m thick in the Singatse and Wassuk Ranges. In the Gillis and Gabbs Valley Ranges, the vitrophyre is somewhat thinner with values up to 12 m thick (Fig. 1).

The amount and size of the lithics in the basal vitrophyre vary across the distribution area of the Guild Mine Member. As a group, the lithics, which are angular to subround, are generally small (5-10 mm), but some range up to 12-13 cm. To quantify the size

variation in lithics between various sections, the lengths of the 10 largest lithics in a 0.5-meter-square area were measured, and the average value for the maximum lithic size was obtained. Visual estimates provide a crude approximation of the proportion of lithics. In the Singatse Range (Fig. 1), visual estimates for lithics are locally variable but range from about 3 to 7%, and the average value for the maximum lithic size is 2.2 cm across. In the western Wassuk Range, the maximum average lithic lengths are 1.7 and 2.2 cm, obtained from two closely spaced 0.5-m² areas. Interestingly, some of the lithics have fluidal morphologies and quenched rinds suggesting these are magma globbs as opposed to accidental fragments. To the north about 5 km, the vitrophyre contains about 2-3% lithics. Clast counts from the basal vitrophyre yield maximum average lithic lengths of 2.6 and 2.8 cm. Several larger clasts (5-6 cm across) were also noted outside the areas in which the clast count data were obtained. In the Gillis Range (Fig. 1), the basal vitrophyre of the Guild Mine Member contains about 3% lithics, and the maximum average lithic length is 4.7 cm. A few outsized clasts are up to 12-13 cm, but most have lengths of 2-4 cm. While the values presented here lack statistical significance, the lithic data suggests that the source for the Guild Mine Member is closer in proximity to the northern Gillis Range (Fig. 1).

Highly lithic-rich horizons in which the amount of lithics exceeds 50% occur sporadically in the basal portions of several sections of the Guild Mine Member. Near Mickey Pass in the Singatse Range (Fig. 1), a highly lithic-rich zone (>50%) occurs approximately 3 meters above the base of the Guild Mine Member. It consists of densely packed, angular clasts, which range up to 5 cm in length, surrounded by devitrified plagioclase and biotite crystal rich ash-flow tuff. The densely packed breccia zone is up to 0.5 meters thick and laterally discontinuous on the scale of the outcrop. At the base of the thick section of the Guild Mine Member near Guild-Bovard Mine, a similar lithic-rich zone is perpendicular to the compaction foliation of the host tuff. The

zone is 15 to 30 cm wide and is traceable up section for about 5 m. The composition of the lithics is predominantly Jurassic basement lithologies, including abundant metamorphosed andesite volcanic fragments. In the northern Gillis Range at Eagle Wash Canyon, a unique occurrence of an extremely lithic-rich zone is near the basal contact of the Guild Mine Member with the underlying Triassic metavolcanic rocks. At this locality, the vitrophyric matrix surrounds and entrains the lithics in diffuse zones broadly parallel to bedding. The zones thicken and thin rapidly along strike, ranging from 1 m to 15 cm thick over a lateral distance of 1 m. The lithics are subangular to round with measurements of select clasts ranging from 16 to 30 cm, and they include a diverse suite of lithologies such as limestone, friable argillite/shale, and Triassic metavolcanic rock fragments.

The basal vitrophyre is overlain by densely welded, chocolate brown, crystal-rich, devitrified tuff, which characterizes the lower part of the Guild Mine Member (Unit 1 of Proffett and Proffett, 1976). Most commonly the contact is abrupt on the scale of individual outcrops with the densely welded, chocolate-brown tuff directly overlying the basal vitrophyre. Several localities exhibit transitional vitric/devitrified zones, consisting of some 5 meters of dominantly devitrified material with thin (<0.3 m), discontinuous zones of vitrophyre. At some localities, a distinctive eutaxitic structure is evident in the incipiently devitrified tuff overlying the vitrophyre. The devitrified, chocolate brown tuff in the lower part of the Guild Mine Member contains conspicuous plagioclase and biotite phenocrysts and lesser amounts of sanidine and quartz crystals. As a rule, fiamme are small (<1 cm) and difficult to discern on outcrops. In the field, the chocolate brown tuff occurs both as low, rubbly exposures and as prominent ridge-forming outcrops.

In several sections, columnar joints occur sporadically throughout the lower and middle parts of the Guild Mine Member. In the Singatse Range (Fig. 1), the sizes of the

individual columns tend to decrease with increasing stratigraphic position. Individual columns in the lower part of the unit range from 0.5 to 1 m in diameter and have lengths up to 6 m. Higher in the section, individual columns have diameters up to 15 cm and lengths up to 0.5 m. In the eastern part of the Buckskin Range (Fig. 1), poorly developed columnar joints are present in the lower 30 meters of the Guild Mine Member; here individual columns have diameters of 0.3 m and lengths of up to 1 m. In the northern Gillis Range (Fig. 1), the lower part of the Guild Mine Member lacks columnar joints but instead displays a distinct platy jointing that is roughly parallel to the compaction foliation; the distance between individual joints is 1-3 cm.

Moving up section, the Guild Mine Member displays gradational changes with respect to the size and degree of flattening of fiamme. Also, the unit shows a systematic increase in the amount of quartz and sanidine phenocrysts and a concurrent decrease in the amount of plagioclase and biotite phenocrysts, as described below. These gradational changes in the Guild Mine Member mark the diffuse boundary between Units 1 and 2 as defined by Proffett and Proffett (1976). Unit 2, which typically occurs in low rubbly outcrops, consists of lavender, crystal-rich, moderately welded tuff containing abundant crystals of quartz, sanidine, plagioclase, and a trace of biotite. The first appearance of distinct, partially flattened white pumices is defined as the boundary between Units 1 and 2. In the lower parts of Unit 2, the pumices are generally flattened and are up to 5 cm long and 1 cm wide. Many are weathered out, but where preserved, they appear as white streaks against a lavender backdrop. With increasing stratigraphic position, the pumices become progressively more inflated and increase in size, ranging up to 10 cm across, although most are only up to 5 cm in length. Near the upper part of Unit 2, the tuff consists of a pink devitrified groundmass with abundant moderately flattened to largely inflated, white pumices, which are up to 6 cm long in their flattened

direction. The upper part of Unit 2 displays vapor phase alteration, which tends to accentuate the white, inflated pumices giving them a sugary appearance.

The crystal content decreases with increasing stratigraphic position from 25-30% crystals in lower part of Unit 2 to about 15% crystals in the upper part of the unit. Quartz and sanidine are the primary phases in Unit 2. Most of the quartz phenocrysts are rounded and embayed, but some have bipyramidal outlines. The sanidine phenocrysts are blocky and euhedral in hand sample. Plagioclase occurs in subordinate amounts, and a small amount of biotite is present. Small lithics (up to 5 mm) are few and far between in Unit 2.

The uppermost part of the Guild Mine Member (Unit 3 of Proffett and Proffett, 1976) consists of about 12 meters of moderately crystal rich (7-10 %), poorly welded to nonwelded, pale lavender to pink tuff with abundant, white, inflated pumices. In the Singatse Range (Fig. 1), pumices are usually up to about 5 cm across. In the northern Gillis Range, one particularly large pumice is 28 cm long and 10 cm wide, and another is completely inflated with dimensions of 7 cm by 10 cm. A few, small lithics (up to 5 mm across) are also present in the uppermost part of the Guild Mine Member. The uppermost part of the Guild Mine Member may represent a co-ignimbrite ash-fall deposit, because it is relatively crystal poor compared to the main part of the member, and no cooling break was observed between it and the main part of the member.

Field Description of the Intermember Ash-Flow Tuffs and Sedimentary Rocks

At various sections, the Guild Mine and Weed Heights Members are separated by a sequence of ash-flow tuffs and volcaniclastic sedimentary rocks (Units 4 and 5 of Proffett and Proffett, 1976). The intermember deposits are well exposed in the

representative section of the MPT near Mickey Pass (Fig. 1), where they are 44.5 m thick. Here, the pink, uppermost part of the Guild Mine Member (Unit 3) is directly overlain by a dominantly white, poorly welded, pumice-rich, 26.5-m-thick ash-flow tuff (Unit 4 of Proffett and Proffett, 1976); the upper 1 meter of the tuff is vapor phase altered to a pink color. The 26.5-m-thick, white tuff is conformably overlain by an 18-m-thick sequence consisting of several thin ash-flow tuffs and interbedded volcanoclastic sedimentary rocks (Unit 5 of Proffett and Proffett, 1976). Directly overlying the 26.5-m-thick ash-flow tuff is a 1.5-m-thick rock consisting of thinly bedded (<1 cm), gray to green, medium- to fine-grained, crystal-rich volcanoclastic sandstone. A 6-m-thick poorly welded ash-flow tuff directly overlies the fine-grained sandstone. The contact is irregular and scalloped, indicating that the tuff may have foundered into the wet, fine-grained sediments when it was deposited. Overlying the thin tuff are about 3 meters of poorly stratified, red to pink, coarse-grained, rhyolitic volcanoclastic sandstones. This in turn is overlain by a 8-m-thick sequence consisting of several, thin (1-2 m thick) poorly welded ash-flow tuffs intercalated with at least one, thin (<1 m thick), fine-grained volcanoclastic sandstone bed.

The thickest of the intermember rhyolite ash-flow tuffs is exposed at several other localities in the Singatse Range. At the section about 1/2 mile south-southwest of Weed Heights (Fig. 1), the intermember tuff between the Guild Mine and Weed Heights Members is approximately 7 meters thick but thins rapidly along strike. The ash-flow tuff here is moderately welded with partially flattened pumices up to several centimeters across. The tuff, which is characteristically white to pink on fresh surfaces and greenish on weathered surface, contains a phenocryst assemblage of round and embayed quartz, blocky sanidine, tabular plagioclase, and biotite. The intermember tuff contains $\approx 1-2\%$ lithics that are subround and up to 2 cm across.

To the south along strike in the Singatse Range (due west of the town of Mason, Nevada), the Guild Mine Member is missing, and the intermember ash-flow tuff sits unconformably upon the Jurassic basement rocks and is overlain by the Weed Heights Member. The 30-m-thick tuff is moderately to poorly welded with abundant lithics (3-5 %) and is overall crystal poor with biotite and sanidine being the dominant phenocrysts. The base of the unit is marked by a dense, black, 3.6-m-thick vitrophyre that grades upward into 1.5 meters of gray vitrophyre. The remainder of the unit consists of devitrified, characteristically lithic-rich, white to cream ash-flow tuff with white, mostly inflated pumices up to ≈ 3 centimeters across. The lithics are generally subangular to subround and range from a few millimeters to 9 cm in length, with most measuring between 4 and 5 cm in length. The composition of the lithics is primarily quartzite and an altered plagioclase-rich volcanic rock fragment similar in composition and appearance to the Jurassic metamorphosed andesite flows that are exposed in the Buckskin Range (Fig. 1). On outcrop, the tuff is highly fractured, which is attributed to abundant small-scale faults with displacements ranging up to 2 meters. Several fragments of petrified wood (one is ≈ 10 cm across) occur within the lithic-rich tuff and are inferred to represent carbonized wood fragments that have been silicified.

The intermember sequence lacks any paleosol horizons between the individual ash-flow tuff and sedimentary rock units.

Field Description of the Weed Heights Member

The upper cooling unit of the MPT is the Weed Heights Member, which has its type section in the Singatse Range about 1/2 mile SSW of the town of Weed Heights (Fig. 1; Proffett and Proffett, 1976). The Weed Heights Members is well exposed in the

Singatse Range, in the Buckskin Range, in the western and northern parts of the Wassuk Range, and in the northern Gillis Range (Fig. 1). Where the contact between the intermember tuff and the Weed Heights Member is exposed west of Mason, it is sharp but slightly irregular with small (<1 cm) erosional scours evident in the top of the intermember tuff.

At most sections throughout its distribution, the base of the Weed Heights Member is marked by a thin, gray vitrophyre. The vitrophyre is lacking at sections studied in the Buckskin Range and in the northern Wassuk Range (Fig. 1). Where present in the Singatse Range, the vitrophyre ranges from 1 to 3 meters thick, and in the western Wassuk Range, it is up to 5.5 m thick. In the Singatse and western Wassuk Ranges, the vitrophyre is moderately welded and consists of a gray groundmass with partially flattened shards that display a well-developed vitroclastic texture in hand specimen. Partially flattened, light gray fiamme are up to 2 cm across at the type section of the Weed Heights Member in the Singatse Range, and they are up to 4 cm in length at the 76-m-thick section of the unit in the western Wassuk Range. The fiamme display slightly lower crystal contents than the host bulk tuff. The crystal content is nearly 25 % in the basal vitrophyre and includes abundant plagioclase, sanidine, quartz, and biotite phenocrysts. Also noteworthy, is the paucity of lithics in the lower parts of the Weed Heights Member in the Buckskin, Singatse, and western Wassuk Ranges. Where observed, however, they are subround to subangular and at most are up to 3 cm in length.

In the Singatse and Wassuk Ranges (Fig. 1), the transition from the gray, basal vitrophyre to the overlying devitrified tuff is abrupt on the scale of individual outcrops. The devitrified tuff is cream to white on fresh surface and contains crystals of quartz, sanidine, biotite, and plagioclase in about the same proportions as the basal vitrophyre. Lithics are sparsely present in the lower part of the Weed Heights Member and are 1-2

cm across. Transitionally overlying the white to cream devitrified tuff in the lower part of the unit is pale pink to lavender devitrified tuff that makes up the bulk of the middle and upper parts of the Weed Heights Member. A distinguishing characteristic of the middle part of the Weed Heights Member is abundant (15%), moderately flattened, white pumices that are conspicuous against a pinkish red groundmass. In the Singatse Range, pumices are up to 5 cm across, and in the western Wassuk Range, they are up to 7 cm in length and have widths up to 1.5 cm. Most of the pumices are quite small, however, with lengths up to 1 cm across. Poorly developed columnar joints are evident in the middle parts of several sections of the Weed Heights Member. Where measured in the Buckskin Range, individual columns have diameters of 0.2 m and lengths of 0.8 m. A few small lithics (up to 3 cm in length) occur sporadically throughout the middle and upper parts of the unit. The middle part of the unit contains approximately 15-20% crystals consisting of plagioclase, biotite, quartz, and sanidine. In its middle to upper parts, the Weed Heights Member is characterized by a orange to deep red groundmass with abundant, white to buff, partially flattened pumices that display devitrification textures such as lithophysae and spherulites.

The uppermost part of the Weed Heights Member consists of 9 to 11 meters of pink, poorly welded to non-welded, vapor phase altered tuff. Pumices, which range up to 9 cm across, are partially flattened to inflated and display devitrification and recrystallization textures, including spherulites and lithophysae. The uppermost part of the unit is moderately to poorly crystal rich containing sanidine and quartz phenocrysts and a small proportion of biotite (<1 %). On outcrop the vapor phase altered tuff either forms low, nondescript outcrops or occurs in several meter high, resistant hoodoos, especially prominent on the east side of the Buckskin Range.

In the northern Gillis Range, the lower part of Weed Heights Member differs from the base of the unit in the Wassuk, Singatse, and Buckskin Ranges (Fig. 1). Instead of

a vitrophyric base, the lower part of the unit grades from devitrified, poorly welded tuff upward into gray vitrophyre and then into black vitrophyre. The lowermost part of the Weed Heights Member in the northern Gillis Range consists of a 2.7-m-thick zone of devitrified, poorly welded, lithic-rich, and pumice-rich tuff. Lithics, which are subangular to round, make up approximately 5% of the vitrophyre, and the average value for the maximum lithic length is 2.5 cm although several range up to 5 cm in length. The abundance and size of lithics in the northern Gillis Range is in marked contrast to the Weed Heights Member in localities farther to the west. In addition to the lithics, black vitrophyric fragments up to 5.1 cm long are evident. The morphology of the vitrophyre inclusions ranges from round to flattened with flame-like terminations and may represent fragments that were cannibalized from the vent during eruption. The lithic-rich devitrified tuff at the base grades vertically upward into 0.9-m-thick zone of gray vitrophyre, which in turn grades upward into 7.8-m-thick, black, moderately welded vitrophyre. Fiamme in the black vitrophyre are partially flattened and have measures up to 6 cm in length by 2 cm wide in plan view. The black vitrophyre is overlain by pink to lavender devitrified, moderately welded tuff that is similar to the middle and upper parts of the Weed Heights Member at other localities. Pumices are white and partially flattened with dimensions that are up to 6 cm by 2 cm in plan view. Lithic abundance drops considerably in the devitrified tuff (0.5-1 %), and the largest lithic noted is up to 3 cm.

The Weed Heights Member is overlain by a thin sequence of tuffaceous sedimentary rocks that separate the MPT from the Singatse Tuff.

Petrography

Petrographic study was undertaken to provide constraints on the crystallization sequence, to document disequilibrium textures and other evidence for petrologic processes such as magma mixing, and to use as a data base to check the credibility of calculated crystal-fractionation models presented in a later section. Proffett and Proffett (1976) carefully documented the mineralogic zonation for the Guild Mine and Weed Heights Members using point counts on stratigraphically controlled samples, and the results of their work are confirmed by the visual estimates of phenocryst modes presented herein (Fig. 3).

Both members of the MPT contain phenocrysts of plagioclase, biotite, and Fe-Ti oxides throughout the compositional range represented by each member (Fig. 3). In addition to these phases, the dacite in the lower part of the Guild Mine Member contains clinopyroxene, orthopyroxene, hornblende, and a small amount of sanidine but lacks quartz. Quartz becomes a principal phase in the rhyodacite and rhyolite in the middle and upper parts of the Guild Mine Member. The high-silica rhyolite near the top of the Guild Mine Member lacks clinopyroxene, orthopyroxene, and hornblende (Fig. 3). In addition to the ubiquitous plagioclase, biotite, and Fe-Ti oxides, the rhyodacite at the base of the Weed Heights Member contains clinopyroxene, orthopyroxene, hornblende, sanidine, and quartz (Fig. 3). Clinopyroxene, orthopyroxene, and hornblende are lacking in the rhyolite in the middle and upper parts of the Weed Heights Member.

A large proportion of the plagioclase phenocrysts in both members display varying degrees of breakage, but the intact crystals are subhedral and euhedral. In the Guild Mine Member, individual plagioclase crystals are up to 2.7 mm in length, and in the Weed Heights Member, they are up to 4.3 mm long. Some of the plagioclase phenocrysts display disequilibrium textures such as embayed margins and resorbed

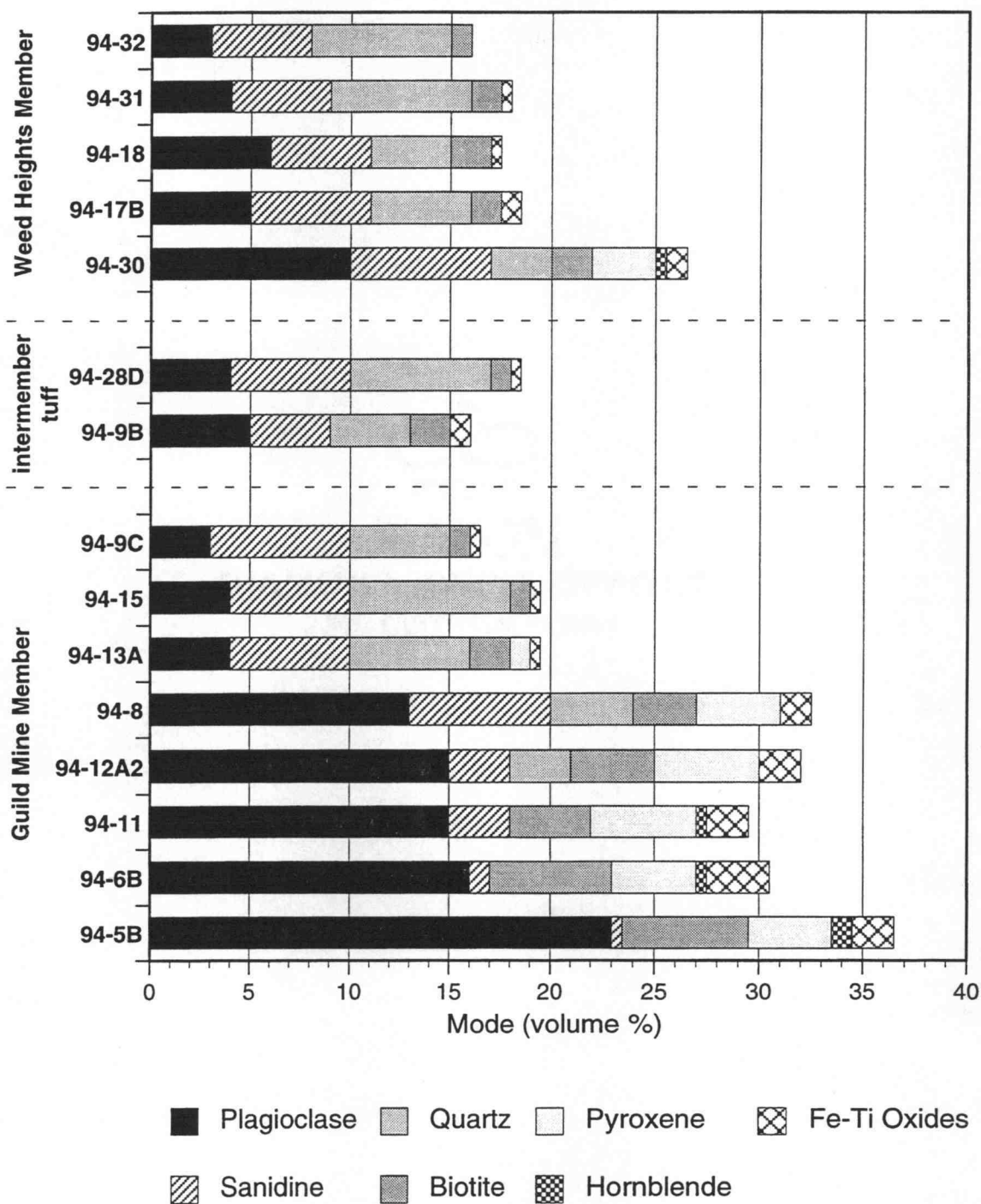


Figure 3a: Modes of select samples of the Guild Mine and Weed Heights Members of the MPT and the rhyolite ash-flow tuff between the two members based on visual estimates. Refer to Table 2 for bulk-tuff geochemical data.

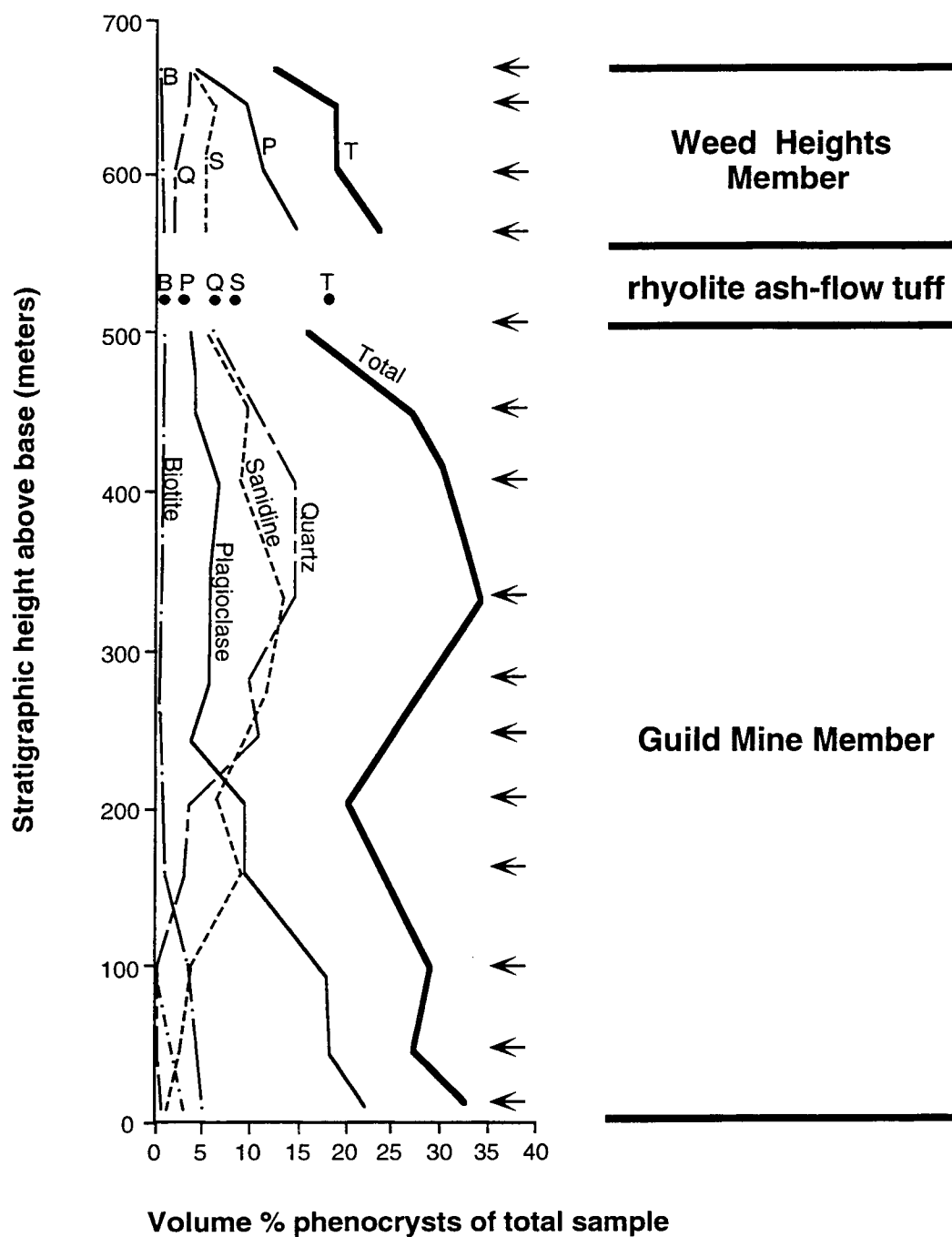


Figure 3b: Graph showing phenocryst types and abundances for the Guild Mine and Weed Heights Members of the Mickey Pass Tuff from the type sections in the Singatse Range (Fig. 1) and for the rhyolite ash-flow tuff separating the members. Arrows indicate the positions of samples (after Proffett and Proffett, 1976). All the samples are bulk tuff.

interiors; this becomes progressively more pronounced in the upper portions of both members of the MPT. Well-developed normal and oscillatory zoning is evident in many grains. In some grains, the cores display twinning while the rims lack twinning, suggesting at least two phases of crystal growth for these particular grains.

Sanidine phenocrysts in the lower part of the Guild Mine Member typically occur as subhedral and anhedral crystals from 0.5 to 1.2 mm long, which are heavily scalloped and embayed along their margins. In the middle and upper parts of the Guild Mine Member, the sanidine phenocrysts are generally larger (1.0 to 3.0 mm long) and occur as euhedral and subhedral crystals that exhibit progressively smaller amounts of disequilibrium textures with increasing stratigraphic position in the unit. Sanidine phenocrysts in the Weed Heights Member are up to 2.9 mm long and exhibit a range in morphologies from euhedral to anhedral crystals. Although some of the sanidine crystals in the Weed Heights Member exhibit blocky outlines, most are rounded and embayed to some degree, and in some cases, the grain margins are intensely scalloped.

Quartz, while not present in the dacite in the lower part of the Guild Mine Member, becomes an important phase in the rhyodacite and rhyolite in the middle and upper parts of the Guild Mine Member (Fig. 3). The quartz phenocrysts in the Guild Mine Member are up to 2.7 mm long, generally occur as subhedral and anhedral crystals, and display scalloped grain margins and resorbed interiors. In the Weed Heights Member, the quartz exhibits distinct morphological changes from the base to the top of the unit. Quartz phenocrysts in the lower parts of the Weed Heights Member are smaller (up to 1.3 mm) and generally occur as subhedral and anhedral crystals with scalloped margins and some resorption in the interiors of grains. In the upper part of the Weed Heights Member, the quartz phenocrysts are up to 3.0 mm across and show a range from euhedral to anhedral crystal morphologies. While many of the quartz phenocrysts in the

upper part show some degree of disequilibrium, some display pseudo-hexagonal outlines and show only minor amounts of resorption.

Biotite phenocrysts in the dacite and rhyodacite in the lower and middle parts of the Guild Mine Member occur as euhedral and subhedral crystals, range up to 1.9 mm long, and are typically aligned parallel to the compaction foliation. In some cases, the biotite phenocrysts are contorted around other types of phenocrysts and lithic fragments. Although most of the biotite phenocrysts in the dacite and rhyodacite are fresh appearing, a small number of grains exhibit skeletal morphology. Overall, the biotite phenocrysts in the rhyolite in the upper part of the Guild Mine Member are smaller (up to 0.5 mm in length) and occur as euhedral and subhedral crystals, although some crystals have irregular margins and skeletal morphologies. Zircon inclusions occur sporadically in some of the biotite crystals. In the Weed Heights Member, the biotite phenocrysts typically occur as euhedral and subhedral crystals that are up to 2 mm long. Most of the biotite phenocrysts from the basal rhyodacite are relatively fresh appearing. A common feature of biotite phenocrysts in both members of the MPT is that with increasing stratigraphic height in each tuff the biotite phenocrysts show progressive degrees of alteration ranging from grains that are preferentially oxidized to hematite along cleavage planes and crystal margins to phenocrysts that are completely oxidized to hematite.

Clinopyroxene and orthopyroxene phenocrysts occur in small quantities in the dacitic, rhyodacitic, and rhyolitic portions of the Guild Mine Member and are absent from the high-silica rhyolite at the top (Fig. 3). The clinopyroxene phenocrysts are generally intact crystals up to 1.3 mm long, but some of the clinopyroxene crystals are broken. Most of the clinopyroxene phenocrysts occur as discrete crystals, but some are intergrown with Fe-Ti oxide crystals forming glomerocrysts. Some of the clinopyroxene phenocrysts contain fine-grained Fe-Ti oxide inclusions. In the lower to

middle part of the Guild Mine Member, the clinopyroxene phenocrysts are primarily fresh appearing, euhedral and subhedral crystals. Where present in the higher parts of the tuff, they are ragged and appear to be out of equilibrium, displaying alteration to a fine-grained low-birefringence mineral that appears tan under uncrossed polars. The orthopyroxene phenocrysts in the Guild Mine Member typically occur as intact crystals, up to 0.9 mm across, that exhibit a range of morphologies from euhedral to anhedral depending on their stratigraphic position within the tuff. Some of the orthopyroxene phenocrysts are resorbed and embayed along their margins. Most of the orthopyroxene crystals occur as discrete crystals, but some are intergrown with plagioclase-forming glomerocrysts. In the Weed Heights Member, clinopyroxene and orthopyroxene phenocrysts are confined to the rhyodacite at the base of the unit. The clinopyroxene phenocrysts are subhedral and anhedral crystals up to 1.2 mm long with irregular grain margins, and the orthopyroxene phenocrysts are euhedral to anhedral crystals up to 1.5 mm long and display morphologies that are somewhat skeletal.

Hornblende is a sparse phase in both members of the MPT and is strictly confined to the lower parts of each tuff (Fig. 3). In the Guild Mine Member, the hornblende phenocrysts occur as small, generally subhedral crystals (up to 1.0 mm across) that in some cases display resorbed and embayed margins. The hornblende phenocrysts in the Weed Heights Member, occurs as relatively fresh appearing, euhedral and subhedral crystals up to 0.9 mm across.

Fe-Ti oxide phenocrysts in the dacitic and rhyodacitic portions of the Guild Mine Member are 0.4 mm across on average and range up to 1.0 mm across. They are typically subhedral and anhedral crystals, but in some instances, they are euhedral. Minor amounts of secondary hematite are evident along the margins of some grains. In the upper rhyolitic part of the Guild Mine Member, the Fe-Ti oxide phenocrysts are notably smaller (about 0.2 mm across), occur strictly as anhedral and subhedral crystals,

and are partially to completely altered to hematite. Fe-Ti oxide phenocrysts in the Weed Heights Member share many of the same characteristics as those in the Guild Mine Member. They are up to 0.6 mm across and occur as subhedral and anhedral crystals, many of which have irregular margins that are embayed and resorbed.

Apatite and zircon are the most common trace phases within the MPT. Apatite typically occurs as very fine-grained, elongate, euhedral crystals up to 0.2 mm long that are generally present as inclusions in plagioclase phenocrysts. The abundance of apatite crystals appears to be greater in the lower, less evolved parts of each member and becomes less abundant in the upper, more evolved parts of each member. Zircon is present in all parts of the MPT, although its abundance also varies with stratigraphic position. Most notably, zircon is sparsely present in the dacite at the base of the Guild Mine Member. Overall, zircon occurs as extremely fine-grained, mostly anhedral and subhedral crystals up to 0.1 mm across. Zircon occurs both as discrete crystals dispersed throughout the groundmass and as inclusions within biotite, pyroxene, and plagioclase phenocrysts. Some of the zircon is metamict, and in a few cases, alteration haloes are evident in the enclosing phenocrysts. Titanite may be present in the rhyodacitic parts of the Weed Heights Member, although the examples are altered and too turbid appearing for conclusive identification. Allanite and monazite were not observed within the MPT.

Bulk-Tuff Composition

Because of the high degrees of welding and, in most cases, pervasive devitrification that characterize both members of the MPT, single fiamme samples are nearly impossible to extract. Therefore, bulk-tuff analyses coupled with mineral and glass

compositions are utilized primarily for the chemical study. During eruption and emplacement, pyroclastic flow deposits may undergo elutriation of the fine-grained vitric ash component, causing the resulting deposit to be enriched in crystals, and thus, the composition of the bulk tuff commonly differs from the original magmatic composition (Lipman, 1967; Walker, 1972; Wolff, 1985). Even though analyses of bulk-tuff samples may only represent a minimum range of magma compositions tapped for a given sampled section, stratigraphically controlled bulk tuff samples have been successfully utilized to document systematic compositional variations in continental silicic magma systems (Hildreth, 1979; Whitney and Stormer, 1985; Fridrich and Mahood, 1987; Grunder and Mahood, 1987; Boden, 1989; Broxton and others, 1989). As done in this study, it is imperative to ensure high-quality results that accidental lithic fragments are meticulously removed and that the crystal contents and proportions in fiamme and bulk tuff are considered.

The major and trace element data are presented in Table 2. Geochemical sample locations are provided in Appendix B. To highlight the similarities in major and trace element trends between the Guild Mine and Weed Heights Members and the rhyolite ash-flow tuff between the members, the chemical data for all these units are plotted together. While the samples from the MPT have elevated total alkali contents and plot barely inside the trachydacite field according to the IUGS classification system (Fig. 4; Le Bas and others, 1986), they are referred to as dacites herein based on the usage of Proffett and Proffett (1976). The terms rhyolite and high-silica rhyolite are utilized for samples with 72-75 wt. % SiO_2 and more than 75 wt. % SiO_2 , respectively, and the term rhyodacite (Streckeisen, 1979) is used for samples with 68-72 wt. % SiO_2 between dacite and rhyolite compositions (all values recalculated to 100% volatile-free; Fig. 4).

Table 2: Whole-rock compositions of the MPT and related samples.

	<i>Guild Mine Member</i>							
	<u>94-5B</u>	<u>94-6B</u>	<u>94-11</u>	<u>94-7</u>	<u>94-12A</u>	<u>94-8</u>	<u>94-13A</u>	<u>94-15</u>
	<i>vbt</i>	<i>vbt</i>	<i>vbt</i>	<i>vbt</i>	<i>vbt</i>	<i>vbt</i>	<i>vbt</i>	<i>dbt</i>
<u>normalized XRF analyses (wt. %)</u>								
SiO ₂	66.6	67.0	67.8	67.2	69.0	70.3	75.4	78.1
Al ₂ O ₃	16.6	16.5	16.3	16.8	15.9	15.4	13.6	12.1
TiO ₂	0.47	0.46	0.44	0.47	0.40	0.36	0.17	0.10
FeO*	3.43	3.31	3.03	3.23	2.78	2.38	1.18	0.90
MnO	0.08	0.08	0.08	0.08	0.07	0.06	0.05	0.02
CaO	3.27	3.20	2.92	3.23	2.60	2.25	1.03	0.67
MgO	1.23	1.07	1.07	1.09	0.90	0.76	0.15	0.19
K ₂ O	4.15	4.09	3.70	3.34	4.10	4.11	4.47	4.90
Na ₂ O	4.01	4.16	4.50	4.49	4.14	4.25	3.96	3.01
P ₂ O ₅	0.15	0.15	0.14	0.15	0.12	0.10	0.03	0.02
TOTAL§	99.13	98.99	98.66	98.49	98.71	98.93	98.78	100.17
<u>XRF analyses (ppm)</u>								
V	41	51	43	38	42	22	nd	nd
Ni	4	4	4	7	4	6	9	10
Cu	8	8	5	6	3	8	5	9
Zn	61	62	60	65	57	55	41	33
Ga	19	23	21	19	18	19	17	17
Rb	109	115	130	111	131	145	258	201
Sr	472	453	427	472	379	322	120	54
Ba	1553	1557	1754	1817	1588	1410	420	138
Y	18	18	17	17	17	17	23	22
Zr	228	234	240	247	225	211	138	97
Nb	9.9	11.2	10.3	10.7	10.6	11.2	15.9	16.3
Pb	21	23	20	21	20	24	29	25
<u>INAA analyses (ppm)</u>								
Sc	6.78	---	5.60	5.94	5.17	4.82	3.03	2.79
Cr	10.8	---	6.3	6.9	5.5	4.6	nd	nd
Co	6.16	---	4.94	5.11	4.03	3.51	0.82	0.72
Cs	5.55	---	5.54	4.61	5.93	5.48	8.73	3.65
As	8.7	---	8.8	8.3	8.8	8.8	10.3	6.7
Sb	0.98	---	1.04	1.02	1.16	1.18	1.34	1.16
Se	1.17	---	nd	1.32	0.74	1.32	2.43	2.32
La	42.2	---	43.0	41.7	44.7	48.4	43.1	36.2
Ce	74	---	77	75	81	84	78	68
Nd	27	---	28	28	29	28	29	25
Sm	4.47	---	4.56	4.32	4.48	4.75	5.23	4.83
Eu	1.14	---	1.08	1.16	1.01	0.99	0.46	0.32
Tb	0.38	---	0.40	0.39	0.34	0.39	0.50	0.47
Yb	1.81	---	1.59	1.55	1.81	1.64	2.05	2.22
Lu	0.28	---	0.23	0.24	0.25	0.29	0.29	0.28
Hf	6.25	---	6.77	6.34	6.17	6.09	4.56	4.37
Ta	0.59	---	0.63	0.58	0.63	0.69	1.12	1.32
Th	12.40	---	12.00	11.40	14.40	14.80	21.70	24.10
U	3.78	---	4.02	3.62	4.56	6.39	8.80	5.60

Major element oxides normalized to 100% volatile-free values. § denotes total is pre-normalization.

FeO* is total iron expressed as FeO. nd = not detected. --- = not analyzed. † denotes value is >120% of WSU's highest standard. vbt = vitric bulk tuff; dbt = devitrified bulk tuff; dp = devitrified pumice; bfr = bulk flow rock.

Table 2: *cont.*

	<i>Guild Mine Member</i>							
	<u>94-9C</u>	<u>94-9C(f)</u>	<u>93-36</u>	<u>93-38</u>	<u>93-62</u>	<u>92-22</u>	<u>94-72B</u>	<u>92-127B</u>
	<i>dbt</i>	<i>dp</i>	<i>vbt</i>	<i>dbt</i>	<i>vbt</i>	<i>dbt</i>	<i>vbt</i>	<i>vbt</i>
<u>normalized XRF analyses (wt. %)</u>								
SiO ₂	77.8	71.6	67.8	69.1	67.7	72.9	76.7	66.1
Al ₂ O ₃	12.4	15.9	16.3	15.7	16.2	14.8	13.2	16.9
TiO ₂	0.11	0.08	0.43	0.40	0.43	0.29	0.14	0.47
FeO*	0.92	0.74	3.23	3.00	3.12	1.89	0.97	3.49
MnO	0.04	0.04	0.08	0.05	0.08	0.02	0.05	0.08
CaO	0.64	0.94	3.06	2.31	3.14	1.36	0.94	4.04
MgO	0.25	0.19	0.92	0.86	0.91	0.23	0.06	1.22
K ₂ O	5.17	†7.31	3.53	4.41	4.10	4.96	3.81	3.85
Na ₂ O	2.74	3.25	4.51	3.99	4.21	3.43	4.20	3.76
P ₂ O ₅	0.02	0.02	0.14	0.13	0.14	0.10	0.02	0.15
TOTAL§	99.78	98.53	99.14	100.61	99.10	100.07	99.08	98.70
<u>XRF analyses (ppm)</u>								
V	6	nd	23	36	33	15	4	40
Ni	11	17	7	5	8	8	12	5
Cu	13	7	8	8	3	5	5	10
Zn	28	22	59	61	58	50	33	66
Ga	16	20	16	17	20	18	17	16
Rb	195	†315	136	120	118	152	200	122
Sr	79	67	527	334	411	194	88	818
Ba	272	133	1671	1533	1574	1046	311	1582
Y	17	16	17	18	18	19	22	16
Zr	101	53	236	226	237	192	113	237
Nb	14.1	15.9	9.0	9.8	9.6	11.1	16.9	7.9
Pb	22	12	19	21	18	21	27	19
<u>INAA analyses (ppm)</u>								
Sc	2.56	---	5.67	5.38	5.68	4.14	---	6.75
Cr	nd	---	7.6	6.1	8.4	4.0	---	12.4
Co	0.68	---	4.88	4.09	4.66	1.98	---	5.84
Cs	4.03	---	6.33	2.62	5.28	3.79	---	11.60
As	12.6	---	9.0	3.1	9.4	4.7	---	9.0
Sb	0.37	---	1.08	0.78	1.02	1.11	---	0.96
Se	2.30	---	nd	1.09	1.29	1.04	---	1.36
La	28.8	---	43.3	44.6	43.5	46.4	---	39.2
Ce	55	---	74	81	79	84	---	67
Nd	19	---	26	30	29	30	---	26
Sm	3.51	---	4.52	4.65	4.52	4.71	---	4.07
Eu	0.36	---	1.10	1.01	1.09	0.77	---	1.14
Tb	0.27	---	0.45	0.45	0.48	0.50	---	0.43
Yb	1.69	---	1.87	2.03	1.89	2.02	---	1.73
Lu	0.25	---	0.29	0.29	0.30	0.31	---	0.27
Hf	3.74	---	6.51	6.04	6.46	5.73	---	5.92
Ta	1.17	---	0.61	0.67	0.64	0.88	---	0.59
Th	20.60	---	13.10	13.10	12.60	17.60	---	11.10
U	3.79	---	4.37	4.72	4.05	5.75	---	3.29

Major element oxides normalized to 100% volatile-free values. § denotes total is pre-normalization.

FeO* is total iron expressed as FeO. nd = not detected. --- = not analyzed. † denotes value is >120% of WSU's highest standard. vbt = vitric bulk tuff; dbt = devitrified bulk tuff; dp = devitrified pumice; bfr = bulk flow rock.

Table 2: *cont.*

	<i>Guild Mine Member</i>						
	<u>93-49B</u>	<u>92-123</u>	<u>94-76D</u>	<u>94-76E1</u>	<u>93-40</u>	<u>93-46A</u>	<u>93-46E</u>
	<i>vbt</i>	<i>dbt</i>	<i>vbt</i>	<i>vbt</i>	<i>vbt</i>	<i>dbt</i>	<i>dbt</i>
<u>normalized XRF analyses (wt. %)</u>							
SiO ₂	67.6	75.9	75.0	74.8	65.7	69.0	74.1
Al ₂ O ₃	16.5	13.5	14.0	14.1	16.9	15.8	13.9
TiO ₂	0.43	0.18	0.20	0.20	0.49	0.39	0.22
FeO*	2.97	0.95	0.87	1.02	3.74	2.91	1.70
MnO	0.07	0.01	0.04	0.03	0.08	0.07	0.06
CaO	3.05	0.80	1.37	1.40	3.65	2.57	1.63
MgO	0.90	0.16	0.03	0.23	1.26	0.42	0.31
K ₂ O	3.61	4.97	5.08	5.12	3.61	5.56	5.02
Na ₂ O	4.70	3.43	3.39	3.07	4.35	3.23	3.00
P ₂ O ₅	0.14	0.05	0.04	0.06	0.15	0.12	0.05
TOTAL§	99.65	101.17	98.70	98.31	99.57	100.14	99.67
<u>XRF analyses (ppm)</u>							
V	38	16	10	13	53	29	18
Ni	7	9	9	10	5	7	8
Cu	8	4	4	5	10	8	6
Zn	60	37	28	36	66	52	46
Ga	19	17	15	16	19	19	13
Rb	119	183	179	184	125	145	163
Sr	442	93	173	165	552	328	123
Ba	1804	519	666	601	1683	1410	699
Y	17	13	19	21	18	17	19
Zr	238	148	128	127	240	215	166
Nb	9.4	13.5	17.0	16.4	8.8	9.7	12.0
Pb	18	17	17	22	15	21	26
<u>INAA analyses (ppm)</u>							
Sc	5.97	3.29	3.52	---	7.22	5.59	3.36
Cr	7.6	2.6	4.6	---	15.3	6.4	3.1
Co	5.07	0.97	0.90	---	6.17	3.58	1.78
Cs	6.94	3.70	8.10	---	10.30	14.30	5.41
As	7.6	3.5	15.6	---	10.2	4.8	3.8
Sb	1.03	1.14	1.95	---	1.01	3.50	1.54
Se	0.94	1.37	1.57	---	nd	nd	1.19
La	43.4	39.2	32.5	---	39.6	41.9	48.0
Ce	76	76	62	---	69	73	87
Nd	28	27	22	---	29	24	29
Sm	4.46	4.10	4.63	---	4.28	4.21	4.55
Eu	1.15	0.58	0.59	---	1.18	1.04	0.69
Tb	0.47	0.39	0.34	---	0.41	0.42	0.62
Yb	1.91	1.81	1.80	---	2.13	1.70	2.03
Lu	0.26	0.26	0.24	---	0.26	0.25	0.29
Hf	6.88	4.91	4.70	---	6.29	5.62	5.08
Ta	0.65	1.13	1.09	---	0.58	0.63	0.90
Th	12.70	21.90	20.20	---	10.80	12.40	18.90
U	1.29	6.77	8.09	---	4.12	4.19	4.83

Major element oxides normalized to 100% volatile-free values. § denotes total is pre-normalization.

FeO* is total iron expressed as FeO. nd = not detected. --- = not analyzed. † denotes value is >120% of WSU's highest standard. vbt = vitric bulk tuff; dbt = devitrified bulk tuff; dp = devitrified pumice; bfr = bulk flow rock.

Table 2: *cont.*

	<i>Weed Heights Member</i>					
	<u>94-30</u>	<u>94-17B</u>	<u>94-18</u>	<u>94-31</u>	<u>94-32</u>	<u>92-87</u>
	<i>vbt</i>	<i>dbt</i>	<i>dbt</i>	<i>dbt</i>	<i>dbt</i>	<i>dbt</i>
<u>normalized XRF analyses (wt. %)</u>						
SiO ₂	71.5	73.2	74.3	75.5	75.2	73.5
Al ₂ O ₃	15.5	14.7	14.4	13.5	13.7	14.6
TiO ₂	0.35	0.29	0.25	0.18	0.19	0.31
FeO*	1.52	1.51	1.35	1.18	1.09	1.94
MnO	0.04	0.01	0.01	0.02	0.02	0.03
CaO	2.36	1.53	1.16	1.07	1.08	1.15
MgO	0.62	0.35	0.24	0.15	0.16	0.27
K ₂ O	3.94	4.88	4.78	4.80	4.85	4.79
Na ₂ O	4.12	3.50	3.43	3.55	3.66	3.25
P ₂ O ₅	0.08	0.07	0.07	0.05	0.05	0.17
TOTAL§	98.97	99.72	99.51	99.76	101.02	100.12
<u>XRF analyses (ppm)</u>						
V	36	23	11	20	38	28
Ni	8	10	7	8	22	9
Cu	5	5	7	7	6	5
Zn	44	40	46	36	35	45
Ga	17	18	19	18	16	17
Rb	194	154	156	184	179	153
Sr	318	222	167	125	130	182
Ba	1183	954	817	488	516	1006
Y	19	15	15	19	18	15
Zr	187	165	151	120	126	170
Nb	14.1	12.7	13.1	15.7	16.1	12.5
Pb	24	25	23	25	17	23
<u>INAA analyses (ppm)</u>						
Sc	5.20	4.40	---	3.21	---	4.80
Cr	8.4	7.8	---	4.5	---	8.6
Co	2.03	2.18	---	1.15	---	1.87
Cs	7.16	4.01	---	4.93	---	2.93
As	11.8	3.7	---	7.9	---	4.9
Sb	1.61	1.14	---	1.39	---	1.77
Se	1.27	1.57	---	2.01	---	1.03
La	40.5	42.9	---	32.6	---	41.0
Ce	74	80	---	64	---	73
Nd	26	30	---	25	---	26
Sm	4.60	4.49	---	4.46	---	4.22
Eu	0.91	0.88	---	0.55	---	0.82
Tb	0.44	0.34	---	0.39	---	0.54
Yb	1.73	1.43	---	1.79	---	1.74
Lu	0.26	0.24	---	0.25	---	0.26
Hf	5.70	5.12	---	4.35	---	5.13
Ta	0.87	0.85	---	1.15	---	0.88
Th	16.90	17.40	---	20.80	---	17.60
U	6.53	4.39	---	4.41	---	5.26

Major element oxides normalized to 100% volatile-free values. § denotes total is pre-normalization.

FeO* is total iron expressed as FeO. nd = not detected. --- = not analyzed. † denotes value is >120% of WSU's highest standard. vbt = vitric bulk tuff; dbt = devitrified bulk tuff; dp = devitrified pumice; bfr = bulk flow rock.

Table 2: *cont.*

	<i>intermember ash-flow tuff</i>			<i>early Tertiary lava flow</i>	<i>Hu Pwi lava flow</i>
	94-9B	94-28D	94-33A	92-106	93-61
	<i>vbt</i>	<i>dbt</i>	<i>vbt</i>	<i>bfr</i>	<i>bfr</i>
<u>normalized XRF analyses (wt. %)</u>					
SiO ₂	74.8	76.1	71.6	60.6	66.6
Al ₂ O ₃	14.3	13.6	15.1	15.8	16.1
TiO ₂	0.24	0.14	0.33	0.75	0.49
FeO*	1.23	1.15	1.98	5.66	3.52
MnO	0.03	0.03	0.05	0.12	0.07
CaO	2.48	1.08	1.85	6.60	3.65
MgO	0.45	0.17	0.58	4.85	1.50
K ₂ O	3.76	3.94	4.60	1.62	3.95
Na ₂ O	2.69	3.79	3.92	3.83	3.91
P ₂ O ₅	0.06	0.03	0.10	0.21	0.16
TOTAL§	97.64	97.90	98.55	100.22	99.21
<u>XRF analyses (ppm)</u>					
V	5	2	20	147	74
Ni	11	11	8	21	18
Cu	1	5	5	15	6
Zn	37	41	50	72	66
Ga	15	16	17	21	19
Rb	101	170	168	114	124
Sr	†877	76	256	717	513
Ba	1031	166	1279	864	1151
Y	14	20	19	19	19
Zr	165	112	211	147	179
Nb	12.9	17.4	12.2	7.9	12.7
Pb	17	27	25	10	22
<u>INAA analyses (ppm)</u>					
Sc	3.45	3.23	4.24	19.50	---
Cr	5.1	nd	3.2	220.0	---
Co	1.43	1.21	2.74	19.00	---
Cs	12.70	33.50	6.84	8.12	---
As	11.4	5.4	12.0	6.2	---
Sb	2.71	1.34	1.37	0.75	---
Se	1.43	2.37	1.24	nd	---
La	35.2	32.9	50.6	22.7	---
Ce	66	65	91	46	---
Nd	25	25	30	20	---
Sm	3.81	4.89	4.96	4.32	---
Eu	0.67	0.40	0.84	1.05	---
Tb	0.19	0.41	0.34	0.52	---
Yb	1.46	1.96	2.05	2.05	---
Lu	0.29	0.25	0.31	0.28	---
Hf	4.41	4.38	6.29	3.90	---
Ta	0.93	1.31	0.76	0.58	---
Th	19.70	23.60	17.50	8.23	---
U	3.46	5.36	5.05	3.07	---

Major element oxides normalized to 100% volatile-free values. § denotes total is pre-normalization.

FeO* is total iron expressed as FeO. nd = not detected. --- = not analyzed. † denotes value is >120% of WSU's highest standard. vbt = vitric bulk tuff; dbt = devitrified bulk tuff; dp = devitrified pumice; bfr = bulk flow rock.

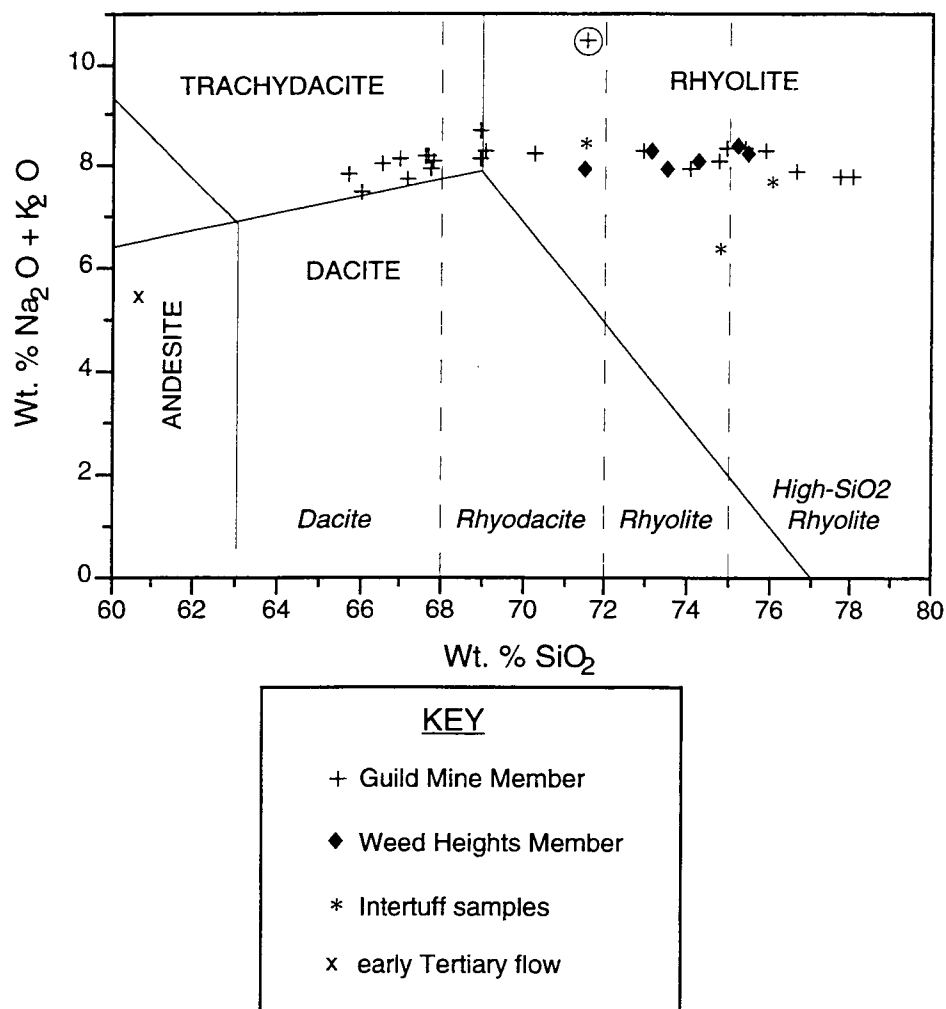


Figure 4: Total alkalis versus silica variation diagram for the MPT. The IUGS classification scheme is shown for reference (Le Bas and others, 1986). The nomenclature utilized within this report is superimposed in italics. All data recalculated to 100% volatile-free values. Devitrified pumice sample encircled.

Major Element Data

The bulk-tuff samples of the Guild Mine Member range from dacite at the base to high-silica rhyolite at the top (Fig. 4; 65.7-78.1 wt. % SiO_2). The Weed Heights Member displays a more limited compositional range from rhyodacite at its base to high-silica rhyolite at the top (Fig. 4; 71.5-75.5 wt. % SiO_2). The dacites and rhyodacites of the Guild Mine Member are metaluminous, whereas the rhyolites from the Guild Mine Member and all the samples from the Weed Heights Member are slightly peraluminous, which presumably reflects secondary loss of alkalis during hydration and weathering.

On Harker variation diagrams (Fig. 5), the overall similarity in the trends between the individual units of the MPT is illuminated. Both members of the MPT systematically decrease in TiO_2 , Al_2O_3 , CaO , Na_2O , MnO , and P_2O_5 concentrations with increasing SiO_2 . FeO^* and MgO also decrease with increasing SiO_2 , but the trends for these elements tend to flatten out in the most evolved samples (Fig. 5). Both Na_2O and MnO scatter considerably compared to other major elements. K_2O is the only major element that exhibits a slight increase with increasing SiO_2 . Note also, that for the Guild Mine Member, there is an apparent compositional gap in the bulk-tuff data that ranges from about 70 to 73 wt. % SiO_2 , excluding the pumice sample (Figs. 4 and 5).

Trace Element Data

Elemental enrichment and depletion patterns for both members of the MPT highlight the compositional gradients within the pre-eruptive magma chamber (Fig. 6). To maintain consistency with other studies that have utilized enrichment factor diagrams (Hildreth, 1979; Mahood, 1981; Ferriz and Mahood, 1987; Broxton and others, 1989),

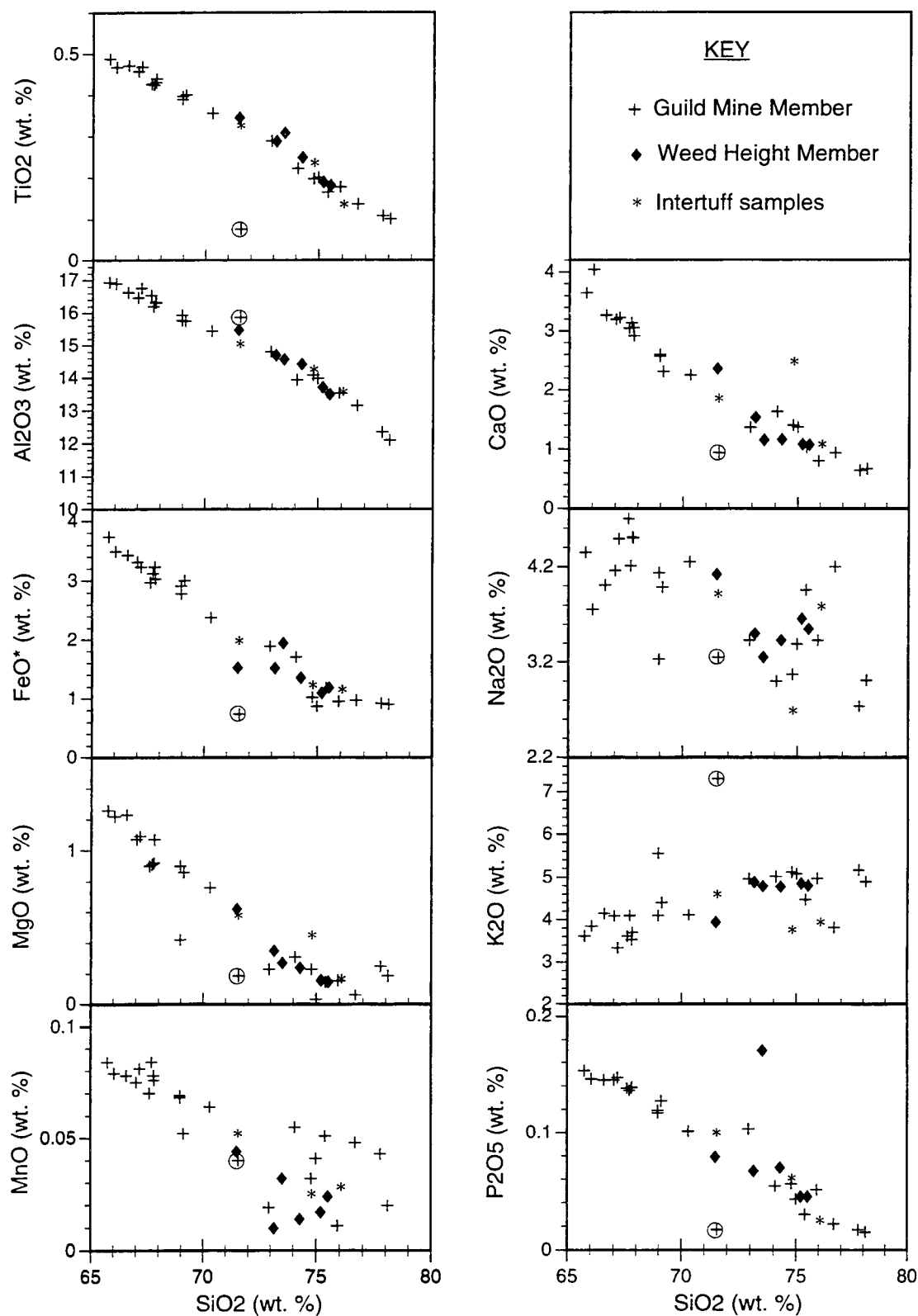


Figure 5: Harker variation diagrams for the MPT. All data recalculated to 100% volatile-free values. Devitrified pumice sample encircled.

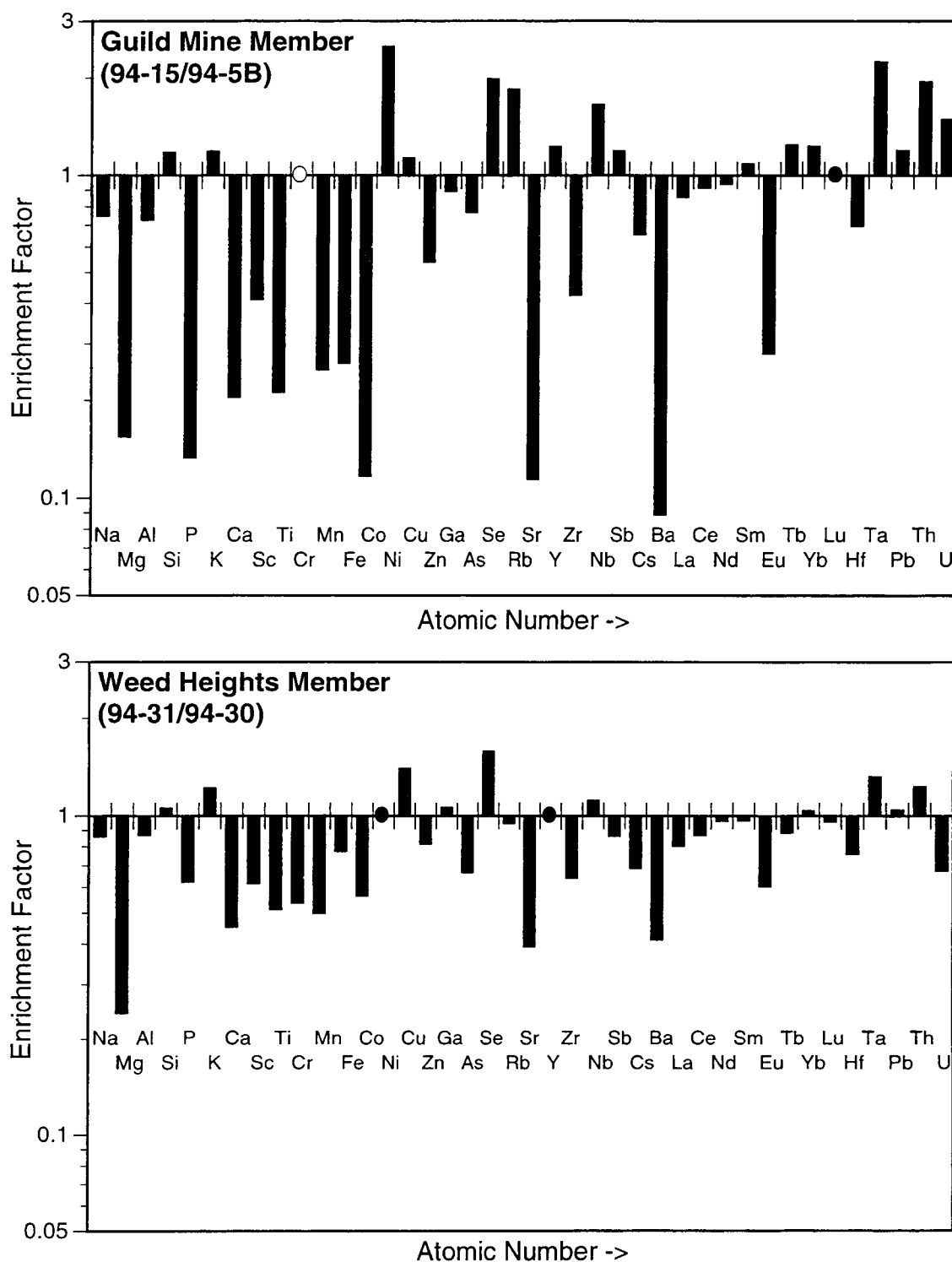


Figure 6: Enrichment factor diagrams. Enrichment factors are determined by dividing the element concentration in the most evolved sample by the element concentration in the least evolved sample. Elements are listed in order of increasing atomic number. ○ = element was not detected in one of the samples; ● = element concentrations are equal in each member, so the enrichment factor equals one.

element concentrations in the most evolved samples from each member are divided by the element concentrations in the less evolved samples. As noted on the Harker variation diagrams (Fig. 5), Si and K are enriched in the most evolved samples, and Mg, Fe, Ca, Ti, P, and Mn are depleted. In terms of trace element concentrations, Sc, Cr, Co, Zn, As, Sr, Zr, Cs, Ba, and Hf are moderately to strongly depleted in the most evolved parts of both members, and Cu, Se, Nb, Ta, Pb, and Th are slightly to moderately enriched (Fig. 6). Some elements show contrasting patterns between the two members: Rb, Sb, and U are enriched in the most evolved parts of the Guild Mine Member and slightly depleted in the Weed Heights Member; Ni and Y are enriched in the most evolved parts of the Guild Mine Member and constant in the Weed Heights Member; and Ga is slightly depleted in the most evolved parts of the Guild Mine Member and slightly enriched in the Weed Heights Member. For the rare-earth elements (REEs), the most evolved samples of both members are depleted in light REEs (Fig. 6). In the Guild Mine Member, except for Eu, both the middle REEs and the heavy REEs are enriched in the most evolved part. In the Weed Heights Member, the middle REEs and the heavy REEs are depleted in the most evolved part, except for Yb, which is slightly enriched (Fig. 6).

The enrichment factor diagrams provide a first-order assessment of the phases that were most likely fractionating to produce the more evolved compositions. The depletion of Al, Ca, Sr, Ba, and Eu in the most evolved parts of both members is consistent with feldspar fractionation throughout the crystallization sequence. The depletion of Mg, Sc, Ti, Mn, Fe, and Co in the most evolved parts of both members is consistent with crystallization and removal of mafic phases, such as biotite, hornblende, pyroxene, and Fe-Ti oxides. The depletion of P, Zr, Hf, and the light REEs in the most evolved parts of both members is consistent with fractionation of accessory phases, such as apatite, zircon, allanite, and/or monazite. The concentrations of a few elements, most notably

Rb, increase with increasing differentiation, even though they are compatible with one or more phases in the observed assemblage.

Numerous element-element variation diagrams were plotted to provide specific constraints on the crystallization sequence and fractionation processes. Because they are both particularly good at emphasizing specific aspects of the petrogenesis and crystallization history, SiO_2 and Ta are utilized as differentiation indices in the following discussion (Figs. 7 and 8). A key aspect of the MPT that is manifest on the variation diagrams is the comparable data trends between the individual members.

For both members of the MPT, Ba, Sr, and Eu decrease systematically with increasing differentiation, indicating that plagioclase is fractionating throughout the entire crystallization scheme. On a variation diagram plotting Sr vs. Ta (Fig. 8), Sr exhibits a rapid decrease with increasing differentiation, showing that plagioclase was a dominant fractionating phase during the early stages of crystallization and that its importance continued throughout differentiation. The variation of K/Ba ratio with SiO_2 indicates that fractionation of sanidine, which preferentially incorporated Ba relative to K, began to significantly affect the bulk-tuff composition at ≈ 70 wt. % SiO_2 (Fig. 7). The dacitic and rhyodacitic portions of the Guild Mine Member have the lowest K/Ba ratios, which increase with increasing SiO_2 . The pronounced break between the gentle linear part and the strong curved part on the K/Ba vs. SiO_2 variation diagram (Fig. 7) is interpreted to represent the onset of sanidine crystallization and concomitant Ba depletion.

The marked decrease in Sc and Cr between the dacitic and rhyodacitic parts of the Guild Mine Member (65.5-69 wt. % SiO_2), which is especially evident on the variation diagrams with Ta (Fig. 8), indicates that clinopyroxene fractionation played a key role early in the crystallization scheme. The continuous depletion of Sc with increasing differentiation (after cessation of clinopyroxene crystallization) indicates that other

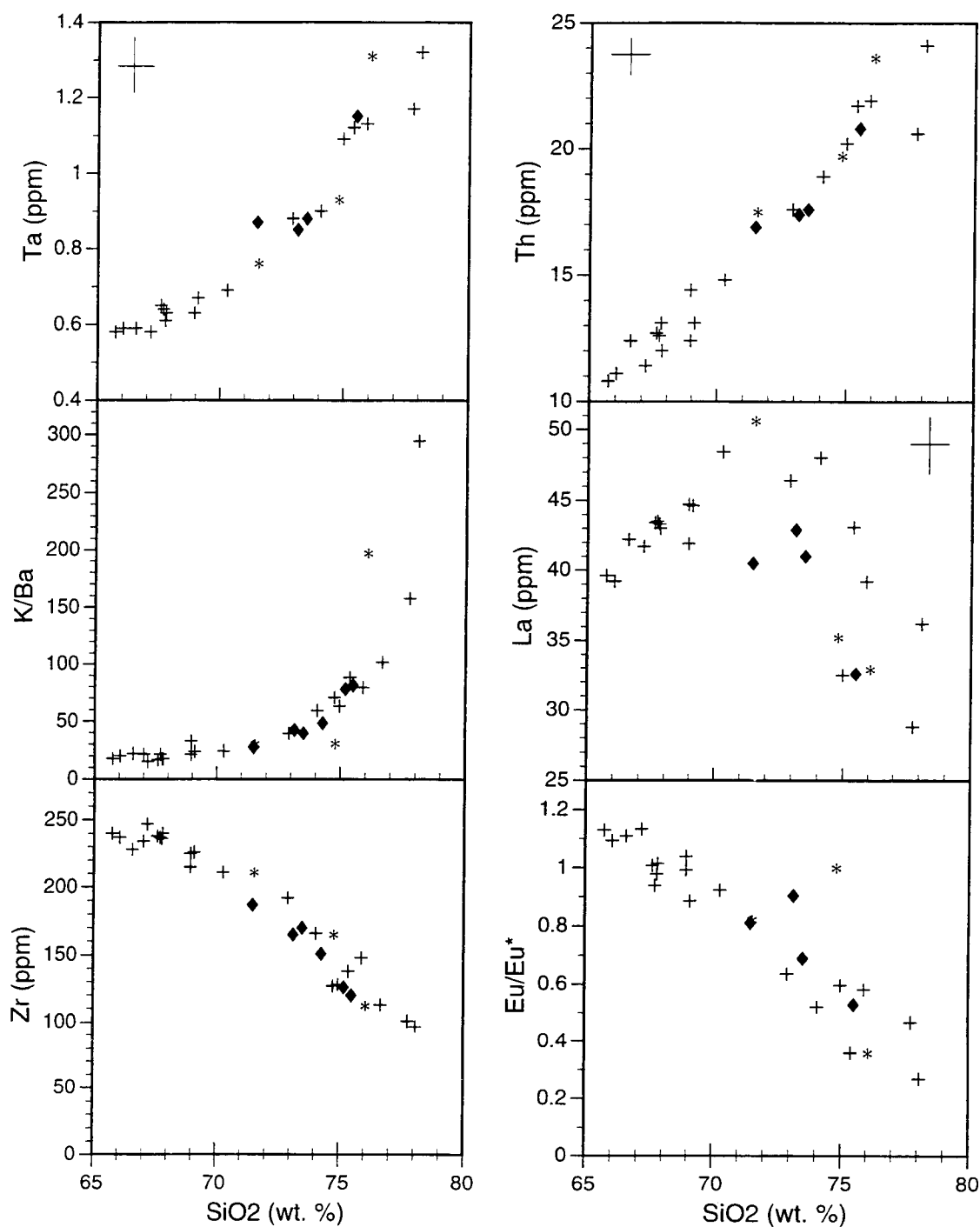


Figure 7: Variations of select trace elements with volatile-free SiO₂. Error bars are shown where typical analytical error (1-sigma relative precision) exceeds symbol size. Symbols the same as in Figures 5 and 8.

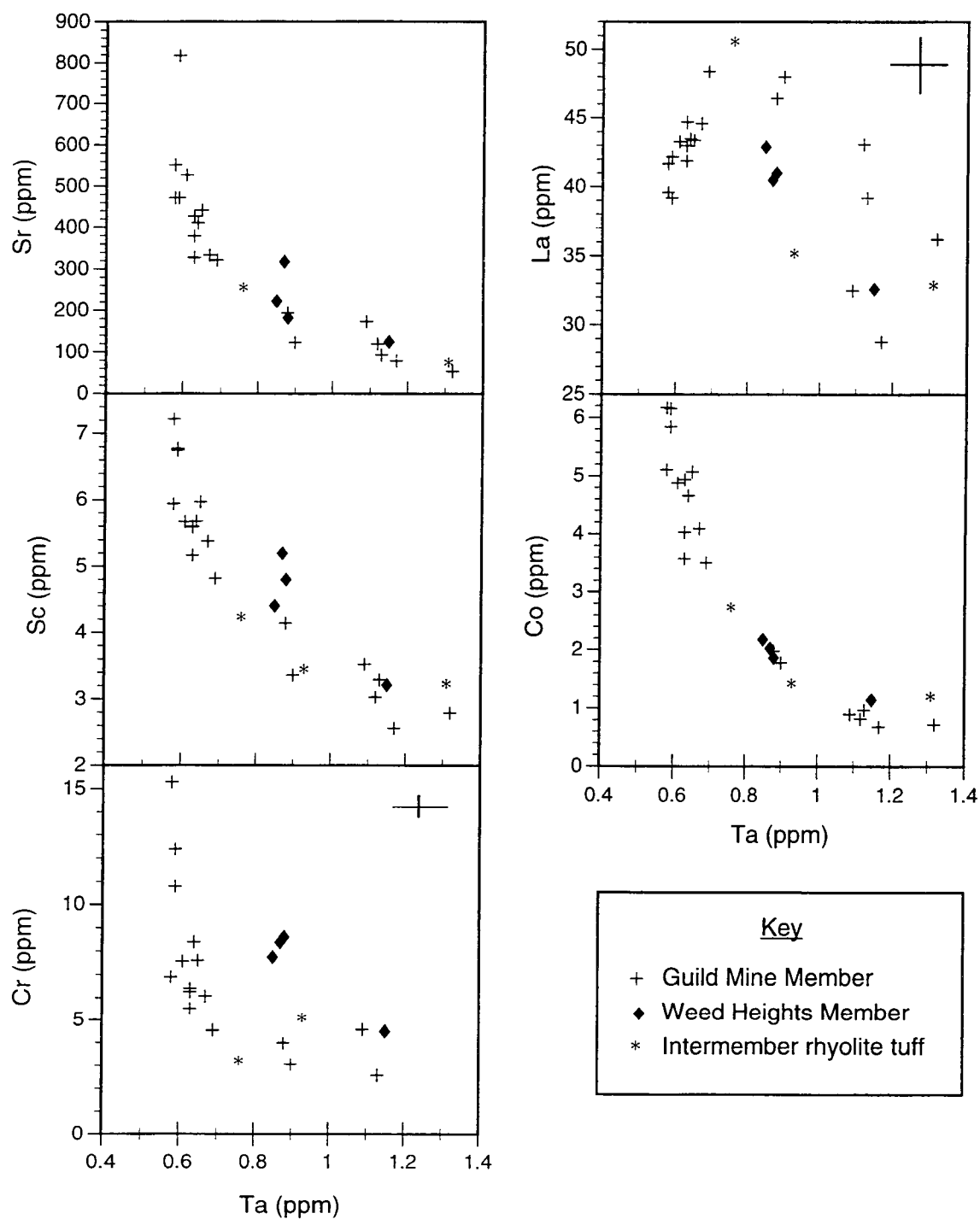


Figure 8: Variations of select trace elements with Ta. Error bars are shown where typical analytical error (1-sigma relative precision) exceeds symbol size.

phases that incorporated Sc, such as biotite and ilmenite, were fractionating throughout the crystallization scheme.

The role of biotite fractionation is assessed by considering the variations of Co with increasing differentiation. Co decreases steadily with increasing differentiation to ≈ 1.1 ppm Ta, which corresponds to ≈ 75 wt. % SiO_2 , where it levels off to a nearly flat trend. This trend indicates that biotite was fractionating through much of the crystallization history of the Guild Mine Member, and then it either stopped crystallizing or became a much less significant fractionating phase.

On a Zr vs. SiO_2 variation diagram (Fig. 7), Zr content is relatively constant from ≈ 65.5 to 68 wt. % SiO_2 , above which Zr decreases with increasing differentiation. Based on the presence of this distinct inflection and related inflections for Hf and Zr present on variation diagrams not shown here (Hf vs. SiO_2 and Zr vs. TiO_2 , respectively), zircon is interpreted to have formed fairly early in the crystallization sequence. Hf and Zr display similar trends with increasing differentiation, indicating that Hf is also compatible with zircon, as expected (partition coefficient for Hf in zircon is an average of 3193.5; Mahood and Hildreth, 1983).

The light REEs, specifically La and Ce, show interesting trends with increasing differentiation (cf., La, Figs. 7 and 8). For brevity, only La variations are discussed in depth, but Ce shows an identical trend. On a variation diagram plotting La vs. Ta (Fig. 8), La displays a steady increase with increasing differentiation to ≈ 0.75 ppm Ta, which corresponds to ≈ 72 wt. % SiO_2 (Fig. 7). At higher values of SiO_2 and Ta, the La content plummets (Figs. 7 and 8). The distinct drop in La and Ce values is interpreted to represent the crystallization of a light-REE enriched phase, such as allanite or monazite (cf., Miller and Mittlefehldt, 1982). In high-silica rhyolites, the distribution coefficient for La in allanite is an average of 2595 (Mahood and Hildreth, 1983), and thus only a small amount of crystallizing allanite would be necessary to affect the La

trend. While other phases, such as apatite, biotite, ilmenite, and zircon, have partition coefficients for the light REEs greater than one (Arth, 1976; Mahood and Hildreth, 1983; Nash and Crecraft, 1985), allanite is considered to be the most likely phase because the decrease in the light REEs is quite substantial.

The TiO_2 content decreases consistently with increasing SiO_2 (Fig. 5), indicating that some combination of ilmenite, biotite, and possibly titanite were crystallizing and being removed from the melt. The dramatic decrease in Cr contents with increasing differentiation from the dacitic to the rhyodacitic portions of the Guild Mine Member is also consistent with ilmenite fractionation (Fig. 8). The variation in the Ta trend with increasing differentiation (Fig. 7) signals a change in the bulk distribution coefficient for Ta, which is inferred to be controlled by ilmenite fractionation (partition coefficient for Ta in ilmenite is >100 ; Nash and Crecraft, 1985) and by the onset of zircon fractionation (partition coefficient for Ta in zircon is an average of 47.5; Mahood and Hildreth, 1983).

To further illustrate the vertical chemical zoning within the Guild Mine and Weed Heights Members of the MPT, REE data are plotted for select samples from the base to the top of both members (Fig. 9). The chondrite-normalized REE patterns are parallel, show light REE enrichment, and display relatively flat trends for the heavy REEs (Fig. 9). In general, the more evolved samples from the upper part of the Guild Mine Member have higher REE contents than the less evolved material, except for Eu. The negative Eu anomaly becomes progressively more pronounced with differentiation, which is emphasized on the Eu/Eu^* vs. SiO_2 variation diagram (Fig. 7). This indicates that plagioclase fractionation played a role in the petrogenesis of the Guild Mine Member (cf., Weill and Drake, 1973; Drake and Weill, 1975).

REE data from the deepest part of the Guild Mine Member across the study area show that there is minimal lateral variability in the composition of the tuff.

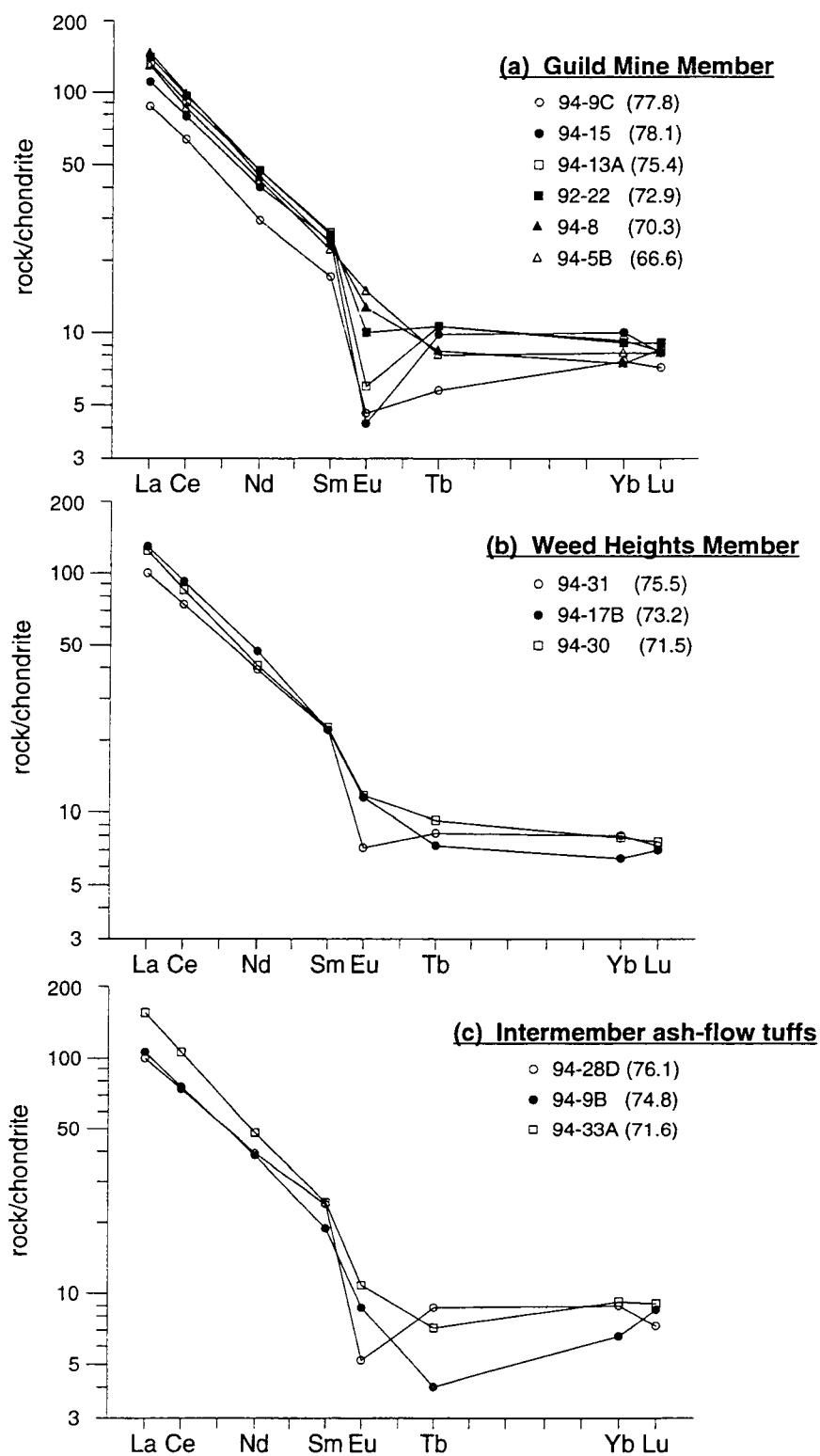


Figure 9: Rare-earth element diagrams for (a) the Guild Mine Member, (b) the Weed Heights Member, and (c) the intermember rhyolite ash-flow tuff. Samples are normalized to chondrite values after Nakamura (1974). Bulk-tuff, volatile-free SiO_2 contents are in parentheses.

Glass Analyses

To provide compositional data for the liquid portion of the magma at the time of eruption, the glass shards composing the matrix and the groundmasses of vitric fiamme in selected samples from the MPT were analyzed using the microprobe (Table 3). The glass analyses, as a group, range from rhyolite to high-silica rhyolite (volatile free), and as such, they are much more silicic than the whole rock samples in which the glass resides (compare Fig. 10 with Fig. 5). In both the Guild Mine and Weed Heights Members, the glass analyses define two general populations in terms of SiO_2 content. The slightly less evolved group of glasses forms a cluster between about 74 and 76 wt. % SiO_2 , and the slightly more evolved group forms a cluster between about 77 and 78.5 wt. % SiO_2 (Fig. 10).

Guild Mine Member

From the base to near the top of the Guild Mine Member, the glass analyses display a systematic decrease in Al_2O_3 , TiO_2 , CaO , and MgO contents with increasing SiO_2 (Fig. 10). The fiamme and groundmass shards in the bulk-tuff dacite at the base of the Guild Mine Member (94-5B) are composed of vitric material that ranges from 71.8 to 76.6 wt. % SiO_2 , but most of the analyses (83%) have SiO_2 contents between 74.3 and 76.0 wt. % and CaO contents from 0.85 to 1.0 wt. % (Fig. 10). A small number of the glass analyses from the bulk-tuff dacite are outside this cluster. The few outliers, which have lower SiO_2 contents (71.8-73.6 wt. %) and higher CaO contents (1.30-1.62 wt. %), are from a darker gray to brown fiamme. Only a couple of the analyses plot in the

Table 3: Representative glass analyses of the MPT.

<u>Sample #</u>	<u>94-5B</u>	<u>94-8</u>	<u>94-8</u>	<u>94-13A</u>	<u>94-30</u>	<u>94-30</u>
<u>Analysis #</u>	<u>gl15.3</u>	<u>gl3.2</u>	<u>gl10.1</u>	<u>gl11.2</u>	<u>gl4.2</u>	<u>gl12.3</u>
normalized analyses (wt. %)						
SiO ₂	75.3	75.8	77.7	77.6	75.3	78.0
Al ₂ O ₃	13.8	13.4	12.5	12.5	13.6	12.3
TiO ₂	0.18	0.15	0.09	0.09	0.22	0.12
FeO*	0.57	0.88	0.51	0.73	1.05	0.69
MnO	0.00	0.05	0.05	0.05	0.03	0.02
CaO	0.89	0.88	0.59	0.58	0.80	0.53
MgO	0.10	0.13	0.03	0.05	0.15	0.07
K ₂ O	5.13	4.86	4.81	4.47	4.75	4.41
Na ₂ O	4.00	3.80	3.72	3.90	3.99	3.86
P ₂ O ₅	0.00	0.04	0.00	0.05	0.08	0.00
Total§	96.2	95.94	97.29	96.74	96.37	96.66

Data normalized to 100% volatile-free values. § denotes total is pre-normalization. FeO* indicates total iron as FeO. Analyses were obtained using a defocused beam with a current of 30 nA and an accelerating voltage of 15 kV. Counting times: 10 seconds for all elements.

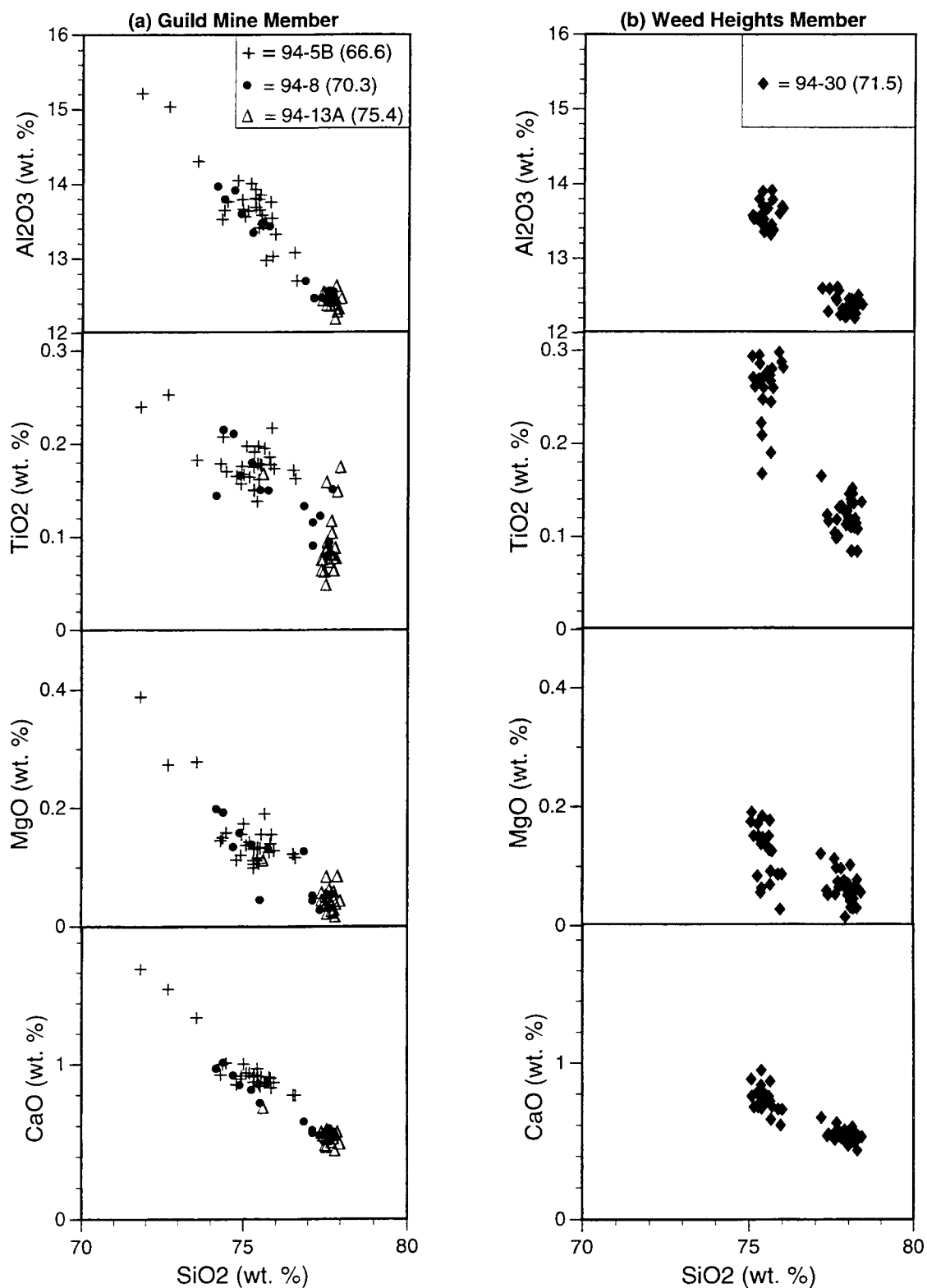


Figure 10: Harker variation diagrams for vitric flamme and ash shards in the groundmass of select samples from the MPT. All data recalculated to 100% volatile-free values. Refer to Table 1 for bulk-tuff compositions of each sample. Bulk-tuff, volatile-free SiO₂ contents are in parentheses.

gap between the two general groups of MPT glasses at about 76.5 wt. % SiO_2 (Fig. 10).

The fiamme and vitric groundmass in the whole-rock rhyodacite in the middle of the Guild Mine Member (94-8) display a range of SiO_2 contents from 74.2 to 77.8 wt % (Fig. 10). The glass analyses from the bulk-tuff rhyodacite are split equally among the two general populations that characterize the MPT as a whole. One group of glass analyses is slightly less evolved with SiO_2 contents between 74.2 and 75.8 wt. % and CaO contents between 0.75 and 1.0 wt. % (Fig. 10). The other group is slightly more evolved and has a more limited range of SiO_2 values, ranging from 76.9 to 77.8 wt. %, and lower CaO contents from 0.53 to 0.63 wt. % (Fig. 10).

All of the vitric shards and fiamme in the bulk-tuff rhyolite near the top of the Guild Mine Member (94-13A), except for one, are within the more evolved group of glasses. The glasses in the whole-rock rhyolite display a limited range of SiO_2 contents between 77.4 and 78.0 wt. % and have CaO contents between 0.44 and 0.58 wt. % (Fig. 10). The sole outlier is compositionally similar to the slightly less evolved group of glass analyses with 75.6 wt. % SiO_2 and 0.72 wt. % CaO.

Weed Heights Member

Glass analyses were obtained from fiamme and shards in the vitrophyric, bulk-tuff rhyodacite at the base of the Weed Heights Member (94-30). Compared to the Guild Mine Member, the Weed Heights glass analyses display a more limited range of SiO_2 contents from 75.1 to 78.4 wt. % (Fig. 10), in part reflecting the more limited sampling but in keeping with the more limited bulk compositional range. Nonetheless, the fiamme and vitric ash shards form two distinct clusters of data, which are

compositionally similar to the two glass populations identified in the Guild Mine Member (Fig. 10). Nearly half of the glass analyses (44%) cluster between SiO_2 contents of 75.1 and 76.0 wt. % and CaO contents of 0.60 and 0.95 wt. %. The remainder (56%) are slightly more evolved with SiO_2 contents between 77.2 and 78.4 wt. % and CaO contents between 0.44 and 0.65 wt. % (Fig. 10). The glass analyses from the Weed Heights Member exhibit an overall decrease in Al_2O_3 , TiO_2 , CaO, and MgO contents with increasing SiO_2 . In terms of TiO_2 , MgO, and CaO contents, however, there is some slight overlap between the less evolved and more evolved groups (Fig. 10).

Mineral Compositions

Mineral compositional data are utilized to document variations in the composition of phenocrysts with stratigraphic position in each member of the MPT and to place constraints on intensive parameters of the pre-eruptive MPT magma chamber. Because of the difficulty in extracting fiamme from both members of the MPT, the mineral content data augment the bulk-tuff chemical data, especially for showing compositional gradients. The complete set of mineral compositional data is tabulated in Appendix C.

Plagioclase

From the base to the top of both members of the MPT, the plagioclase phenocrysts display a systematic decrease in An content (Fig. 11). In general, the less evolved, lower parts of each member contain the most calcic plagioclase phenocrysts (up to $\text{An}_{76.5}$), and they become progressively more sodic (down to $\text{An}_{12.6}$) in the more

(a) Guild Mine Member

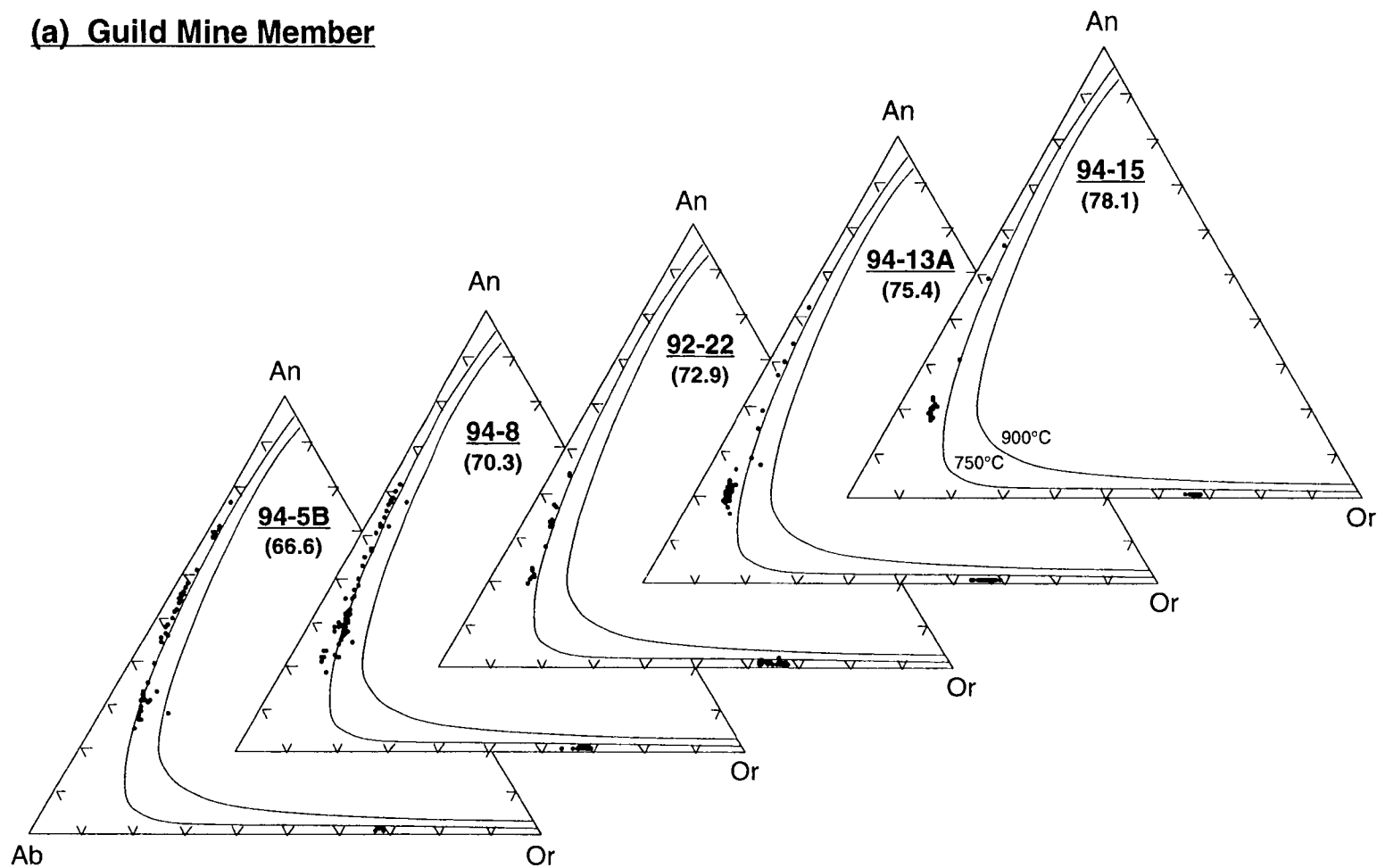


Figure 11: Feldspar compositional data from the MPT plotted on ternary feldspar diagrams. Sample numbers are in bold print, and bulk-tuff, volatile-free SiO_2 values are in parentheses. Isotherms (750°C at 1 kbar, 900°C at 0.5 kbar) are after Fuhrman and Lindsley (1988). Ternary compositions: Ab is albite ($\text{NaAlSi}_3\text{O}_8$); An is anorthite ($\text{CaAl}_2\text{Si}_2\text{O}_8$); and Or is orthoclase (KAlSi_3O_8). (a) Guild Mine Member.

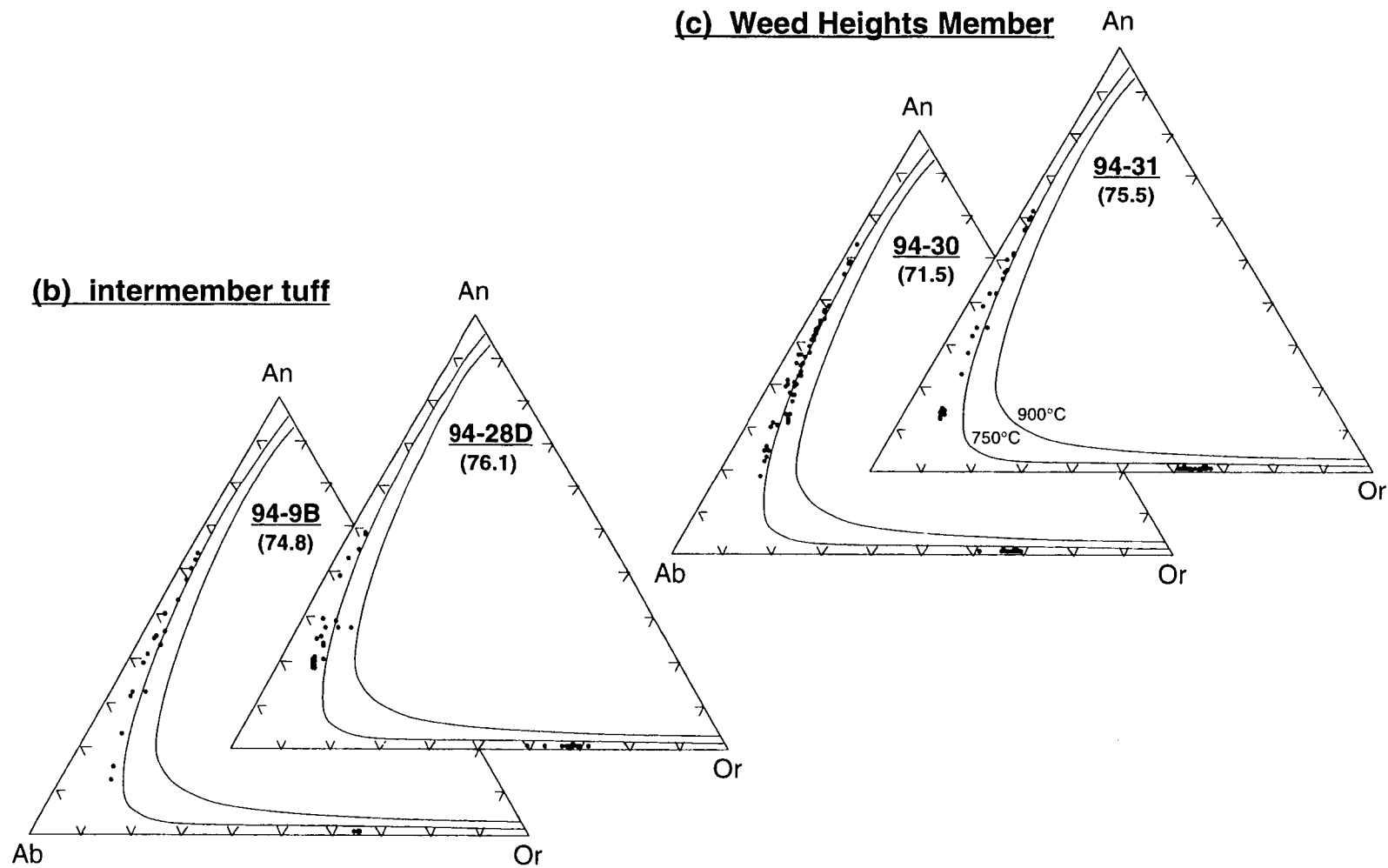


Figure 11: *continued.* (b) Weed Heights Member; (c) intermember rhyolite ash-flow tuff.

evolved, upper parts of both members. The zoning characteristics also vary systematically with increasing stratigraphic height. The predominant type of zoning in the plagioclase phenocrysts in the less evolved parts of both members is normal with some minor oscillatory zoning superimposed. Smaller plagioclase crystals in the less evolved samples lack significant zoning and are compositionally similar to the rims of the zoned phenocrysts. In the more evolved, upper parts of both members, the plagioclase phenocrysts also display normal zoning, but the range of An contents is limited to about 10 mol percent or less. In addition to the zoned crystals, many of the plagioclase grains in the more silicic parts of each member are homogeneous and display minimal zoning. Representative plagioclase analyses for the MPT are presented in Table 4.

Guild Mine Member

The dacite at the base of the Guild Mine Member (94-5B) contains plagioclase phenocrysts that range from bytownite ($An_{76.5}$) to oligoclase (An_{26}) with the bulk of the analyses ranging from labradorite to andesine (Fig. 11). Most of the plagioclase phenocrysts in the dacite display normal zoning, and in some grains minor oscillatory zoning is superimposed. Normally zoned grains have cores with $An_{76.5}$ - An_{50} and rims clustered around An_{30} (Fig. 11; Table 4). The smaller plagioclase phenocrysts within the dacite tend to lack zoning, although a few exhibit slight reverse zoning. Generally, the smaller plagioclase crystals have An contents that are similar to the rims of the more strongly zoned grains ($\approx An_{30}$; Table 4).

The plagioclase phenocrysts in the rhyodacite in the middle part of the Guild Mine Member (94-8) range from labradorite (An_{62}) to oligoclase (An_{19}) (Fig. 11). Overall, most of the plagioclase phenocrysts in the rhyodacite are normally zoned with minor oscillatory zoning superimposed. As in the basal dacite, the normal zoning in the

Table 4: Representative plagioclase analyses of the MPT.

<u>Sample #</u>	<u>94-5B</u>	<u>94-5B</u>	<u>94-5B</u>	<u>94-8</u>	<u>94-8</u>	<u>94-13a</u>	<u>94-13a</u>	<u>94-15</u>	<u>94-15</u>
<u>Analysis #</u>	<u>fe1.1</u>	<u>fe1.5</u>	<u>fe9.6</u>	<u>fe18.1</u>	<u>fe18.6</u>	<u>fe4.2</u>	<u>fe4.3</u>	<u>fe17.1</u>	<u>fe17.4</u>
<i>position</i>	<i>core</i>	<i>rim</i>	<i>core (sg)</i>	<i>core</i>	<i>rim</i>	<i>core</i>	<i>rim</i>	<i>core</i>	<i>rim</i>
SiO ₂	50.1	59.1	59.4	55.0	60.4	61.4	62.3	62.8	61.0
Al ₂ O ₃	31.6	25.0	25.1	28.7	25.0	24.3	23.3	23.6	23.2
FeO*	0.28	0.17	0.26	0.22	0.29	0.11	0.14	0.17	0.15
MgO	0.02	0.00	0.01	0.03	0.01	0.01	0.00	0.00	0.00
CaO	14.2	6.34	6.46	10.6	6.30	5.51	4.47	4.65	4.28
Na ₂ O	3.46	7.14	7.14	5.05	7.19	8.00	8.30	8.18	8.36
K ₂ O	0.24	1.33	1.13	0.43	1.11	0.92	1.18	0.92	1.06
BaO	0.06	0.24	0.14	0.06	0.09	0.02	0.03	0.02	0.01
Total	99.94	99.36	99.66	100.06	100.37	100.26	99.66	100.29	98.05
Ab	30.2	62.0	62.3	45.1	63.1	68.7	71.9	72.0	73.2
Or	1.4	7.6	6.5	2.5	6.4	5.2	6.7	5.3	6.1
An	68.4	30.4	31.2	52.4	30.5	26.1	21.4	22.6	20.7

<u>Sample #</u>	<u>92-22</u>	<u>92-22</u>	<u>94-30</u>	<u>94-30</u>	<u>94-31</u>	<u>94-31</u>	<u>94-28D</u>	<u>94-9B</u>	<u>94-9B</u>
<u>Analysis #</u>	<u>fe4.2</u>	<u>fe4.3</u>	<u>fe17.1</u>	<u>fe17.5</u>	<u>fe4.6</u>	<u>fe1.6</u>	<u>fe4.3</u>	<u>fe5.2</u>	<u>fe5.4</u>
<i>position</i>	<i>core</i>	<i>rim</i>	<i>core</i>	<i>rim</i>	<i>rim (sg)</i>	<i>rim (sg)</i>	<i>core (sg)</i>	<i>core</i>	<i>rim</i>
SiO ₂	59.3	62.0	54.5	59.6	63.9	58.9	62.8	54.1	58.6
Al ₂ O ₃	25.2	23.3	28.2	24.9	22.1	25.5	23.2	28.6	25.2
FeO*	0.25	0.18	0.31	0.31	0.13	0.25	0.15	0.27	0.20
MgO	0.02	0.00	0.03	0.01	0.00	0.03	0.00	0.03	0.01
CaO	6.87	4.41	10.5	6.81	2.84	6.93	4.07	10.4	6.61
Na ₂ O	6.97	8.21	5.20	6.77	9.04	7.02	8.35	5.57	7.39
K ₂ O	0.91	1.35	0.55	1.21	1.39	0.72	1.15	0.35	0.76
BaO	0.13	0.01	0.12	0.15	0.00	0.06	0.03	0.07	0.12
Total	99.62	99.47	99.45	99.77	99.37	99.34	99.80	99.40	98.97
Ab	61.3	71.2	45.7	59.7	78.4	62.0	73.6	48.2	64.0
Or	5.2	7.7	3.2	7.0	7.9	4.2	6.7	2.0	4.3
An	33.4	21.1	51.1	33.2	13.6	33.8	19.8	49.8	31.6

"sg" refers to single grain. FeO* indicates total iron as FeO. Analyses were obtained using a beam current of 30 nA and an accelerating voltage of 15 kV. Counting times: 10 seconds for Fe, Mg, Ca, Na, and K; 20 seconds for Si and Al; and 30 seconds for Ba.

plagioclase phenocrysts is pronounced, ranging from An_{62} to An_{50} in the interior portions of the crystals to about An_{30} along the rims (Table 4). Some of the lower An content plagioclase phenocrysts also display normal zoning but over a more limited An content range; others display slight oscillatory zoning, or they lack zoning altogether. The An contents of the homogeneous grains are similar to the rims of the strongly zoned phenocrysts, but in most crystals, the An contents are lower (An_{19} - An_{30}). Some of the plagioclase crystals are intergrown with other phases forming glomerocrysts.

The plagioclase phenocrysts in the rhyolitic part of the Guild Mine Member (92-22 and 94-13A) display much less compositional variability than those in the dacite and rhyodacite (Fig. 11). Despite the wide range of compositions from labradorite (An_{62}) to oligoclase (An_{16}), most of the analyses are oligoclase, ranging from An_{17} to An_{24} (Fig. 11). The oligoclase crystals either lack zoning, or they display slight normal zoning with An content variations limited to about 3-5 mol percent (Table 4). The small proportion of higher An content plagioclase phenocrysts in the rhyolite typically display normal zoning.

While the range of plagioclase compositions in the high-silica rhyolite at the top the Guild Mine Member (94-15) is also relatively wide, ranging from labradorite (An_{56}) to oligoclase (An_{17}), the majority of the plagioclase phenocrysts display a limited range of An contents in the oligoclase field (An_{17} - An_{23}) (Fig. 11). Overall, the plagioclase phenocrysts are homogeneous, but some crystals exhibit minor amounts of either normal or reverse zoning (Table 4). The highest An plagioclase phenocryst in the high-silica rhyolite is a highly embayed crystal that exhibits normal zoning from $An_{56.4}$ to An_{31} .

Intermember rhyolite ash-flow tuff

Overall, plagioclase phenocrysts in the ash-flow tuff between the Guild Mine and Weed Heights Members range from labradorite to oligoclase (Fig. 11). Considered individually, the rhyolite ash-flow tuff sample (94-9B) contains plagioclase phenocrysts with a wider range of An contents (An_{64} - An_{13}) compared to the high-silica rhyolite intertuff sample (94-28D), which contains plagioclase phenocrysts that range from An_{49} to An_{18} (Fig. 11). The plagioclase crystals in each intertuff sample also display different zoning characteristics. In general, plagioclase phenocrysts from the rhyolite ash-flow tuff display normal zoning with some minor oscillatory zoning superimposed. These zoned phenocrysts consist of a central portions with An contents from An_{40} to An_{50} and margins with An contents from An_{23} to An_{32} (Table 4); a few grains are homogeneous. In contrast, most of the plagioclase phenocrysts in the high-silica rhyolite are homogeneous to slightly normally zoned (Table 4).

Weed Heights Member

Plagioclase phenocrysts in the rhyodacite at the base of the Weed Heights Member (94-30) exhibit a wide range of compositions from bytownite (An_{73}) to oligoclase (An_{18}) (Fig. 11). Most, however, are labradorite to andesine. In general, the plagioclase phenocrysts exhibit normal zoning from An_{50-55} in crystal interiors to An_{30-35} on grain margins (Table 4), with minor oscillatory zoning superimposed in some crystals. One heavily resorbed phenocryst has a much lower An content (An_{22-25}) than most of the other grains in this sample (Fig. 11).

The rhyolite in the upper part of the Weed Heights Member (94-31) contains plagioclase phenocrysts that range from labradorite (An_{60}) to oligoclase (An_{13}) (Fig. 11). The rhyolite is characterized by two populations of plagioclase phenocrysts based on An content (Table 4) and type of zoning. The higher An content plagioclase

phenocrysts (Fig. 11) exhibit normal zoning that either spans a large range of An values (An_{50} - An_{28}) or is confined to a relatively narrow range (An_{48} - An_{42}). The lower An content crystals (An_{13} - An_{16}) are either homogeneous or show slight reverse zoning.

Sanidine

Based on optical properties and chemical composition, the alkali feldspar phenocrysts in the MPT are classified as sanidine. Overall, the analyses from the sanidine phenocrysts define a fairly tight grouping between Or_{60} and Or_{70} on the ternary feldspar diagrams (Fig. 11). The sanidine phenocrysts in the more mafic parts of both members have Or contents in the upper half of this range (Or_{65} - Or_{70}). The sanidine crystals in the less evolved samples are generally homogeneous, displaying minimal zoning with respect to Or content (1-2 mol percent). A few crystals, however, are zoned from cores with higher Or contents (Or_{67} - Or_{69}) to rims with lower Or contents (Or_{63} - Or_{65}). In comparison, the sanidine phenocrysts from the more silicic, upper parts of each member have lower Or contents (Or_{60} - Or_{65}), and zoned crystals are much more common, ranging from cores with higher Or contents to rims with lower Or contents. While no general zoning trends with respect to BaO contents were observed for the MPT as a whole, within-sample trends are noted below. Representative sanidine analyses for the MPT are presented in Table 5.

Guild Mine Member

The dacite at the base of the Guild Mine Member (94-5B) contains sparse sanidine crystals. Two sanidine grains were analyzed and range from $Or_{66.5}$ to $Or_{68.4}$ (Fig. 11;

Table 5: Representative sanidine analyses of the MPT.

<u>Sample #</u>	<u>94-5B</u>	<u>94-5B</u>	<u>94-8</u>	<u>94-8</u>	<u>94-13a</u>	<u>94-13a</u>	<u>94-15</u>	<u>94-15</u>
<u>Analysis #</u>	<u>fe13.1</u>	<u>fe14.2</u>	<u>fe10.4</u>	<u>fe10.1</u>	<u>fe14.2</u>	<u>fe14.4</u>	<u>fe11.1</u>	<u>fe11.5</u>
<i>position</i>	<i>rim (sg)</i>	<i>rim (sg)</i>	<i>core</i>	<i>rim</i>	<i>core</i>	<i>rim</i>	<i>core</i>	<i>rim</i>
SiO ₂	65.8	63.5	65.2	65.5	65.1	65.6	63.8	64.2
Al ₂ O ₃	19.2	19.0	19.0	19.1	19.3	19.3	19.2	19.5
FeO*	0.11	0.17	0.07	0.08	0.1	0.10	0.07	0.04
MgO	0.00	0.00	0.00	0.01	0.00	0.00	0.00	0.00
CaO	0.27	0.23	0.20	0.25	0.21	0.18	0.21	0.21
Na ₂ O	3.42	3.55	3.41	3.46	3.58	4.04	3.53	3.77
K ₂ O	11.7	11.1	11.8	11.4	11.64	10.9	11.6	11.4
BaO	0.08	0.58	0.34	0.14	0.1	0.13	0.14	0.19
Total	100.65	98.19	99.99	99.93	100.12	100.22	98.58	99.23
Ab	30.3	32.3	30.2	31.2	31.50	35.8	31.3	33.2
Or	68.4	66.5	68.8	67.6	67.4	63.3	67.7	65.8
An	1.3	1.2	1.0	1.3	1.0	0.9	1.0	1.0

<u>Sample #</u>	<u>92-22</u>	<u>92-22</u>	<u>94-30</u>	<u>94-30</u>	<u>94-31</u>	<u>94-31</u>	<u>94-28D</u>	<u>94-28D</u>	<u>94-9B</u>
<u>Analysis #</u>	<u>fe8.1</u>	<u>fe8.3</u>	<u>fe10.1</u>	<u>fe10.4</u>	<u>fe10.3</u>	<u>fe10.1</u>	<u>fe10.3</u>	<u>fe10.1</u>	<u>fe8.3</u>
<i>position</i>	<i>core</i>	<i>rim</i>	<i>core</i>	<i>rim</i>	<i>core</i>	<i>rim</i>	<i>core</i>	<i>rim</i>	<i>rim (sg)</i>
SiO ₂	63.9	64.3	64.2	63.8	65.1	65.7	66.5	64.8	65.0
Al ₂ O ₃	19.0	19.2	19.1	19.3	19.0	19.1	19.0	19.1	19.2
FeO*	0.09	0.14	0.14	0.13	0.11	0.13	0.06	0.07	0.10
MgO	0.00	0.00	0.00	0.00	0.00	0.00	0.01	0.00	0.00
CaO	0.22	0.29	0.19	0.26	0.18	0.25	0.15	0.18	0.19
Na ₂ O	3.56	3.84	3.37	3.65	3.80	4.29	3.47	3.69	3.88
K ₂ O	11.4	10.7	11.4	11.1	11.1	10.3	11.5	11.4	11.2
BaO	0.34	0.60	0.33	0.80	0.01	0.01	0.04	0.00	0.03
Total	98.51	98.99	98.75	99.03	99.26	99.77	100.72	99.24	99.55
Ab	31.8	34.9	30.7	32.9	33.9	38.4	31.2	32.7	34.1
Or	67.1	63.6	68.3	65.8	65.2	60.4	68.1	66.5	65.0
An	1.1	1.5	1.0	1.3	0.9	1.2	0.7	0.9	0.9

"sg" refers to single grain. FeO* indicates total iron as FeO. Analyses were obtained using a beam current of 30 nA and an accelerating voltage of 15 kV. Counting times: 10 seconds for Fe, Mg, Ca, Na, and K; 20 seconds for Si and Al; and 30 seconds for Ba.

Table 5). BaO decreases by a factor of 10 from 0.6 wt. % at Or_{66.5} to 0.08 wt. % at Or_{68.4} (Table 5).

The sanidine phenocrysts in the rhyodacite in the middle of the Guild Mine Member (94-8) are zoned from Or₆₉ in the centers of crystals down to Or_{63.5} along the margins (Fig. 11). Despite this large range, most (70%) of the sanidine phenocrysts have Or contents between Or₆₇ and Or_{68.5} (Table 5). Overall, the BaO contents vary from as low as 0.04 wt. % in the cores to as high as 0.67 wt. % along the rims.

Sanidine phenocrysts in the two samples of rhyolite from the Guild Mine Member were analyzed. In one of the rhyolites (92-22), the interior portions of the sanidine phenocrysts have higher Or contents (Or₆₅-Or₆₇) (Fig. 11) and BaO contents down to 0.11 wt. %, and the margins have lower Or contents (Or₆₁-Or₆₃) and BaO contents up to 1.37 wt. % (Table 5). The other rhyolite sample (94-13A), which is from near the top of the Guild Mine Member, contains sanidine phenocrysts that are either homogeneous or are zoned from Or₆₉ in the center to Or₆₃ at the margins (Fig. 11; Table 5). Some of the sanidine phenocrysts are homogeneous with Or contents that are similar to the interior portions of the zoned grains. The BaO content is either consistently low across individual sanidine phenocrysts (only up to 0.10 wt. %; Table 5), or it is slightly elevated towards the center of grains (up to 0.40 wt. %).

The sanidine phenocrysts in the high-silica rhyolite at the top of the Guild Mine Member (94-15) are either homogeneous, or they are zoned from Or₆₈ in the center of crystals to Or₆₅ along the margins (Fig. 11; Table 5). BaO is consistently low in most of the sanidine phenocrysts from the high-silica rhyolite, but some crystals exhibit slight zoning in terms of BaO. For instance, one crystal grades from 0.22 wt. % BaO in the center to 0.06 wt. % at the margin.

Intermember rhyolite ash-flow tuff

Sanidine phenocrysts in two samples of the rhyolite ash-flow tuff that occurs between the Guild Mine and Weed Heights Members were analyzed. The sanidine phenocrysts in one of the rhyolite intertuff samples (94-9B) are homogeneous with Or contents of about Or₆₅ and BaO contents up to 0.08 wt. % (Fig. 11; Table 5). Compared to 94-9B, the sanidine phenocrysts in the high-silica rhyolite intertuff sample (94-28D), as a group, display a much larger range in Or contents from Or₇₂ to Or₅₉ (Fig. 11). Most of the sanidine phenocrysts lack zoning with respect to Or, only varying up to 1 mol percent. The center of one of the phenocrysts in this sample shows a dramatic drop in Or content (Or₅₉; Fig. 11), which is opposite from the zoning in most of the sanidine phenocrysts in the MPT. BaO contents in the high-silica rhyolite intertuff sample are relatively low, with most less than 0.10 wt. % (Table 5) and a few up to 0.54 wt. %. In most, BaO content increases towards the center of the grain, and in a few, it increase towards the margins.

Weed Heights Member

Sanidine phenocrysts in the rhyodacite at the base of the Weed Heights Member (94-30) have a comparatively small range of Or contents from Or_{65.4} to Or_{68.5} (Fig. 11). The outlier (Or₆₁; Fig. 11) is from a sanidine crystal intergrown with other sanidine crystals forming a glomerocryst. Most of the sanidine phenocrysts in the rhyodacite display zoning with centers of crystals that typically have Or contents up to Or_{68.5} and BaO contents as low 0.01 wt. %, whereas the rims have Or contents as low as Or_{65.4} and BaO contents up to 0.85 wt. % (Table 5).

The rhyolite from the upper part of the Weed Heights Member (94-31) contains sanidine phenocrysts that display a much wider span of Or contents than the rhyodacite ranging from Or₆₀ to Or₆₇ (Fig. 11). Individual sanidine crystals in the rhyolite are

zoned with respect to Or and BaO content (Table 5). While the compositional zoning in some phenocrysts spans nearly the entire range of Or contents (Or_{62} - Or_{67}), most of the sanidine crystals display a more limited range of Or contents, varying only 1-3 mol percent from core to rim. The BaO contents in the centers of a few sanidine phenocrysts are as low as 0.01 wt. % and up to 0.39 wt. % along the margins. Most sanidine crystals, however, display consistently low BaO contents in both core and rim (only up to 0.10 wt. %; Table 5).

Pyroxene

Both clinopyroxene and orthopyroxene phenocrysts occur sparsely in the lower, less evolved parts of both members of the MPT, are generally lacking in the upper, most silicic parts of both members, and are completely absent in the intermember rhyolite ash-flow tuff (Fig. 3). To facilitate classification and comparison of the individual members of the MPT, the pyroxene compositional data are projected onto the four-component system, $\text{CaMgSi}_2\text{O}_6(\text{Di})$ - $\text{CaFeSi}_2\text{O}_6(\text{Hd})$ - $\text{Mg}_2\text{Si}_2\text{O}_6(\text{En})$ - $\text{Fe}_2\text{Si}_2\text{O}_6(\text{Fs})$ (Fig. 12).

Almost exclusively, the clinopyroxene phenocrysts from the MPT are augite with compositions ranging from $\text{Wo}_{41.7}\text{En}_{49.9}\text{Fs}_{8.4}$ to $\text{Wo}_{41.4}\text{En}_{31.4}\text{Fs}_{27.2}$ (Fig. 12). Except in the cores of some of the augite grains in the dacite at the base of the Guild Mine Member, the clinopyroxene phenocrysts in the Weed Heights Member as a group have lower ferrosilite contents than those in the Guild Mine Member (Fig. 12; Table 6). As a group, the clinopyroxene phenocrysts from the MPT are largely homogeneous, only varying by 1-3 mol percent Fs from centers to rims. However, zoning with respect to ferrosilite and TiO_2 contents is quite pronounced in a few phenocrysts in the dacite at the base of the Guild Mine Member (Table 6).

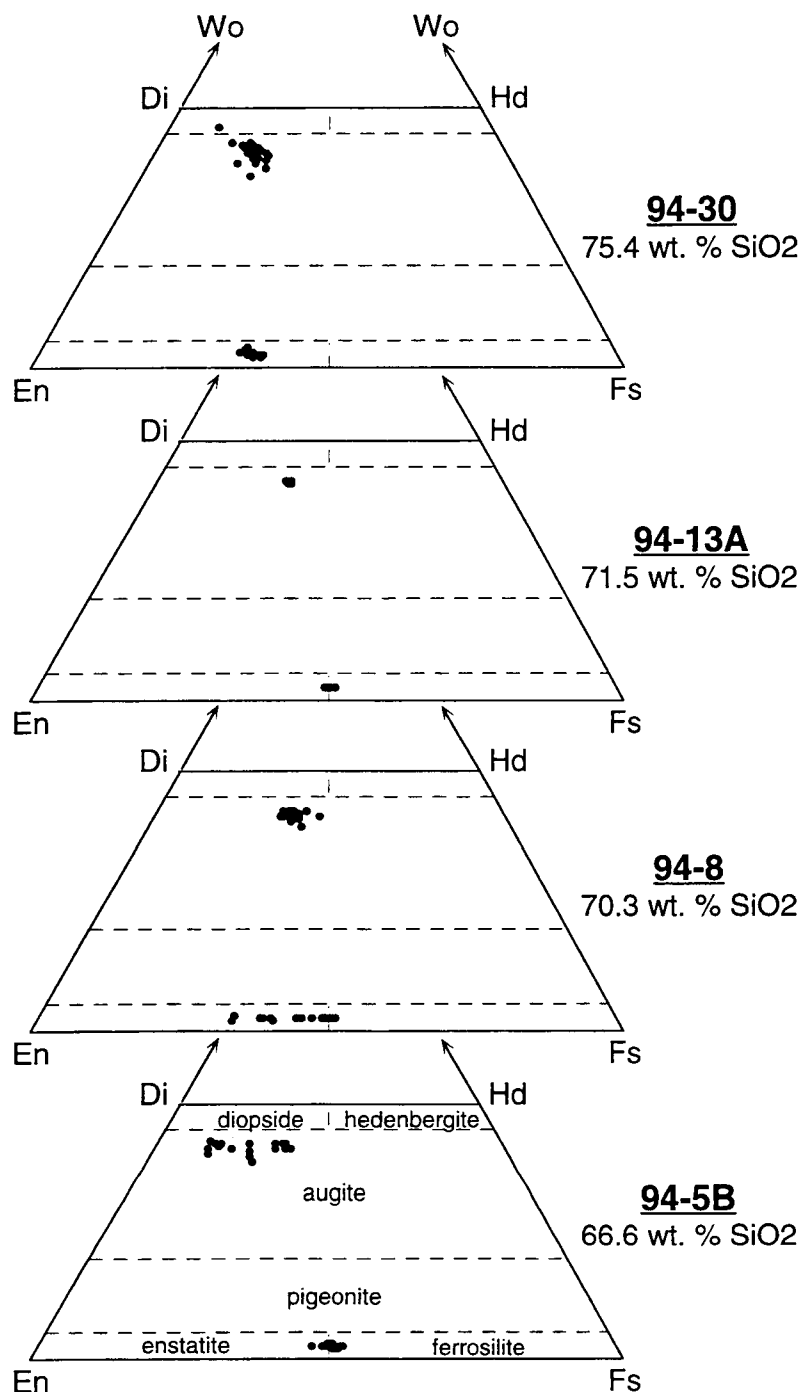


Figure 12: Pyroxene compositional data from the MPT plotted in the system wollastonite (Wo), enstatite (En), and ferrosilite (Fs). Compositions normalized to Ca, Mg, and ΣFe atoms, where $\Sigma\text{Fe} = \text{Fe}^{+2} + \text{Fe}^{+3} + \text{Mn}^{+2}$. The pyroxene quadrilateral consists of the four-component system $\text{CaMgSi}_2\text{O}_6(\text{Di})$ - $\text{CaFeSi}_2\text{O}_6(\text{Hd})$ - $\text{Mg}_2\text{Si}_2\text{O}_6(\text{En})$ - $\text{Fe}_2\text{Si}_2\text{O}_6(\text{Fs})$. Classification scheme for pyroxenes after Morimoto (1988).

Table 6: Representative clinopyroxene and orthopyroxene analyses of the MPT.

<u>Sample #</u> <u>Analysis #</u>	<u>94-5B</u> <u>ma8.1</u>	<u>94-5B</u> <u>ma8.3</u>	<u>94-5B</u> <u>ma12.3</u>	<u>94-8</u> <u>ma10.1</u>	<u>94-8</u> <u>ma10.3</u>	<u>94-13A</u> <u>ma7.5</u>	<u>94-30</u> <u>ma4.1</u>	<u>94-30</u> <u>ma4.7</u>
SiO ₂	52.0	51.2	52.5	52.7	52.1	52.2	52.8	51.8
Al ₂ O ₃	0.97	2.92	2.35	0.77	1.14	0.98	1.02	2.03
TiO ₂	0.15	0.67	0.36	0.16	0.19	0.15	0.24	0.66
FeO#	12.3	8.50	5.84	12.6	13.4	12.8	9.57	10.5
Fe ₂ O ₃ #	0.05	0.59	0.40	0.10	0.00	0.00	0.29	0.78
MnO	0.57	0.27	0.21	0.54	0.71	0.63	0.54	0.30
MgO	12.4	14.6	16.9	12.7	12.2	12.3	14.4	15.6
CaO	20.1	20.2	20.4	20.3	19.5	19.9	20.5	18.0
Na ₂ O	0.34	0.33	0.22	0.31	0.33	0.34	0.34	0.29
Cr ₂ O ₃	0.01	0.00	0.06	0.00	0.02	0.00	0.00	0.03
Total	98.83	99.17	99.21	100.13	99.51	99.34	99.69	99.92
En	36.5	42.5	48.0	36.5	35.8	35.9	41.1	44.6
Wo	42.3	42.3	41.8	42.1	41.0	41.9	42.2	37.0
Fs	21.3	15.2	10.2	21.4	23.2	22.1	16.7	18.4

<u>Sample #</u> <u>Analysis #</u>	<u>94-5B</u> <u>ma13.3</u>	<u>94-5B</u> <u>ma10.4</u>	<u>94-8</u> <u>ma11.6</u>	<u>94-8</u> <u>ma18.1</u>	<u>94-8</u> <u>ma18.6</u>	<u>94-13A</u> <u>ma8.2</u>	<u>94-30</u> <u>ma12.1</u>	<u>94-30</u> <u>ma12.3</u>
SiO ₂	51.2	51.3	51.3	51.0	52.5	50.9	52.9	52.9
Al ₂ O ₃	0.68	0.34	0.45	0.77	1.25	0.48	0.50	1.21
TiO ₂	0.14	0.09	0.11	0.14	0.24	0.19	0.14	0.33
FeO#	28.0	28.7	28.7	27.4	22.5	28.4	22.1	20.5
Fe ₂ O ₃ #	0.00	0.00	0.00	0.00	0.03	0.00	0.00	0.55
MnO	1.42	1.74	1.39	1.32	0.77	1.35	1.10	0.59
MgO	16.6	16.2	16.4	16.6	21.3	16.3	21.6	22.8
CaO	1.45	0.95	1.24	1.10	1.21	1.22	1.15	1.43
Na ₂ O	0.03	0.02	0.03	0.03	0.03	0.04	0.01	0.06
Cr ₂ O ₃	0.00	0.00	0.01	0.01	0.01	0.00	0.00	0.02
Total	99.49	99.35	99.61	98.37	99.93	98.87	99.51	100.46
En	48.6	47.7	47.9	49.6	60.4	48.1	60.9	63.4
Wo	3.1	2.0	2.6	2.4	2.5	2.6	2.3	2.9
Fs	48.3	50.3	49.4	48.1	37.1	49.3	36.8	33.8

"#" indicates FeO and Fe₂O₃ calculated using charge balance equation of Papike and others (1974).

Analyses were obtained using a beam current of 50 nA and an accelerating voltage of 15 kV. Counting times: 10 seconds for Mn, Ca, Na, and Cr; 20 seconds for Si, Al, Fe, and Mg; and 30 seconds for Ti.

For the most part, the orthopyroxene phenocrysts in the MPT are enstatite, or they straddle the boundary between the enstatite and ferrosilite fields, with compositions ranging from $\text{Wo}_{1.9}\text{En}_{65.9}\text{Fs}_{32.2}$ to $\text{Wo}_{2.4}\text{En}_{41}\text{Fs}_{50.6}$ (Fig. 12). Except for a few crystals in the rhyodacitic part of the Guild Mine Member, which display considerable zoning with respect to ferrosilite contents, most of the orthopyroxene phenocrysts are homogeneous and display minimal zoning (Table 6). The orthopyroxene phenocrysts in the Weed Heights Member have lower ferrosilite contents than most of the orthopyroxene grains in the Guild Mine Member (Fig. 12). A notable exception is the central portions of some phenocrysts in the Guild Mine rhyodacite, which interestingly are remarkably similar in composition to the orthopyroxene phenocrysts in the rhyodacitic base of the Weed Heights Member (Table 6).

Guild Mine Member

The clinopyroxene phenocrysts in the dacite at the base of the Guild Mine Member (94-5B) are augite and plot in three discrete compositional clusters on the pyroxene quadrilateral (Fig. 12). As a group, they tend to have the lowest hedenbergite contents compared to the clinopyroxene analyses from the upper parts of the Member. Most of the augite analyses from the dacite (50%) have compositions clustering at $\approx\text{Wo}_{42}\text{En}_{37}\text{Fs}_{21}$ (Fig. 12) and TiO_2 contents ranging from 0.15 to 0.25 wt. % (Table 6). A small number of the analyses, which are from the center of a large phenocryst, define a cluster at $\approx\text{Wo}_{41}\text{En}_{43}\text{Fs}_{16}$ (Fig. 12). This phenocryst has somewhat higher TiO_2 contents, ranging from 0.59 to 0.76 wt. % (Table 6). The composition of the rim of this phenocryst is similar to the clinopyroxenes with higher hedenbergite contents (Fig. 12; Table 6). The remainder of the clinopyroxene analyses, which are also from a single phenocryst, define a cluster at about $\approx\text{Wo}_{42}\text{En}_{49}\text{Fs}_9$ (Fig. 12) and have TiO_2 contents ranging from 0.20 to 0.36 wt. % (Table 6). The orthopyroxene phenocrysts

within the dacite are relatively homogeneous, with compositions that span the boundary between the enstatite and ferrosilite fields on the pyroxene quadrilateral ($\text{Wo}_{2.6-2.4}\text{En}_{50.3-47}\text{Fs}_{47.1-50.6}$; Fig. 12); one analysis lies outside this range.

Augite phenocrysts in the rhyodacite near the middle of the Guild Mine Member (94-8) define a cluster at $\approx\text{Wo}_{42}\text{En}_{35}\text{Fs}_{23}$ (Fig. 12; Table 6); only one analysis lies outside the cluster. As a group, TiO_2 contents range from 0.11 to 0.23 wt. %. Compared to the dacite, the orthopyroxene phenocrysts in the rhyodacite display a much wider range of compositions ($\text{Wo}_{1.9-2.6}\text{En}_{65.9-47.9}\text{Fs}_{32.2-49.4}$; Fig. 12). Most of the orthopyroxene analyses plot in the enstatite field on the pyroxene quadrilateral, and a small number of the analyses plot on the join between the enstatite and ferrosilite fields (Fig. 12). The wide range of compositions in this sample reflects the fact that a few of the orthopyroxene phenocrysts display considerable normal zoning (Table 6). Some phenocrysts are not zoned and plot in a well-defined cluster of data at $\approx\text{Wo}_{2.5}\text{En}_{49.5}\text{Fs}_{48}$ (Fig. 12); the compositions of these phenocrysts are similar to the rims of the strongly zoned grains (Table 6). The range of TiO_2 contents for the orthopyroxene phenocrysts in the rhyodacite is 0.10 to 0.24 wt. %, and TiO_2 contents vary inversely with ferrosilite contents.

The few augite phenocrysts in the rhyolite near the top of the Guild Mine Member (94-13A) define a tight cluster of data at $\approx\text{Wo}_{42}\text{En}_{36}\text{Fs}_{22}$ (Fig. 12), and they have consistent TiO_2 contents of about 0.15 wt. % (Table 6). The only orthopyroxene phenocryst analyzed in the rhyolite yields a tight cluster of data straddling the boundary between the enstatite and ferrosilite fields on the pyroxene quadrilateral ($\approx\text{Wo}_3\text{En}_{49}\text{Fs}_{48}$; Fig. 12); TiO_2 contents range from 0.13 to 0.19 wt. % (Table 6).

Weed Heights Member

In the Weed Heights Member, augite phenocrysts are confined to the rhyodacite at the base of the unit (94-30). While the clinopyroxene analyses in the rhyodacite display a fairly wide range of compositions ($\text{Wo}_{38.4-46.3}\text{En}_{41.4-45.2}\text{Fs}_{20.2-8.5}$), the vast majority of the analyses (93%) form a diffuse cluster of data at $\approx\text{Wo}_{42}\text{En}_{41}\text{Fs}_{17}$ (Fig. 12). Most of the augite phenocrysts exhibit minor zoning with respect to hedenbergite and TiO_2 content; commonly, the central portions of grains have slightly higher hedenbergite and TiO_2 contents (Table 6). The centers of some crystals display the opposite situation, however, and have slightly lower hedenbergite contents in their cores. The analyses that lie outside of the diffuse data cluster are from areas of phenocrysts that display textural evidence for exsolution. The most striking example is the datum that plots in the diopside field (Fig. 12), which is from an area of an augite phenocryst that exhibits exsolution lamellae.

The orthopyroxene phenocrysts in the basal rhyodacite of the Weed Heights Member define a fairly tight cluster of data within the enstatite field ($\text{Wo}_{2.8-2.5}\text{En}_{63.7-59.7}\text{Fs}_{33.5-37.8}$; Fig. 12). Individual orthopyroxene crystals have fairly consistent ferrosilite and TiO_2 contents, but minor zoning is evident in some grains. In the slightly zoned phenocrysts, the interior portions of the crystals have lower ferrosilite contents and higher TiO_2 contents than the rims (Table 6).

Amphibole

Amphibole phenocrysts occur sparsely in the MPT and are restricted to the lower, more mafic parts of the Guild Mine and Weed Heights Members (Fig. 3). For this reason, only a small number of amphibole analyses were obtained (Appendix C). As a

group, the amphibole phenocrysts in the MPT are classified as calcic amphiboles (Leake, 1978).

The amphibole phenocrysts in the dacite at the base of the Guild Mine Member (94-5B) are variously classified as ferroan pargasitic hornblende, pargasitic hornblende, and edenitic hornblende (Leake, 1978). Even though a range of hornblende types are represented, the amphiboles display a narrow range of Mg#'s, from 67 to 75, and TiO₂ contents, from 1.46 to 2.18 wt. % (Table 7).

Two analyses from one amphibole phenocryst in the rhyodacitic middle part of the Guild Mine Member (94-8) were obtained. Compared to the amphibole phenocrysts in the dacite, the amphibole crystal in the rhyodacite has a slightly lower Mg# (62) and a higher TiO₂ content (up to 3.8 wt. % TiO₂; Table 7), and as such, is classified as titanian ferroan pargasitic hornblende (Leake, 1978).

The amphibole phenocrysts in the rhyodacite at the base of the Weed Heights Member are compositionally distinct from those in the Guild Mine Member (Table 7). The Mg#'s for the Weed Heights amphiboles range from 60 to 62, but because they have less Na and K in the A site ((Na+K)_A is slightly greater than 0.5), they are classified as magnesio-hornblendes and edenites (Leake, 1978).

Biotite

Biotite is an ubiquitous phase in both members of the MPT and in the intermember rhyolite ash-flow tuff (Fig. 3). Not only will the compositional data from the biotite phenocrysts in the MPT prove useful in reconstructing the compositional zoning of the pre-eruptive magma chamber, but it will also be critical in elucidating the dynamics of the cataclysmic eruptions that formed the Guild Mine and Weed Heights Members

Table 7: Representative biotite and amphibole analyses of the MPT.

<u>Sample #</u> <u>Analysis #</u>	<i>biotite</i>									<i>amphibole</i>			
	<u>94-5B</u> <u>ma1.1</u>	<u>94-8</u> <u>ma4.5</u>	<u>94-13a</u> <u>ma1.2</u>	<u>94-13a</u> <u>ma6.2</u>	<u>94-15</u> <u>ma7.1</u>	<u>94-30</u> <u>ma12.5</u>	<u>94-30</u> <u>ma18.2</u>	<u>94-31</u> <u>ma10.2</u>	<u>94-9B</u> <u>ma13.3</u>	<u>Sample #</u> <u>Analysis #</u>	<u>94-5B</u> <u>ma3.3</u>	<u>94-8</u> <u>ma6.2</u>	<u>94-30</u> <u>ma10.3</u>
SiO ₂	36.1	36.4	35.7	36.7	36.0	37.3	39.0	37.9	36.1	SiO ₂	43.0	42.0	47.7
Al ₂ O ₃	13.5	13.5	13.2	12.4	12.6	13.6	13.0	13.0	13.6	Al ₂ O ₃	11.5	11.4	6.21
TiO ₂	5.93	6.14	6.01	5.01	4.77	6.40	4.85	4.81	5.30	TiO ₂	2.18	3.82	1.54
FeO*	18.0	18.1	17.7	20.1	22.0	14.0	15.4	15.9	16.4	FeO#	11.3	13.7	15.3
MgO	10.6	10.6	10.2	9.12	8.32	13.3	12.3	12.9	12.2	Fe ₂ O ₃ #	0.50	0.05	0.04
MnO	0.20	0.14	0.19	0.33	0.57	0.14	0.31	0.38	0.36	MgO	14.6	12.4	13.8
CaO	0.06	0.01	0.00	0.02	0.00	0.03	0.04	0.02	0.06	MnO	0.14	0.22	0.77
Na ₂ O	0.46	0.47	0.51	0.47	0.43	0.58	0.57	0.61	0.47	CaO	10.7	10.7	10.6
K ₂ O	9.05	8.88	9.04	9.43	9.43	8.70	9.09	9.14	8.84	Na ₂ O	1.90	2.27	1.42
Rb ₂ O	0.07	0.06	0.05	0.09	0.09	0.09	0.07	0.10	0.06	K ₂ O	0.78	0.87	0.70
Cs ₂ O	0.00	0.00	0.01	0.01	0.02	0.00	0.00	0.02	0.01	Cr ₂ O ₃	0.00	0.05	0.04
BaO	0.92	1.28	0.89	0.00	0.03	1.40	0.57	0.00	1.50	F	0.33	0.36	0.43
F	0.56	0.58	0.64	0.90	0.82	1.11	0.63	0.77	0.64	Cl	0.03	0.03	0.08
Cl	0.15	0.11	0.13	0.19	0.22	0.12	0.09	0.16	0.14	-O=F, Cl	0.15	0.16	0.20
-O=F, Cl	0.27	0.27	0.30	0.42	0.39	0.49	0.29	0.36	0.30				
Total	95.26	95.99	93.88	94.34	94.96	96.19	95.69	95.39	95.48	Total	96.78	97.69	98.37
Mg#	51.3	51.0	50.7	44.7	40.2	62.9	58.9	59.1	57.1	Mg#	69.8	61.8	61.7

For biotite, FeO* indicates total iron as FeO, and Mg# = (molecular Mg/(Mg + Fe*)). For amphibole, "#" denotes FeO and Fe₂O₃ calculated using the charge balance equation of Papike and others (1974). Analyses were obtained using a beam current of 30 nA and an accelerating voltage of 15 kV. Counting times for both biotite and amphibole, except where indicated: 10 seconds for Si, Al, Ti, Fe (for biotite), Mg, Mn, Ca, Na, K, Cs, and Cl; 20 seconds for Fe (for amphibole), Ba, and F; and 30 seconds for Rb.

(cf., Boden, 1989; Schuraytz and others, 1989). Magnesium number (Mg#) of the biotite phenocrysts varies systematically from the base to the top of both members and decreases with increasing stratigraphic position (Fig. 13). Compared to the Guild Mine Member, the Mg#s of the biotite phenocrysts in the Weed Heights Member and the intermember tuffs are consistently higher (Fig. 13). The TiO_2 and BaO contents in the biotite phenocrysts also change with increasing stratigraphic position (i.e., with increasing bulk SiO_2), so these elements are highlighted in the following discussion as well. Representative biotite analyses are provided in Table 7.

Guild Mine Member

Biotite phenocrysts in the dacite at the base of the Guild Mine Member (94-5B) define a tight cluster of data in terms of Mg#, with 90% of the biotite analyses between 49.7 and 53.4 (Fig. 13). Compared to the biotite phenocrysts in the rhyolitic upper parts of the Guild Mine Member, the biotite phenocrysts in the dacite have higher TiO_2 contents, ranging from 5.12 to 6.21 wt. %, and higher BaO contents, ranging from 0.52 to 1.68 wt. % (Table 7). Overall, the biotite phenocrysts in the dacite are homogeneous and display minimal zoning. A few analyses are outliers with respect to Mg# (Fig. 13), as well as displaying lower TiO_2 and BaO contents. These analyses are from the center of one biotite phenocryst and from biotite crystals that are intergrown with plagioclase crystals forming glomerocrysts.

Biotite phenocrysts in the rhyodacite in the middle of the Guild Mine Member (94-8) are compositionally indistinguishable from the biotite phenocrysts in the underlying dacite, with 93% percent of the analyses yielding Mg#'s between 50 and 54 (Fig. 13). TiO_2 and BaO contents are also similar, ranging from 4.7 to 6.7 wt. % TiO_2 and from 0.55 to 1.72 wt. % BaO (Table 7). Two of the analyses are outliers (Fig. 13): the analysis with the higher Mg# is from a biotite crystal that occurs as an inclusion within a

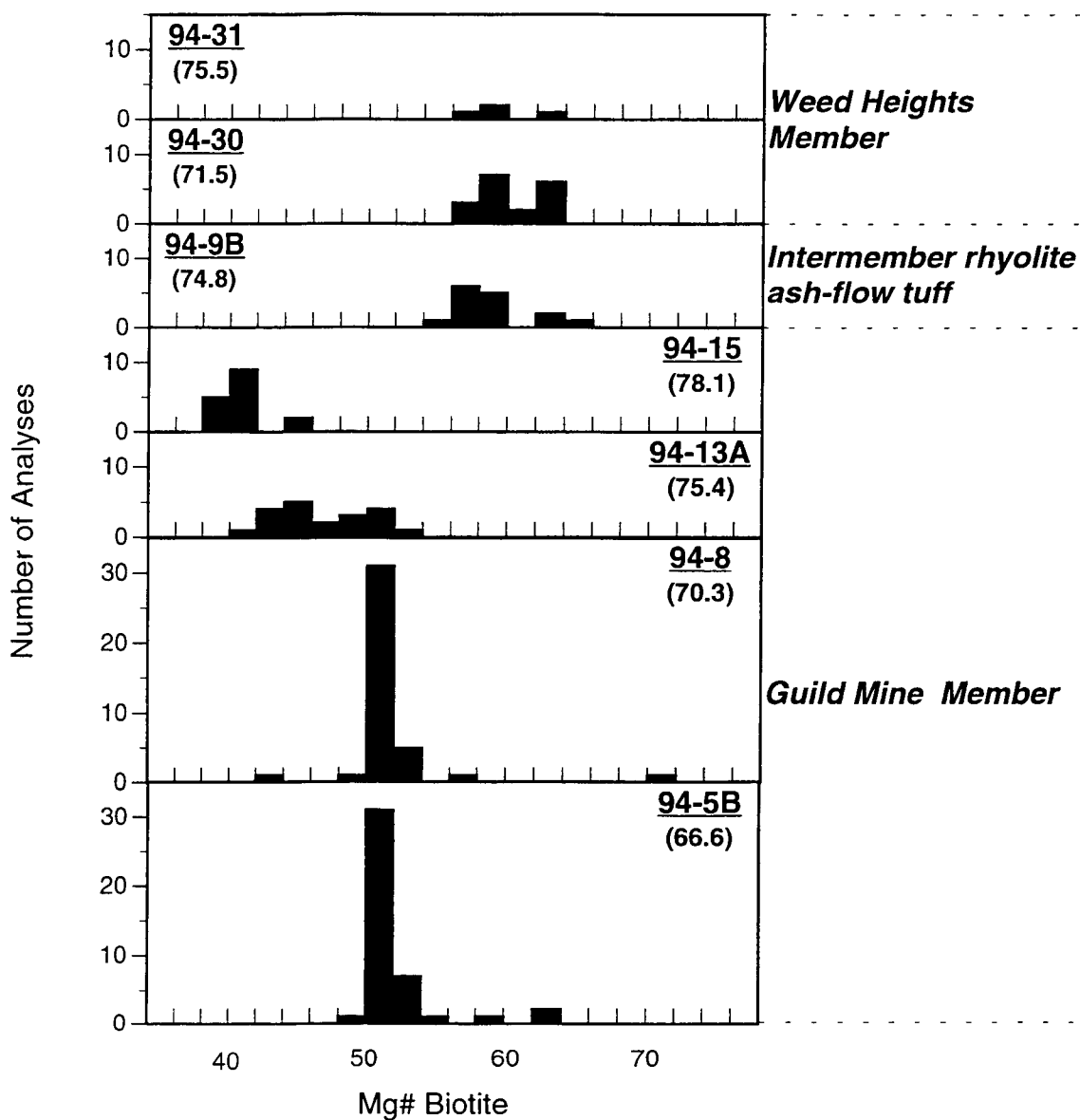


Figure 13: Histogram of Mg# (molecular $\text{Mg}/(\text{Mg}+\text{Fe}^*)$) for biotite phenocrysts in the MPT. Bulk-tuff, volatile-free SiO_2 contents are in parentheses.

pyroxene phenocryst, and the analysis with the lower Mg# is from a biotite phenocryst that is compositionally similar to the biotite crystals in the overlying rhyolitic parts of the Guild Mine Member.

Biotite phenocrysts in the rhyolite near the top of the Guild Mine Member (94-13A) are grouped into two diffuse populations in terms of Mg# (Fig. 13). One group of biotite phenocrysts is compositionally similar to the biotite phenocrysts in the dacitic and rhyodacitic parts of the Guild Mine Member with Mg#'s between 50 and 52. Most of the rest of the biotite phenocrysts in the rhyolite have Mg#'s between 43 and 46. The biotite phenocrysts with higher Mg#'s (50-52) have TiO₂ contents ranging from 5.77 to 6.12 wt. % and BaO contents ranging from 0.67 to 1.41 wt. % (Table 7). In comparison, the group of biotite phenocrysts with lower Mg#'s (43-46) have TiO₂ contents ranging from 4.60 to 5.11 wt. % and BaO contents only up to 0.81 wt. %. A few of the biotite phenocrysts have Mg#'s that are transitional between the two groups, ranging from 46 to 50, and one biotite phenocryst has an Mg# between 40 and 42 (Fig. 13).

The biotite phenocrysts in the high-silica rhyolite at the top of the Guild Mine Member (94-15) yield the lowest Mg#'s observed for any sample from the MPT. Most of the biotite phenocrysts (88%) have Mg#'s between 38.3 and 41.5, and a few of the phenocrysts have Mg#'s up to 44.7 (Fig. 13). In the group of biotite phenocrysts with Mg#'s from 38-42, TiO₂ contents range from 4.63 to 5.26 wt. %, and in most, BaO contents are only up to 0.09 wt. % (Table 7). Some of the biotite phenocrysts have BaO contents up to 1.57 wt. %, which is somewhat anomalous for biotite phenocrysts with such low Mg#'s.

Intermember rhyolite ash-flow tuff

Biotite phenocrysts in the rhyolite ash-flow tuff between the Guild Mine and Weed Heights Members (94-9B) are similar in composition to the lower Mg# biotite phenocrysts in the Weed Heights Member described below. Analyses of the biotite phenocrysts from the intermember tuff define a cluster of data with Mg#'s ranging from 55.6 to 59.3 (Fig. 13). TiO₂ values range from 4.87 to 5.50 wt. %, and BaO contents range up to 1.50 wt. % (Table 7). The intermember tuff sample also contains a biotite-plagioclase phyric inclusion. Analyses of the biotite crystals in the inclusion are distinct from the biotite phenocrysts in the matrix, with Mg#'s ranging from 62.8 to 64.7 (Fig. 13).

Weed Heights Member

The rhyodacite at the base of the Weed Heights Member contains biotite phenocrysts that cluster into two groups based on Mg# (Fig. 13). One group of biotite phenocrysts have lower Mg#'s, which range from 56.4 to 60.3 and have an average value of 58.8 (Fig. 13). The TiO₂ contents in this group of biotites range from 4.64 to 5.30 wt. %, and BaO contents range up to 1.07 wt. % (Table 7). The other group of biotite phenocrysts have slightly higher Mg#'s, which range from 61.4 to 63.7 and have an average value of 62.9 (Fig. 13). In the group of biotite phenocrysts with slightly higher Mg#'s, TiO₂ contents range from 6.26 to 6.45 wt. %, and BaO contents range from 0.96 to 1.96 wt. % (Table 7).

Most of the biotite phenocrysts in the rhyolite near the top of the Weed Heights Member are altered completely to hematite. Of the four analyses that are considered unaltered, three are similar to the slightly lower Mg# group that was observed in the rhyodacite, and one is similar to the slightly higher Mg# group (Fig. 13). The TiO₂ content for the higher Mg# analysis is 5.86 wt. %, and its BaO content is 0.79 Wt. %.

The TiO_2 contents for the lower Mg# biotites range from 4.81 to 5.12 wt. %, and their BaO contents are up to 0.93 wt. % (Table 7).

Fe-Ti Oxides

In the MPT, Fe-Ti oxide phenocrysts are present, albeit sparsely, from the base to the top of both members and in the intermember rhyolite ash-flow tuff (Fig. 3). Based on microprobe analyses, magnetite appears to be the more common species of Fe-Ti oxide phenocryst in the Guild Mine Member, and ilmenite, where present, is more prevalent in the Weed Heights Member and the intermember rhyolite ash-flow tuff (Appendix C). Ilmenite is largely confined to the lower, more mafic parts of the Guild Mine and Weed Heights Members, and it is absent in their upper rhyolitic parts. Within the individual units of the MPT, the ilmenite phenocrysts are remarkably similar, but between the units they display some variations. In the Guild Mine Member, TiO_2 and MnO are higher and MgO is lower, whereas the ilmenite crystals in the Weed Heights Member and the intermember rhyolite have lower TiO_2 and MnO and higher MgO (Table 8). Magnetite phenocrysts within the MPT, overall, have similar TiO_2 contents, ranging from about 9 to 12 wt. % TiO_2 , although the dacite at the base of the Guild Mine Member exhibits a much wider range of TiO_2 contents (Appendix C). In the following description for each member, TiO_2 is used to highlight the compositional variations between the Fe-Ti oxides phenocrysts within individual samples.

Several other elements, specifically MnO, MgO, and V_2O_5 , display systematic changes in the Fe-Ti oxide phenocrysts from the base to the top of both the Guild Mine and Weed Heights Members (Table 8). While the ranges for these elements overlap from one sample to the next, average values for each element vary systematically with

Table 8: Representative Fe-Ti oxide analyses of the MPT.

<u>Sample #</u>	<u>94-5B</u>	<u>94-8</u>	<u>94-13A</u>		<u>94-9B</u>	<u>94-30</u>	
<u>Analysis #</u>	<u>ox5.1-5.3</u>	<u>ox8.1-8.3</u>	<u>ox4.1-4.4</u>		<u>ox5.1-5.6</u>	<u>ox9.1-9.5</u>	
SiO ₂	0.02	0.02	0.02		0.01	0.02	
TiO ₂	49.1	50.0	48.6		44.7	45.4	
Al ₂ O ₃	0.10	0.11	0.20		0.22	0.19	
Cr ₂ O ₃	0.00	0.01	0.01		0.02	0.02	
FeO*	47.0	47.7	46.8		51.7	50.8	
V ₂ O ₅	0.28	0.30	0.29		0.41	0.39	
MnO	1.03	0.99	1.13		0.66	0.64	
MgO	1.71	1.66	1.51		2.35	2.40	
ZnO	0.04	0.03	0.03		0.06	0.04	
NiO	0.01	0.00	0.01		0.01	0.01	
ZrO ₂	0.00	0.06	0.06		0.06	0.11	
Nb ₂ O ₅	0.00	0.07	0.03		0.04	0.06	
Total*	99.38	100.93	98.70		100.26	100.11	
Fe ₂ O ₃ #	7.72	7.40	7.74		18.3	16.6	
FeO#	40.1	41.0	39.9		35.3	35.9	
Total#	100.15	101.54	99.38		101.99	101.60	
<u>Sample #</u>	<u>94-5B</u>	<u>94-8</u>	<u>94-13A</u>	<u>94-15</u>	<u>94-9B</u>	<u>94-30</u>	<u>94-31</u>
<u>Analysis #</u>	<u>ox5.4,5.5</u>	<u>ox1.1-1.5</u>	<u>fe14.3</u>	<u>ox1.2-1.4</u>	<u>ox6.1</u>	<u>fe15.1</u>	<u>ox7.1,7.2</u>
SiO ₂	0.09	0.19	0.13	0.07	2.23	0.11	0.23
TiO ₂	13.6	10.2	10.2	11.2	3.10	5.94	11.1
Al ₂ O ₃	2.03	1.90	1.47	1.09	0.61	2.16	1.69
Cr ₂ O ₃	0.03	0.02	0.05	0.01	0.05	0.01	0.12
FeO*	77.8	81.0	78.5	80.1	83.4	84.4	73.1
V ₂ O ₅	0.32	0.48	0.41	0.11	0.14	0.25	0.57
MnO	0.60	0.58	0.70	1.70	0.96	0.45	4.22
MgO	1.00	0.75	0.73	0.09	0.03	1.21	0.01
ZnO	0.26	0.16	0.21	0.26	0.26	0.24	0.57
NiO	0.02	0.01	0.00	0.02	0.04	0.07	0.01
ZrO ₂	0.00	0.01	0.02	0.00	0.02	0.02	0.07
Nb ₂ O ₅	0.00	0.03	0.05	0.04	0.03	0.07	0.05
Total*	95.74	95.30	92.40	94.73	90.93	94.97	91.72
Fe ₂ O ₃ #	40.1	46.5	45.1	45.2	54.3	55.4	41.5
FeO#	41.7	39.2	37.9	39.4	34.6	34.6	35.8
Total#	99.76	99.91	96.85	99.22	96.32	100.42	95.75
T (°C)	775	703	718	----	702	757	----
log fO ₂	-15.2	-16.9	-16.4	----	-14.4	-13.6	----

FeO* indicates total iron as FeO. "#" indicates FeO and Fe₂O₃ calculated after Carmichael (1967).

Analyses were obtained using a beam current of 50 nA and an accelerating voltage of 15 kV. Counting times: 10 seconds for Si, Ti, Al, Cr, Fe, Mn, Mg, Zn, Ni, Zr, and Nb; and 20 seconds for V.

increasing stratigraphic position. This variation is observed in both types of Fe-Ti oxide phenocrysts, but it is most prevalent in the magnetite phenocrysts. In general, the Fe-Ti oxides phenocrysts in the more mafic parts of the Guild Mine and Weed Heights Members have lower MnO and higher MgO than those in the more silicic parts of each member. In the magnetite phenocrysts in the Guild Mine Member, MnO increases from an average of 0.64 wt. % in the basal dacite to 1.21 wt. % in the high-silica rhyolite at the top. MgO in the magnetite phenocrysts decreases from an average of 1.01 to 0.08 wt. % from the base to the top, and V_2O_5 exhibits a slight decrease from 0.39 to 0.11 wt. % (Appendix C). The magnetite phenocrysts in the Weed Heights Member show similar compositional variations. MnO increases from an average of 0.48 wt. % in the basal rhyodacite to 3.75 wt. % in the rhyolite at the top. MgO in the magnetite phenocrysts decreases from an average of 1.32 to 0.02 wt. % from the base to the top, and V_2O_5 shows a slight decrease from 0.53 to 0.46 wt. % (Appendix C). The ilmenite phenocrysts show similar trends, although the data set is too limited to be considered representative.

Guild Mine Member

In the dacite at the base of the Guild Mine Member (94-5B), ilmenite is represented by one homogeneous crystal that is intergrown with a biotite phenocryst (Table 8). In contrast to the ilmenite phenocryst, the magnetite phenocrysts, as a group and as individual crystals, display a wide range of TiO_2 contents from 3.71 to 26.94 wt. %. Despite the large range of TiO_2 contents, most of the analyses utilized in the Fe-Ti oxide geothermometry calculation for this composition have TiO_2 contents between about 10 and 15 wt. % (Table 8). The outliers with respect to TiO_2 , especially those less than about 7 wt. % TiO_2 , display elevated Fe_2O_3 contents (>52 wt. %; Appendix C) revealing secondary alteration. The wide range of TiO_2 contents within individual

magnetite phenocrysts indicates that they have been affected by post-emplacement exsolution.

In the rhyodacite in the middle of the Guild Mine Member (94-8), ilmenite phenocrysts are also sparsely represented, and magnetite is the dominant Fe-Ti oxide species. The single ilmenite phenocryst analyzed is homogeneous (Table 8). Even though the magnetite phenocrysts range from 5.79 to 17.78 wt. % TiO_2 , most of the analyses (77%) are between 9 and 12 wt. % TiO_2 (Table 8).

In the rhyolite near the top of the Guild Mine Member (94-13A), ilmenite is represented by a homogeneous crystal (Table 8) that is intergrown with biotite crystals forming a glomerocryst. Although the magnetite phenocrysts display a fairly wide range of TiO_2 contents from 5.84 to 13.91 wt. %, many are about 10 wt. % TiO_2 (Table 8).

In the high-silica rhyolite at the top of the Guild Mine Member (94-15), the only type of Fe-Ti oxide phenocryst observed is magnetite. Overall, the magnetite phenocrysts have consistent compositions with TiO_2 contents ranging from 10.76 to 12.60 wt. % (Table 8).

Intermember rhyolite ash-flow tuff

The rhyolite ash-flow tuff between the Guild Mine and Weed Heights Members (94-9B) appears to have more ilmenite represented than magnetite (Appendix C). Only one magnetite analysis obtained from this sample had a recalculated total greater than 95% (Table 8). The three ilmenite crystals analyzed have similar compositions.

Weed Heights Member

The rhyodacite at the base of the Weed Heights Member (94-30) also appears to have more ilmenite crystals than magnetite (Appendix C), reflecting the fact that many of the magnetite phenocrysts appear altered under reflected light and thus were not

analyzed. In general, the ilmenite phenocrysts are homogeneous, with most of the ilmenite analyses displaying TiO_2 contents between 44 and 46 wt. % (Appendix C). Only one magnetite analysis has a recalculated total near 100% (Table 8); the rest are slightly greater than 95%, reflecting alteration to hematite.

Magnetite is the only Fe-Ti oxide species present in the rhyolite near the top of the Weed Heights Member (Table 8). Most of the magnetite phenocrysts are partially altered and yield low totals. As a group, the compositions of the magnetite phenocrysts are consistent between grains, with TiO_2 contents ranging from 10.16 to 11.12 wt. %, and the individual phenocrysts are homogeneous.

QUANTITATIVE ANALYSIS OF THE MPT COMPOSITIONAL DATA

Estimation Of Intensive Parameters

Temperature and Oxygen Fugacity using Fe-Ti Oxide Geothermometry

The compositions of equilibrium pairs of magnetite and ilmenite within the MPT were used to estimate the pre-eruptive temperature and oxygen fugacity for the Guild Mine and Weed Heights Members and the rhyolite intertuff. Because petrographic evidence for equilibrium is sparse, the chemical test provided by Bacon and Hirschman (1988) was employed to determine which pairs were possibly in equilibrium and thus suitable to use in the temperature calculations. This method considers the partitioning of Mg and Mn between coexisting pairs of ilmenite and magnetite and provides a means to critically evaluate whether the pairs of Fe-Ti oxides are in equilibrium (Bacon and Hirschman, 1988). The pairs of ilmenite and magnetite from each member of the MPT plotting within the two-sigma error envelope are consistent with equilibrium (Fig. 14).

The geothermometers presented by Anderson and Lindsley (1988) and Ghiorso and Sack (1991) were used in this study to calculate temperature and oxygen fugacity of Fe-Ti oxide equilibration. At lower temperatures (less than $\approx 650^{\circ}\text{C}$), the results from the models diverged, but in the temperature range where the models are applicable, the two geothermometers produced consistent results. For this reason, only the temperature and oxygen fugacity results determined using the thermodynamic formulation of Ghiorso and Sack (1991) are displayed in Figure 15 and discussed herein. Magnetite analyses that yielded differences in calculated temperatures between the two models in excess of $\pm 50^{\circ}\text{C}$ when paired with ilmenite were dropped from further temperature

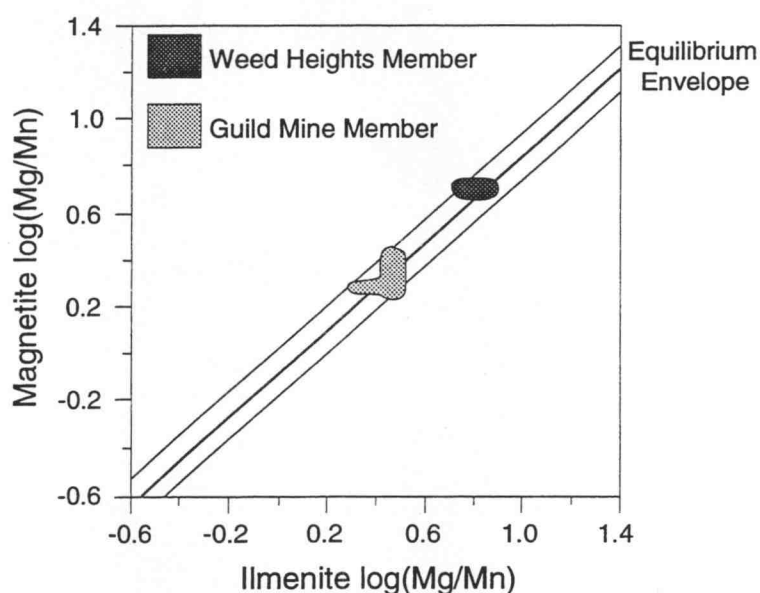


Figure 14: Plot of log Mg/Mn (molar) ilmenite versus log Mg/Mn (molar) magnetite. Error envelope is for ± 2 sigma (after Bacon and Hirschman, 1988). Fields enclose coexisting pairs of oxides from each member of the MPT that are considered to be in equilibrium.

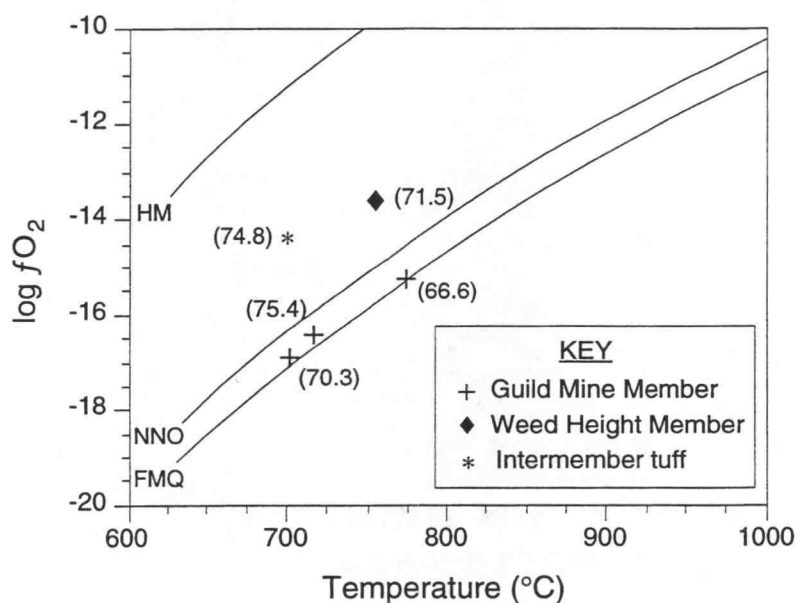


Figure 15: Temperature and oxygen fugacity determined for coexisting Fe-Ti oxides from the MPT. Numbers in parentheses are volatile-free wt. % SiO₂ for the host bulk-tuff sample. Experimental oxygen-buffer curves, HM, NNO, and FMQ, are shown for reference.

calculations, even though they may be in equilibrium according to the chemical test. These magnetite analyses display elevated Fe_2O_3 contents and have low TiO_2 contents (Appendix C), indicating that they have been altered to secondary hematite.

For the Guild Mine Member, the temperature and oxygen fugacities vary systematically with bulk-tuff composition and stratigraphic position. The dacite at the base of the Guild Mine Member (94-5B) yields a temperature and oxygen fugacity of 775°C and $10^{-15.2}$ bars (Fig. 15). This estimate was obtained by pairing the average compositions from an ilmenite grain and a magnetite grain (Table 8), which are intergrown with the same biotite phenocryst. As a check on this temperature, the average ilmenite composition (Table 8) was paired with the average of all the magnetite analyses (Appendix C) that (1) yielded consistent temperature results between the two geothermometers, and (2) are considered to be in equilibrium with the average ilmenite composition according to Mg/Mn partitioning (Bacon and Hirschman, 1988). This equilibrium pair yields temperature and oxygen fugacity results that are identical to the pair above (776°C and $10^{-15.2}$ bars; Fig. 15).

Fe-Ti oxides from the rhyodacitic part of the Guild Mine Member (94-8) yield consistent temperature and oxygen fugacity results when the average composition from one ilmenite grain (Table 8) is paired with the average composition of two separate magnetite grains. The average of magnetite analyses 4.1-4.3 (Appendix C) yields a temperature and oxygen fugacity of 708°C and $10^{-16.8}$ bars, and the average of magnetite analyses 1.1-1.5 yields a temperature and oxygen fugacity of 703°C and $10^{-16.9}$ bars (Table 8; Fig. 15). As a check, the average of most of the magnetite analyses (Appendix C) yields a temperature and oxygen fugacity of 709°C and $10^{-16.7}$ bars when paired with the average composition from one ilmenite grain.

The rhyolite near the top of the Guild Mine Member (94-13A) contains only one magnetite analysis that is in equilibrium with the average ilmenite composition according

to the chemical test of Bacon and Hirschman (1988) (Fig. 14). This equilibrium pair yields a temperature and oxygen fugacity of 718°C and $10^{-16.4}$ bars (Table 8; Fig. 15). The average of all the magnetite analyses (Appendix C) paired with the average ilmenite composition produces identical temperature and oxygen fugacity results, even though they are not in equilibrium.

The rhyodacite at the base of the Weed Heights Member (94-30) yields a temperature and oxygen fugacity of 761°C and $10^{-13.4}$ bars using the average of most of the ilmenite analyses (Appendix C) and the best magnetite analysis (Table 8) as an equilibrium pair. When the average composition of one ilmenite phenocryst (9.1-9.5) is paired with the same magnetite analysis, the temperature and oxygen fugacity results are indistinguishable (757°C and $10^{-13.6}$ bars; Table 8; Fig. 15). The altered magnetite phenocrysts with low totals (Appendix C) yield spurious temperature results when paired with the average ilmenite composition, even though they are in equilibrium according to Mg/Mn partitioning (Bacon and Hirschman, 1988). The rhyolite in the upper part of the Weed Heights Member lacks ilmenite (Appendix C), so it is not possible to consider temperature and oxygen fugacity variations with stratigraphic position and bulk-tuff composition in this unit.

In the rhyolite ash-flow tuff between the Guild Mine and Weed Heights Members (94-9B), no ilmenite and magnetite crystals are in equilibrium based on Mg/Mn partitioning (Fig. 14). Even so, the most reliable analyses yield a temperature and oxygen fugacity of 702°C and $10^{-14.4}$ bars (Fig. 15), which are considered reasonable estimates.

Two-feldspar Geothermometry

To supplement the Fe-Ti oxide temperature results, two-feldspar geothermometry was applied to the individual units of the MPT. The partitioning of the albite (Ab) component between equilibrium pairs of sanidine and plagioclase phenocrysts depends on temperature and pressure. This has served as the basis for the formulation of a variety of thermometers and barometers that treat the feldspars as a binary system (Johannes, 1979, and references therein). In an effort to improve upon the graphical binary models, both Ghiorso (1984) and Fuhrman and Lindsley (1988) utilized a thermodynamic approach to develop ternary solution models that consider the distribution of albite, orthoclase (Or), and anorthite (An) components between coexisting pairs of feldspars.

The geothermometer derived by Fuhrman and Lindsley (1988) is employed in this study, primarily because it treats the feldspars as a ternary system by simultaneously considering the Ab, An, and Or components, and it also takes into account the celsian (Cn) component in the alkali feldspars. In their detailed geothermometry study of the Taylor Creek Rhyolite, Duffield and DuBray (1990) preferred the temperatures calculated from the geothermometer of Fuhrman and Lindsley (1988), because they appear to most closely reflect magmatic conditions. In the Fuhrman and Lindsley model, the compositions of the molecular end-members are allowed to vary up to 2 molecular percent, which represents typical analytical precision, and calculates three separate temperatures for equilibrium between each of the three molecular end-members. By considering the match between the three calculated temperatures, Fuhrman and Lindsley's model provides a method by which to infer whether the feldspar species crystallized under equilibrium conditions.

Because two-feldspar geothermometry is pressure dependent, it is necessary to estimate the pressure of the pre-eruptive magma chamber. While the pressure of the MPT magma chamber has not been independently determined, the temperatures were calculated by specifying a pressure of 2 kbars. Based on comparisons with compositionally similar ash-flow tuffs, which were erupted from shallow-crustal levels (cf., Mahood, 1981; Ferriz and Mahood, 1987; Grunder and Mahood, 1988; Johnson and Rutherford, 1989a; Chesner, 1998), a pressure between 1 and 4 kbars is considered reasonable for the MPT. In addition, at pressures of 5 kbars and greater, feldspar pairs from some compositions failed to yield convergent temperatures, but they did converge at 2 kbars. The effect of pressure on the temperatures determined using the two-feldspar geothermometer of Fuhrman and Lindsley (1988) was further examined by calculating temperatures for selected samples with the pressure specified from 1 to 7 kbars at 1-kbar intervals. For one composition, an increase from 1 to 7 kbars caused a temperature increase of 93.5°C, but for individual 1-kbar intervals, the temperatures do not vary systematically but instead change an average of 28.5°C.

For each composition, a series of representative rim compositions of plagioclase and sanidine phenocrysts were selected for thermometry. The Ab, Or, An, and Cn components for each pair of feldspars were input into the Fuhrman and Lindsley model to calculate the temperature of equilibrium crystallization. Tie lines between feldspar crystals representing the equilibrium pairs that crystallized last are shown in Figure 16. The calculated temperatures for these pairs are compiled along with the results from Fe-Ti oxide and two-pyroxene geothermometry in Figure 17.

Overall, the two-feldspar temperatures from the MPT, which are interpreted to represent the temperature at which the last equilibrium pair of feldspars crystallized for each composition, are indistinguishable from the temperatures calculated using Fe-Ti oxide compositional data (Fig. 17). Within the individual members of the MPT, the

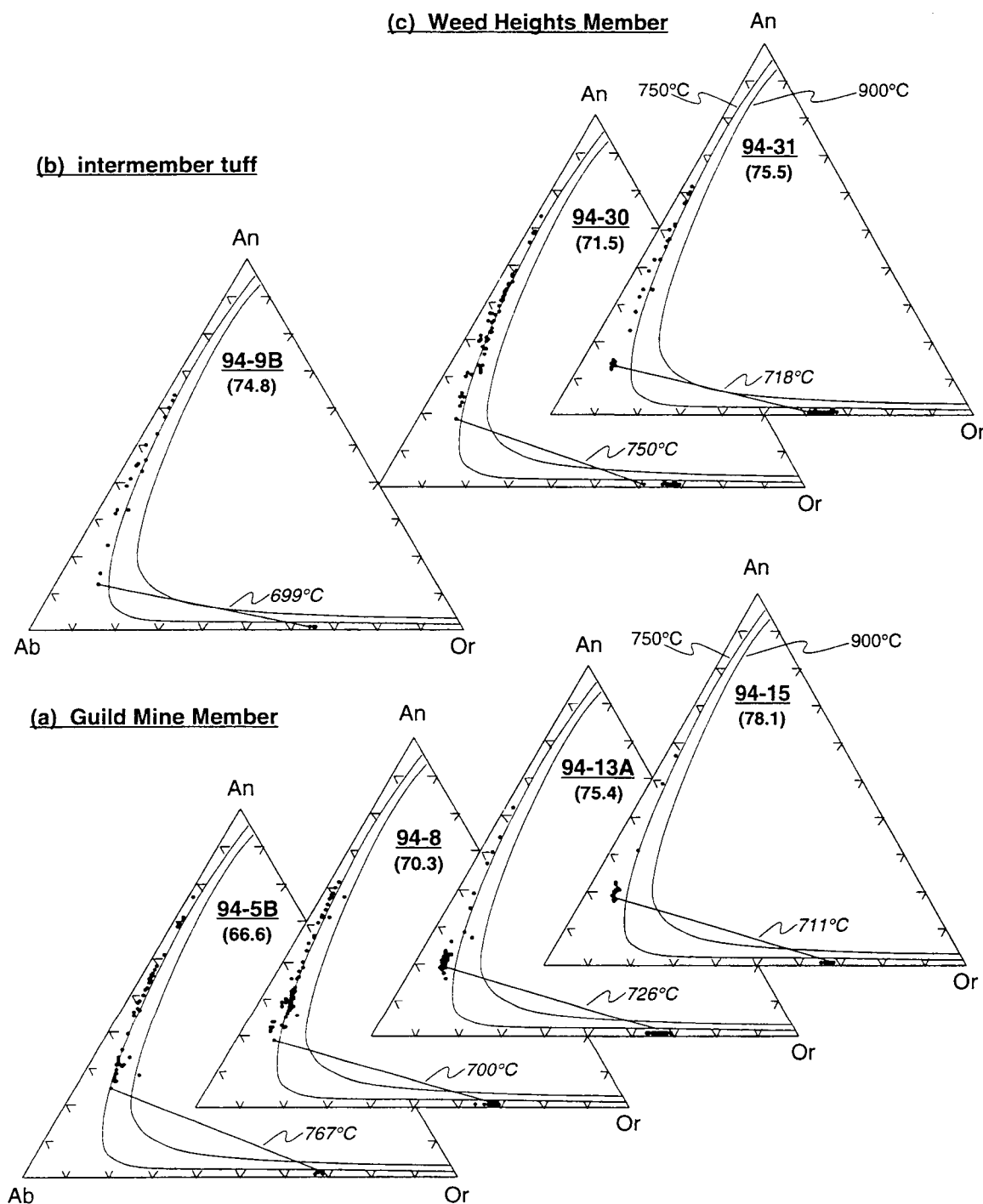


Figure 16: Ternary feldspar diagrams with tie lines connecting equilibrium pairs of plagioclase and sanidine analyses used for two-feldspar geothermometry. Temperatures, shown in italics, were calculated using the model of Fuhrman and Lindsley (1988). Labelled isotherms (750°C at 1 kbar, 900°C at 0.5 kbar) are after Fuhrman and Lindsley (1988). Sample numbers given in bold print in the upper part of each diagram, and bulk-tuff, volatile-free SiO₂ contents are in parentheses beneath. (a) Guild Mine Member; (b) intermember rhyolite ash-flow tuff; and (c) Weed Heights Member.

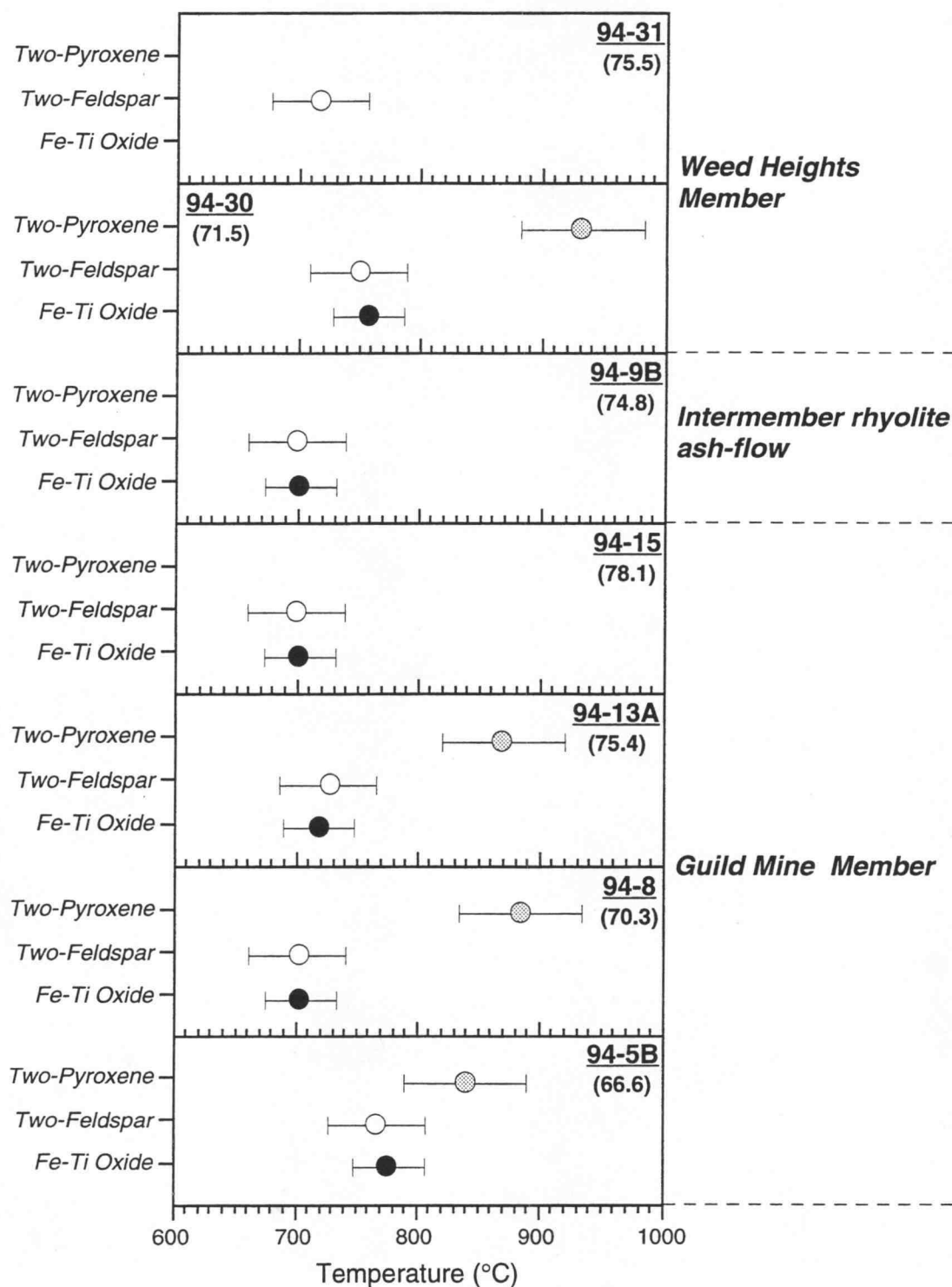


Figure 17: Compiled temperature diagram for the MPT. Fe-Ti oxide temperatures determined using the model of Ghiorso and Sack (1991). Two-feldspar temperatures obtained using the geothermometer of Fuhrman and Lindsley (1988). Two-pyroxene temperatures calculated using the geothermometer of Lindsley (1983). Error bars are $\pm 30^{\circ}\text{C}$ for oxide temperatures, $\pm 40^{\circ}\text{C}$ for feldspar temperatures, and $\pm 50^{\circ}\text{C}$ for pyroxene temperatures.

two-feldspar temperatures decrease up section with increasing differentiation (Fig. 16). The maximum range of temperatures between the base and the top of each member is 70°C, which is outside the absolute analytical error for the Fuhrman and Lindsley model. Even so, the precision within the suite of MPT samples is most likely better than the error depicted (Fig. 17).

The dacite at the base of the Guild Mine Member yields a two-feldspar temperature of 767°C, which is determined by pairing the lowest An content plagioclase analysis with the slightly higher Or content sanidine analysis (Fig. 16). This is the lowest two-feldspar temperature calculated for the dacite and thus represents the temperature at which the last equilibrium pair crystallized. The feldspar pairs from the more evolved parts of the Guild Mine Member yield lower temperatures (Fig. 17). The rhyodacite (94-8) near the middle of the unit has a temperature of 700°C, which is a result of pairing the lowest An content plagioclase analysis with a higher Or content sanidine analysis (Fig. 16). The rhyolite and high-SiO₂ rhyolites from the upper parts of the Guild Mine Member yield temperatures of 726 and 711°C, respectively. In each of these calculations, a higher Or content sanidine analysis was paired with the lowest An content plagioclase analysis (Fig. 16).

Using the compositional data from the rims of feldspar phenocrysts, the rhyodacite at the base of the Weed Heights Member yields a temperature of 750°C. This temperature results from pairing the lowest An content plagioclase analysis with the lowest Or content sanidine analysis (Fig. 16). A number of the calculated temperatures (≈60%) for the rhyodacite are between 790 and 810°C, which represent earlier stages of the thermal history as indicated by An contents for the plagioclase phenocrysts near An₃₀. Plagioclase and sanidine phenocrysts in the rhyolite at the top of the Weed Heights Member (94-31) yield a temperature of 718°C, which results from pairing the

lowest An plagioclase with a lower Or content sanidine (Fig. 16). This temperature represents the temperature at which the last equilibrium pair of feldspars crystallized.

The rhyolite ash-flow tuff between the Guild Mine and Weed Heights Members (94-9B) yields a temperature of 699°C (Fig. 16), which is from a pair of intergrown plagioclase and sanidine phenocrysts. The range of temperatures for this sample extends up to 784°C, but the higher temperatures result from pairing the sanidine analyses with higher An plagioclase analyses and thus reflect earlier stages of the thermal history for this tuff.

Two-pyroxene Geothermometry

The distribution of Ca, Mg, and Fe contents in coexisting clinopyroxene and orthopyroxene phenocrysts is a function of temperature and is the foundation for two-pyroxene geothermometry (Kretz, 1982). This study employed the two-pyroxene geothermometer within the QUILF program (Andersen and others, 1993) to estimate the temperature of equilibrium crystallization of the clinopyroxene and orthopyroxene phenocrysts, which are largely confined to the lower and middle parts of the individual members of the MPT (Fig. 3). The two-pyroxene geothermometer in the QUILF program is based on the graphical model presented by Lindsley (1983), which stipulated that pyroxene compositions be projected onto the pyroxene quadrilateral using a scheme that reflects the bulk activities of Wo, En, and Fs (Lindsley and Andersen, 1983). The QUILF program has a built-in routine that takes this stipulation into account, so the pyroxene compositional data from the MPT were simply plotted onto the quadrilateral (Fig. 12) using a standard method (Morimoto, 1988).

The temperatures presented below were calculated by stipulating a pressure of 2 kbars. In an evaluation of the effects of increasing pressure on the two-pyroxene temperature estimates, the temperature increased 3°C for every 1-kbar increase in pressure. Because the pyroxenes from the MPT have low contents of non-quadrilateral components, the temperature results presented herein have an accuracy of approximately $\pm 50^\circ\text{C}$ (Lindsley, 1983). To evaluate whether the pyroxenes represent an equilibrium pair, the QUILF program also provides a value of uncertainty for each temperature; this is provided for each temperature reported below.

For nearly the entire compositional range represented by the MPT, except for the dacite at the base of the Guild Mine Member, the two-pyroxene temperatures are significantly higher than the temperatures calculated using Fe-Ti oxide and two-feldspar geothermometry (Fig. 17). The two-pyroxene geothermometry results indicate that the pyroxenes in the rhyodacitic and rhyolitic parts of both members of the MPT were not in equilibrium with the rest of the assemblage. Petrographic features such as ragged grain margins and other disequilibrium textures within the pyroxene phenocrysts also indicate non-equilibrium between the pyroxene phenocrysts and the melt. Nonetheless, the pyroxene temperature data provide information regarding the thermal history of the MPT magma system so the two-pyroxene temperatures considered most representative from each composition are presented in Figure 17, which illustrates the great disparity between the temperatures calculated by various methods. The pyroxene phenocrysts are perhaps relicts of a more mafic parent magma, or more likely, they represent an earlier, higher temperature stage of the dacitic magma. The similarity between the elevated two-feldspar temperatures that were calculated using the highest An content cores of some plagioclase phenocrysts supports the latter.

For the dacite at the base of the Guild Mine Member (94-5B), a temperature of $840 \pm 33^\circ\text{C}$ (Fig. 17) was calculated by pairing the rim compositions from clinopyroxene

phenocrysts with the highest hedenbergite contents and orthopyroxene phenocrysts with the highest ferrosilite contents. Even though the clinopyroxene analyses from the dacite plot in three distinct compositional clusters, the clinopyroxene phenocrysts with the highest Fs contents are interpreted to be in equilibrium with the relatively tight cluster of orthopyroxene analyses at about $\text{Wo}_{2.5}\text{En}_{49}\text{Fs}_{48.5}$ (Fig. 17), because these pairs yield the lowest uncertainties. It is interesting to note that the dacite yields lower two-pyroxene temperature results than the Guild Mine rhyodacite and rhyolite (Fig. 17).

The pyroxene phenocrysts in the rhyodacitic part of the Guild Mine Member (94-8) yield a temperature of $885 \pm 34^\circ\text{C}$ (Fig. 17). This temperature is obtained by pairing the rim compositions from the Fe-rich clinopyroxene and orthopyroxene phenocrysts. A pair of clinopyroxene and orthopyroxene crystals in the rhyodacite are intergrown and yield a temperature of $898 \pm 61^\circ\text{C}$, which is similar to the temperature calculated using the rim compositions. For the rhyolite near the top of the Guild Mine Member (94-13A), the rim compositions from a pair of Fe-rich pyroxene phenocrysts yield a temperature of $871 \pm 26^\circ\text{C}$ (Fig. 17).

For the rhyodacite at the base of the Weed Heights Member, the compositional data from the rims of the pyroxene phenocrysts with elevated Fs contents yield a temperature of $933 \pm 24^\circ\text{C}$ (Fig. 17). Interestingly, the two-pyroxene temperatures from the Weed Heights Member are higher overall than those from the Guild Mine Member (Fig. 17).

Total Pressure

The experimentally-derived geobarometers based on the Al content in igneous hornblende are utilized herein to provide a quantitative estimate for the total pressure of the MPT magma chamber. Hornblende geobarometry is based on the co-linear

relationship between pressure and total aluminum in hornblende (Hammarstrom and Zen, 1986; Hollister and others, 1987; Johnson and Rutherford, 1989b; Schmidt, 1992). The experimentally-calibrated geobarometers are specifically applicable to systems in which hornblende is in equilibrium with quartz, plagioclase, sanidine, biotite, titanite, and magnetite or ilmenite (Johnson and Rutherford, 1989b; Schmidt, 1992). In the absence of this assemblage, total pressure is probably one of the most difficult magmatic parameters to assess (Whitney and Stormer, 1985).

Al-in-hornblende geobarometry is applicable to the rhyodacite at the base of the Weed Heights Members, because it displays the appropriate assemblage (Fig. 3). However, these geobarometers are not applicable to any compositions of the Guild Mine Member, because where hornblende is present in the basal dacite, it is not in equilibrium with quartz (Fig. 3), and where hornblende and quartz occur together in the rhyodacite, sphene is absent. The hornblendes in the Guild Mine Member yield anomalously high pressures, which is attributed to the improper assemblage.

The rim compositional data from hornblende phenocrysts in the rhyodacite at the base of the Weed Heights Member yield pressures between 1.0 and 2.1 kbars depending on the geobarometer utilized (Johnson and Rutherford, 1989b; Schmidt, 1992), which correspond to depths of approximately 3.4 to 7.1 km. The Johnson and Rutherford model, which yields pressures in the lower part of the range, is probably most applicable to the MPT in terms of compositional similarities and the temperature and pressure range. Using the representative Weed Heights hornblende analysis (Table 7), the Johnson and Rutherford calibration yields a pressure of 1.1 ± 0.5 kbars, which corresponds to a depth of about 3.7 km. Anderson and Smith (1995) incorporated the effect of temperature in their recalibration of the hornblende geobarometer, which utilized the experimental data of Johnson and Rutherford (1989b) and Schmidt (1992). Using a temperature of 757°C determined from Fe-Ti oxide geothermometry (Fig. 15),

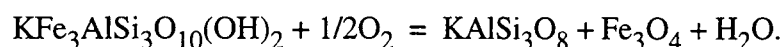
Anderson and Smith's calibration yields a pressure of 1.2 ± 0.6 kbars for the MPT, which is identical to the pressure determined using Johnson and Rutherford's model. The inferred depths for the MPT magma system are comparable to values reported for the Toquima caldera complex (≈ 5.5 km; Boden, 1994) and for the Bishop Tuff (≈ 6 km; Johnson and Rutherford, 1989b) but lower than those reported for the Fish Canyon Tuff (≈ 8 km; Johnson and Rutherford, 1989a), for the tuffs of the Timber Mountain Group (≈ 14 km; Mills and others, 1997), and for the Toba Tuff (≈ 10 km; Chesner, 1998).

Although this upper crustal pressure is appropriate for caldera formation (Cas and Wright, 1987), no caldera has been identified for the MPT. The MPT is faulted and probably half of its paleodistribution is buried by younger sediments.

Water Content Estimated from Experimental Phase Equilibria

Hydrous phases in the MPT, such as ubiquitous biotite and sparsely present hornblende (Fig. 3), provide evidence for the presence of water in the pre-eruptive magma chamber. Also, the relatively low temperatures of equilibration for most of the compositions of the MPT (Figs. 15, 16, and 17) are consistent with elevated H_2O pressures.

Water contents in the pre-eruptive MPT magma chamber are estimated by utilizing the dehydration reaction of biotite in the presence of oxygen to form sanidine, magnetite, and water (Wones and Eugster, 1965):



To solve for H_2O , this equation is rewritten as follows:

$$\log f_{H_2O} = G/2.303RT + \log a_{KFe_3AlSi_3O_{10}(OH)_2} + 1/2 \log f_{O_2} - \log a_{KAlSi_3O_8} - \log a_{Fe_3O_4},$$

where $G/2.303RT = 8674/T + 2.461 + 0.00392*(P-1)/T$ (Hildreth, 1977, cited in Boden, 1994).

While accurate temperature and oxygen fugacity determinations are obviously important to how well fH_2O can be constrained, the determination of fH_2O also depends upon the method by which the activity of the annite component in biotite is calculated. Wones (1972) suggested that the activity of annite depends most upon the fraction of Fe^{+2} in the octahedral site. Because of the large number of element substitutions possible in biotite, the activity of annite has subsequently been shown to depend on the mole fractions of K, Fe, Al, Si, and OH in their respective sites (e.g., Bohlen and others, 1980). Hence, the activity of annite is determined from the following equation after Bohlen and others (1980):

$$a_{KFe_3AlSi_3O_{10}(OH)_2} = \frac{(X_K^{X\text{-site}} * (X_{Fe}^{Y\text{-site}})^3 * X_{Al}^{Z\text{-site}} * (X_{Si}^{Z\text{-site}})^3 * (X_{OH}^{hyd})^2)}{0.105}$$

The results for fH_2O , P_{H_2O} , and weight percent H_2O calculations are presented in Table 9. The Guild Mine Member yields fH_2O values ranging from 76 and 115 bars in the dacite and rhyodacitic parts of the member to 226 and 322 bars in the rhyolitic upper parts of the member. Weight percents corresponding to these fugacities, which were derived from the data of Burnham and Davis (1974), range from 0.8 to 2.2 wt. %. P_{H_2O} values are much lower than the total pressure of 2 kbars, indicating that the system was undersaturated with respect to water. The Weed Heights Member and the rhyolite ash-flow tuff between the two members rhyolite ash-flow tuff yield much higher fH_2O values (1075 and 1215 bars, respectively) with corresponding wt. % H_2O values of 5.1 and 6.0, respectively (Table 9). P_{H_2O} values for the intermember rhyolite ash-flow tuff and the Weed Heights Member are in the range of total pressures determined via hornblende geobarometry, indicating that the system was saturated or approaching saturation with respect to water.

Table 9: Water estimates at 2 kbar using the biotite-sanidine-magnetite geobarometer.

	T (°C)	activity annite	activity sanidine	activity magnetite	logfO ₂	logfH ₂ O	fH ₂ O (bars)	PH ₂ O (bars)	wt. % H ₂ O
<i>Guild Mine Member</i>									
94-5B	840	0.056	0.683	0.492	-15.2	1.8833	76.44	92.54	0.8
94-8	703	0.0561	0.6742	0.585	-16.9	2.0592	114.61	170.81	1.3
94-13A	718	0.0796	0.6316	0.591	-16.4	2.3505	224.13	321.57	2
94-15	711	0.1033	0.6558	0.593	-16.4	2.5081	322.17	480.13	2.2
<i>intermember rhyolite ash-flow tuff</i>									
94-9B	702	0.0381	0.6395	0.761	-14.4	3.0843	1214.32	1809.71	6
<i>Weed Heights Member</i>									
94-30	757	0.0335	0.6038	0.677	-13.6	3.0286	1068.17	1429.94	5.1

T (°C) and logfO₂ from Figure 15 and Table 8.

activity annite: see text (from Bohlen and others, 1980).

activity sanidine: mole fraction Or in sanidine (X_{Or, san}).

activity magnetite: $0.5 * n_{(Fe3+,F)} * X_{(Fe2+,S2+)} * X_{(Fe3+,S3+)}$, where $n_{(Fe3+,F)}$ is the number of Fe³⁺ ions per formula unit (from Stormer, 1983).

logfH₂O: see text (from Hildreth, 1977, cited in Boden, 1994).

P_{H₂O}: Determined using fugacity coefficients from Burnham and others (1969).

wt. % H₂O: Determined from data and tables of Burnham and Davis (1974).

Magmatic water contents of 2 to 5 wt. % H₂O for the Guild Mine dacite, 0 to 4.25 wt. % H₂O for the Guild Mine rhyodacite, rhyolite, and high-SiO₂ rhyolite, and 0 to 4.25 wt. % H₂O for the Weed Heights rhyodacite and rhyolite were estimated by comparing the observed phenocryst assemblages to experimental phase equilibria for synthetic granite and granodiorite compositions at 2 and 8 kbars (Naney, 1983). The water estimates derived from the biotite-sanidine-magnetite barometer for the Guild Mine rhyodacite, rhyolite, and high-SiO₂ rhyolite are generally consistent with those determined using the experimental phase equilibria derived by Naney (1983). However, for the Guild Mine dacite and the Weed Heights rhyodacite, there is a slight discrepancy between water content estimated from the two different methods.

Density

Anhydrous and hydrous densities were calculated for both the bulk tuff and glass using the partial molar volumes and coefficients of thermal expansion and compressibility for the oxide components provided by Lange and Carmichael (1990). For hydrous density calculations, the partial molar volume for water is assumed to be 20 cm³/mole (Lange and Carmichael, 1990). Temperatures were derived from Fe-Ti oxide compositions (Fig. 15), and water content was estimated using the biotite-sanidine-magnetite barometer (Table 9). The density of the phase assemblage is calculated by combining modal data for the MPT (Fig. 3) with published mineral density data (Hurlbut and Klein, 1985; Deer and others, 1992).

The least differentiated, stratigraphically lowest magma for both the Guild Mine and the Weed Heights Members yields greater densities than the more silicic magma (Fig. 18). The bulk-tuff anhydrous density estimates of the Guild Mine Member range from

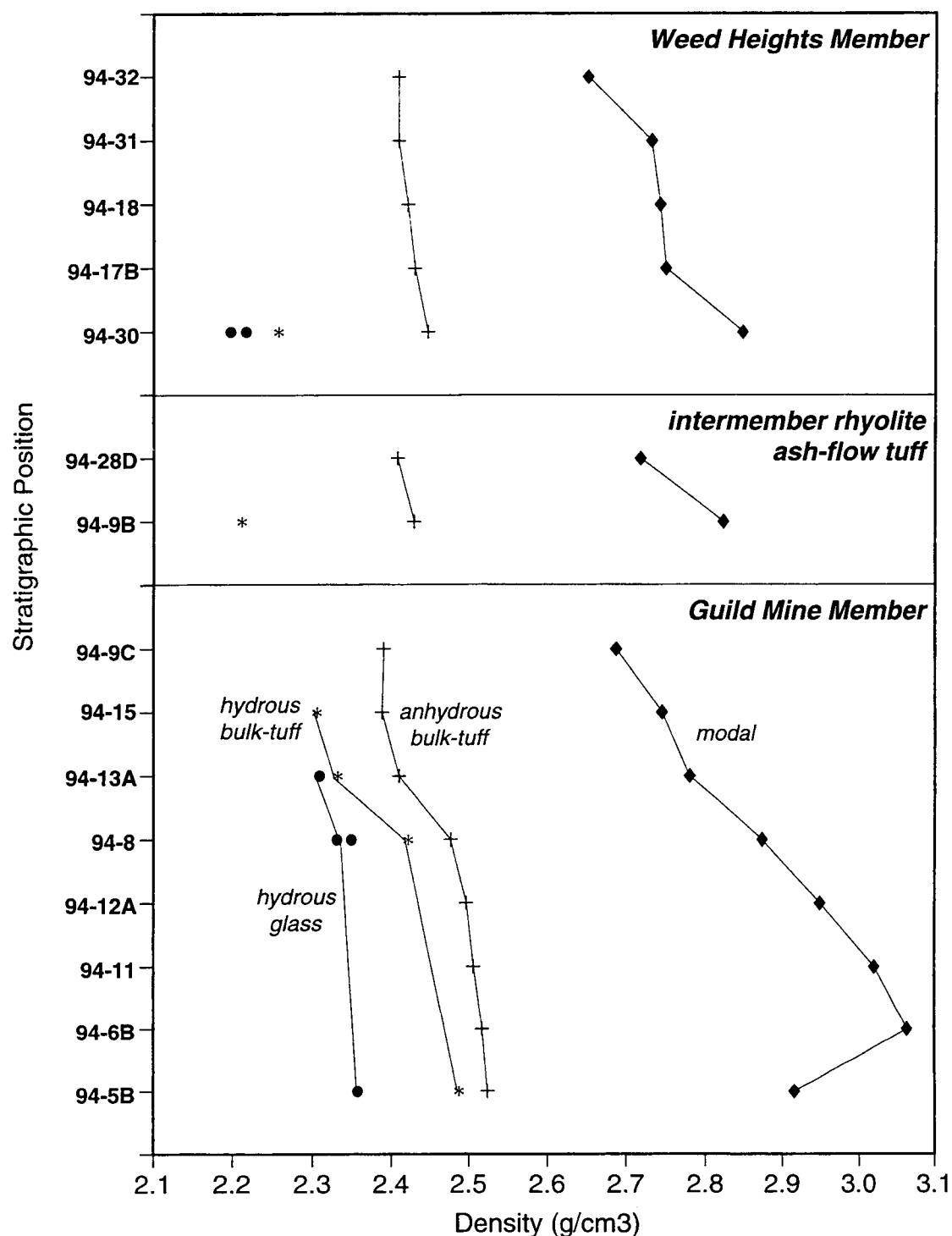


Figure 18: The results of the density calculations for pre-eruptive MPT. The samples are arranged according to relative stratigraphic position and degree of differentiation. Modal density values calculated using modal mineral proportions given in Figure 3 and published mineral densities. Anhydrous and hydrous bulk-tuff values calculated using bulk-tuff geochemical data (Table 2), glass data (Table 3), and partial molar volumes from Lange and Carmichael (1990).

2.52 g/cm³ for the dacite at the base to 2.39 g/cm³ for the high-SiO₂ rhyolite at the top. For the Weed Heights Member, the density estimates range from 2.45 g/cm³ for the rhyodacite at the base to 2.41 g/cm³ for the rhyolite at the top. The bulk-tuff hydrous density estimates slightly accentuate the density gradient for the Guild Mine Member (Fig. 18). The water-poor dacite at the base of the Guild Mine Member yields a density of 2.49 g/cm³, and the relatively more water-rich upper part of the Member yields a density of 2.31 g/cm³. Anhydrous glass densities show minimal change with stratigraphic position, but hydrous glass densities illustrate a density gradient from 2.36 g/cm³ in the slightly less evolved glass population to 2.31 g/cm³ for the more evolved glass population (Fig. 18). The density estimates of the mineral phase assemblages at specific compositions also decrease with increasing stratigraphic position and greater degree of differentiation.

Viscosity

The viscosity of the pre-eruptive magma is estimated using the methodology of Shaw (1972) and by using temperatures from Fe-Ti oxide compositional data and water estimates from the biotite-sanidine-magnetite barometer. For the Guild Mine Member, calculated viscosity values range from 10⁸ P for the dacite at the base to 10⁹ P for the high-silica rhyolite at the top. The Weed Heights Member yields lower viscosities at 10⁶ P owing to its higher H₂O content.

Mechanisms of Differentiation

The chemical trends within the Guild Mine Member are qualitatively consistent with crystal fractionation and certain trends within the Weed Heights Member are suggestive of magma mixing (Figs. 5, 7, and 8). For the Guild Mine Member, the trace element diagrams showing variations with Ta (Fig. 8) display curved trends or even distinct inflections or changes in the direction of the liquid path, which are considered to be key characteristics of liquids evolving by fractional crystallization (Cox and others, 1979). The near identity of the REE patterns between the dacites, rhyodacites, and rhyolites, especially in the Guild Mine Member (Fig. 9), also provides qualitative evidence that the more evolved magmas were derived from less evolved magmas by crystal fractionation. On some of the trace element variation diagrams, data from the Weed Heights Member display linear trends that cut across the curved trends defined by the data from the Guild Mine Member (Fig. 8). The linear trends in the Weed Heights data probably do not represent fractional crystallization and are more consistent with mixing.

In the following sections, bulk-tuff chemical and mineralogical compositional data are utilized to model and constrain the petrogenetic processes responsible for the compositional zonation within each member of the MPT. First, least-squares mass balance calculations are applied to the geochemical data base to evaluate fractional crystallization as a plausible model for the evolution of the MPT magmatic system.

Major Element, Least-Squares Models

The least-squares mass balance calculations within XLFRAC-MAC (Stormer and Nicholls, 1978) are utilized herein to test the hypothesis that crystal fractionation is a

viable mechanism for the chemical evolution of the compositional zonation within each member of the MPT. XLFRAC solves a set of linear least-squares mass-balance equations to determine the modal proportions of added or subtracted phases required to yield a fractionated daughter rock from the stipulated parent. Well-studied samples of dacite, rhyodacite, rhyolite, and high-SiO₂ rhyolite from each member were chosen as the parent and derivative magmas in a series of step-wise models (Table 10). The phase assemblages and mineral compositions were permitted to change over reasonable ranges to obtain the best-fit models. Several criteria were used to evaluate whether a given model is considered plausible: first, the chosen phases must be removed from the parent magma; and second, the sum of squares of the residuals (ΣR^2) must be minimized.

In utilizing least-squares mass balance calculations, the number of phases should not be more than about half the components, because with an increasing number of phases the equations are over determined which in turn results in falsely improved ΣR^2 values (Stormer and Nichols, 1978; Cox and others; 1979). While the five-phase models presented below may be at the limit of acceptability, all of the phases in these models were observed in the parent composition.

The dacite from the base of the Guild Mine Member (94-5B) serves as the parent magma for the rhyodacite from the middle of the Guild Mine Member (94-8). A fractionating assemblage consisting predominantly of plagioclase and biotite with subordinate amounts of clinopyroxene, orthopyroxene, hornblende and/or magnetite for a total of approximately 15-18% crystallization yield the best models for this compositional range (Table 10). The representative biotite analysis (Table 7; Mg#=51.3) is paired with plagioclase analyses displaying a range of An contents. The interiors of the zoned plagioclase phenocrysts, which are characterized by the highest An contents (An₆₀₋₇₀), yield models with the lowest ΣR^2 value (Table 10). Two clinopyroxene analyses, which span the range of Fs contents for the dacite (Fig. 12),

Table 10: Results of the major element least squares calculations for the MPT.

<u>Model</u>	<u>Parent</u>	<u>Daughter</u>	<u>PLAG</u>	<u>BIOT</u>	<u>SANI</u>	<u>QTZ</u>	<u>CPX</u>	<u>OPX</u>	<u>HBL</u>	<u>MGT</u>	<u>TOTAL</u>	<u>Sum R²</u>
<u><i>Guild Mine Member</i></u>												
Dac->Rhyodac	94-5B	94-8	57.3	42.7	---	---	---	---	---	---	14.7	0.14
Dac->Rhyodac	94-5B	94-8	56.1	39.7	---	---	4.3	---	---	---	15.0	0.11
Dac->Rhyodac	94-5B	94-8	58.8	34.7	---	---	---	6.5	---	---	15.3	0.11
Dac->Rhyodac	94-5B	94-8	56.3	40.1	---	---	---	---	3.6	---	14.8	0.14
Dac->Rhyodac	94-5B	94-8	61.6	31.8	---	---	0.8	5.7	---	---	17.0	0.14
¹ Dac->Rhyodac	94-5B	94-8	64.5	26.9	---	---	5.7	---	---	2.8	17.8	0.18
Rhyodac->Rhyo	94-8	94-13A	70.3	29.7	---	---	---	---	---	---	22.0	0.18
Rhyodac->Rhyo	94-8	94-13A	60.3	---	23.0	---	---	16.7	---	---	31.7	0.17
Rhyodac->Rhyo	94-8	94-13A	60.5	20.4	5.5	13.6	---	---	---	---	36.4	0.18
² Rhyodac->Rhyo	94-8	94-13A	65.3	19.4	5.1	8.3	---	---	---	1.9	28.5	0.09
Rhyo->HSRhyo	92-22	94-15	55.3	16.1	28.5	---	---	---	---	---	25.8	0.33
³ Rhyo->HSRhyo	92-22	94-15	43.1	2.1	43.5	7.6	---	---	---	3.6	33.5	0.08
Rhyo->HSRhyo	94-13A	94-15	90.6	9.4	---	---	---	---	---	---	15.5	0.08
Rhyo->HSRhyo	94-13A	94-15	88.8	9.4	---	1.8	---	---	---	---	16.1	0.08
Rhyo->HSRhyo	94-13A	94-15	89.0	---	7.8	---	---	---	---	3.2	15.7	0.05
⁴ Rhyo->HSRhyo	94-13A	94-15	70.0	0.4	16.2	10.9	---	---	---	2.5	21.5	0.05
<u><i>Weed Heights Member</i></u>												
⁵ Rhyo->HSRhyo	94-17B	94-31	16.0	10.5	49.3	24.2	---	---	---	---	46.5	0.66

Dac = dacite; Rhyodac = rhyodacite; Rhyo = rhyolite; HSRhyo = high-silica rhyolite. Refer to Table 2 for bulk-tuff compositional data. Refer to Tables 4-8 for mineral data used in models. Superscripted numbers indicate major element models used for trace element fractionation models in Figure 19.

and the representative orthopyroxene analysis (Table 6) are each combined with plagioclase and biotite to deduce the role of pyroxene fractionation. The lowest ΣR^2 values (<0.2) are produced when the highest An content plagioclase analyses are combined with the representative biotite and either the higher Fs content clinopyroxene (Fs_{21.3}) or the representative orthopyroxene (Table 6). Adding hornblende to the fractionating assemblage of plagioclase and biotite also produces a plausible model (Table 10). Four-phase models, consisting of plagioclase (An_{46.2}-An_{69.1}), biotite, clinopyroxene, and either orthopyroxene or magnetite, are satisfactory with low sum of squares of residuals ($\Sigma R^2 < 0.2$; Table 10). Five-phase models in which either magnetite or hornblende are combined with an assemblage of plagioclase, biotite, clinopyroxene, and orthopyroxene are invalid, because in the first case, orthopyroxene is not subtracted from the melt, and in the second case, hornblende is not subtracted from the melt.

For the next compositional step, the rhyodacite (94-8) is used as the parent magma for the more evolved material near the top of the Guild Mine Member (94-13A). A fractionating assemblage consisting of plagioclase and biotite produces acceptable models (Table 10). The biotite (Table 7; Mg#=51), which is indistinguishable from the biotite in the dacite (Fig. 13), is paired with a range of plagioclase analyses. The models with the lowest ΣR^2 values (<0.2) are produced by using plagioclase analyses with An contents between An₃₅ and An₄₅ (Table 10). It is not possible to satisfactorily model a fractionating assemblage consisting of sanidine and plagioclase, as indicated by high ΣR^2 values. Also, it is not possible to add sanidine to the fractionating assemblage of plagioclase and biotite, because sanidine is always an added phase rather than a subtracted phase. An assemblage consisting of plagioclase, sanidine, and orthopyroxene crystals with higher Fs contents (Fs_{49.1}) is a viable model (Table 10), but this assemblage is not plausible using lower Fs content orthopyroxenes. A fractionating assemblage of clinopyroxene, plagioclase, and sanidine, however, is not

feasible because of the large ΣR^2 values that result. A five-phase model consisting of plagioclase, biotite, sanidine, quartz, and magnetite yields a low ΣR^2 value (Table 10). Adding orthopyroxene to this assemblage instead of magnetite also yields a satisfactory model.

The low-SiO₂ rhyolite (92-22) is used as a parent for the high-SiO₂ rhyolite at the top of the Guild Mine Member (94-15); an assemblage consisting of plagioclase, biotite, and sanidine yields marginally acceptable ΣR^2 values for this compositional range (Table 10). A five-phase model consisting plagioclase, biotite, sanidine, quartz, and magnetite yields a much lower ΣR^2 value (0.5; Table 10).

The rhyolite (94-13A) is also used as the parent for the high-SiO₂ rhyolite at the top of the Guild Mine Member (94-15). A simple phase assemblage of plagioclase and biotite yields the lowest ΣR^2 values (<0.10; Table 10) when the lowest An content plagioclase analyses (<An₂₀) are combined with the representative biotite analysis from the rhyolite (Table 7; Mg# 44.7). Models with three phases are satisfactory depending on the An content of the plagioclase phenocrysts. A fractionating assemblage consisting of biotite, quartz, and low An content plagioclase (<An₂₂) produces a valid model (Table 10). Models combining magnetite and plagioclase with sanidine produce the best fit if the lowest An content plagioclase analysis is paired with a high Or content sanidine analysis and the representative magnetite analysis (Table 10). Assemblages consisting of biotite, plagioclase, and sanidine; magnetite, plagioclase, and quartz; and magnetite, quartz, and sanidine all yield unsatisfactory models. Four-phase and five-phase models are only plausible with the lowest An content plagioclase. A five-phase model consisting of plagioclase, biotite, sanidine, quartz, and magnetite yields one of the lower ΣR^2 values for this increment (Table 10).

For the Weed Heights Member, the origin of the compositional zoning within the more silicic parts of the member can also be modelled using fractional crystallization,

although this model is of dubious reliability. It is possible to yield the high-SiO₂ rhyolite at the top of the Weed Heights Member (94-31) from the rhyolite (94-17B) directly overlying the rhyodacite using a fractionating assemblage consisting of plagioclase (An₃₃), biotite (Mg# 59), sanidine (Or₆₆), and quartz (Table 10). The ΣR^2 value is near the upper end of acceptability ($\Sigma R^2 = 0.66$), and this model requires a relatively high amount of crystallization (46.5%). Five-phase models consisting of plagioclase, biotite, sanidine, quartz and either ilmenite or magnetite are unacceptable, because in both models, the Fe-Ti oxide phase is not subtracted from the melt.

It is not possible, however, to derive the rhyolite in the upper part of the Weed Heights Member from the rhyodacite at the base using a crystal fractionation mechanism. In every attempt to realistically model fractional crystallization using least-squares calculations, the ΣR^2 values were far too high (up to 5), and in many cases, the modelled phases were not removed from the magma but instead were added.

Trace Element Fractionation Models

The major element least-squares calculations indicate that fractional crystallization is a plausible mechanism to explain the origin of the compositional variation in the Guild Mine Member and in the more silicic parts of the Weed Heights Member. The trace element data from each member are used to further test the simple fractional crystallization models proposed above. The calculated modal results from the best-fit, four- and five-phase, least-squares models (Table 10) are combined with published partition coefficients (Table 11; Arth, 1976; Gill, 1981; Nash and Crecraft, 1985) to calculate the concentration of a series of trace elements in the derivative magma assuming Rayleigh fractional crystallization. Whenever possible, the partition

Table 11: Partition coefficients used in trace element models.

	Dac->Rhyodac 94-5B->94-8	Rhyodac->Rhyo 94-8->94-13A	Rhyo->HSRhyo 92-22->94-13A	Rhyo->HSRhyo 94-13A->94-15	Rhyo->HSRhyo 94-17B->94-31
Th plagioclase	0.04 ^{NC}	0.04 ^{NC}	0.04 ^{NC}	0.04 ^{NC}	0.04 ^{NC}
biotite	0.495 ^{NC}	0.495 ^{NC}	0.495 ^{NC}	0.495 ^{NC}	0.495 ^{NC}
sanidine	---	0.03 ^{NC}	0.02 ^{NC}	0.02 ^{NC}	0.02 ^{NC}
quartz	---	0.009 ^{NC}	0.008 ^{NC}	0.008 ^{NC}	0.008 ^{NC}
magnetite	0.19 ^{NC}	0.19 ^{NC}	0.19 ^{NC}	0.19 ^{NC}	---
clinopyroxene	0.15 ^{NC}	---	---	---	---
Sc plagioclase	0.05 ^{NC}	0.053 ^{NC}	0.06 ^{NC}	0.06 ^{NC}	0.05 ^{NC}
biotite	10.45 ^{NC}	10.45 ^{NC}	10.45 ^{NC}	10.45 ^{NC}	15.567 ^{NC}
sanidine	---	0.023 ^{NC}	0.02 ^{NC}	0.02 ^{NC}	0.04 ^{NC}
quartz	---	0.012 ^{NC}	0.01 ^{NC}	0.01 ^{NC}	0.015 ^{NC}
magnetite	10.6 ^{NC}	10.6 ^{NC}	10.6 ^{NC}	10.6 ^{NC}	---
clinopyroxene	53 ^{NC}	---	---	---	---
Rb plagioclase	0.048 ^A	0.12 ^{NC}	0.075 ^{NC}	0.075 ^{NC}	0.048 ^A
biotite	2.24 ^A	3.65 ^{NC}	3.65 ^{NC}	3.65 ^{NC}	3.65 ^{NC}
sanidine	---	2.4 ^{NC}	0.34 ^A	1.7 ^{NC}	0.34 ^A
quartz	---	0.016 ^{NC}	0.014 ^{NC}	0.014 ^{NC}	0.16 ^{NC}
magnetite	0.01 ^G	0.01 ^G	0.01 ^G	0.01 ^G	---
clinopyroxene	0.032 ^A	---	---	---	---
Ba plagioclase	0.36 ^A	1.19 ^{NC}	1.965 ^{NC}	1.965 ^{NC}	1.965 ^{NC}
biotite	6.36 ^A	9.7 ^A	9.7 ^A	17.3 ^{NC}	6.36 ^A
sanidine	---	15.6 ^{NC}	6.12 ^A	15.6 ^{NC}	6.12 ^A
quartz	---	0.004 ^{NC}	0.038 ^{NC}	0.038 ^{NC}	0.004 ^{NC}
magnetite	0.01 ^G	0.01 ^G	0.01 ^G	0.01 ^G	---
clinopyroxene	0.131 ^A	---	---	---	---
Eu plagioclase	2.11 ^A	4.45 ^{NC}	5.85 ^{NC}	5.85 ^{NC}	4.45 ^{NC}
biotite	0.145 ^A	0.68 ^{NC}	0.68 ^{NC}	0.68 ^{NC}	0.68 ^{NC}
sanidine	---	4.6 ^{NC}	1.13 ^A	4.9 ^{NC}	4.6 ^{NC}
quartz	---	0.08 ^{NC}	0.052 ^{NC}	0.052 ^{NC}	0.08 ^{NC}
magnetite	1.01 ^{NC}	1.01 ^{NC}	1.01 ^{NC}	1.01 ^{NC}	---
clinopyroxene	4.1 ^{NC}	---	---	---	---
Sr plagioclase	2.84 ^A	4.4 ^A	4.4 ^A	9.9 ^A	4.4 ^A
biotite	0.12 ^A	0.405 ^{NC}	0.405 ^{NC}	0.405 ^{NC}	0.405 ^{NC}
sanidine	---	5.1 ^{NC}	6 ^{NC}	6 ^{NC}	6 ^{NC}
quartz	---	n/a	n/a	n/a	n/a
magnetite	0.01 ^G	0.01 ^G	0.01 ^G	0.01 ^G	---
clinopyroxene	0.516 ^A	---	---	---	---

References: A = Arth (1976); G = Gill (1981); NC = Nash and Crecraft (1985).

coefficients were chosen from the literature to specifically match the compositional increment that was being modelled. In a number of cases, more than one value was provided in the literature for a particular composition, so the average of the available values was used. It should be noted that in a few select circumstances (Ba) the partition coefficients were adjusted over the available range of values for the compositional range in question to achieve a closer fit between the modelled trend and the observed data. The trace elements modelled, Eu, Sr, Ba, Sc, and Rb, are those most likely to be substituted for the major elements in a mineral assemblage consisting of plagioclase, biotite, clinopyroxene, orthopyroxene, sanidine, quartz, and/or magnetite. Thorium is used as a differentiation index because it is incompatible throughout the compositional spectrum for both members (Fig. 7). Figure 19 plots the results of the Rayleigh fractional crystallization calculations superimposed upon the observed concentrations in the Guild Mine and Weed Heights Members. For the Guild Mine Member, the calculations were done for different increments throughout the compositional range in an attempt to best account for the changes in terms of composition and temperature in the magma chamber that affect the phase assemblage, the chemical compositions of the phenocrysts, and the partition coefficients.

For the increment from dacite to rhyodacite, an assemblage consisting of plagioclase, biotite, clinopyroxene, and magnetite (Table 10) yields modelled trends for Sc, Eu, Ba, and Sr that are consistent with the observed trends (Fig. 19). With increasing differentiation, the observed trend for Rb increases slightly more steeply than the modelled trend.

The increment between rhyodacite and rhyolite is successfully modelled using an assemblage consisting of plagioclase, biotite, sanidine, quartz, and magnetite (Table 10). For this compositional increment, the modelled trends are generally consistent with the observed trends for Sc, Rb, Ba, Eu, and Sr (Fig. 19).

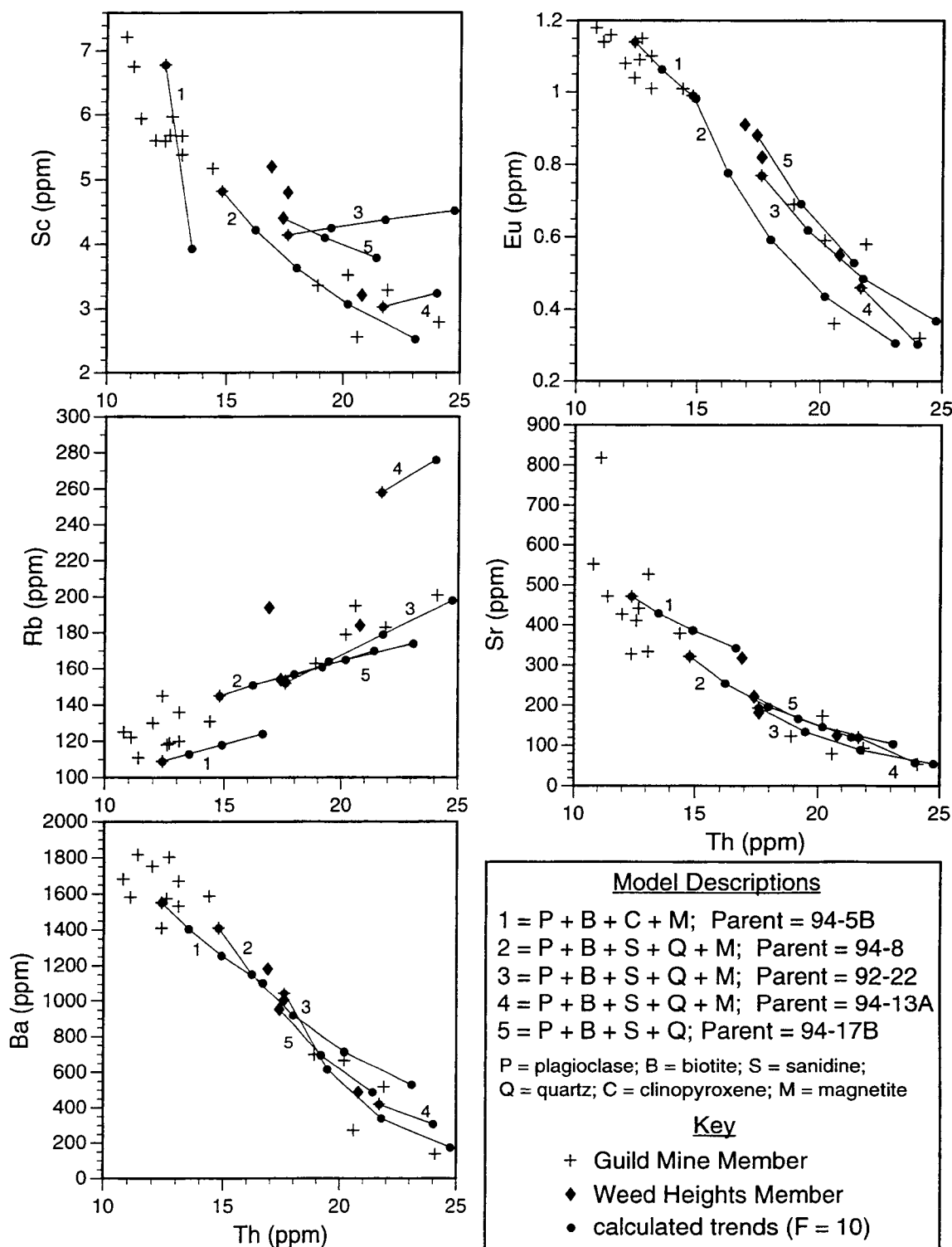


Figure 19: Plots of select trace elements versus Th, which is used as a differentiation index, for the MPT. The observed geochemical trends are shown with symbols as indicated. The calculated trends for each element assuming a Rayleigh fractional crystallization model are superimposed upon the observed data. The trace element models are based on the major element mixing models presented in Table 10. Each solid dot represents an F-value of 10.

For the range from low-SiO₂ rhyolite to high-SiO₂ rhyolite, an assemblage consisting of plagioclase, biotite, sanidine, quartz, and magnetite (Table 10) effectively accounts for the observed trends in Rb, Ba, Eu, and Sr (Fig. 19). The increment from higher SiO₂ rhyolite to highest SiO₂ rhyolite can also be modelled with an assemblage of plagioclase, biotite, sanidine, quartz, and magnetite (Table 10). For both of these compositional increments, the observed trend for Sc decreases with increasing differentiation, but the modelled trend shows that Sc is incompatible with this assemblage. A possible explanation for the differences between the observed and modelled trends may be found by considering the role of two accessory phases, zircon and allanite. Both zircon and allanite have relatively high partition coefficients for Sc in this compositional range (68.6 and 55.8, respectively; Mahood and Hildreth, 1983). The problem with this argument is that Th also has fairly high partition coefficients for these phases, so both Sc and Th would be affected by adding trace amounts of zircon and allanite to the assemblage.

For the Weed Heights Member, an assemblage consisting of plagioclase, biotite, sanidine, and quartz (Table 10) produces modelled trends that are generally in agreement with the observed trends for Rb, Ba, Eu, and Sr (Fig. 19). The modelled trend for Sc is slightly higher than the observed trend, even though a small amount of ilmenite and magnetite (1%) was factored into this particular trace element model.

Overall, the modelled trends for most of the trace element are consistent with crystal fractionation to yield the compositional variation observed in the Guild Mine and Weed Heights Members. The trace element models require specific fractionating assemblages consisting of plagioclase, biotite, magnetite, clinopyroxene, sanidine, and/or quartz depending on the compositional increment modelled (Fig. 19), whereas the major element models yield ambiguous results (Table 10).

Magma Mixing Models

Major-element least-squares calculations demonstrate that fractional crystallization cannot account for the compositional variation within the Weed Heights Member. On the major element variation diagrams, some of the samples from the Weed Heights Member and the compositionally similar intermember rhyodacitic to rhyolitic tuff plot within the compositional gap shown by the Guild Mine Member (Fig. 5). Secondly, on some variation diagrams (Fig. 8; La vs. Ta, Sc vs. Ta, and Cr vs. Ta), the Weed Heights Member cuts across the curved trends displayed by the Guild Mine Member. For these reasons, a mixing hypothesis is considered.

Two tests were applied to the MPT geochemical data to evaluate the credibility of the magma mixing hypothesis. The first method utilized the mass-balance mixing calculations within the MacGPP software package, which are based on the least-squares equations devised by Bryan and others (1969). For each calculation, a more mafic composition was mixed with a composition at the most silicic end of the spectrum to produce a resulting daughter composition. The sum of the squares of the residuals (ΣR^2) is a measure of the differences between the calculated daughter magma and the observed daughter composition. The best-fit solution is calculated such that the sum of the squares of the residuals is minimized. Values for the sum of the squares of the residuals less than 1 are considered reasonable, values less than 0.3 are considered to be a good fit, and values less than 0.1 are considered to be excellent.

An element/element ratio plot and its companion plot were constructed to provide a second test of the mixing hypothesis (Fig. 20). A curved trend of data on the ratio-ratio plot and a linear array on the companion plots provide evidence that magma mixing is at least plausible (Langmuir and others, 1978; Cox and others, 1979). The geochemical data from the mixed end members were used to calculate mixing hyperbolas (Fig. 20)

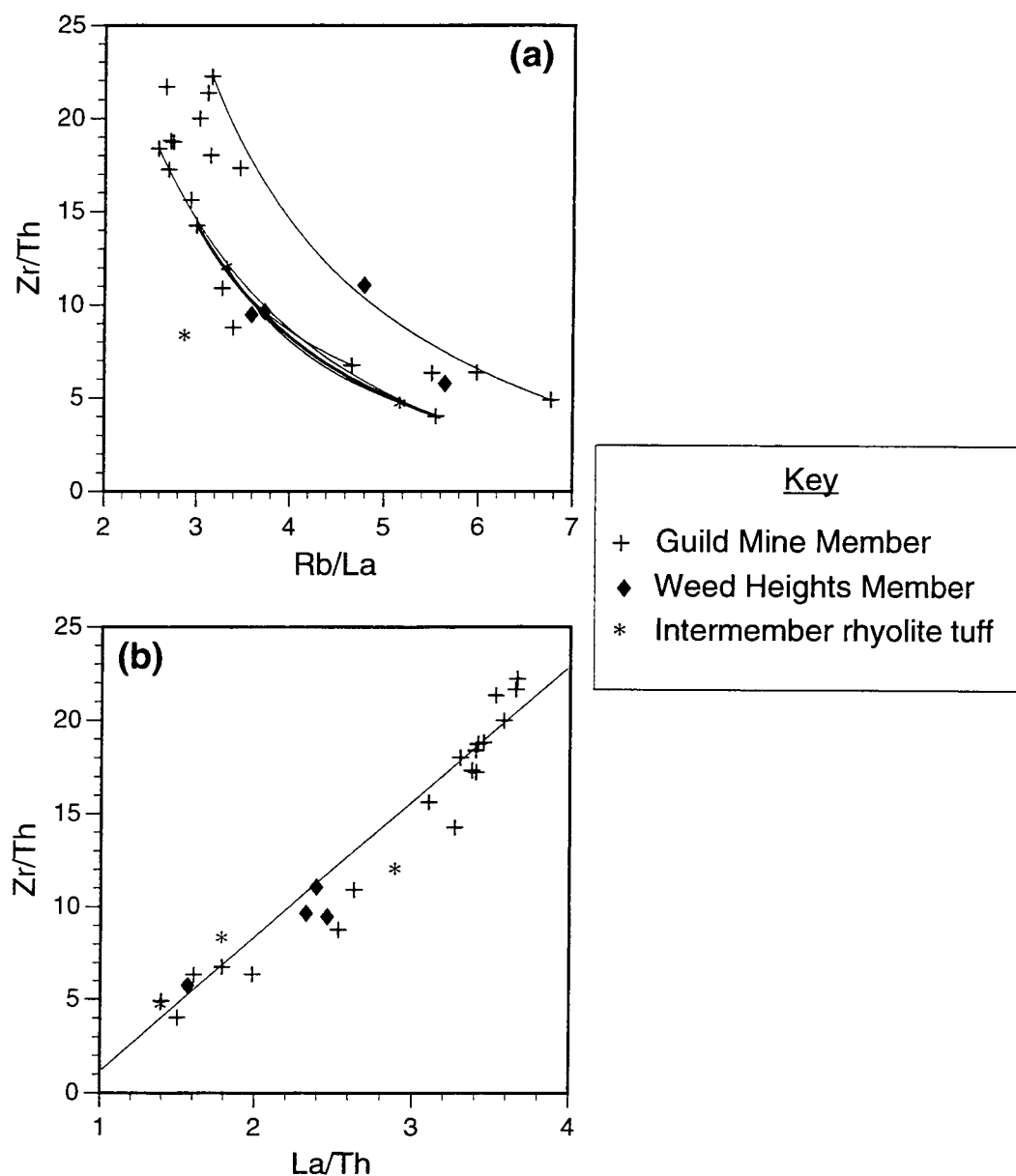


Figure 20: Ratio-ratio plot (a) and companion plot (b) for the MPT. Hyperbolas shown in (a) were calculated using equations presented by Langmuir and others (1978) and represent mixing lines; best-fit line is shown in (b).

following the methods of Langmuir and others (1978). The mixed magma should lie on the hyperbola between the two end members.

In the first mixing model, the dacite at the base of the Guild Mine Member (94-5B) is mixed with the high-SiO₂ rhyolite at the top of the unit (94-15) to yield the rhyolite near the base of the Weed Heights Member (94-17B). The ΣR^2 value for this mixing model is 1.03, which is at the limit of acceptability, but the Weed Heights rhyolite does plot close to the hyperbola calculated using the dacite and the high-SiO₂ rhyolite as end members (Fig. 20). In the second mixing model, the Guild Mine dacite (94-5B) is mixed with the Guild Mine high-SiO₂ rhyolite (94-15) to produce the intermember rhyodacite (94-33A) as the daughter magma. This mix yields a ΣR^2 value of 0.60, which is considered reasonable to good, and the intermember rhyodacite plots on the calculated hyperbola between these two end members (Fig. 20). In the third mixing model, the Guild Mine rhyodacite (94-8) is mixed with a slightly less evolved, high-SiO₂ rhyolite from the Guild Mine Member (92-123) to yield the intermember rhyodacite (94-33A). The ΣR^2 value for this model is 0.15, and the daughter product lies on the calculated hyperbola (Fig. 20). The Guild Mine rhyodacite (94-8) can also be mixed with the high-SiO₂ rhyolite (94-15) to yield the intermember rhyodacite (94-33A), and in this case, the ΣR^2 value is 0.25, and the hyperbola test is satisfied as well (Fig. 20). In the fourth mixing model, the intermember rhyodacite (94-33A) and intermember rhyolite (94-28D) are mixed to produce the Weed Heights rhyolite (94-17B). The ΣR^2 value for this calculation is 0.51, and the daughter magma lies on the hyperbola calculated between the two end members (Fig. 20). A mix of the same intermember compositions to produce the Weed Heights rhyodacite (94-30) is unacceptable, however, because the ΣR^2 value is too high (1.15), and the daughter magma does not lie on the calculated hyperbola (Fig. 20). A fifth mixing model, which combines another Guild Mine dacite (93-40) with a high-SiO₂ rhyolite (94-9C) to produce the

Weed Heights rhyodacite (94-30), is unacceptable model ($\Sigma R^2 = 2.08$), even though the daughter product lies on the calculated hyperbola between the two end members (Fig. 20).

DISCUSSION:

EVOLUTION OF THE MPT MAGMA SYSTEM

The individual ash-flow tuffs within the MPT are genetically related, and as such, they represent successive samplings from the same evolving chamber at distinct moments in time. The detailed geochemical data base for the MPT provides constraints on the petrologic evolution of a continental silicic magmatic system through time.

The model proposed herein for the origin and formation of the MPT must be consistent with a series of observations. The individual members of the MPT display systematic mineralogic and compositional variations from the base to the top of each deposit. Less evolved magmatic material occurs at the base each unit and grades into more evolved material in the upper parts of the deposits. Plagioclase is the predominant feldspar phase in the lower parts of each member, and sanidine and quartz become progressively more abundant in the upper parts of each member. Biotite is ubiquitous throughout each unit but decreases steadily up section. Clinopyroxene, orthopyroxene, and hornblende are confined to the lower parts of each member. The compositions of the phenocrysts and the pre-eruptive magmatic parameters, such as temperature, water content, and density, further reflect the systematic variation with stratigraphic position and bulk tuff composition in each member.

Configuration of the Pre-eruptive MPT Magma Chamber

The Guild Mine Member grades from two-pyroxene, hornblende, biotite dacite at the base to biotite high-silica rhyolite at the top (65.7 to 78.1 wt. % SiO_2), with a compositional gap between 70 and 73 wt % SiO_2 . The reverse compositional zoning in

the Guild Mine Member and the relatively larger proportion of dacite, rhyodacite, and lower silica rhyolite in the lower and middle parts of the unit compared to the relatively smaller proportion of higher silica rhyolite and high-silica rhyolite in the upper part of the unit requires a non-flat chamber roof geometry (Fig. 21). Brown and others (1998) invoked a similar complex magma chamber configuration to account for the origin of the reverse compositional zoning in the Whakamaru group ignimbrites in the Taupo Volcanic Zone, New Zealand (Table 1).

The MPT magma chamber resided at relatively shallow crustal levels (3-7 km depth) as indicated by pressures estimated by Al-in-hornblende geobarometry. Prior to the eruption of the Guild Mine Member, the MPT magma chamber consisted of a zoned body of silicic magma, ranging from dacite in the lowest part of the chamber (that was tapped) to high-SiO₂ rhyolite in the uppermost part of the chamber (Fig. 21).

Temperature, water, and density calculations show that the dacite magma in the lower parts of the chamber was relatively hotter, drier, and denser than more evolved magma in the upper parts of the chamber. The dacite from the base of the Guild Mine Member yields the highest Fe-Ti oxide temperature, and the rhyolite and high-SiO₂ rhyolite from the middle and upper parts of the unit yield lower Fe-Ti oxide temperatures. As demonstrated by the anhydrous and hydrous bulk-tuff and glass density calculations and the modal density estimates (Fig. 18), a pronounced density gradient existed in the pre-eruptive chamber, ranging from a stratigraphically lower portion of higher density dacite to lower density rhyolite and high-SiO₂ rhyolite in the upper parts of the chamber.

Several lines of evidence indicate that prior to the eruption of the Guild Mine Member the MPT magma chamber was zoned in a step-wise fashion rather than in a continuous manner. The compositional gap within the bulk-tuff chemical data represents a distinct interface that existed in the pre-eruptive MPT chamber between dacite and rhyodacite in the lower portions of the chamber and rhyolite and high-SiO₂

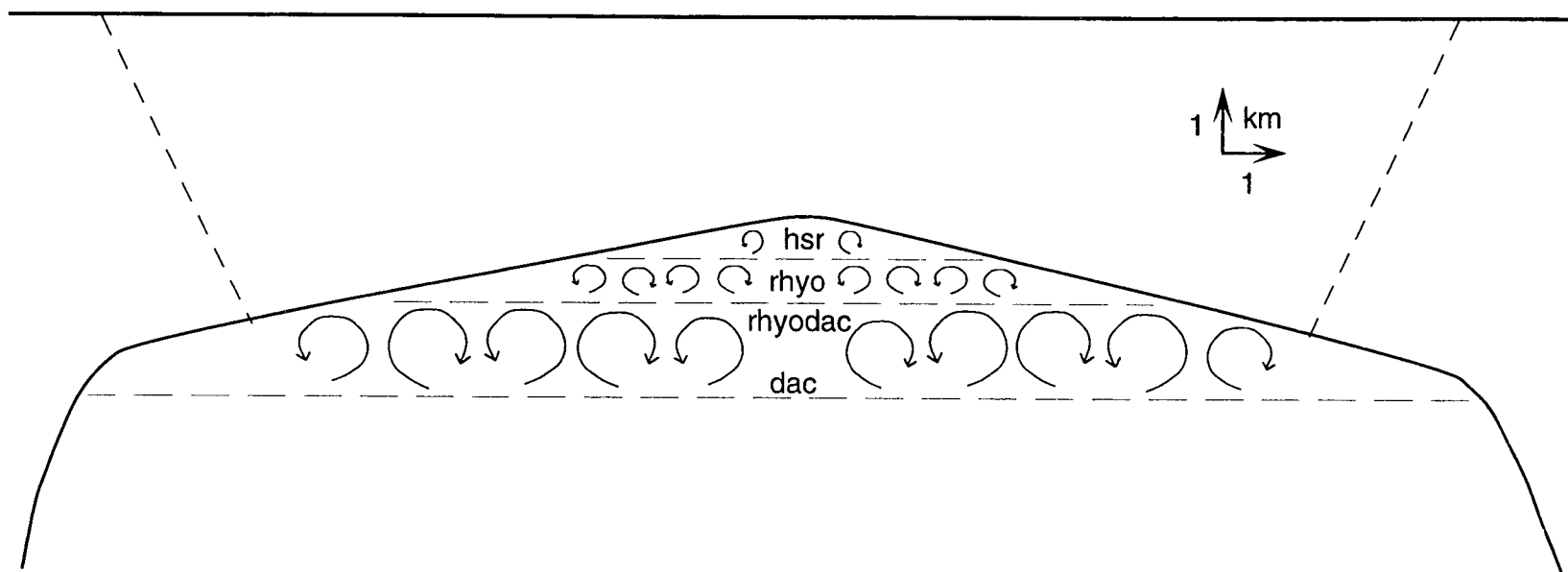


Figure 21: Schematic representation of the pre-eruptive MPT magma system. The dimensions of the chamber are derived by assuming an eruption volume of 600 km^3 , a caldera diameter of 25 km, a magma thickness of 2 km, and that less than half of the magma was extracted for a 1 km draw down. This yields a chamber with an aspect ratio of $\approx 10:1$. The compositional zoning within the MPT magma chamber prior to eruption of the Guild Mine Member is also represented. Individual layers show convection. The evidence for the boundaries between the layers is discussed within the text. Abbreviations are: dac = dacite; rhyodac = rhyodacite; rhyo = rhyolite; and hsr = high-silica rhyolite.

rhyolite in the upper portions of the chamber (Fig. 21). Compositional gaps have been identified and documented in a number of ash-flow tuffs, both in the bulk-tuff data and in the fiamme and pumice data (cf., Ferriz and Mahood, 1987; Fridrich and Mahood, 1987; Boden, 1989; Schuraytz and others, 1989). Compositional gaps represent sharp interfaces between magmas of different compositions in the chamber prior to eruption and are possible evidence for magmatic convection (Smith, 1979; Hildreth, 1981). Fridrich and Mahood (1987) carefully documented the existence of several compositional gaps within the Grizzly Peak Tuff and interpreted these to represent discrete layers of magma in the chamber that were convecting internally but were not mixing between the layers.

The existence of a compositional gap does not necessarily mean that such gaps existed in the pre-eruptive magma chamber. Numerical simulations of magma withdrawal have shown that compositional gaps can be produced either by a brief eruption hiatus or by an increase or decrease in the magma discharge rate during eruption (Spera and others, 1986). Alternatively, a compositional gap could be produced during the deep tapping of a zoned magma chamber, as is discussed below for the origin of the reverse compositional zoning in the MPT. Spiegel and Farrant (1984) documented the changes in the density structure of a stratified water supply that was tapped over long periods of time from a point in the wall of the reservoir. Relating this study to zoned magma systems, Blake and Ivey (1986a) noted that eruption from a point in the wall of a zoned chamber should produce a steep density gradient and possibly a compositional gap. Several observations indicate that the compositional gap observed in the bulk-tuff chemical data is an artifact of the conditions in the pre-eruptive MPT magma column and is not a function of the eruption dynamics. Specifically, the glass and biotite compositional data provide discrete samplings of magma from various positions within the chamber (Fig. 21).

Glass analyses from the Guild Mine Member cluster into a slightly less evolved group (74-76 wt. % SiO_2) and a slightly more evolved group (77-78 wt. % SiO_2) (Fig. 10). The two distinct populations of glass data provide further evidence that the pre-eruptive MPT magma chamber was zoned in a step-wise manner.

The biotite compositional data provide critical evidence with regard to the multi-layered arrangement of the pre-eruptive chamber. Discontinuities in the compositions of biotite phenocrysts from several zoned ash-flow tuffs have been used as evidence for distinct interfaces between discrete layers of magma (Boden, 1989; Flood and others, 1989; Schuraytz and others, 1989). The biotite phenocrysts in the dacitic and rhyodacitic parts of the Guild Mine Member are compositionally identical and display relatively higher magnesium numbers (Mg#s). In comparison, the biotite phenocrysts in the rhyolite and in the high- SiO_2 rhyolite from the middle and upper parts of the unit are compositionally distinct with progressively lower Mg#s (Fig. 13). Based on Mg numbers, the biotite phenocrysts define multiple populations, showing that the pre-eruptive MPT chamber consisted of compositionally distinct layers of magma that were separated by well-defined interfaces.

The compositional gap in the bulk-tuff data, the discrete groups of glass analyses, and the multiple populations of biotite phenocrysts indicate that the pre-eruptive MPT magma chamber consisted of at least two discrete layers (Fig. 21). Based on comparisons to other systems with similar compositional attributes (Fridrich and Mahood, 1987; Boden, 1989; Schuraytz and others, 1989), the layers of the MPT magma chamber are interpreted to represent individual layers that were convecting internally with minimal mixing occurring between the layers. Rayleigh number calculations for the MPT assuming a thickness of 1 km for the individual layers in the pre-eruptive magma chamber (cf., Fridrich and Mahood, 1987) greatly exceed the critical Rayleigh number (Ra) necessary for convection to occur: the Guild Mine dacite

yields $Ra \approx 10^{10}$; the Guild Mine rhyolite yields $Ra \approx 10^7$; and the Weed Heights rhyodacite yields $Ra \approx 10^{11}$. The critical value ($Ra = 1708$; Philpotts, 1990) is exceeded in each case when the thickness of the magma layer is greater than 5.5 m, 28 m, and 1.6 m, respectively. Numerous experimental studies in which aqueous solutions were heated or were allowed to crystallize along the margins of the tanks result in a series of convecting layers that are each internally homogeneous with respect to composition and temperature (Sparks and others, 1984, and references therein). These fluid dynamic studies of density stratified fluids attest to convection within distinct layers as opposed to whole-scale convection.

Origin of Reverse Compositional Zoning

The Guild Mine and Weed Heights Members are unique amongst most zoned ash-flow tuffs in that they display reverse compositional zoning. The origin for the reverse compositional zoning in the MPT is constrained from the physical volcanological attributes and the compositional gradations within each of the units.

Both members of the MPT display nearly continuous compositional and mineralogical gradients from the base to the top of the units. The REE data from the base to the top of the Guild Mine Member illustrate the vertical chemical zoning within this unit (Fig. 9). The REE patterns in the Guild Mine Member are parallel and have light REE enrichment, and the more evolved material in the upper part of the Guild Mine Member has higher REE contents than the least evolved material, except for Eu. The REE patterns show that no compositional discontinuity existed in the magma chamber between the deeper mafic material and the silicic material and that the rhyolitic magma is a differentiation product of the dacitic magma. Major element, least squares models and

trace element, Rayleigh fractional crystallization models indicate that the dacite, rhyodacite, rhyolite, and high-SiO₂ rhyolite of the Guild Mine Member are petrogenetically related. The density calculations for the pre-eruptive magma in each member show that the first erupted material was of higher density than the successively erupted material.

The observations are consistent with the eruption of a zoned magma chamber with a silicic cap, except that they occur in the reverse order from what has been documented in most other ash-flow tuffs. The normal or mafic-upward zoning that typifies most other ash-flow tuffs has been attributed to inversion of a silicic upward zoned magma chamber during eruption. The origin of reverse compositional zoning in the MPT is interpreted to represent tapping the deeper portions of a magma chamber that was zoned from silicic material at the top to more mafic- and crystal-rich material with depth (Fig. 21). The non-flat roof geometry that is interpreted for the MPT system enabled a ring-fracture fault to penetrate into a deeper part of the magma chamber where a silicic cap was either thin or non-existent (cf., Brown and others, 1998). This configuration allowed more mafic compositions to be removed preferentially, and then as the eruption proceeded more silicic compositions were entrained into the magma conduit. The reverse zonation in the MPT and others tuffs produced by a deeper tapping mechanism is not fundamentally different from normally zoned tuffs other than being inverted. The reversely zoned Hells Mesa and Lemitar Tuffs in New Mexico (Table 1) have also been attributed to a tapping mechanism in which the deeper parts of a normally zoned chamber were tapped first (Eggleston and others, 1983).

Besides a deep tapping mechanism, several other mechanisms, which all involve tapping the upper parts of a chamber that was actually zoned in a mafic-upward fashion, have been proposed to explain reverse compositional zoning in ash-flow tuffs. Density contrasts between the upper mafic magma and the lower silicic magma would make this

configuration gravitationally unstable. To account for this, a dense cap might be temporarily formed if the first pulse of magma injected into the chamber was less evolved, and it became sufficiently crystal-rich such that the yield strength would prevent it from sinking through more silicic magma that may have been subsequently intruded beneath it; a corollary to this is that the mafic top may not be so crystal-rich to prevent its eruption. An upper limit for the crystal content of the more mafic tuff would approach 50%. Alternatively, vesiculation of deeper, more mafic magma that is saturated with respect to H_2O may occur when it is brought into contact with cooler silicic magma (Eichelberger, 1980); rapid vesiculation in the lower part of the chamber could cause it to overturn bringing the more mafic material to the conduit first. Finally, a silicic magma may have intruded a less silicic chamber and initiated eruption.

The physical attributes and compositional zoning of the MPT preclude these mechanisms as tenable explanations for the origin of the reverse compositional zoning. First and foremost, the individual units of the MPT lack abundant evidence of mixing or mingling of magmas during eruption. The reversely zoned tuff produced by these mechanisms should show evidence of magma mixing on outcrop, in thin section, or in the mineral chemistry. On the scale of outcrops, the individual units in the MPT lack magma mingling textures, and pumices and fiamme appear homogeneous. In thin section, minor amounts of magma mixing are evident in a few sparse fiamme within the Weed Heights Member, but overall these textures are lacking. Additionally, for each of these alternative scenarios, no continuity or gradations are required to exist between the more mafic and silicic parts of the chamber in terms of composition, mineralogy, or intensive parameters. For both members of the MPT, the less evolved material in the lower parts of each unit is petrogenetically related to the more evolved material at the top. Lastly, the dacite at the base of the Guild Mine Member, which represents that deepest levels of the chamber tapped, yields low P_{H_2O} values (Table 9), thus rapid

vesiculation in the lower part of the chamber to cause it to "roll over" is an unlikely mechanism.

Another mechanism that may account for reverse compositional zoning is the processes of flow in a conduit (Koyaguchi, 1985; Blake and Campbell, 1986). Magma withdrawal experiments show that during eruptions from stratified chambers which tap layers of magma with different viscosities the slower flowing silicic magma can be overtaken by the faster flowing mafic magma, in situations where the feeder conduit is still propagating away from the chamber (Blake and Campbell, 1986), or where the conduit is sufficiently long (Koyaguchi, 1985). As in the previously described alternative mechanisms, evidence for magma mixing should be abundant in the resulting pyroclastic deposits. Also, the low pressure of the MPT would preclude this mechanism, because $\approx 500\text{-}1000 \text{ km}^3$ of magma was erupted from $<10 \text{ km}$ depth.

Apparent reverse compositional zoning may result if the rate of compositional change in the chamber exceeds the eruption rate. In this case, the first eruptive pulse is more mafic, and subsequent eruptive pulses are more silicic. The resulting tuff in this scenario would be a compound cooling unit reflecting this time progression. Each of the individual members of the MPT represents a simple cooling unit, and they both lack any partings or other evidence indicating any break during the eruption.

In summary, the nearly continuous compositional gradients both in bulk tuff and mineral chemistries and the lack of magma mixing textures indicate that the reverse compositional zoning in the MPT is a result of tapping the deeper, more mafic parts of a magma chamber that was zoned from more silicic material at the top to less evolved material at deeper levels normally zoned magma chamber. Attending the deeper tapping mechanism is a more complex, non-flat roof magma chamber geometry (Fig. 21).

Eruption Dynamics of Reversely Zoned Tuffs

Several detailed studies on normally zoned ash-flow tuffs have provided constraints for the eruption dynamics of zoned continental silicic magma systems in which the uppermost part of the chamber is tapped first and deeper, less evolved portions of the chamber are successively tapped (Fridrich and Mahood, 1987; Boden, 1989; Schuraytz and others, 1989). As discussed above, the MPT magma system is unusual in this respect, because it represents tapping the lower parts of a magma chamber that was zoned from silicic material at the top to more mafic material at deeper levels (Fig. 21). The eruption dynamics of the MPT system are discussed in the light of these studies in which the upper part of the magma chamber is tapped.

Numerical and experimental modelling techniques have also provided a basis for understanding the eruption of magma from density stratified reservoirs (Blake, 1981; Spera, 1984; Blake and Campbell, 1986; Blake and Ivey, 1986a; 1986b; Spera and others, 1986). During the eruption of a zoned magma chamber in which the upper part is tapped first, it has been shown by numerical and experimental modelling that the interfaces between the discrete convecting layers are deflected upward beneath the opening vent producing a draw-up cone (Spera, 1984; Blake and Campbell, 1986; Blake and Ivey, 1986a; 1986b). For magma systems, such as the MPT, in which the lower portions of the density stratified chamber are tapped first to produce reversely zoned tuffs, Blake and Ivey (1986b) calculated that the higher viscosity, lower density magma (rhyolite) will be drawn down through the lower viscosity, higher density magma (andesite). Following the calculations of Blake and Ivey (1986b), the interfaces between the compositional layers in the MPT magma chamber are interpreted to have been deformed downward towards the pressure drop at the vent. Thus, instead of

producing a draw up cone, a draw down deflection of the compositional layers will be produced.

The eruption scenario envisioned for the MPT is one in which the silicic magma was pulled down to the vent opening displacing and disrupting the original layering in the chamber. This may account for the mixing, disruption, and virtual reorganization of the MPT chamber during the eruption of the Guild Mine Member to produce the successively erupted units, as discussed below (Fig. 22). One thing that is lacking in the individual units of the MPT is evidence of increasing heterogeneity in the later erupted material. This is in contrast to several field and geochemical studies (Fridrich and Mahood, 1987; Boden, 1989; Schuraytz and others, 1989) which have documented an increase in heterogeneity of the bulk properties of the magma system. The lack of abundant heterogeneity in the later erupted MPT material is attributed to viscosity controls during magma withdrawal. In magma systems in which the top of the chamber is tapped and the most silicic material is removed first, the less viscous, more mafic magma has been inferred to move more rapidly towards the vent conduit thus creating a greater amount of heterogeneity. In the case of the MPT, the lower viscosity, more mafic material was erupted first followed successively by higher viscosity, more evolved material. This scenario apparently inhibited dynamic mixing between the less evolved and more evolved magmas during eruption and emplacement.

Tectonic Implications of the Eruption of Reversely Zoned Tuffs

The origin of reversely zoned tuffs by tapping the deeper parts of a silicic-upward zoned magma chamber may have some implications to understanding the evolution of regions of extension. There appears to be a relationship between the timing of eruption

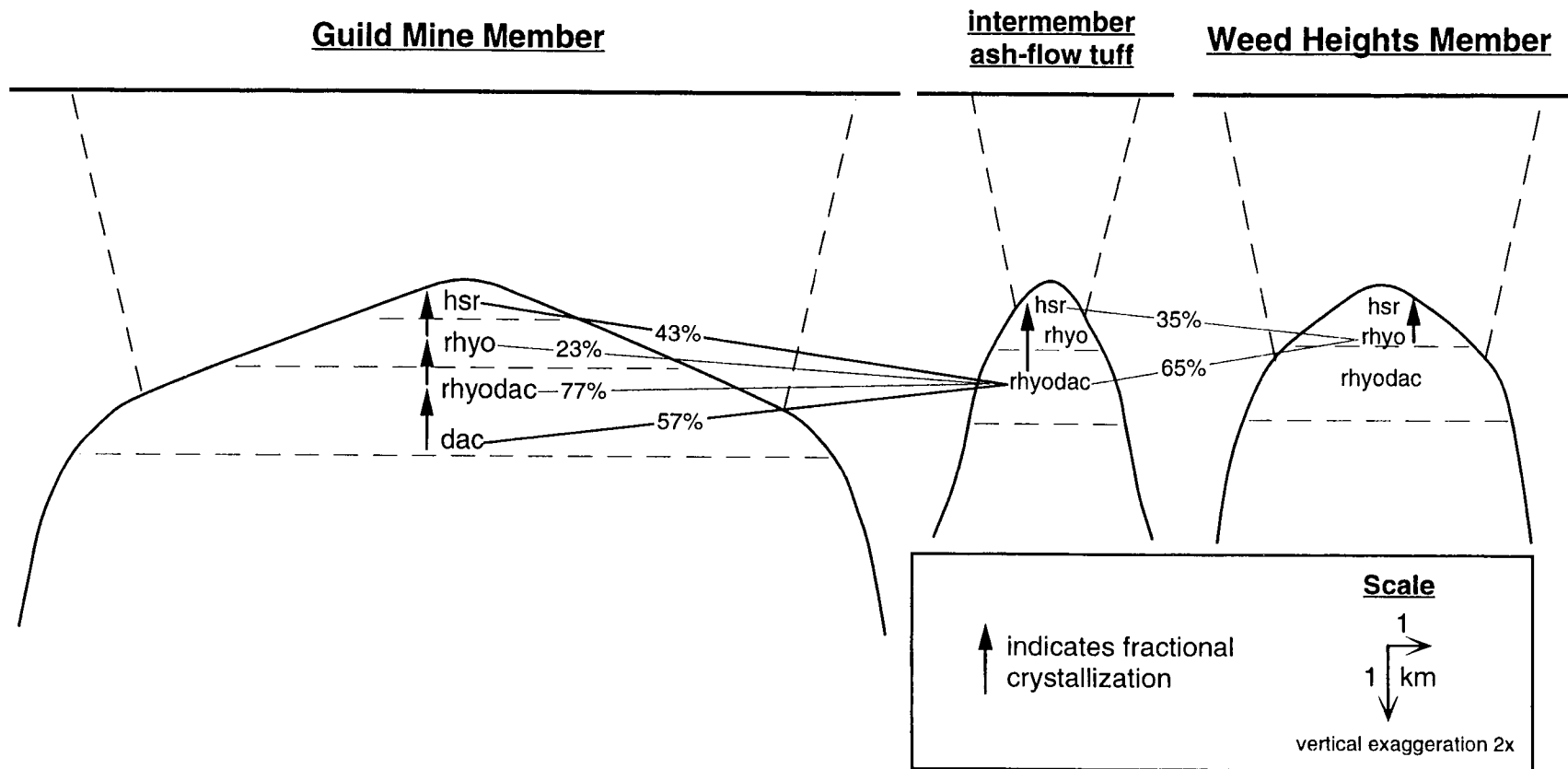


Figure 22: Schematic representation of the MPT magma system through time. The compositional zoning prior to eruption of the individual members is represented. During eruption of the individual members, density stratification was disrupted as the more evolved compositions were drawn down through less evolved compositions (after Blake and Ivey, 1986b) resulting in syneruptive mixing of the chamber. The mixing scenarios to yield the compositions in the overlying units are shown, as discussed in the text. Abbreviations are: dac = dacite; rhyodac = rhyodacite; rhyo = rhyolite; and hsr = high-silica rhyolite.

of reversely zoned tuffs and early phases of faulting in the central Walker Lane, the Socorro region of the Rio Grande Rift, and in the Eldorado Mountains in the Colorado River extensional corridor. This relationship is evident in Figure 23, which depicts the relative amount of faulting and magmatism versus time for each of these areas.

The MPT was emplaced in an area that lies in and adjacent to the central Walker Lane, which is a 40-km-wide zone of right-lateral strike-slip and normal faulting in west-central Nevada (Fig. 1). Based on the available data, the MPT was erupted just prior to or at the onset of earliest Walker Lane strike-slip and extensional faulting. In many areas throughout its distribution, the MPT is localized in northwest-striking paleovalleys, as well documented by Proffett and Proffett (1976); the origin of the paleovalleys may be directly related to the earliest phases of tectonism. According to Dilles (1993), at some localities in the northern Wassuk Range there is a slight angular discordance between the early Tertiary ash-flow tuffs (28.6 Ma) and the overlying MPT. Although the paleovalleys and the angular unconformity are suggestive of an early phase of tectonism, the major phase of middle Tertiary faulting in the central Walker Lane was between 26 and 23 Ma (Dilles, 1993; Dilles and others, 1993; Dilles and Gans, 1995; Fig. 23). It is also important to note that all other Oligocene to early Miocene ash-flow tuffs erupted in the Walker Lane after the MPT are not reversely zoned, and either show normal zoning or are compositionally homogeneous.

In the Socorro, New Mexico region, two major middle Tertiary ash-flow tuffs (the Hells Mesa Tuff and the Lemitar Tuff; Table 1) show reverse compositional zoning and "may be related to incipient Rio Grande rift-related extensional fractures" (Eggleson and others, 1983). It appears that the 27.9-Ma Lemitar Tuff was erupted at the onset of major Rio Grande Rift extension in the Socorro area (Fig. 23). The relationship of the eruption of the 32-Ma Hells Mesa Tuff to earlier extension in the Rio Grande Rift is not exactly clear, but some workers have suggested that the eruption of the Hells Mesa Tuff

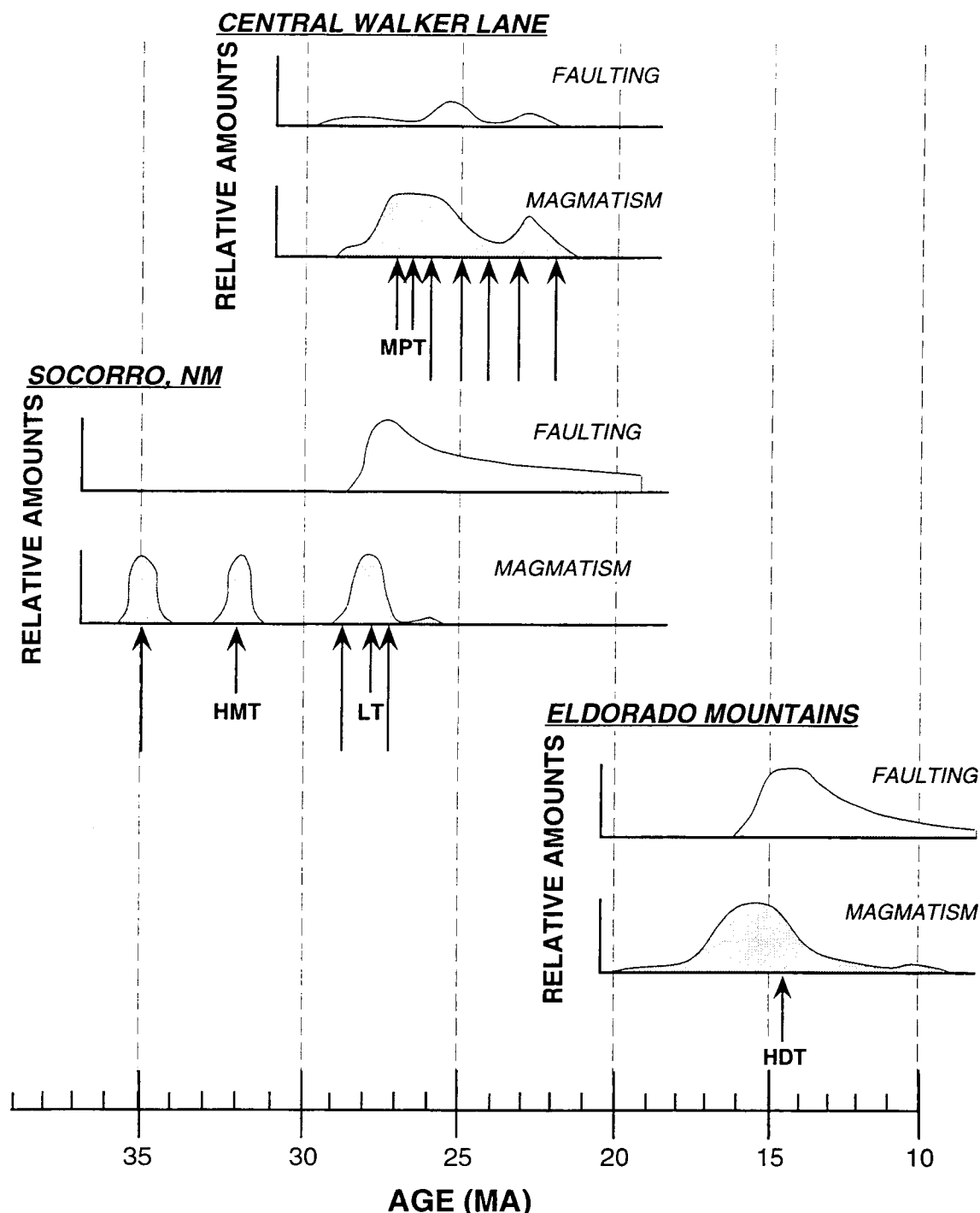


Figure 23: Relative amounts of faulting and magmatism versus time for the central Walker Lane, NV (Dilles, 1993; Dilles and others, 1993; Dilles and Gans, 1995), the Socorro, NM area (Gans and others, 1989), and the Eldorado Mountains in southern NV and northern AZ (Gans and others, 1989). Long arrows represent normally zoned tuffs; short arrows with abbreviations designate reversely zoned tuffs mentioned in text (MPT=Mickey Pass Tuff; HMT=Hells Mesa Tuff; LT=Lemitar Tuff; HDT=tuff of Hoover Dam).

is the the earliest volcanic event linked to the Rio Grande Rift extension in the Socorro area (Eggleson and others, 1983; Elston, 1984).

The eruption of Tertiary volcanic rocks and extension are also temporally and spatially coincident in the Eldorado Mountains. The Eldorado Mountains are within part of the 80- to 100-km wide, Colorado River extensional corridor in southern Nevada and northwestern Arizona. Mills (1985) and Smith and others (1990) identified a reversely zoned tuff in the northern part of the Eldorado Mountains near Hoover Dam (Table 1). The tuff of Hoover Dam is zoned from andesite (56 wt. % SiO_2) at its base to dacite (68 wt. % SiO_2) at its stratigraphic top. The tuff of Hoover Dam (14.3 Ma; from Smith and others, 1990) lies in roughly the same stratigraphic position and is broadly age correlative with the tuff of Bridge Spring (15.10 ± 0.04 Ma; Ar-Ar from Gans and Bohrsen, 1998) in the central and southern Eldorado Mountains. However, they are chemically and lithologically distinct and thus are not correlative. The tuff of Hoover Dam and the tuff of Bridge Spring were erupted just prior to the initial stages of extension in this region (Fig. 23). The peak extension in the Eldorado Mountains was between 15 and 13 Ma based on the identification of an angular unconformity between flat-lying or gently dipping 13-14 Ma basalts and steeply dipping older strata (Anderson and others, 1972). Gans and Bohrsen (1998) have constrained the inception of extension between 15.1 and 15.0 Ma, immediately following the eruption of the tuff of Bridge Spring.

The data for the Central Walker Lane, the Socorro region, and the Eldorado Mountains indicate that the eruption of reversely zoned tuffs occurred during or just prior to the earliest phases of normal and/or strike-slip faulting for these areas and appears to be signalling the onset of tectonism. In regions with average geothermal gradients ($20^\circ\text{C}/\text{km}$), the depth to the brittle/plastic transition is approximately 15 km (Suppe, 1985). In east-central Nevada, the depth to the extensional brittle-ductile

transition ranges from 5-7 km to 10-12 km, depending on the proximity to thermal perturbations induced by pluton emplacement (Gans, 1987). Pressure estimates indicate that the MPT magma system equilibrated under relatively shallow crustal conditions of 1-2 kbars, corresponding to depths between approximately 3 and 7 km. The depth of the MPT magma chamber was well within the range necessary for brittle deformation. Thus, the Walker Lane faults were capable of penetrating to the depths required to tap the lower, more mafic portions of the MPT magma chamber (Fig. 21). With prolonged extension, the crust was progressively heated thereby increasing the geothermal gradient and reducing the depth of the brittle/ductile transition.

Petrogenetic Evolution of the MPT Magma System

The Guild Mine Member represents the eruption of $\approx 600 \text{ km}^3$ of compositionally zoned magma from a continental silicic magma chamber. The compositional zoning within the Guild Mine Member originated dominantly through fractional crystallization processes (Fig. 22), as indicated by a series of major element, least squares models and trace element fractionation models. The fractionation models were devised incrementally between the various compositions within the Guild Mine Member, and they involve a fractionating assemblage consisting mostly of plagioclase, biotite, and magnetite with smaller amounts of clinopyroxene, sanidine, and/or quartz depending on the compositional increment modelled (Table 10). A series of Rayleigh fractional crystallization models were devised using the modal results from the major element, least squares models. The modal results were combined with the published partition coefficients for a suite of trace elements that were most likely substituted for major elements in the fractionating assemblages (Eu, Sr, Ba, Sc, and Rb). The modelled trace

element trends for all of the elements (except for Sc in the more silicic compositions) are consistent with crystal fractionation to produce the observed compositional variation in the Guild Mine Member (Fig. 19). Based on the study by Grove and Donnelly-Nolan (1986) of the intermediate and silicic compositions at Medicine Lake Volcano in California, the compositional gap in the Guild Mine Member is inferred to have been generated by fractional crystallization at low pressures (1-2 kbars).

The bulk-tuff and mineral content data available for the MPT indicate that the compositional variation in the Weed Heights Member and in the intermember ash-flow tuff was not entirely derived by simple fractional crystallization processes. In comparison with the Guild Mine Member, the Weed Heights Member displays a narrower compositional range from two-pyroxene, hornblende, biotite rhyodacite at the base to biotite rhyolite at the top (71.5 to 75.5 wt. % SiO_2). The samples from the thickest ash-flow tuff between the Guild Mine and Weed Heights Members range from rhyodacite to high-silica rhyolite (71.6-76.1 wt. % SiO_2). In addition to having a similar compositional range, the Weed Heights Member and the intermember tuff share other compositional similarities that distinguish them from the Guild Mine Member. Some of the compositions from the Weed Heights Member and the intermember ash-flow tuff are intermediate between the less evolved and more evolved compositions in the Guild Mine Member. On some of the variation diagrams, linearly trending data from the Weed Heights Member cut across the curved trends defined by the Guild Mine Member (Fig. 8). The linear trends displayed by the Weed Heights Member do not represent fractional crystallization but instead are indicative of magma mixing. Most importantly, though, is the fact that fractional crystallization models are completely unsatisfactory to explain the origin of the rhyolite in the upper parts of the Weed Heights Member as a differentiation product of the rhyodacite at the base of the unit.

Based on the available data, it appears that mixing of the magma column during the dynamic eruption of the MPT magma chamber may, in part, account for the observed compositions in the successively erupted units. The magma mixing scenario envisioned involves the disruption of the compositional interface between lower, less evolved magma and upper, more evolved magma in the chamber. During eruption of the Guild Mine Member, the chamber was mixed and reorganized to yield the rhyodacitic intermember ash-flow tuff. Mixing calculations show that a mixture of Guild Mine dacite (57%) and high-SiO₂ rhyolite (43%) or a mixture of Guild Mine rhyodacite (77%) and rhyolite (23%) are both plausible models to produce the intermember rhyodacite (Fig. 22).

The intermember rhyodacite, rhyolite, and high-silica rhyolite ash-flow tuff samples are all from the thickest ash-flow tuff between the Guild Mine and Weed Heights Member. The rhyodacite and high-silica rhyolite are petrographically and compositionally similar with parallel REE patterns (Fig. 9), qualitatively indicating that the high-silica rhyolite can be derived from the rhyodacite by fractional crystallization (Fig. 22). During the eruption of the intermember tuff, the chamber experienced further mixing and reorganization to produce part of the Weed Heights Member. Mixing models indicate that it is possible to mix the intermember rhyodacite (65%) and high-SiO₂ rhyolite (35%) to produce the rhyolite that lies directly above the rhyodacite at the base of the Weed Heights Member (Fig. 22).

A fractional crystallization model is viable for the origin of the compositional zoning within the more evolved parts of the Weed Heights Member (Fig. 22). Specifically, the high-SiO₂ rhyolite at the top of the Weed Heights Member can be derived from the rhyolite in the lower part of the unit via a crystal fractionation model involving an assemblage of plagioclase, biotite, sanidine, and quartz (Table 10; Fig. 19). The relationship of the rhyodacite at the base of the Weed Heights Member to the remainder

of the unit is not clearly established by crystal fractionation mechanisms or mixing processes.

During the cataclysmic eruption of the Guild Mine Member, the MPT chamber became more oxidizing as indicated by the mafic phases within the Weed Heights Member and the intermember tuff. The Weed Heights Member and the intermember rhyolite ash-flow tuff yield higher oxygen fugacities (above the NNO buffer curve) than the Guild Mine Member (between NNO and FMQ buffer curves) (Fig. 15). The mafic phases reequilibrated with the new magma chamber conditions, and compositional data from the mafic phases reflect the higher oxygen fugacity conditions in the pre-eruptive magma chamber. The biotite phenocrysts in the intermember rhyolite ash-flow tuff and in the Weed Heights Member are compositionally similar and yield higher Mg numbers compared with those in the Guild Mine Member (Fig. 13). The higher Mg numbers for the biotite phenocrysts in the intermember tuff and the Weed Heights Member reflect the higher oxygen fugacity values estimated for these units. A similar positive correlation between higher Mg number values and higher oxygen fugacity values has been documented in phase equilibria studies (e.g., Wones and Eugster, 1965), in studies of silicic batholiths (e.g., Dilles, 1987), and in other studies of multicyclic ash-flow systems (e.g., Flood and others, 1989; Boden, 1994). The pyroxene compositional data also reflect the increasing oxidizing conditions with time in the MPT magma system. In general, the clinopyroxene and orthopyroxene phenocrysts in the Weed Heights Member have lower hedenbergite and ferrosilite contents than those in the Guild Mine Member. The presence of titanite in the Weed Heights Member and its absence in the Guild Mine Member also attests to higher oxygen fugacities in the later erupted units.

Several studies have documented similar magma mixing scenarios for the multicyclic Timber Mountain-Oasis Valley Caldera Complex in the southwest Nevada volcanic field (Flood and others, 1989; Cambray and others, 1995). In their study of the Timber

Mountain Group, Cambray and others (1995) documented a scenario in which two discrete high-silica rhyolite batches were mixed during eruption of the Rainier Mesa ash flow sheet to yield the high-silica rhyolite composition in the Ammonia Tanks ash flow sheet.

Flood and others (1989) documented a similar magma mixing scenario for the Paintbrush Tuff, which is also in the southwest Nevada volcanic field. The large volume Topopah Spring Member ($>1200 \text{ km}^3$) represents a zoned magma chamber consisting of an upper high-silica rhyolite and a lower quartz latite separated by a distinct compositional interface (Schuraytz and others, 1989; Flood and others, 1989). The overlying Pah Canyon Member ($<40 \text{ km}^3$) consists of compositions that are intermediate between the most evolved and the least evolved compositions of the Topopah Spring Member. Flood and others (1989) determined that the Pah Canyon Member was derived by mixing approximately equal amounts of high-silica rhyolite and quartz latite during the cataclysmic eruption of the Topopah Spring Member. The similarities between the Paintbrush Tuff and the MPT are striking. Both systems consist of a large volume compositionally zoned ash-flow tuff erupted first followed by smaller volume ash-flow tuff(s) displaying more limited compositional ranges. In both systems, mafic phenocrysts (magnetite and ilmenite, and biotite) reequilibrated with the new chamber conditions. This is reflected in the observation that biotite phenocrysts in the early erupted unit are bimodal with respect to Mg#, and the biotite phenocrysts in the later erupted tuff(s) are unimodal with higher Mg#s.

The time between the eruption of the individual members of the MPT is not precisely known. The Guild Mine Member has yielded an ^{40}Ar - ^{39}Ar date on sanidine of $27.0 \pm 0.1 \text{ Ma}$ (McIntosh and others, 1992a), and the Weed Heights Member has yielded K-Ar age dates on sanidine of $26.8 \pm 0.9 \text{ Ma}$ (Proffett and Proffett, 1976) and on biotite of $26.6 \pm 0.8 \text{ Ma}$ (Bingler and others, 1980). Using these age data, the eruption interval

between the Guild Mine and Weed Heights Members is a maximum of 1.3 million years. The eruption interval was presumably much shorter, however, owing to the lack of soil horizons in the intermember sequence separating the members.

The 1.3-m.y. interval is greater than that observed in other continental silicic magma systems for the re-establishment of compositional gradients. The repose period between major caldera-forming eruptions for several well-studied multicyclic silicic magma systems is 0.27-0.37 m.y. for the Bandelier Tuff (Spell and others, 1990), 0.7 m.y. for the Yellowstone system (Christiansen and Blank, 1972; Christiansen, 1984), and less than 0.2 Ma for the Timber Mountain Caldera system (Cambray and others, 1995). The Toba Caldera Complex has erupted three compositionally zoned ash-flow tuffs and one relatively homogeneous tuff with a repose period of 0.34-0.43 m.y. (Chesner and Rose, 1991; Chesner and others, 1991). The compositional zoning within the individual Toba tuffs was derived from extensive crystal fractionation (Chesner, 1998). These studies indicate that a repose period of ≈ 0.3 -0.4 m.y. is necessary to re-establish compositional gradients within multi-cyclic continental silicic magma systems.

The relative timing of the petrogenetic processes operating throughout the evolution of the MPT magma system can be constrained from the physical and geochemical attributes of the individual units. Taken on face value, the available age data indicate a repose period between the Guild Mine and Weed Heights Members of 0.2 million years, which indicates that large amounts of magma remained in the chamber after eruption of the Guild Mine Member (cf., Cambray and others, 1995). Between eruptions of the MPT system, enough time elapsed for compositional gradations in the pre-eruptive chamber to be re-established, and the driving mechanism for this re-establishment was fractional crystallization (Fig. 22). In the case of the intermember tuff, the parallel REE patterns (Fig. 9) qualitatively show that the high-silica rhyolite is a differentiation product of the rhyodacite, which was derived by mixing less evolved and more evolved

compositions of the Guild Mine Member during the eruption. For the Weed Heights Member, the high-silica rhyolite at the top of the unit was derived by fractional crystallization from the rhyolite near the base of the unit, which was produced by mixing the intermember rhyodacite and the intermember high-silica rhyolite. Also, enough time elapsed between the syneruptive mixing event and the eruption of the next ash-flow unit for the mafic phases (magnetite and ilmenite, and biotite) to equilibrate with the higher oxidizing conditions and for a new phase to begin crystallizing (titanite). Finally, throughout the MPT, scarce evidence is preserved in the form of textures and compositional heterogeneities that would indicate of mixing. Thus, the repose period between eruptions was of sufficient length to allow mixing textures to be obliterated, but yet it was short enough to allow the chemical evidence for mixing to be preserved.

SUMMARY AND CONCLUSION

The MPT of west-central Nevada consists of two, voluminous ash-flow tuff members that are separated by a volumetrically minor ash-flow tuff and interbedded volcanoclastic sedimentary rocks. The Guild Mine and Weed Heights Members of the MPT and the intermember ash-flow tuff have overlapping areal distributions, were erupted over a relatively short period of time given the available age constraints, and most importantly, have strikingly similar compositions and zoning characteristics. For these reasons, the three ash-flow tuffs are interpreted to be petrogenetically related, and hence, they provide successive samplings from the same evolving continental silicic magma chamber. Pressure estimates determined using Al-in-hornblende geobarometry indicate that the MPT chamber resided at relatively shallow levels in the crust (3-7 km depth).

The Guild Mine and the Weed Heights Members of the MPT are unique in that they both exhibit reverse compositional zoning. In terms of bulk-tuff compositions, the Guild Mine Member grades from dacite at the base to high-silica rhyolite at the top (65.7- 78.1 wt. % SiO₂) with a compositional gap between 70 and 73 wt. % SiO₂. The Weed Heights Member displays a more limited compositional range from rhyodacite at the base to high-silica rhyolite at the top (71.5- 75.5 wt. % SiO₂).

The reverse zoning is also reflected in the mineralogy and the mineral content data. Both members of the MPT display a systematic change in mineralogy from the base to the top of each unit. Plagioclase, sanidine, biotite, and Fe-Ti oxides are present throughout the entire stratigraphic thickness of both members. In the dacite at the base of the Guild Mine Member, mafic phases such as clinopyroxene, orthopyroxene, and hornblende are also present in addition to these phases. Moving up section, the amount of plagioclase and mafic phases decreases and the amount of sanidine and quartz

increases. Both the rhyodacite and rhyolite near the middle and upper parts of the Guild Mine Member, respectively, have quartz in addition to these phases but lack hornblende. The high-silica rhyolite at the top of the unit also lacks clinopyroxene and orthopyroxene. In addition to the ubiquitous plagioclase, biotite, and Fe-Ti oxides, the rhyodacite at the base of the Weed Heights Member contains sanidine, quartz, clinopyroxene, orthopyroxene, hornblende, and trace amounts of sphene, and the rhyolite at the top of the unit also contains all of these phases except clinopyroxene, orthopyroxene, and hornblende.

Considering the mineral content data, the compositional gradation from the base to the top of both members is well reflected by the plagioclase compositions. The plagioclase phenocrysts display a systematic decrease in An contents from the less evolved compositions in the lower parts of each unit to the more evolved compositions in the upper parts of each unit. Normal zoning is most pronounced in the plagioclase phenocrysts in the less evolved compositions, and zoning is much more limited in the more evolved compositions.

The bulk-tuff compositional data and the biotite and glass content data were used in concert with the intensive parameters calculated from mineral content data to further constrain the compositional zoning and gradations within the pre-eruptive MPT magma chamber. Prior to the eruption of the Guild Mine Member, the lowest part of the magma column tapped consisted of higher temperature, denser dacitic magma with relatively low water contents. The chamber was zoned upward to successively lower temperature, less dense, more evolved compositions with progressively higher water contents. The compositional gap in the bulk-tuff compositional data, the bimodality of the glass analyses, and the multiple populations of biotite analyses based on Mg# indicate that the pre-eruptive magma chamber was zoned in a step-wise manner. These data are consistent with a chamber configuration that consisted of individually convecting layers

that were separated by distinct isocompositional surfaces. Convection is indicated by calculated Rayleigh numbers which greatly exceed the critical value.

The origin of the compositional zoning in the Guild Mine Member was derived by crystal fractionation processes. The variation of select trace elements with increasing differentiation is qualitatively consistent with fractionation of an assemblage consisting of plagioclase, sanidine, biotite, clinopyroxene, Fe-Ti oxides, zircon, and a LREE-enriched accessory phase. Major element, least-squares calculations and trace element, Rayleigh fractional crystallization models support this qualitative assessment and indicate that the zoning within the pre-eruptive MPT magma chamber was derived by fractionation of an assemblage consisting of plagioclase, biotite, and magnetite with clinopyroxene, sanidine, and/or quartz depending on the compositional increment modelled.

On several trace element variation diagrams, the Weed Heights Member exhibits trends that are suggestive of mixing. Moreover, major element, least-squares models were not plausible to explain the derivation of the more evolved compositions in the upper parts of the Weed Heights Member from the rhyodacite at the base of the unit by fractional crystallization processes. Major element, mass balance mixing models and calculated mixing hyperbolas on an element/element ratio diagram indicate that mixing is a plausible hypothesis to explain some of the compositions in the Weed Heights Member and in the intermember ash-flow tuff. During the eruption of the Guild Mine Member, the less evolved compositions in the lower parts of the chamber were mixed with the more evolved compositions in the upper parts of the chamber to yield the intermember rhyodacite. The relationship between the intermember rhyodacite and intermember high-silica rhyolite was not constrained by field relations, but they do have parallel REE trends, suggesting that the high-silica rhyolite was derived from the rhyodacite by fractional crystallization. During the eruption of the intermember tuff, the intermember

rhyodacite and high-silica rhyolite were mixed to yield the Weed Heights rhyolite that directly overlies the rhyodacite at the base of the member. The high-silica rhyolite at the top of the Weed Heights Member was derived by fractionation of an assemblage consisting of plagioclase, biotite, sanidine, and quartz.

The zoning within the Guild Mine and Weed Heights Members is consistent with eruption of a normally zoned magma chamber with a silicic cap, except that the compositional gradations are inverted. For this reason, the reverse compositional zoning is interpreted to represent tapping the lower, more mafic parts of a normally zoned chamber. The reverse compositional zoning indicates that the chamber geometry was complex and that the tapping mechanism was fundamentally different from most systems. During eruption, the isocompositional interfaces separating the individual layers in the pre-eruptive magma column were drawn down to the vent opening. This type of dynamic eruption mechanism re-organized and mixed the diverse compositions in the chamber to yield some of the compositions in the successively erupted units. The repose period between eruptions was sufficiently long for the phenocrysts to re-equilibrate to the new magmatic conditions. Both the rhyodacite at the base of the Weed Heights Member and the intermember tuff yield higher oxygen fugacities and have water contents 2-3 times higher than the underlying Guild Mine Member. The biotite phenocrysts in the intermember ash-flow tuff and the Weed Heights Members have similar compositions with higher Mg#s than any of the biotite analyses in the Guild Mine Member, reflecting the higher oxygen fugacity conditions.

The origin of reverse compositional zoning in ash-flow tuffs by tapping the lower, more mafic parts of a normally zoned chamber has important temporal implications in several extensional tectonic regimes in the western United States. In the central Walker Lane, the Rio Grande Rift, and the Colorado River extensional corridor, the eruption of

reversely zoned tuffs occurred just prior to or during the earliest stages of extension and may be a precursor to rapid rates of extension.

Reversely zoned tuffs are scarce in the rock record, and of those reversely zoned tuffs that have been mentioned, very little data has been reported. This study has documented the compositional variations within two genetically related, reversely zoned tuffs and has provided insight into the origin of these unique ash-flow tuff deposits in terms of chamber configuration, eruption dynamics, and tectonic implications.

BIBLIOGRAPHY

- Andersen, D. J., and Lindsley, D. H., 1988, Internally consistent solution models for Fe-Mg-Mn-Ti oxides: Fe-Ti oxides: *American Mineralogist*, v. 73, p. 714-726.
- Andersen, D. J., Lindsley, D. H., and Davidson, P. M., 1993, QUILF: A PASCAL program to assess equilibria among Fe-Mg-Mn-Ti oxides, pyroxenes, olivine, and quartz: *Computers and Geosciences*, v. 19, p. 1333-1350.
- Anderson, R. E., Longwell, C. R., Armstrong, R. L., and Marvin, R. F., 1972, Significance of K-Ar ages of Tertiary volcanic rocks from the Lake Mead region, Nevada-Arizona: *Geological Society of America Bulletin*, v. 83, p. 273-288.
- Arth, J. G., 1976, Behavior of trace elements during magmatic processes-A summary of theoretical models and their applications: *U. S. Geological Survey Journal of Research*, v. 4, p. 41-47.
- Bacon, C. R., and Hirschmann, M. M., 1988, Mg/Mn partitioning as a test for equilibrium between coexisting Fe-Ti oxides: *American Mineralogist*, v. 73, p. 57-61.
- Baker, B. N., and McBirney, A. R., 1985, Liquid fractionation. Part III: Geochemistry of zoned magmas and the compositional effects of liquid fractionation: *Journal of Volcanology and Geothermal Resources*, v. 24, p. 55-81.
- Best, M. G., Christiansen, E. H., Deino, A. L., Grommé, C. S., McKee, E. H., and Noble, D. C., 1989, Eocene through Miocene volcanism in the Great Basin of the western United States, *in* Chapin, C. E., and Zidek, J., eds., *Field excursions to volcanic terranes in the western United States, Volume II: Cascades and Intermountain West*: New Mexico Bureau of Mine and Mineral Resources Memoir 47, p. 91-133.
- Bingler, E. C., 1977, Geologic map of the New Empire Quadrangle: Nevada Bureau of Mines and Geology, Map 59, scale 1:24,000.
- Bingler, E. C., 1978a, Abandonment of the name Hartford Hill Rhyolite Tuff and adoption of new formation names for middle Tertiary ash-flow tuffs in the Carson City-Silver City area, Nevada: *U. S. Geological Survey Bulletin* 1457-D, 19 p.

- Bingler, E. C., 1978b, Geologic map of the Schurz Quadrangle: Nevada Bureau of Mines and Geology, Map 60, scale 1:48,000.
- Bingler, E. C., Silberman, M. L., and McKee, E. H., 1980, K-Ar ages of volcanic and plutonic rocks in the northern Wassuck Range, central-western Nevada: *Isochron/West*, v. 27, p. 13-16.
- Blake, S., 1981, Eruptions from zoned magma chambers: *Journal Geological Society London*, v. 138, p. 281-287.
- Blake, S., and Campbell, I. H., 1986, The dynamics of magma-mixing during flow in volcanic conduits: *Contributions to Mineralogy and Petrology*, v. 94, p. 72-81.
- Blake, S., and Ivey, G. N., 1986a, Density and viscosity gradients in zoned magma chambers, and their influence on withdrawal dynamics: *Journal of Volcanology and Geothermal Resources*, v. 30, p. 201-230.
- Blake, S., and Ivey, G. N., 1986b, Magma-mixing and the dynamics of withdrawal from stratified reservoirs: *Journal of Volcanology and Geothermal Resources*, v. 27, p. 153-178.
- Boden, D. R., 1989, Evidence for step-function zoning of magma and eruptive dynamics, Toquima caldera complex, Nevada: *Journal of Volcanology and Geothermal Research*, v. 37, p. 39-57.
- Boden, D. R., 1994, Mid-Tertiary magmatism of the Toquima caldera complex and vicinity, Nevada: development of explosive high-K, calc-alkaline magmas in the central Great Basin, USA: *Contributions to Mineralogy and Petrology*, v. 116, p. 247-276.
- Bohlen, S. R., Peacor, D. R., and Essene, E. J., 1980, Crystal chemistry of a metamorphic biotite and its significance in water barometry: *American Mineralogist*, v. 65, p. 55-62.
- Brown, S. J. A., Wilson, C. J. N., Cole, J. W., and Wooden, J., 1998, The Whakamaru group ignimbrites, Taupo Volcanic Zone, New Zealand: evidence for reverse tapping of a zoned silicic magmatic system: *Journal of Volcanology and Geothermal Research*, v. 84, p. 1-37.
- Broxton, D. E., Warren, R. G., Byers, F. M., and Scott, R. B., 1989, Chemical and mineralogical trends within the Timber Mountain-Oasis Valley caldera complex,

- Nevada: Evidence for multiple cycles of chemical evolution in a long-lived silicic magma system: *Journal of Geophysical Research*, v. 94, p. 5961-5985.
- Bryan, W. B., Finger, L. W., and Chayes, F., 1969, Estimating proportions in petrographic mixing equations by least-squares approximation: *Science*, v. 163, p. 926-927.
- Burnham, C. W., Holloway, J. R., and Davis, N. F., 1969, Thermodynamic properties of water to 1,000°C and 10,000 bars: *Geological Society of America Special Paper* 132, 96 p.
- Burnham, C. W., and Davis, N. F., 1974, The role of H₂O in silicate melts: II. Thermodynamic and phase relations in the system NaAlSi₃O₈-H₂O to 10 kilobars, 700° to 1100°C: *American Journal of Science*, v. 274, p. 902-940.
- Cambray, F. W., Vogel, T. A., and Mills, J. G., Jr., 1995, Origin of compositional heterogeneities in tuffs of the Timber Mountain Group: The relationship between magma batches and magma transfer and emplacement in an extensional environment: *Journal of Geophysical Research*, v. 100, p. 15793-15805.
- Carmichael, I. S. E., 1967, The iron-titanium oxides of salic volcanic rocks and their associated ferromagnesian silicates: *Contributions to Mineralogy and Petrology*, v. 14, p. 36-64.
- Cas, R. A. F., and Wright, J. V., 1987, *Volcanic Successions, Modern and Ancient*: London, Unwin Hyman, 528 p.
- Chesner, C. A., 1998, Petrogenesis of the Toba Tuffs, Sumatra, Indonesia: *Journal of Petrology*, v. 39, p. 397-438.
- Chesner, C. A., and Rose, W. I., 1991, Stratigraphy of the Toba Tuffs and the evolution of the Toba Caldera Complex, Sumatra, Indonesia: *Bulletin of Volcanology*, v. 53, p. 343-356.
- Chesner, C. A., Rose, W. I., Deino, A., Drake, R., and Westgate, J. A., 1991, Eruptive history of Earth's largest Quaternary caldera (Toba, Indonesia) clarified: *Geology*, v. 19, p. 200-203.
- Christiansen, R. L., 1984, Yellowstone magmatic evolution: Its bearing on understanding large-volume explosive volcanism, *in* *Explosive Volcanism: Inception, Evolution, and Hazards*: Washington, D. C., National Academy Press, p. 84-95.

- Christiansen, R. L., and Blank, H. R., Jr., 1972, Volcanic stratigraphy of the Quaternary rhyolite plateau in Yellowstone National Park: U.S. Geological Survey Professional Paper 729-B, 18 p.
- Cook, H. E., 1968, Ignimbrite flows, plugs, and dikes in the southern part of the Hot Creek Range Nye County, Nevada: Geological Society of America Memoir 116, p. 107-152.
- Cox, K. G., Bell, J. D., and Pankhurst, R. J., 1979, The Interpretation of Igneous Rocks: London, George Allen and Unwin, 450 p.
- Cross, T. A., and Pilger, R. H., Jr., 1978, Constraints on absolute motion and plate interaction inferred from Cenozoic igneous activity in the western United States: American Journal of Science, v. 278, p. 865-902.
- Dalrymple, G. B., 1979, Critical tables for conversion of K-Ar ages from old to new constants: Geology, v. 7, p. 558-560.
- Deer, W. A., Howie, R. A., and Zussman, J., 1992, An Introduction to the Rock-Forming Minerals: Essex, England, Longman Scientific and Technical, 696 p.
- Dilles, J. H., 1987, Petrology of the Yerington batholith, Nevada: Evidence for evolution of porphyry copper ore fluids: Economic Geology, v. 82, p. 1750-1789.
- Dilles, J. H., 1993, Cenozoic normal and strike-slip faults in the northern Wassuk Range, western Nevada, *in* Craig, S. D., ed., Structure, tectonics and mineralization of the Walker Lane: Reno, Geological Society of Nevada, Walker Lane Symposium Proceedings, p. 114-136.
- Dilles, J. H., John, D. A., and Hardyman, R. F., 1993, Evolution of Cenozoic magmatism and tectonism along a northeast-southwest transect across the northern Walker Lane, west-central Nevada -- Part I, *in* Lahren, M. M., Trexler, J. H., Jr., and Spinoso, C., eds., Crustal Evolution of the Great Basin and Sierra Nevada: Cordilleran/Rocky Mountain Section, Geological Society of America Guidebook: Reno, NV, Department of Geological Sciences, University of Nevada, Reno, p. 409-452.
- Dilles, J. H., and Gans, P. B., 1995, The chronology of Cenozoic volcanism and deformation in the Yerington area, western Basin and Range and Walker Lane: Geological Society of America Bulletin, v. 107, p. 474-486.

- Drake, M. J., and Weill, D. F., 1975, Partition of Sr, Ba, Ca, Y, Eu^{2+} , Eu^{3+} , and other REE between plagioclase feldspar and magmatic liquid: an experimental study: *Geochimica et Cosmochimica Acta*, v. 39, p. 689-712.
- Duffield, W. A., and Du Bray, E. A., 1990, Temperature, size, and depth of the magma reservoir for the Taylor Creek Rhyolite, New Mexico: *American Mineralogist*, v. 75, p. 1059-1070.
- Eggleson, T. L., Osburn, G. R., and Chapin, C. E., 1983, Reversely zoned Hells Mesa Tuff and Socorro Cauldron: EOS American Geophysical Union Transactions, v. 64, p. 884.
- Eichelberger, J. C., 1980, Vesiculation of mafic magma during replenishment of silicic magma reservoirs: *Nature*, v. 288, p. 446-450.
- Ekren, E. B., Byers, F. M., Jr., Hardyman, R. F., Marvin, R. F., and Silberman, M. L., 1980, Stratigraphy, preliminary petrology, and some structural features of Tertiary volcanic rocks in the Gabbs Valley and Gillis Ranges, Mineral County, Nevada: U. S. Geological Survey Bulletin 1464, 54 p.
- Ekren, E. B., and Byers, F. M., Jr., 1984, The Gabbs Valley Range--A well exposed segment of the Walker Lane in west-central Nevada, in Lintz, J., Jr., ed., *Western Geological Excursions*; Vol. 4: Geological Society of America Guidebook, p. 203-215.
- Elston, W. E., 1984, Mid-Tertiary ash flow tuff cauldrons, southwestern New Mexico: *Journal of Geophysical Research*, v. 89, p. 8,733-8,750.
- Ferriz, H., and Mahood, G. A., 1987, Strong compositional zonation in a silicic magmatic system: Los Humeros, Mexican Neovolcanic Belt: *Journal of Petrology*, v. 28, p. 171-209.
- Flood, T. P., Schuraytz, B. C., and Vogel, T. A., 1989, Magma mixing due to disruption of a layered magma body: *Journal of Volcanology and Geothermal Research*, v. 36, p. 241-255.
- Fridrich, C. J., and Mahood, G. A., 1987, Compositional layers in the zoned magma chamber of the Grizzly Peak Tuff: *Geology*, v. 15, p. 299-303.
- Fuhrman, M. L., and Lindsley, D. H., 1988, Ternary-feldspar modeling and thermometry: *American Mineralogist*, v. 73, p. 201-215.

- Gans, P. B., 1987, An open-system, two-layer crustal stretching model for the eastern Great Basin: *Tectonics*, v. 6, p. 1-12.
- Gans, P. B., and Bohrsen, W. A., 1998, Suppression of volcanism during rapid extension in the Basin and Range Province, United States: *Science*, v. 279, p. 66-68.
- Gans, P. B., Mahood, G. A., and Schermer, E., 1989, Synextensional magmatism in the Basin and Range Province; A case study from the eastern Great Basin: *Geological Society of America Special Paper 233*, 53 p.
- Geissman, J. W., Van der Voo, R., and Howard, K. L., Jr., 1982, A paleomagnetic study of the structural deformation in the Yerington district, Nevada: *American Journal of Science*, v. 282, p. 1042-1109.
- Ghiorso, M. S., 1984, Activity/composition relations in the ternary feldspars: *Contributions to Mineralogy and Petrology*, v. 87, p. 282-296.
- Ghiorso, M. S., and Sack, R. O., 1991, Fe-Ti oxide geothermometry: thermodynamic formulation and the estimation of intensive variables in silicic magmas: *Contributions to Mineralogy and Petrology*, v. 108, p. 485-510.
- Gill, J. B., 1981, *Orogenic Andesites and Plate Tectonics*: Berlin, Springer, 390 p.
- Grove, T. L., and Donnelly-Nolan, J. M., 1986, The evolution of young silicic lavas at Medicine Lake Volcano, California: Implications for the origin of compositional gaps in calc-alkaline series lavas: *Contributions to Mineralogy and Petrology*, v. 92, p. 281-302.
- Grunder, A. L., and Mahood, G. A., 1988, Physical and chemical models of zoned silicic magmas: The Loma Seca Tuff and Calabozos Caldera, Southern Andes: *Journal of Petrology*, v. 29, p. 831-867.
- Hammarstrom, J. M., and Zen, E., 1986, Aluminum in hornblende: An empirical igneous barometer: *American Mineralogist*, v. 71, p. 1297-1313.
- Hardyman, R. F., Ekren, E. B., and Byers, F. M., 1975, Cenozoic strike-slip, normal and detachment faults in northern part of the Walker Lane, west-central Nevada: *Geological Society of America Abstracts with Programs*, v. 7, p. 1100.

- Hardyman, R. F., 1978, Volcanic stratigraphy and structural geology of Gillis Canyon Quadrangle, northern Gillis Range, Mineral County, Nevada [PhD Thesis]: University of Nevada, Reno, 248 p.
- Hardyman, R. F., 1984, Strike-slip, normal, and detachment faults in the northern Gillis Range, Walker Lane of west-central Nevada, *in* Lintz, J., Jr., ed., Western Geological Excursions; Vol. 4: Geological Society of America Guidebook, p. 184-199.
- Hardyman, R. F., and Oldow, J. S., 1991, Tertiary tectonic framework and Cenozoic history of the central Walker Lane, Nevada, *in* Raines, G. L., Lisle, R. E., Schafer R. W., and Wilkinson, W. H., eds., Geology and Ore Deposits of the Great Basin, Symposium Proceedings, April, 1990: v. 1, p. 279-301.
- Hardyman, R. F., McKee, E. H., Snee, L. W., and Whitebread, D. H., 1993, The Camp Terrill and Dicalite Summit Faults: Two contrasting examples of detachment faults in the Central Walker Lane, western Nevada, *in* Craig, S. D., ed., Structure, Tectonics and Mineralization of the Walker Lane, Proceedings Volume, Walker Lane Symposium, April 24, 1992: Reno, NV, Geological Society of Nevada, p. 93-113.
- Hildreth, W., 1979, The Bishop Tuff: Evidence for the origin of compositional zonation in silicic magma chambers, *in* Chapin, C. E., and Elston, W. E., eds., Ash-Flow Tuffs: Geological Society of America Special Paper 180, p. 43-75.
- Hildreth, W., 1981, Gradients in silicic magma chambers: Implications for lithospheric magmatism: *Journal of Geophysical Research*, v. 86, p. 10153-10192.
- Hollister, L. S., Grissom, G. C., Peters, E. K., Stowell, H. H., and Sisson, V. B., 1987, Confirmation of the empirical correlation of Al in hornblende with pressure of solidification of calc-alkaline plutons: *American Mineralogist*, v. 72, p. 231-239.
- Johannes, W., 1979, Ternary feldspars: Kinetics and possible equilibria at 800°C: *Contributions to Mineralogy and Petrology*, v. 68, p. 221-230.
- Johnson, M. C., and Rutherford, M. J., 1989a, Experimentally determined conditions in the Fish Canyon Tuff, Colorado, magma chamber: *Journal of Petrology*, v. 30, p. 711-737.
- Johnson, M. C., Rutherford, M. J., 1989b, Experimental calibration of the aluminum-in-hornblende geobarometer with application to Long Valley caldera (California) volcanic rocks: *Geology*, v. 17, p. 837-841.

- Klein, C., and Hurlbut, C. S., Jr., 1985, *Manual of Mineralogy* (after James D. Dana): New York, John Wiley and Sons, 596 p.
- Koyaguchi, T., 1985, Magma mixing in a conduit: *Journal of Volcanology and Geothermal Resources*, v. 25, p. 365-369.
- Kretz, R., 1982, Transfer and exchange equilibria in a portion of the pyroxene quadrilateral as deduced from natural and experimental data: *Geochimica et Cosmochimica Acta*, v. 46, p. 411-421.
- Lange, R. L., and Carmichael, I. S. E., 1990, Thermodynamic properties of silicate liquids with emphasis on density, thermal expansion and compressibility, *in* Nicholls, J., and Russell, J. K., eds., *Modern Methods of Igneous Petrology: Understanding Magmatic Processes*: Washington, D. C., Mineralogical Society of America, v. 24, p. 25-64.
- Langmuir, C. H., Vocke, R. D., Jr., Hanson, G. N., and Hart, S. R., 1978, A general mixing equation with applications to Icelandic basalts: *Earth and Planetary Science Letters*, v. 37, p. 380-392.
- Le Bas, M. J., Le Maitre, R. W., Streckeisen, A., and Zanettin, B., 1986, A chemical classification of volcanic rocks based on the total alkali-silica diagram: *Journal of Petrology*, v. 27, p. 745-750.
- Leake, B. E., 1978, Nomenclature of amphiboles: *American Mineralogist*, v. 63, p. 1023-1052.
- Lindsley, D. H., 1983, Pyroxene thermometry: *American Mineralogist*, v. 68, p. 477-493.
- Lindsley, D. H., and Andersen, D. J., 1983, A two-pyroxene thermometer: *Journal of Geophysical Research*, v. 88, p. 887-906.
- Lipman, P. W., 1967, Mineral and chemical variations within an ash-flow sheet from Aso caldera, southwestern Japan: *Contributions to Mineralogy and Petrology*, v. 16, p. 300-327.
- Mahood, G. A., 1981, Chemical evolution of a Pleistocene rhyolitic center: Sierra La Primavera, Jalisco, Mexico: *Contributions to Mineralogy and Petrology*, v. 77, p. 129-149.

- Mahood, G., and Hildreth, W., 1983, Large partition coefficients for trace elements in high-silica rhyolites: *Geochimica et Cosmochimica Acta*, v. 47, p. 11-30.
- McIntosh, W. C., Sutter, J. F., Chapin, C. E., and Kedzie, L. L., 1990, High-precision $^{40}\text{Ar}/^{39}\text{Ar}$ sanidine geochronology of ignimbrites in the Mogollon-Datil volcanic field, southwestern New Mexico: *Bulletin of Volcanology*, v. 52, p. 584-601.
- McIntosh, W. C., Geissman, J. W., Chapin, C. E., Kunk, M. J., and Henry, C. D., 1992, Calibration of the latest Eocene-Oligocene geomagnetic polarity time scale using $^{40}\text{Ar}/^{39}\text{Ar}$ dated ignimbrites: *Geology*, v. 20, p. 459-463.
- Miller, C. F., and Mittlefehldt, D. W., 1982, Depletion of light rare-earth elements in felsic magmas: *Geology*, v. 10, p. 129-133.
- Mills, J. G., 1985, The geology and geochemistry of volcanic and plutonic rocks in the Hoover Dam 7 1/2 minute quadrangle, Clark County, Nevada and Mohave County, Arizona [M. S. Thesis]: University of Nevada, Las Vegas, 119 p.
- Mills, J. G., Jr., Saltoun, B. W., and Vogel, T. A., 1997, Magma batches in the Timber Mountain magmatic system, Southwestern Nevada Volcanic Field, Nevada, USA: *Journal of Volcanology and Geothermal Research*, v. 78, p. 185-208.
- Morimoto, N., 1988, Nomenclature of Pyroxenes: *Mineralogical Magazine*, v. 52, p. 535-550.
- Nakamura, N., 1974, Determination of REE, Ba, Fe, Mg, Na, and K in carbonaceous and ordinary chondrites: *Geochimica et Cosmochimica Acta*, v. 38, p. 757-775.
- Naney, M. T., 1983, Phase equilibria of rock-forming ferromagnesian silicates in granitic systems: *American Journal of Science*, v. 283, p. 993-1033.
- Nash, W. P., and Crecraft, H. R., 1985, Partition coefficients for trace elements in silicic magmas: *Geochimica et Cosmochimica Acta*, v. 49, p. 2309-2322.
- Nielsen, R. L., 1965, Right-lateral strike-slip faulting in the Walker lane, west-central Nevada: *Geological Society of America*, v. 76, p. 1301-1308.
- Oldow, J. S., 1993, Late Cenozoic displacement partitioning in the northwest Great Basin, in Craig, S. D., ed., *Structure, tectonics and mineralization of the Walker*

Lane: Reno, Geological Society of Nevada, Walker Lane Symposium Proceedings, p. 17-52.

Osburn, G. R., and Chapin, C. E., 1983, Ash-flow tuffs and cauldrons in the northeast Mogollon-Datil volcanic field: A summary, *in* Chapin, C. E., and Callender, J. F., eds., Socorro Region II: Guidebook 34: New Mexico Geological Society, p. 197-207.

Papike, J. J., Cameron, K. L., and Baldwin, K., 1974, Amphiboles and pyroxenes: Characterization of other than quadrilateral components and estimates of ferric iron from microprobe data: Geological Society of America Abstracts with Programs, v. 6, p. 1053-1054.

Philpotts, A. R., 1990, Principles of Igneous and Metamorphic Petrology: Englewood Cliffs, N.J., Prentice Hall, 498 p.

Proffett, J. M., Jr., 1977, Cenozoic geology of the Yerington district, Nevada, and implications for the nature and origin of Basin and Range faulting: Geological Society of America Bulletin, v. 88, p. 247-266.

Proffett, J. M., Jr., and Proffett, B. H., 1976, Stratigraphy of the Tertiary ash-flow tuffs in the Yerington district, Nevada: Nevada Bureau of Mines and Geology, Report 27, 28 p.

Proffett, J. M., Jr., and Dilles, J. H., 1984, Geologic map of the Yerington district, Nevada: Nevada Bureau of Mines and Geology, Map 77, scale 1:24,000.

Schmidt, M. W., 1992, Amphibole composition in tonalite as a function of pressure: an experimental calibration of the Al-in-hornblende barometer: Contributions to Mineralogy and Petrology, v. 110, p. 304-310.

Schuraytz, B. C., Vogel, T. A., and Younker, L. W., 1989, Evidence for dynamic withdrawal from a layered magma body: the Topopah Spring Tuff, southwestern Nevada: Journal of Geophysical Research, v. 94, p. 5925-5942.

Seedorff, E., 1991, Magmatism, extension, and ore deposits of Eocene to Holocene age in the Great Basin - Mutual effects and preliminary proposed genetic relationships, *in* Raines, G. L., Lisle, R. E., Schafer R. W., and Wilkinson, W. H., eds., Geology and Ore Deposits of the Great Basin, Symposium Proceedings, April, 1990: v. 1, p. 133-178.

- Shaw, H. R., 1972, Viscosities of magmatic silicate liquids: An empirical method of prediction: *American Journal of Science*, v. 272, p. 870-893.
- Smith, E. I., Feuerbach, D. L., Naumann, T. R., and Mills, J. G., 1990, Mid-Miocene volcanic rocks and plutonic rocks in the Lake Mead area of Nevada and Arizona; Production of intermediate igneous rocks in an extensional environment, *in* Anderson, J. L., ed., *The nature and origin of Cordilleran magmatism*: Geological Society of America Memoir 174, p. 169-194.
- Smith, R.L., 1979, Ash-flow magmatism, *in* Chapin, C. E., and Elston, W. E., eds., *Ash-Flow Tuffs*: Geological Society of America Special Paper 180, p. 5-27.
- Sparks, R. S. J., Huppert, H. E., and Turner, J. S., 1984, The fluid dynamics of evolving magma chambers: *Philosophical Transactions Royal Society London*, v. A310, p. 511-534.
- Spell, T. L., Harrison, T. M., and Wolff, J. A., 1990, $^{40}\text{Ar}/^{39}\text{Ar}$ dating of the Bandelier Tuff and San Diego Canyon ignimbrites, Jemez Mountains, New Mexico: Temporal constraints on magmatic evolution: *Journal of Volcanology and Geothermal Research*, v. 43, p. 175-193.
- Spera, F. J., 1984, Some numerical experiments on the withdrawal of magma from crustal reservoirs: *Journal of Geophysical Research*, v. 89, p. 8222-8236.
- Spera, F. J., Yuen, D. A., Greer, J. C., and Sewell, G., 1986, Dynamics of magma withdrawal from stratified magma chambers: *Geology*, v. 14, p. 723-726.
- Spigel, R. H., and Farrant, B., 1984, Selective withdrawal through a point sink and pycnocline formation in a linearly stratified flow: *Journal of Hydraulic Research*, v. 22, p. 35-51.
- Stewart, J. H., and Carlson, J. E., 1976, Cenozoic rocks of Nevada: Nevada Bureau of Mines and Geology, Map 52, scale 1:1,000,000.
- Stewart, J. H., 1988, Tectonics of the Walker Lane belt, western Great Basin: Mesozoic and Cenozoic deformation in a zone of shear, *in* Ernst, W. G., eds., *Metamorphism and crustal evolution of the western United States*: Englewood Cliffs, N.J., Prentice Hall, Rubey Volume VII, p. 684-713.
- Stormer, J. C., Jr., 1983, The effects of recalculation on estimates of temperature and oxygen fugacity from analyses of multicomponent iron-titanium oxides: *American Mineralogist*, v. 68, p. 586-594.

- Stormer, J. C., and Nicholls, J., 1978, XLFRAC: A program for the interactive testing of magmatic differentiation models: *Computers and Geosciences*, v. 4, p. 143-159.
- Streckeisen, A., 1979, Classification and nomenclature of volcanic rocks, lamprophyres, carbonatites, and melilitic rocks: Recommendations and suggestions of the IUGS Subcommittee on the Systematics of Igneous Rocks: *Geology*, v. 7, p. 331-335.
- Suppe, J., 1985, *Principles of Structural Geology*: Englewood Cliffs, N.J., Prentice-Hall, 537 p.
- Walker, G. P. L., 1972, Crystal concentration in ignimbrites: *Contributions to Mineralogy and Petrology*, v. 36, p. 135-146.
- Weill, D. F., and Drake, M. J., 1973, Europium anomaly in plagioclase feldspar: Experimental results and semiquantitative model: *Science*, v. 180, p. 1059-1060.
- Whitney, J. A., and Stormer, J. C., Jr., 1985, Mineralogy, petrology, and magmatic conditions from the Fish Canyon Tuff, central San Juan Volcanic Field, Colorado: *Journal of Petrology*, v. 26, p. 726-762.
- Wolff, J. A., 1985, The effect of explosive eruption processes on geochemical patterns within pyroclastic deposits: *Journal of Volcanology and Geothermal Research*, v. 26, p. 189-201.
- Wones, D. R., and Eugster, H. P., 1965, Stability of biotite: Experiment, theory, and application: *American Mineralogist*, v. 50, p. 1228-1272.
- Wones, D. R., 1972, Stability of biotite: A reply: *American Mineralogist*, v. 57, p. 316-617.

APPENDICES

Appendix A: Microprobe analytical conditions.

a. Glass			b. Feldspars			c. Pyroxenes		
<u>Element</u>	<u>Standard</u>	<u>Counting Time</u> (seconds)	<u>Element</u>	<u>Standard</u>	<u>Counting Time</u> (seconds)	<u>Element</u>	<u>Standard</u>	<u>Counting Time</u> (seconds)
Si	rhyo	10	Si	kano	20	Si	kaug	20
Al	rhyo	10	Al	labr	20	Al	kaug	20
Ti	basl	10	Fe*	kaugbas	10	Ti	basl	30
Fe*	basl	10	Mg	kaugbas	10	Fe*	kaug	20
Mn	pymn	10	Ca	labr	10	Mn	pymn	10
Ca	basl	10	Na	kano	10	Mg	kaug	20
Mg	kaugbas	10	K	sani	10	Ca	kaug	10
K	sani	10	Ba	sani	30	Na	kano	10
Na	kanopc1	10				Cr	crom	10
P	flap	10						

Appendix A: Continued.

d. Biotite			e. Amphibole			f. Fe-Ti Oxides		
Element	Standard	Counting Time (seconds)	Element	Standard	Counting Time (seconds)	Element	Standard	Counting Time (seconds)
Si	flogpc1	10	Si	kaugbas	10	Si	qtz	10
Al	flogpc1	10	Al	labrpc1	10	Ti	ruti	10
Ti	baslpc1	10	Ti	baslpc1	10	Al	coru	10
Fe*	fayl	20	Fe*	kaugbas	20	Cr	crom	10
Mg	flogpc1	10	Mg	kaugbas	10	Fe*	magt	10
Mn	pymn	10	Mn	pymn	10	V	v	20
Ca	kaugbas	10	Ca	kaugbas	10	Mn	pymn	10
Na	kanopc1	10	Na	kanopc1	10	Mg	crom	10
K	flogpc1	10	K	flogpc1	10	Zn	gahn	10
Rb	rbglas	30	Cr	crom	10	Ni	nisi	10
Cs	poll	10	F	flogpc1	20	Zr	zirc	10
Ba	sani	20	Cl	tugt	10	Nb	nb	10
F	flogpc1	20						
Cl	tugt	10						

Appendix B: Geochemical sample locations.

<u>Sample #</u>	<u>General Location</u>	<u>7.5'-Quadrangle Map</u>	<u>Latitude</u>	<u>Longitude</u>
<i>Guild Mine Member</i>				
94-5B	Weed Heights	Yerington, NV	38°58'37"	119°12'18"
94-6B	Weed Heights	Yerington, NV	38°58'34"	119°12'25"
94-11	Weed Heights	Yerington, NV	38°58'30"	119°12'29"
94-7	Weed Heights	Yerington, NV	38°58'30"	119°12'36"
94-12A	Weed Heights	Yerington, NV	38°58'25"	119°12'54"
94-8	Weed Heights	Yerington, NV	38°58'23"	119°12'53"
94-13A	Weed Heights	Yerington, NV	38°58'21"	119°13'03"
94-15	Weed Heights	Yerington, NV	38°58'10"	119°13'08"
94-9C	Weed Heights	Yerington, NV	38°58'04"	119°13'12"
94-9C(f)	Weed Heights	Yerington, NV	38°58'04"	119°13'12"
93-36	Singatse Peak	Yerington, NV	38°59'07"	119°13'45"
93-38	Singatse Peak	Yerington, NV	38°59'14"	119°13'42"
93-62	Mound House	New Empire, NV	39°11'27"	119°39'40"
92-22	Mound House	New Empire, NV	39°11'31"	119°39'46"
94-72B	N. Gillis Range	Ghost Dance Ridge, NV	38°49'35"	118°37'27"
92-127B	Calavada Summit	Luning, NV	38°35'49"	118°09'27"
93-49B	W. Wassuk Range	Yerington NE, NV	38°58'36"	119°01'22"
92-123	W. Wassuk Range	Yerington NE, NV	38°58'44"	119°01'34"
94-76D	W. Wassuk Range	Yerington NE, NV	38°57'33"	119°01'21"
94-76E1	W. Wassuk Range	Yerington NE, NV	38°57'33"	119°01'21"
93-40	Hwy. 95A	Weber Reservoir, NV	39°02'10"	118°59'56"
93-46A	Hwy. 95A	Hinkson Slough, NV	39°02'59"	119°00'12"
93-46E	Hwy. 95A	Hinkson Slough, NV	39°03'00"	119°00'15"
<i>Weed Heights Member</i>				
94-30	Weed Heights	Yerington, NV	38°58'39"	119°13'05"
94-17B	Weed Heights	Yerington, NV	38°58'37"	119°13'05"
94-18	Weed Heights	Yerington, NV	38°58'35"	119°13'08"
94-31	Weed Heights	Yerington, NV	38°58'34"	119°13'11"
94-32	Weed Heights	Yerington, NV	38°58'38"	119°13'11"
92-87	Mason Pass	Lincoln Flat, NV	39°02'00"	119°14'04"
<i>intermember ash-flow tuff</i>				
94-9B	Weed Heights	Yerington, NV	38°58'04"	119°13'13"
94-33A	Mason	Yerington, NV	38°56'53"	119°12'17"
94-28D	Singatse Peak	Yerington, NV	38°59'22"	119°14'05"
<i>miscellaneous samples</i>				
92-106	W. Wassuk Range	Yerington NE, NV	38°35'49"	118°09'27"
93-61	N. Wassuk Range	Hinkson Slough, NV	38°59'38"	118°56'20"

Appendix C: Complete microprobe data for Mickey Pass Tuff.

<u>Sample</u>	<u>Mineral</u>	<u>SiO2</u>	<u>Al2O3</u>	<u>FeO*</u>	<u>MgO</u>	<u>CaO</u>	<u>Na2O</u>	<u>K2O</u>	<u>BaO</u>	<u>Total</u>	<u>Ab</u>	<u>Or</u>	<u>An</u>
94-5B fe1.1	feldspar	50.13	31.56	0.28	0.02	14.18	3.46	0.24	0.06	99.94	30.2	1.4	68.4
94-5B fe1.2	feldspar	53.36	29.24	0.28	0.02	11.42	5.08	0.39	0.05	99.84	43.6	2.2	54.2
94-5B fe1.3	feldspar	52.73	29.44	0.26	0.00	11.68	4.88	0.36	0.06	99.42	42.2	2.1	55.8
94-5B fe1.4	feldspar	53.38	29.47	0.24	0.01	11.76	4.70	0.34	0.07	99.96	41.1	1.9	56.9
94-5B fe1.5	feldspar	59.13	25.00	0.17	0.00	6.34	7.14	1.33	0.24	99.36	62.0	7.6	30.4
94-5B fe2.1	feldspar	58.51	25.01	0.28	0.02	6.51	7.10	1.10	0.13	98.67	62.2	6.3	31.5
94-5B fe2.2	feldspar	55.65	27.62	0.23	0.01	9.35	6.08	0.59	0.10	99.63	52.3	3.3	44.4
94-5B fe2.3	feldspar	54.98	28.34	0.21	0.01	10.00	5.71	0.47	0.06	99.77	49.5	2.7	47.9
94-5B fe2.4	feldspar	48.97	32.28	0.23	0.01	14.70	3.16	0.18	0.01	99.54	27.7	1.1	71.2
94-5B fe2.5	feldspar	49.52	31.95	0.29	0.01	14.49	3.43	0.19	0.04	99.91	29.6	1.1	69.3
94-5B fe3.1	feldspar	51.83	29.65	0.33	0.01	11.72	4.91	0.34	0.05	98.84	42.3	1.9	55.8
94-5B fe3.2	feldspar	52.62	29.44	0.23	0.01	11.52	4.93	0.34	0.04	99.14	42.8	1.9	55.3
94-5B fe3.3	feldspar	52.61	29.63	0.28	0.03	11.81	4.71	0.34	0.04	99.44	41.1	1.9	57.0
94-5B fe4.1	feldspar	60.64	24.47	0.19	0.01	5.89	7.26	1.25	0.10	99.80	64.0	7.3	28.7
94-5B fe4.2	feldspar	54.42	28.03	0.18	0.01	10.10	5.65	0.51	0.03	98.93	48.8	2.9	48.3
94-5B fe4.3	feldspar	52.24	30.01	0.25	0.03	12.18	4.65	0.31	0.02	99.68	40.1	1.8	58.1
94-5B fe4.4	feldspar	53.46	29.07	0.25	0.04	10.96	5.05	0.38	0.03	99.23	44.5	2.2	53.4
94-5B fe4.5	feldspar	51.68	30.21	0.22	0.00	12.72	4.27	0.29	0.04	99.43	37.2	1.7	61.2
94-5B fe5.1	feldspar	49.64	31.97	0.25	0.01	14.46	3.43	0.21	0.07	100.05	29.7	1.2	69.1
94-5B fe5.2	feldspar	55.71	27.81	0.23	0.03	9.43	5.96	0.52	0.08	99.77	51.8	3.0	45.3
94-5B fe5.3	feldspar	58.92	25.36	0.26	0.02	7.21	6.74	0.90	0.16	99.57	59.5	5.3	35.2
94-5B fe6.1	feldspar	53.50	29.49	0.24	0.02	11.62	4.85	0.36	0.07	100.15	42.2	2.1	55.8
94-5B fe6.2	feldspar	53.70	29.47	0.30	0.01	11.46	5.06	0.35	0.06	100.41	43.6	2.0	54.4
94-5B fe6.3	feldspar	54.01	29.43	0.21	0.00	11.28	5.16	0.39	0.08	100.57	44.3	2.2	53.5
94-5B fe6.4	feldspar	59.40	25.17	0.21	0.00	6.40	6.99	1.38	0.27	99.82	61.1	8.0	30.9
94-5B fe6.5	feldspar	59.36	25.03	0.31	0.01	6.51	7.24	1.06	0.15	99.66	62.8	6.1	31.2
94-5B fe7.1	feldspar	60.75	24.12	0.20	0.00	5.53	7.53	1.41	0.14	99.68	65.4	8.0	26.5
94-5B fe7.2	feldspar	60.56	24.49	0.23	0.02	5.69	7.36	1.28	0.14	99.78	64.8	7.4	27.7
94-5B fe7.3	feldspar	59.04	25.27	0.25	0.02	6.42	7.10	1.09	0.11	99.30	62.5	6.3	31.2
94-5B fe7.4	feldspar	59.66	24.27	0.20	0.00	5.82	6.71	2.22	0.20	99.09	58.9	12.8	28.2
94-5B fe8.1	feldspar	52.69	29.53	0.39	0.02	11.59	4.86	0.38	0.11	99.57	42.2	2.2	55.6
94-5B fe8.2	feldspar	54.18	28.39	0.32	0.02	10.41	5.47	0.48	0.08	99.34	47.4	2.7	49.9
94-5B fe8.3	feldspar	53.89	28.63	0.33	0.02	10.75	5.23	0.45	0.07	99.37	45.6	2.6	51.8
94-5B fe8.4	feldspar	58.41	25.39	0.35	0.02	7.14	6.76	0.97	0.09	99.12	59.6	5.6	34.8
94-5B fe8.5	feldspar	54.05	28.60	0.33	0.01	10.74	5.28	0.44	0.07	99.51	45.9	2.5	51.6
94-5B fe9.1	feldspar	60.74	24.17	0.24	0.01	5.41	7.41	1.44	0.09	99.50	65.3	8.3	26.3
94-5B fe9.2	feldspar	58.37	25.25	0.22	0.02	6.85	7.11	1.01	0.08	98.90	61.5	5.7	32.8
94-5B fe9.4	feldspar	59.52	25.01	0.22	0.00	6.59	7.18	1.09	0.11	99.71	62.2	6.2	31.6
94-5B fe9.5	feldspar	59.59	24.77	0.20	0.02	6.33	6.96	1.21	0.11	99.19	61.8	7.1	31.1
94-5B fe9.6	feldspar	59.45	25.07	0.26	0.01	6.46	7.14	1.13	0.14	99.66	62.3	6.5	31.2

Appendix C: Continued.

Sample	Mineral	SiO2	Al2O3	FeO*	MgO	CaO	Na2O	K2O	BaO	Total	Ab	Or	An
94-5B fe9.7	feldspar	58.59	25.26	0.25	0.00	6.82	6.69	1.40	0.16	99.17	58.8	8.1	33.1
94-5B fe9.8	feldspar	58.43	24.95	0.26	0.00	6.62	7.07	1.05	0.11	98.49	61.9	6.1	32.0
94-5B fe9.9	feldspar	56.63	26.40	0.28	0.03	8.17	6.36	0.78	0.11	98.76	55.8	4.5	39.7
94-5B fe10.1	feldspar	53.22	29.68	0.27	0.01	11.43	4.98	0.31	0.12	100.02	43.3	1.8	54.9
94-5B fe10.2	feldspar	61.35	23.71	0.26	0.01	4.96	7.59	1.42	0.05	99.36	67.4	8.3	24.3
94-5B fe11.1	feldspar	55.53	28.07	0.25	0.01	9.76	5.82	0.58	0.10	100.12	50.2	3.3	46.5
94-5B fe11.2	feldspar	60.04	24.79	0.28	0.02	6.13	7.24	1.18	0.14	99.82	63.5	6.8	29.7
94-5B fe11.3	feldspar	60.04	24.58	0.25	0.02	6.11	7.28	1.22	0.08	99.57	63.5	7.0	29.5
94-5B fe11.4	feldspar	59.31	25.17	0.20	0.01	6.75	7.12	1.05	0.14	99.77	61.7	6.0	32.3
94-5B fe12.1	feldspar	56.09	27.66	0.28	0.02	9.63	5.77	0.63	0.07	100.17	50.1	3.6	46.2
94-5B fe12.2	feldspar	48.75	31.98	0.36	0.03	14.54	3.17	0.24	0.04	99.09	27.9	1.4	70.7
94-5B fe12.3	feldspar	58.61	25.15	0.28	0.02	6.60	7.13	1.07	0.12	98.99	62.1	6.2	31.8
94-5B fe14.3	feldspar	58.78	24.92	0.26	0.00	6.49	7.22	1.12	0.14	98.94	62.5	6.4	31.1
94-5B fe19.1	feldspar	47.60	33.19	0.26	0.02	16.07	2.63	0.13	0.02	99.93	22.7	0.8	76.5
94-5B fe19.2	feldspar	58.50	25.54	0.27	0.02	6.97	7.12	0.96	0.10	99.48	61.3	5.5	33.2
94-5B fe13.1	feldspar	65.84	19.22	0.11	0.00	0.27	3.42	11.72	0.08	100.65	30.3	68.4	1.3
94-5B fe13.2	feldspar	65.16	19.13	0.05	0.01	0.30	3.55	11.53	0.16	99.87	31.4	67.1	1.5
94-5B fe13.3	feldspar	64.14	19.24	0.07	0.00	0.28	3.42	11.60	0.18	98.93	30.5	68.1	1.4
94-5B fe13.4	feldspar	65.05	19.09	0.11	0.00	0.24	3.40	11.52	0.07	99.48	30.6	68.2	1.2
94-5B fe14.1	feldspar	63.58	19.31	0.06	0.01	0.30	3.51	11.16	0.80	98.72	31.8	66.7	1.5
94-5B fe14.2	feldspar	63.52	19.05	0.17	0.00	0.23	3.55	11.09	0.58	98.19	32.3	66.5	1.2
94-8 fe1.1	feldspar	61.68	23.31	0.16	0.00	4.80	7.96	0.96	0.03	98.90	70.8	5.6	23.6
94-8 fe1.2	feldspar	61.85	22.85	0.20	0.00	4.33	8.17	1.09	0.03	98.51	72.4	6.4	21.2
94-8 fe1.3	feldspar	61.61	23.07	0.16	0.00	4.54	8.14	1.03	0.04	98.58	71.9	6.0	22.2
94-8 fe1.4	feldspar	61.85	23.18	0.15	0.00	4.52	8.09	1.09	0.05	98.93	71.6	6.4	22.1
94-8 fe1.5	feldspar	61.28	23.25	0.17	0.01	4.78	7.99	1.08	0.02	98.58	70.4	6.3	23.3
94-8 fe1.6	feldspar	62.83	22.39	0.24	0.00	3.79	8.21	1.45	0.00	98.91	72.9	8.5	18.6
94-8 fe2.1	feldspar	53.63	28.30	0.28	0.02	10.49	5.11	0.45	0.06	98.34	45.6	2.6	51.7
94-8 fe2.2	feldspar	53.11	28.84	0.30	0.01	11.05	4.96	0.41	0.05	98.74	43.7	2.4	53.9
94-8 fe2.3	feldspar	51.52	30.13	0.25	0.01	12.49	4.10	0.28	0.03	98.80	36.6	1.7	61.7
94-8 fe2.4	feldspar	52.21	29.45	0.24	0.03	11.71	4.57	0.38	0.14	98.73	40.5	2.2	57.3
94-8 fe2.5	feldspar	54.76	27.66	0.24	0.00	9.57	5.56	0.57	0.11	98.48	49.5	3.4	47.1
94-8 fe2.6	feldspar	51.94	29.52	0.24	0.00	12.02	4.51	0.31	0.10	98.64	39.7	1.8	58.5
94-8 fe2.7	feldspar	60.08	23.97	0.20	0.01	5.67	7.23	1.37	0.14	98.67	64.2	8.0	27.8
94-8 fe3.1	feldspar	58.97	25.52	0.31	0.00	7.14	6.60	0.88	0.12	99.54	59.3	5.2	35.5
94-8 fe3.2	feldspar	53.16	29.33	0.22	0.01	11.50	4.16	0.85	0.04	99.27	37.5	5.1	57.4
94-8 fe3.3	feldspar	52.42	29.36	0.23	0.03	11.70	4.51	0.32	0.03	98.60	40.3	1.9	57.8
94-8 fe3.4	feldspar	58.13	25.48	0.25	0.02	7.30	6.55	0.86	0.10	98.70	58.7	5.1	36.2
94-8 fe3.5	feldspar	55.57	27.47	0.22	0.01	9.50	5.61	0.57	0.09	99.04	49.9	3.3	46.7
94-8 fe4.1	feldspar	60.73	23.82	0.24	0.01	5.45	7.32	1.35	0.09	99.00	65.2	7.9	26.8

Appendix C: Continued.

<u>Sample</u>	<u>Mineral</u>	<u>SiO2</u>	<u>Al2O3</u>	<u>FeO*</u>	<u>MgO</u>	<u>CaO</u>	<u>Na2O</u>	<u>K2O</u>	<u>BaO</u>	<u>Total</u>	<u>Ab</u>	<u>Or</u>	<u>An</u>
94-8 fe4.2	feldspar	53.03	29.31	0.29	0.00	11.70	4.66	0.30	0.04	99.34	41.2	1.8	57.1
94-8 fe4.3	feldspar	52.46	30.02	0.25	0.01	12.10	4.32	0.27	0.07	99.51	38.6	1.6	59.8
94-8 fe4.4	feldspar	58.02	25.93	0.24	0.00	7.73	6.54	0.79	0.10	99.35	57.7	4.6	37.7
94-8 fe4.5	feldspar	53.08	29.50	0.30	0.00	11.89	4.52	0.31	0.07	99.67	40.0	1.8	58.2
94-8 fe4.6	feldspar	53.50	29.10	0.28	0.00	11.36	4.79	0.37	0.08	99.48	42.4	2.1	55.5
94-8 fe4.7	feldspar	57.01	26.86	0.26	0.01	8.72	6.00	0.65	0.11	99.61	53.3	3.8	42.8
94-8 fe4.8	feldspar	60.59	24.57	0.22	0.01	6.03	7.11	1.10	0.14	99.78	63.6	6.5	29.9
94-8 fe5.1	feldspar	55.16	28.36	0.29	0.03	10.64	5.10	0.57	0.06	100.20	44.9	3.3	51.8
94-8 fe5.2	feldspar	54.90	28.37	0.28	0.03	10.35	5.35	0.45	0.03	99.76	47.1	2.6	50.4
94-8 fe5.3	feldspar	54.55	28.43	0.24	0.02	10.48	4.88	0.71	0.16	99.47	43.8	4.2	52.0
94-8 fe5.4	feldspar	56.34	27.40	0.27	0.04	9.27	5.96	0.53	0.05	99.86	52.1	3.1	44.8
94-8 fe6.1	feldspar	59.13	25.81	0.17	0.01	7.34	6.97	0.66	0.13	100.21	60.8	3.8	35.4
94-8 fe6.2	feldspar	60.85	24.53	0.17	0.01	6.11	7.29	0.94	0.16	100.05	64.6	5.5	29.9
94-8 fe6.3	feldspar	60.99	24.53	0.21	0.00	6.04	7.56	0.90	0.21	100.44	65.8	5.2	29.0
94-8 fe6.4	feldspar	60.66	24.36	0.17	0.00	5.85	7.28	1.00	0.17	99.51	65.2	5.9	28.9
94-8 fe6.5	feldspar	61.18	24.22	0.20	0.02	5.70	7.52	1.01	0.20	100.05	66.4	5.8	27.8
94-8 fe6.6	feldspar	60.95	24.21	0.17	0.00	5.66	7.47	0.97	0.19	99.62	66.5	5.7	27.8
94-8 fe6.7	feldspar	60.64	24.36	0.18	0.00	5.82	7.21	0.99	0.20	99.42	65.1	5.9	29.0
94-8 fe6.8	feldspar	60.36	24.50	0.22	0.00	6.05	7.34	1.04	0.15	99.67	64.5	6.0	29.4
94-8 fe6.9	feldspar	62.67	23.13	0.12	0.01	4.59	7.83	1.40	0.07	99.81	69.4	8.1	22.5
94-8 fe6.10	feldspar	62.81	22.89	0.15	0.00	4.41	7.52	1.57	0.06	99.44	68.4	9.4	22.2
94-8 fe7.1	feldspar	62.83	23.72	0.13	0.00	5.12	7.57	1.31	0.03	100.73	67.2	7.7	25.1
94-8 fe7.2	feldspar	63.64	23.19	0.14	0.00	4.51	7.88	1.52	0.02	100.91	69.3	8.8	21.9
94-8 fe7.3	feldspar	62.20	23.76	0.15	0.01	5.39	7.55	1.31	0.08	100.45	66.3	7.5	26.1
94-8 fe7.4	feldspar	62.83	23.62	0.15	0.02	5.11	7.59	1.37	0.06	100.74	67.1	8.0	25.0
94-8 fe8.1	feldspar	61.44	24.22	0.40	0.02	5.72	7.28	1.19	0.08	100.34	64.8	7.0	28.2
94-8 fe8.2	feldspar	58.10	26.50	0.19	0.01	8.22	6.35	0.71	0.24	100.32	55.9	4.1	40.0
94-8 fe8.3	feldspar	58.54	26.19	0.25	0.01	7.84	6.36	0.84	0.20	100.23	56.6	4.9	38.5
94-8 fe8.4	feldspar	60.55	24.99	0.24	0.01	6.58	6.93	1.03	0.18	100.51	61.7	6.0	32.3
94-8 fe8.5	feldspar	60.54	24.92	0.21	0.02	6.45	7.02	1.05	0.20	100.40	62.2	6.1	31.6
94-8 fe8.6	feldspar	61.30	24.15	0.26	0.02	5.74	7.43	1.27	0.08	100.25	64.9	7.3	27.7
94-8 fe8.7	feldspar	62.50	23.66	0.20	0.02	5.09	7.17	1.72	0.06	100.42	64.5	10.2	25.3
94-8 fe8.8	feldspar	60.61	25.01	0.25	0.02	6.48	6.98	0.97	0.12	100.42	62.3	5.7	32.0
94-8 fe8.9	feldspar	61.30	24.36	0.25	0.02	5.80	7.11	1.17	0.06	100.07	64.1	6.9	28.9
94-8 fe8.10	feldspar	61.33	24.24	0.25	0.00	5.65	7.16	1.22	0.23	100.08	64.6	7.2	28.2
94-8 fe8.11	feldspar	60.73	24.71	0.25	0.00	6.18	6.97	1.12	0.21	100.18	62.6	6.6	30.7
94-8 fe8.12	feldspar	60.72	24.88	0.26	0.03	6.29	7.02	1.06	0.18	100.44	62.7	6.2	31.0
94-8 fe8.13	feldspar	60.58	24.93	0.25	0.00	6.28	7.12	1.09	0.25	100.50	63.0	6.3	30.7
94-8 fe18.1	feldspar	54.95	28.71	0.22	0.03	10.62	5.05	0.43	0.06	100.06	45.1	2.5	52.4
94-8 fe18.2	feldspar	60.62	24.41	0.24	0.00	5.78	7.04	1.24	0.12	99.44	63.7	7.4	28.9

Appendix C: Continued.

<u>Sample</u>	<u>Mineral</u>	<u>SiO2</u>	<u>Al2O3</u>	<u>FeO*</u>	<u>MgO</u>	<u>CaO</u>	<u>Na2O</u>	<u>K2O</u>	<u>BaO</u>	<u>Total</u>	<u>Ab</u>	<u>Or</u>	<u>An</u>
94-8 fe18.3	feldspar	60.62	24.58	0.31	0.00	6.03	7.06	1.23	0.16	100.00	63.0	7.2	29.8
94-8 fe18.4	feldspar	61.35	24.26	0.29	0.01	5.60	7.20	1.34	0.13	100.17	64.4	7.9	27.7
94-8 fe18.5	feldspar	60.03	24.86	0.25	0.02	6.36	6.94	1.12	0.12	99.70	62.0	6.6	31.4
94-8 fe18.6	feldspar	60.39	25.00	0.29	0.01	6.30	7.19	1.11	0.09	100.37	63.1	6.4	30.5
94-8 fe17.1	feldspar	60.15	25.31	0.27	0.01	6.77	6.89	1.02	0.14	100.57	60.9	6.0	33.1
94-8 fe17.2	feldspar	61.52	24.40	0.22	0.00	5.56	7.29	1.37	0.16	100.52	64.7	8.0	27.3
94-8 fe17.3	feldspar	60.67	25.20	0.26	0.00	6.46	6.91	1.16	0.13	100.78	61.4	6.8	31.8
94-8 fe9.1	feldspar	65.30	18.81	0.10	0.00	0.23	3.56	11.45	0.18	99.63	31.7	67.2	1.1
94-8 fe9.2	feldspar	65.57	19.01	0.07	0.01	0.23	3.65	11.43	0.05	100.02	32.3	66.6	1.1
94-8 fe9.3	feldspar	65.75	18.87	0.06	0.00	0.18	3.52	11.55	0.07	99.99	31.4	67.8	0.9
94-8 fe9.4	feldspar	65.70	18.86	0.08	0.00	0.22	3.54	11.54	0.04	99.99	31.4	67.5	1.1
94-8 fe10.1	feldspar	65.49	19.08	0.08	0.01	0.25	3.46	11.42	0.14	99.93	31.2	67.6	1.3
94-8 fe10.2	feldspar	65.58	18.91	0.05	0.00	0.24	3.34	11.75	0.12	100.00	29.8	69.0	1.2
94-8 fe10.3	feldspar	65.37	18.81	0.11	0.00	0.21	3.50	11.67	0.17	99.83	31.0	68.0	1.0
94-8 fe10.4	feldspar	65.20	18.97	0.07	0.00	0.20	3.41	11.79	0.34	99.99	30.2	68.8	1.0
94-8 fe10.5	feldspar	65.62	19.05	0.10	0.00	0.22	3.59	11.30	0.35	100.24	32.2	66.7	1.1
94-8 fe11.1	feldspar	65.63	19.03	0.10	0.02	0.18	3.45	11.62	0.21	100.24	30.8	68.3	0.9
94-8 fe11.2	feldspar	65.57	19.01	0.08	0.00	0.17	3.50	11.49	0.14	99.96	31.4	67.7	0.9
94-8 fe11.3	feldspar	65.54	19.03	0.10	0.00	0.19	3.47	11.48	0.26	100.08	31.1	67.9	1.0
94-8 fe11.4	feldspar	65.16	19.03	0.08	0.00	0.18	3.49	11.55	0.19	99.68	31.2	67.9	0.9
94-8 fe12.1	feldspar	64.30	18.69	0.08	0.03	0.31	3.36	11.24	0.55	98.54	30.7	67.7	1.6
94-8 fe12.2	feldspar	65.34	18.91	0.09	0.00	0.27	3.31	11.41	0.18	99.52	30.2	68.4	1.3
94-8 fe12.3	feldspar	65.26	18.84	0.09	0.00	0.28	3.36	11.43	0.21	99.47	30.4	68.2	1.4
94-8 fe14.1	feldspar	66.08	19.10	0.07	0.00	0.22	3.97	10.82	0.35	100.61	35.4	63.5	1.1
94-8 fe14.2	feldspar	66.16	19.03	0.09	0.00	0.25	3.39	11.44	0.09	100.45	30.6	68.1	1.2
94-8 fe14.3	feldspar	66.26	19.04	0.07	0.00	0.20	3.53	11.57	0.09	100.77	31.4	67.6	1.0
94-8 fe14.4	feldspar	66.28	18.99	0.05	0.00	0.22	3.44	11.68	0.08	100.74	30.6	68.3	1.1
94-8 fe14.5	feldspar	66.53	19.14	0.09	0.01	0.22	3.73	11.12	0.17	101.01	33.4	65.5	1.1
94-8 fe16.1	feldspar	64.61	19.03	0.13	0.00	0.27	3.48	11.12	0.67	99.31	31.8	66.9	1.3
94-8 fe16.2	feldspar	64.90	18.81	0.05	0.00	0.23	3.59	11.35	0.23	99.15	32.1	66.8	1.1
94-8 fe16.3	feldspar	65.54	18.89	0.11	0.00	0.22	3.49	11.32	0.16	99.73	31.6	67.3	1.1
94-8 fe16.4	feldspar	65.79	18.86	0.11	0.00	0.22	3.49	11.53	0.27	100.26	31.2	67.8	1.1
94-8 fe16.5	feldspar	65.58	18.94	0.10	0.00	0.18	3.53	11.43	0.13	99.89	31.7	67.4	0.9
94-13a fe1.1	feldspar	63.03	23.18	0.17	0.01	4.14	8.64	1.13	0.00	100.29	74.0	6.4	19.6
94-13a fe1.2	feldspar	63.32	23.02	0.14	0.02	4.09	8.63	1.14	0.00	100.36	74.1	6.4	19.4
94-13a fe1.3	feldspar	62.55	23.65	0.16	0.01	4.61	8.39	0.99	0.00	100.36	72.4	5.6	22.0
94-13a fe1.4	feldspar	62.41	23.55	0.09	0.00	4.42	8.58	1.01	0.00	100.06	73.4	5.7	20.9
94-13a fe1.5	feldspar	62.75	23.07	0.15	0.01	4.04	8.75	1.09	0.00	99.87	74.8	6.1	19.1
94-13a fe2.1	feldspar	63.46	23.03	0.12	0.02	4.02	8.68	1.13	0.00	100.46	74.5	6.4	19.1
94-13a fe2.2	feldspar	62.65	23.40	0.18	0.00	4.31	8.55	1.04	0.00	100.15	73.6	5.9	20.5

Appendix C: Continued.

<u>Sample</u>	<u>Mineral</u>	<u>SiO2</u>	<u>Al2O3</u>	<u>FeO*</u>	<u>MgO</u>	<u>CaO</u>	<u>Na2O</u>	<u>K2O</u>	<u>BaO</u>	<u>Total</u>	<u>Ab</u>	<u>Or</u>	<u>An</u>
94-13a fe2.3	feldspar	62.28	23.60	0.21	0.01	4.58	8.53	0.98	0.01	100.19	72.9	5.5	21.6
94-13a fe2.4	feldspar	61.91	23.97	0.18	0.01	4.85	8.51	0.98	0.06	100.47	71.9	5.4	22.6
94-13a fe2.5	feldspar	61.54	23.79	0.16	0.00	4.81	8.36	0.95	0.08	99.70	71.8	5.4	22.8
94-13a fe2.6	feldspar	61.59	23.93	0.15	0.00	5.01	8.35	0.87	0.03	99.94	71.4	4.9	23.7
94-13a fe3.1	feldspar	63.08	23.44	0.17	0.01	4.41	8.60	1.21	0.02	100.94	72.7	6.7	20.6
94-13a fe3.2	feldspar	62.74	23.67	0.12	0.00	4.67	8.24	1.12	0.01	100.58	71.3	6.4	22.3
94-13a fe3.3	feldspar	63.30	23.12	0.09	0.00	4.21	8.57	1.16	0.00	100.45	73.5	6.6	20.0
94-13a fe3.4	feldspar	62.47	23.35	0.15	0.03	4.40	8.53	1.18	0.00	100.10	72.6	6.6	20.7
94-13a fe3.5	feldspar	63.00	22.97	0.18	0.00	3.97	8.52	1.26	0.00	99.90	73.8	7.2	19.0
94-13a fe3.6	feldspar	62.30	23.50	0.12	0.01	4.36	8.36	1.18	0.00	99.83	72.4	6.7	20.8
94-13a fe4.1	feldspar	61.40	23.53	0.09	0.02	4.70	8.20	1.23	0.00	99.18	70.7	7.0	22.4
94-13a fe4.2	feldspar	61.37	24.32	0.11	0.01	5.51	8.00	0.92	0.02	100.26	68.7	5.2	26.1
94-13a fe4.3	feldspar	62.29	23.25	0.14	0.00	4.47	8.30	1.18	0.03	99.66	71.9	6.7	21.4
94-13a fe5.1	feldspar	62.40	23.59	0.22	0.01	4.74	8.22	1.14	0.02	100.35	70.9	6.5	22.6
94-13a fe5.2	feldspar	61.45	23.50	0.15	0.02	4.67	8.32	1.08	0.00	99.20	71.6	6.1	22.2
94-13a fe5.3	feldspar	62.35	23.64	0.18	0.00	4.54	8.26	1.06	0.05	100.07	72.0	6.1	21.9
94-13a fe6.3	feldspar	57.59	26.62	0.25	0.00	8.10	6.54	0.69	0.07	99.87	57.0	4.0	39.0
94-13a fe6.4	feldspar	60.46	24.02	0.23	0.02	5.55	7.21	1.59	0.12	99.19	63.7	9.2	27.1
94-13a fe7.1	feldspar	61.99	23.58	0.13	0.00	4.39	8.45	1.14	0.00	99.68	72.7	6.4	20.9
94-13a fe7.2	feldspar	62.80	22.92	0.16	0.00	3.83	8.61	1.20	0.00	99.52	74.8	6.9	18.4
94-13a fe8.1	feldspar	51.49	30.46	0.26	0.02	12.79	4.21	0.25	0.05	99.51	36.8	1.4	61.8
94-13a fe8.2	feldspar	54.32	28.43	0.19	0.00	10.22	5.32	0.47	0.04	98.98	47.2	2.7	50.1
94-13a fe17.1	feldspar	63.28	22.69	0.12	0.00	3.62	8.55	1.36	0.04	99.66	74.7	7.8	17.5
94-13a fe17.2	feldspar	63.98	22.88	0.12	0.00	3.94	8.56	1.26	0.03	100.77	74.0	7.2	18.8
94-13a fe17.3	feldspar	63.96	22.34	0.17	0.00	3.37	8.59	1.56	0.04	100.04	74.8	9.0	16.2
94-13a fe17.4	feldspar	62.92	23.16	0.16	0.00	4.19	8.46	1.19	0.05	100.12	73.2	6.8	20.0
94-13a fe18.1	feldspar	58.42	25.92	0.21	0.00	7.31	6.90	0.86	0.16	99.80	60.0	4.9	35.1
94-13a fe18.2	feldspar	53.92	29.32	0.30	0.02	11.27	5.01	0.38	0.08	100.31	43.6	2.2	54.2
94-13a fe18.3	feldspar	56.07	28.29	0.19	0.01	10.00	5.94	0.50	0.11	101.11	50.4	2.8	46.8
94-13a fe18.6	feldspar	60.91	24.69	0.16	0.02	5.87	7.37	1.19	0.10	100.32	64.7	6.9	28.5
94-13a fe18.7	feldspar	60.96	24.52	0.19	0.01	5.81	7.32	1.22	0.16	100.19	64.6	7.1	28.3
94-13a fe6.1	feldspar	65.40	19.07	0.07	0.00	0.18	3.61	11.45	0.09	99.86	32.1	67.0	0.9
94-13a fe6.2	feldspar	64.86	19.27	0.06	0.00	0.20	3.79	11.12	0.09	99.39	33.8	65.2	1.0
94-13a fe9.1	feldspar	64.89	19.02	0.07	0.01	0.18	3.79	11.38	0.06	99.41	33.3	65.8	0.9
94-13a fe9.2	feldspar	64.73	19.21	0.09	0.00	0.24	3.66	11.24	0.34	99.52	32.7	66.1	1.2
94-13a fe9.3	feldspar	63.89	19.27	0.09	0.00	0.23	3.64	11.04	0.53	98.68	33.0	65.9	1.1
94-13a fe10.1	feldspar	65.20	19.25	0.08	0.00	0.22	4.02	10.91	0.10	99.78	35.5	63.4	1.1
94-13a fe10.2	feldspar	64.88	19.22	0.07	0.01	0.18	3.73	11.57	0.08	99.73	32.6	66.5	0.9
94-13a fe10.3	feldspar	65.02	19.14	0.11	0.02	0.16	3.63	11.36	0.09	99.53	32.4	66.7	0.8
94-13a fe10.4	feldspar	64.77	19.24	0.06	0.00	0.19	3.70	11.62	0.09	99.67	32.3	66.8	0.9

Appendix C: Continued.

<u>Sample</u>	<u>Mineral</u>	<u>SiO2</u>	<u>Al2O3</u>	<u>FeO*</u>	<u>MgO</u>	<u>CaO</u>	<u>Na2O</u>	<u>K2O</u>	<u>BaO</u>	<u>Total</u>	<u>Ab</u>	<u>Or</u>	<u>An</u>
94-13a fe10.5	feldspar	65.02	19.20	0.08	0.00	0.18	3.72	11.65	0.10	99.96	32.4	66.7	0.9
94-13a fe10.6	feldspar	65.55	19.07	0.10	0.00	0.19	3.87	10.93	0.08	99.80	34.7	64.4	0.9
94-13a fe11.1	feldspar	64.23	19.23	0.08	0.00	0.21	3.68	11.36	0.31	99.10	32.6	66.3	1.0
94-13a fe11.2	feldspar	64.72	19.14	0.10	0.02	0.17	3.66	11.55	0.16	99.51	32.2	66.9	0.8
94-13a fe11.3	feldspar	64.89	19.09	0.09	0.00	0.19	3.69	11.52	0.08	99.55	32.5	66.6	0.9
94-13a fe11.4	feldspar	65.21	19.14	0.12	0.00	0.21	3.70	11.33	0.01	99.71	32.8	66.1	1.0
94-13a fe12.1	feldspar	64.46	19.06	0.09	0.00	0.20	3.61	11.50	0.09	99.00	32.0	67.0	1.0
94-13a fe12.2	feldspar	64.93	19.29	0.11	0.02	0.18	3.33	11.57	0.03	99.45	30.1	69.0	0.9
94-13a fe13.1	feldspar	64.87	19.33	0.10	0.00	0.20	3.71	11.36	0.10	99.68	32.8	66.2	1.0
94-13a fe13.2	feldspar	65.77	19.30	0.08	0.02	0.21	3.67	11.44	0.14	100.62	32.4	66.6	1.0
94-13a fe13.3	feldspar	65.44	19.13	0.02	0.01	0.20	3.72	11.30	0.03	99.86	33.0	66.0	1.0
94-13a fe13.4	feldspar	64.29	19.42	0.08	0.00	0.21	3.80	11.54	0.02	99.36	33.0	66.0	1.0
94-13a fe14.1	feldspar	66.23	19.16	0.06	0.00	0.21	3.55	11.56	0.11	100.88	31.5	67.5	1.0
94-13a fe14.2	feldspar	65.13	19.31	0.11	0.00	0.21	3.58	11.64	0.13	100.12	31.5	67.4	1.0
94-13a fe14.3	feldspar	65.55	19.21	0.11	0.00	0.21	3.64	11.77	0.08	100.58	31.7	67.3	1.0
94-13a fe14.4	feldspar	65.64	19.25	0.10	0.00	0.18	4.04	10.87	0.13	100.22	35.8	63.3	0.9
94-13a fe15.1	feldspar	65.32	19.16	0.03	0.00	0.15	3.58	11.48	0.08	99.81	31.9	67.3	0.7
94-13a fe15.2	feldspar	65.25	19.22	0.04	0.00	0.18	3.61	11.55	0.05	99.92	31.9	67.2	0.9
94-13a fe16.1	feldspar	64.13	19.16	0.06	0.03	0.19	3.46	11.41	0.42	98.84	31.2	67.9	0.9
94-13a fe16.2	feldspar	65.52	19.22	0.10	0.02	0.20	3.98	10.73	0.26	100.03	35.7	63.3	1.0
94-13a fe18.4	feldspar	65.40	19.34	0.08	0.00	0.19	3.91	11.23	0.06	100.22	34.3	64.8	0.9
94-13a fe18.5	feldspar	65.92	19.07	0.09	0.01	0.15	3.44	11.76	0.07	100.51	30.5	68.7	0.8
94-13a fe18.8	feldspar	64.98	19.26	0.07	0.01	0.20	3.62	11.63	0.18	99.94	31.8	67.2	1.0
94-15 fe1.2	feldspar	63.13	23.31	0.17	0.00	4.20	8.31	1.09	0.00	100.21	73.2	6.3	20.5
94-15 fe1.4	feldspar	63.00	23.32	0.15	0.00	4.20	8.48	1.11	0.00	100.26	73.6	6.3	20.1
94-15 fe2.1	feldspar	61.50	23.03	0.13	0.01	3.94	8.63	1.08	0.00	98.31	75.0	6.1	18.9
94-15 fe2.2	feldspar	63.75	22.86	0.15	0.01	3.80	8.58	1.26	0.00	100.40	74.6	7.2	18.2
94-15 fe2.3	feldspar	61.73	23.06	0.11	0.00	4.03	8.68	1.16	0.01	98.77	74.4	6.5	19.1
94-15 fe3.1	feldspar	61.43	23.09	0.13	0.01	3.94	8.46	1.11	0.02	98.20	74.4	6.4	19.2
94-15 fe3.3	feldspar	61.96	22.68	0.13	0.01	3.61	8.59	1.25	0.00	98.23	75.3	7.2	17.5
94-15 fe4.3	feldspar	62.88	23.00	0.14	0.00	4.11	8.39	1.05	0.02	99.59	73.9	6.1	20.0
94-15 fe5.2	feldspar	62.58	22.41	0.17	0.00	3.75	8.54	1.17	0.00	98.63	75.0	6.8	18.2
94-15 fe5.3	feldspar	62.82	22.75	0.13	0.03	3.86	8.48	1.17	0.00	99.24	74.5	6.8	18.7
94-15 fe6.1	feldspar	60.93	23.15	0.13	0.00	4.35	8.40	1.21	0.01	98.18	72.4	6.9	20.7
94-15 fe6.2	feldspar	60.73	23.28	0.18	0.00	4.35	8.30	1.12	0.03	98.00	72.5	6.4	21.0
94-15 fe6.3	feldspar	62.95	23.22	0.15	0.01	4.26	8.44	1.23	0.00	100.26	72.7	7.0	20.3
94-15 fe6.4	feldspar	61.01	23.32	0.15	0.00	4.30	8.45	1.19	0.01	98.43	72.8	6.8	20.4
94-15 fe6.5	feldspar	61.03	23.48	0.15	0.02	4.41	8.42	1.13	0.04	98.69	72.6	6.4	21.0
94-15 fe17.1	feldspar	62.77	23.58	0.17	0.00	4.65	8.18	0.92	0.02	100.29	72.0	5.3	22.6
94-15 fe17.2	feldspar	62.85	23.46	0.15	0.01	4.57	8.36	0.93	0.03	100.36	72.7	5.3	22.0

Appendix C: Continued.

<u>Sample</u>	<u>Mineral</u>	<u>SiO2</u>	<u>Al2O3</u>	<u>FeO*</u>	<u>MgO</u>	<u>CaO</u>	<u>Na2O</u>	<u>K2O</u>	<u>BaO</u>	<u>Total</u>	<u>Ab</u>	<u>Or</u>	<u>An</u>
94-15 fe17.3	feldspar	62.77	23.55	0.15	0.02	4.52	8.24	0.98	0.03	100.26	72.4	5.7	21.9
94-15 fe17.4	feldspar	60.96	23.24	0.15	0.00	4.28	8.36	1.06	0.01	98.05	73.2	6.1	20.7
94-15 fe18.1	feldspar	55.11	28.17	0.25	0.02	10.24	5.55	0.51	0.11	99.95	48.1	2.9	49.0
94-15 fe18.2	feldspar	52.04	29.56	0.31	0.01	11.71	4.75	0.38	0.07	98.82	41.4	2.2	56.4
94-15 fe18.3	feldspar	60.37	24.90	0.26	0.01	6.34	7.12	1.08	0.11	100.20	62.8	6.2	30.9
94-15 fe7.1	feldspar	63.70	19.00	0.04	0.00	0.15	3.59	11.41	0.02	99.58	31.5	67.4	1.1
94-15 fe7.2	feldspar	65.95	19.24	0.08	0.00	0.17	3.66	11.53	0.08	100.17	31.8	67.1	1.1
94-15 fe7.3	feldspar	64.35	19.15	0.02	0.00	0.18	3.50	11.56	0.15	99.72	32.2	67.0	0.9
94-15 fe7.4	feldspar	64.49	19.24	0.07	0.00	0.21	3.53	11.62	0.14	98.58	32.0	67.2	0.8
94-15 fe7.5	feldspar	64.28	19.26	0.12	0.00	0.21	3.61	11.57	0.14	98.69	31.8	67.4	0.9
94-15 fe8.3	feldspar	64.16	19.25	0.08	0.01	0.20	3.58	11.60	0.20	100.54	31.9	67.0	1.1
94-15 fe9.1	feldspar	64.78	19.16	0.10	0.00	0.20	3.57	11.65	0.19	98.86	31.9	67.3	0.8
94-15 fe9.3	feldspar	65.36	19.49	0.04	0.00	0.21	3.77	11.36	0.19	99.23	32.1	67.1	0.8
94-15 fe10.1	feldspar	65.40	19.15	0.06	0.01	0.17	3.66	11.21	0.14	100.11	32.2	66.9	0.8
94-15 fe10.3	feldspar	65.15	19.23	0.06	0.01	0.20	3.68	11.50	0.17	100.24	31.2	67.9	0.9
94-15 fe11.1	feldspar	63.77	19.21	0.07	0.00	0.16	3.57	11.54	0.04	100.19	31.3	67.7	1.0
94-15 fe11.2	feldspar	63.78	19.07	0.05	0.00	0.17	3.91	11.34	0.01	99.83	31.9	67.1	1.0
94-15 fe11.3	feldspar	65.61	19.05	0.07	0.00	0.17	3.73	11.47	0.00	98.16	31.6	67.4	1.0
94-15 fe11.4	feldspar	63.97	19.29	0.06	0.00	0.15	3.58	11.67	0.03	98.37	31.4	67.6	1.0
94-15 fe11.5	feldspar	64.17	19.17	0.07	0.00	0.14	3.65	11.77	0.00	100.85	33.2	65.8	1.0
94-15 fe12.2	feldspar	65.71	19.16	0.06	0.01	0.18	3.65	11.34	0.09	99.95	32.9	66.3	0.8
94-15 fe13.4	feldspar	65.40	19.13	0.09	0.00	0.17	3.63	11.50	0.06	99.48	32.4	66.6	1.0
94-15 fe14.5	feldspar	65.60	19.11	0.10	0.02	0.15	3.68	11.45	0.07	99.86	31.7	67.5	0.8
94-15 fe14.6	feldspar	65.27	23.58	0.17	0.00	4.65	8.18	0.92	0.02	100.29	34.1	65.1	0.8
94-15 fe15.1	feldspar	63.67	23.46	0.15	0.01	4.57	8.36	0.93	0.03	100.36	32.8	66.4	0.8
94-15 fe15.3	feldspar	63.59	23.55	0.15	0.02	4.52	8.24	0.98	0.03	100.26	31.6	67.7	0.7
94-15 fe15.4	feldspar	66.04	23.24	0.15	0.00	4.28	8.36	1.06	0.01	98.05	31.8	67.5	0.7
94-15 fe16.1	feldspar	65.46	28.17	0.25	0.02	10.24	5.55	0.51	0.11	99.95	32.6	66.5	0.9
94-15 fe16.3	feldspar	64.90	29.56	0.31	0.01	11.71	4.75	0.38	0.07	98.82	32.2	67.0	0.8
94-15 fe16.5	feldspar	65.29	24.90	0.26	0.01	6.34	7.12	1.08	0.11	100.20	32.6	66.7	0.7
92-22 fe2.5	feldspar	62.34	23.04	0.17	0.00	4.30	8.14	1.41	0.00	99.41	71.1	8.1	20.8
92-22 fe2.6	feldspar	61.37	22.88	0.08	0.01	4.35	8.02	1.36	0.02	98.08	70.9	7.9	21.3
92-22 fe4.1	feldspar	59.06	25.13	0.28	0.00	6.54	6.96	0.94	0.12	99.04	62.2	5.5	32.3
92-22 fe4.2	feldspar	59.27	25.20	0.25	0.02	6.87	6.97	0.91	0.13	99.62	61.3	5.2	33.4
92-22 fe4.3	feldspar	62.05	23.26	0.18	0.00	4.41	8.21	1.35	0.01	99.47	71.2	7.7	21.1
92-22 fe4.4	feldspar	61.67	23.49	0.21	0.01	4.78	8.00	1.18	0.05	99.38	70.0	6.8	23.1
92-22 fe4.5	feldspar	62.75	22.80	0.15	0.01	4.06	8.46	1.31	0.00	99.55	73.1	7.5	19.4
92-22 fe4.6	feldspar	62.08	23.21	0.21	0.02	4.29	8.30	1.27	0.01	99.40	72.1	7.3	20.6
92-22 fe4.7	feldspar	61.94	23.36	0.16	0.00	4.74	8.25	1.22	0.00	99.68	70.7	6.9	22.4
92-22 fe5.2	feldspar	54.89	27.12	0.25	0.00	9.14	6.01	0.57	0.10	98.08	52.5	3.3	44.2

Appendix C: Continued.

<u>Sample</u>	<u>Mineral</u>	<u>SiO2</u>	<u>Al2O3</u>	<u>FeO*</u>	<u>MgO</u>	<u>CaO</u>	<u>Na2O</u>	<u>K2O</u>	<u>BaO</u>	<u>Total</u>	<u>Ab</u>	<u>Or</u>	<u>An</u>
92-22 fe5.4	feldspar	54.90	27.24	0.17	0.00	9.12	5.88	0.59	0.10	98.01	52.0	3.4	44.6
92-22 fe6.1	feldspar	57.80	25.00	0.20	0.00	6.70	7.08	1.04	0.20	98.02	61.7	6.0	32.3
92-22 fe6.3	feldspar	58.11	24.99	0.24	0.01	6.69	6.93	0.98	0.20	98.15	61.5	5.7	32.8
92-22 fe9.1	feldspar	58.48	25.38	0.21	0.02	6.95	7.11	0.87	0.07	99.09	61.7	4.9	33.3
92-22 fe9.2	feldspar	59.99	24.54	0.22	0.02	5.78	7.41	1.13	0.11	99.19	65.3	6.6	28.1
92-22 fe9.6	feldspar	60.15	24.46	0.27	0.00	5.81	7.47	1.16	0.08	99.40	65.3	6.7	28.1
92-22 fe10.4	feldspar	59.11	26.02	0.23	0.02	7.65	6.68	0.64	0.07	100.41	58.9	3.7	37.3
92-22 fe16.1	feldspar	58.21	26.01	0.33	0.02	7.66	6.72	0.79	0.12	99.86	58.6	4.6	36.9
92-22 fe16.2	feldspar	57.64	25.39	0.21	0.01	6.92	6.84	0.90	0.20	98.10	60.8	5.3	34.0
92-22 fe1.1	feldspar	63.37	19.40	0.13	0.00	0.25	3.60	10.73	1.37	98.84	33.3	65.4	1.3
92-22 fe1.2	feldspar	64.04	19.49	0.13	0.00	0.45	3.54	10.70	1.24	99.59	32.7	65.0	2.3
92-22 fe1.3	feldspar	64.40	19.08	0.06	0.00	0.24	3.49	11.30	0.30	98.88	31.6	67.2	1.2
92-22 fe1.4	feldspar	65.16	19.10	0.12	0.00	0.28	3.48	11.14	0.26	99.56	31.7	66.9	1.4
92-22 fe1.5	feldspar	65.03	19.04	0.10	0.01	0.28	3.59	11.10	0.33	99.48	32.5	66.1	1.4
92-22 fe1.6	feldspar	63.49	19.55	0.08	0.01	0.41	3.94	10.19	1.20	98.88	36.3	61.7	2.1
92-22 fe2.1	feldspar	64.54	19.11	0.07	0.00	0.29	3.89	10.53	0.14	98.56	35.4	63.1	1.4
92-22 fe2.2	feldspar	64.41	18.92	0.08	0.00	0.17	3.71	11.13	0.13	98.55	33.4	65.8	0.8
92-22 fe2.3	feldspar	64.35	19.09	0.06	0.00	0.30	4.05	10.60	0.09	98.54	36.2	62.3	1.5
92-22 fe2.4	feldspar	64.48	18.95	0.05	0.00	0.29	4.04	10.66	0.15	98.62	36.1	62.5	1.4
92-22 fe3.1	feldspar	63.92	19.12	0.12	0.00	0.31	4.11	10.71	0.13	98.41	36.3	62.2	1.5
92-22 fe3.2	feldspar	63.76	19.27	0.09	0.00	0.23	3.71	11.41	0.14	98.61	32.7	66.2	1.1
92-22 fe3.3	feldspar	63.46	19.18	0.06	0.00	0.19	3.66	11.42	0.12	98.10	32.4	66.6	0.9
92-22 fe3.4	feldspar	64.03	19.43	0.04	0.00	0.22	3.55	11.31	0.14	98.71	31.9	67.0	1.1
92-22 fe3.5	feldspar	64.29	19.04	0.09	0.00	0.23	3.89	11.06	0.11	98.70	34.4	64.4	1.1
92-22 fe7.2	feldspar	64.33	19.13	0.08	0.00	0.26	3.93	10.53	0.56	98.82	35.7	63.0	1.3
92-22 fe7.3	feldspar	63.75	19.29	0.14	0.01	0.32	3.87	10.66	0.58	98.61	35.0	63.4	1.6
92-22 fe7.4	feldspar	63.42	19.17	0.05	0.00	0.31	4.02	10.37	0.66	98.02	36.5	61.9	1.6
92-22 fe8.1	feldspar	63.94	18.96	0.09	0.00	0.22	3.56	11.40	0.34	98.51	31.8	67.1	1.1
92-22 fe8.2	feldspar	63.97	19.19	0.05	0.01	0.24	3.73	11.27	0.48	98.95	33.1	65.7	1.2
92-22 fe8.3	feldspar	64.27	19.20	0.14	0.00	0.29	3.84	10.65	0.60	98.99	34.9	63.6	1.5
92-22 fe9.3	feldspar	64.67	19.16	0.04	0.01	0.24	3.79	11.13	0.20	99.23	33.7	65.1	1.2
92-22 fe9.4	feldspar	64.65	19.10	0.06	0.01	0.23	3.91	11.18	0.14	99.28	34.3	64.6	1.1
92-22 fe9.5	feldspar	63.95	19.18	0.14	0.00	0.26	4.07	10.79	0.30	98.70	35.9	62.8	1.3
92-22 fe10.3	feldspar	65.40	19.28	0.12	0.00	0.30	3.92	10.43	0.53	100.00	35.8	62.7	1.5
92-22 fe11.1	feldspar	63.93	18.92	0.09	0.00	0.20	3.68	11.54	0.16	98.51	32.3	66.7	1.0
92-22 fe11.2	feldspar	63.77	18.93	0.04	0.01	0.19	3.66	11.27	0.09	97.96	32.8	66.3	0.9
92-22 fe11.3	feldspar	65.66	18.98	0.08	0.00	0.22	3.76	11.02	0.12	99.85	33.8	65.1	1.1
92-22 fe11.4	feldspar	65.38	18.90	0.05	0.00	0.16	3.88	10.51	0.83	99.70	35.7	63.5	0.8
92-22 fe11.5	feldspar	64.96	18.99	0.10	0.00	0.23	4.03	10.34	0.82	99.46	36.8	62.1	1.1
92-22 fe18.1	feldspar	65.60	19.10	0.09	0.00	0.21	4.18	10.64	0.05	99.88	37.0	62.0	1.0

Appendix C: Continued.

<u>Sample</u>	<u>Mineral</u>	<u>SiO2</u>	<u>Al2O3</u>	<u>FeO*</u>	<u>MgO</u>	<u>CaO</u>	<u>Na2O</u>	<u>K2O</u>	<u>BaO</u>	<u>Total</u>	<u>Ab</u>	<u>Or</u>	<u>An</u>
92-22 fe18.2	feldspar	65.44	19.08	0.08	0.01	0.29	4.12	10.51	0.05	99.57	36.8	61.8	1.4
94-30 fe2.1	feldspar	54.30	28.42	0.30	0.05	10.55	5.12	0.49	0.12	99.34	45.4	2.9	51.7
94-30 fe2.2	feldspar	54.29	29.53	0.37	0.04	11.82	4.63	0.39	0.06	101.12	40.5	2.2	57.2
94-30 fe2.3	feldspar	52.85	29.08	0.39	0.01	11.31	4.86	0.39	0.07	98.96	42.8	2.2	55.0
94-30 fe2.4	feldspar	58.84	24.64	0.32	0.03	6.25	6.79	1.31	0.20	98.38	61.1	7.8	31.1
94-30 fe2.5	feldspar	55.59	28.44	0.28	0.01	10.74	5.06	0.50	0.11	100.73	44.7	2.9	52.4
94-30 fe2.6	feldspar	56.60	26.63	0.34	0.03	8.58	6.06	0.76	0.17	99.16	53.6	4.4	42.0
94-30 fe2.7	feldspar	58.65	26.23	0.31	0.02	8.18	6.18	0.84	0.17	100.58	54.9	4.9	40.2
94-30 fe2.8	feldspar	58.86	24.78	0.35	0.01	6.50	6.90	1.28	0.18	98.87	60.9	7.5	31.7
94-30 fe3.1	feldspar	61.37	25.12	0.32	0.03	6.63	6.87	1.25	0.23	101.83	60.5	7.3	32.2
94-30 fe3.2	feldspar	55.58	28.90	0.27	0.03	10.99	5.01	0.46	0.11	101.35	44.0	2.7	53.3
94-30 fe3.3	feldspar	53.04	29.76	0.37	0.04	11.91	4.69	0.36	0.08	100.25	40.8	2.1	57.2
94-30 fe3.4	feldspar	57.37	27.70	0.34	0.02	9.63	5.68	0.63	0.12	101.48	49.7	3.6	46.6
94-30 fe3.5	feldspar	55.23	28.21	0.33	0.02	10.17	5.42	0.58	0.10	100.05	47.4	3.3	49.2
94-30 fe3.6	feldspar	58.36	25.77	0.25	0.03	7.66	6.36	1.00	0.16	99.59	56.5	5.9	37.6
94-30 fe3.7	feldspar	57.63	26.69	0.27	0.01	8.30	6.21	0.76	0.17	100.05	55.0	4.4	40.6
94-30 fe3.8	feldspar	56.62	27.39	0.30	0.04	9.16	5.91	0.67	0.06	100.15	51.8	3.9	44.4
94-30 fe3.9	feldspar	59.48	25.18	0.36	0.01	6.78	6.89	1.14	0.15	99.98	60.5	6.6	32.9
94-30 fe4.1	feldspar	63.37	22.52	0.28	0.00	3.76	8.21	1.49	0.03	99.66	72.8	8.7	18.4
94-30 fe4.2	feldspar	57.76	26.47	0.14	0.00	8.19	6.56	0.52	0.05	99.70	57.4	3.0	39.6
94-30 fe4.3	feldspar	59.43	26.53	0.21	0.00	8.33	6.49	0.54	0.04	101.58	56.7	3.1	40.2
94-30 fe4.4	feldspar	57.65	26.79	0.20	0.00	8.42	6.35	0.53	0.06	100.01	56.0	3.1	41.0
94-30 fe4.5	feldspar	62.22	23.70	0.26	0.02	4.87	7.58	1.19	0.01	99.84	68.6	7.1	24.4
94-30 fe6.1	feldspar	56.79	26.44	0.29	0.02	8.55	6.00	0.84	0.11	99.03	53.2	4.9	41.9
94-30 fe6.2	feldspar	52.34	29.47	0.48	0.01	12.05	4.48	0.39	0.03	99.25	39.3	2.3	58.5
94-30 fe6.3	feldspar	55.18	28.94	0.32	0.02	11.21	4.88	0.49	0.03	101.07	42.8	2.8	54.3
94-30 fe6.4	feldspar	50.33	30.93	0.42	0.03	13.75	3.71	0.27	0.02	99.45	32.3	1.5	66.2
94-30 fe6.5	feldspar	48.89	32.01	0.47	0.03	15.06	2.98	0.18	0.04	99.67	26.1	1.0	72.9
94-30 fe6.6	feldspar	59.43	25.65	0.37	0.04	7.68	6.39	0.82	0.13	100.53	57.2	4.8	38.0
94-30 fe5.1	feldspar	50.38	31.61	0.40	0.03	14.26	3.35	0.24	0.04	100.31	29.4	1.4	69.2
94-30 fe5.2	feldspar	52.76	29.70	0.43	0.01	12.14	4.51	0.40	0.07	100.01	39.3	2.3	58.5
94-30 fe13.1	feldspar	61.90	23.33	0.18	0.01	4.66	7.86	1.28	0.02	99.24	69.7	7.5	22.8
94-30 fe13.2	feldspar	61.26	23.94	0.29	0.01	5.13	7.60	1.06	0.04	99.32	68.2	6.3	25.5
94-30 fe13.3	feldspar	61.41	23.05	0.25	0.02	4.49	7.88	1.30	0.03	98.43	70.3	7.6	22.1
94-30 fe13.4	feldspar	61.65	23.84	0.26	0.00	5.03	7.86	1.09	0.02	99.75	69.2	6.3	24.5
94-30 fe14.1	feldspar	49.57	31.68	0.35	0.02	14.16	3.46	0.19	0.06	99.48	30.4	1.1	68.6
94-30 fe14.2	feldspar	57.14	27.68	0.33	0.02	9.62	5.74	0.40	0.12	101.06	50.7	2.3	46.9
94-30 fe14.3	feldspar	55.38	27.72	0.29	0.03	9.47	5.70	0.38	0.13	99.11	51.0	2.2	46.8
94-30 fe14.4	feldspar	57.73	27.25	0.29	0.01	9.16	5.91	0.46	0.09	100.90	52.4	2.7	44.9
94-30 fe14.5	feldspar	55.06	28.99	0.27	0.02	11.32	4.71	0.52	0.10	100.98	41.7	3.0	55.3

Appendix C: Continued.

<u>Sample</u>	<u>Mineral</u>	<u>SiO2</u>	<u>Al2O3</u>	<u>FeO*</u>	<u>MgO</u>	<u>CaO</u>	<u>Na2O</u>	<u>K2O</u>	<u>BaO</u>	<u>Total</u>	<u>Ab</u>	<u>Or</u>	<u>An</u>
94-30 fe14.6	feldspar	59.86	24.58	0.21	0.01	6.15	7.33	0.85	0.10	99.09	64.9	4.9	30.1
94-30 fe14.7	feldspar	61.36	24.47	0.19	0.01	6.25	7.13	0.81	0.09	100.32	64.1	4.8	31.1
94-30 fe14.8	feldspar	58.19	26.38	0.31	0.01	8.30	6.33	0.49	0.08	100.08	56.3	2.8	40.8
94-30 fe15.1	feldspar	59.58	26.27	0.30	0.03	8.19	6.33	0.89	0.13	101.72	55.3	5.1	39.5
94-30 fe15.2	feldspar	54.03	28.40	0.26	0.03	10.55	5.36	0.51	0.10	99.22	46.5	2.9	50.6
94-30 fe15.3	feldspar	56.09	27.31	0.31	0.02	9.26	5.86	0.68	0.12	99.65	51.3	3.9	44.8
94-30 fe15.4	feldspar	53.50	28.32	0.33	0.02	10.42	5.19	0.52	0.09	98.39	46.0	3.1	51.0
94-30 fe15.5	feldspar	55.54	28.92	0.35	0.02	10.95	5.09	0.46	0.10	101.43	44.5	2.6	52.9
94-30 fe16.1	feldspar	57.57	25.87	0.30	0.03	7.68	6.43	0.96	0.12	98.96	56.9	5.6	37.6
94-30 fe16.2	feldspar	59.76	25.36	0.32	0.02	7.30	6.48	1.04	0.14	100.41	57.8	6.1	36.0
94-30 fe17.1	feldspar	54.52	28.20	0.31	0.03	10.52	5.20	0.55	0.12	99.45	45.7	3.2	51.1
94-30 fe17.2	feldspar	56.61	28.49	0.35	0.04	10.42	5.24	0.56	0.10	101.82	46.1	3.3	50.6
94-30 fe17.3	feldspar	55.82	27.63	0.32	0.03	9.71	5.50	0.69	0.14	99.83	48.6	4.0	47.4
94-30 fe17.4	feldspar	56.91	26.98	0.38	0.02	8.87	5.96	0.72	0.12	99.97	52.6	4.2	43.2
94-30 fe17.5	feldspar	59.60	24.92	0.31	0.01	6.81	6.77	1.21	0.15	99.77	59.7	7.0	33.2
94-30 fe18.1	feldspar	59.92	25.50	0.32	0.06	5.80	6.68	0.93	0.20	99.41	63.6	5.8	30.6
94-30 fe18.2	feldspar	54.94	28.43	0.43	0.02	10.83	5.18	0.52	0.12	100.48	45.0	3.0	52.0
94-30 fe18.3	feldspar	55.11	28.70	0.32	0.02	10.76	5.13	0.50	0.11	100.65	45.0	2.9	52.2
94-30 fe1.1	feldspar	63.96	19.05	0.12	0.00	0.21	3.43	11.35	0.17	98.29	31.1	67.8	1.1
94-30 fe1.2	feldspar	63.40	19.01	0.10	0.01	0.19	3.30	11.35	0.76	98.11	30.3	68.7	1.0
94-30 fe7.1	feldspar	64.56	18.92	0.11	0.01	0.17	3.76	11.07	0.03	98.63	33.7	65.4	0.9
94-30 fe7.2	feldspar	65.60	18.82	0.13	0.00	0.18	3.50	11.53	0.02	99.79	31.3	67.8	0.9
94-30 fe7.3	feldspar	66.41	18.65	0.04	0.01	0.19	3.49	11.55	0.02	100.35	31.2	67.9	0.9
94-30 fe7.4	feldspar	66.60	18.92	0.07	0.00	0.20	3.49	11.54	0.03	100.85	31.2	67.8	1.0
94-30 fe7.5	feldspar	64.68	19.09	0.04	0.01	0.21	3.57	11.52	0.00	99.12	31.7	67.3	1.0
94-30 fe7.6	feldspar	65.23	18.91	0.06	0.01	0.21	3.33	11.74	0.04	99.53	29.8	69.2	1.0
94-30 fe8.1	feldspar	63.98	18.96	0.05	0.01	0.19	3.44	11.63	0.02	98.28	30.7	68.4	1.0
94-30 fe8.2	feldspar	66.32	18.94	0.13	0.00	0.20	3.46	11.59	0.02	100.67	30.9	68.1	1.0
94-30 fe8.3	feldspar	64.20	19.05	0.06	0.02	0.21	3.41	11.53	0.01	98.50	30.7	68.3	1.0
94-30 fe8.4	feldspar	63.89	19.29	0.17	0.00	0.22	3.48	11.36	0.68	99.10	31.4	67.4	1.1
94-30 fe8.5	feldspar	63.63	19.16	0.11	0.01	0.24	3.47	11.29	0.54	98.45	31.4	67.3	1.2
94-30 fe9.1	feldspar	64.42	19.05	0.08	0.01	0.19	3.41	11.63	0.02	98.82	30.5	68.5	0.9
94-30 fe9.2	feldspar	64.42	18.95	0.09	0.00	0.20	3.49	11.64	0.03	98.82	31.0	68.0	1.0
94-30 fe9.3	feldspar	64.21	18.95	0.05	0.00	0.19	3.44	11.59	0.01	98.45	30.8	68.2	0.9
94-30 fe9.4	feldspar	65.66	18.96	0.10	0.01	0.21	3.49	11.15	0.01	99.60	31.9	67.0	1.1
94-30 fe10.1	feldspar	64.23	19.12	0.14	0.00	0.19	3.37	11.37	0.33	98.75	30.7	68.3	1.0
94-30 fe10.2	feldspar	65.99	19.11	0.07	0.00	0.18	3.47	11.43	0.41	100.65	31.3	67.8	0.9
94-30 fe10.3	feldspar	65.48	19.26	0.08	0.00	0.23	3.42	11.33	0.85	100.65	31.1	67.8	1.2
94-30 fe10.4	feldspar	63.79	19.31	0.13	0.00	0.26	3.65	11.09	0.80	99.03	32.9	65.8	1.3
94-30 fe11.1	feldspar	64.42	19.18	0.12	0.00	0.28	3.43	11.35	0.07	98.86	31.0	67.6	1.4

Appendix C: Continued.

<u>Sample</u>	<u>Mineral</u>	<u>SiO2</u>	<u>Al2O3</u>	<u>FeO*</u>	<u>MgO</u>	<u>CaO</u>	<u>Na2O</u>	<u>K2O</u>	<u>BaO</u>	<u>Total</u>	<u>Ab</u>	<u>Or</u>	<u>An</u>
94-30 fe11.2	feldspar	64.53	19.15	0.09	0.02	0.25	3.52	11.29	0.07	98.91	31.8	67.0	1.2
94-30 fe11.3	feldspar	64.74	19.02	0.14	0.00	0.23	3.58	11.48	0.05	99.24	31.8	67.1	1.1
94-30 fe11.4	feldspar	66.53	18.92	0.11	0.00	0.21	3.63	11.22	0.30	100.93	32.7	66.3	1.0
94-30 fe12.1	feldspar	64.92	19.04	0.12	0.00	0.22	3.62	11.33	0.10	99.36	32.3	66.6	1.1
94-30 fe12.2	feldspar	65.29	19.22	0.06	0.01	0.21	3.55	11.51	0.05	99.89	31.6	67.4	1.0
94-30 fe12.3	feldspar	66.70	19.34	0.17	0.00	0.23	4.20	10.30	0.60	101.53	37.8	61.0	1.1
94-30 fe12.4	feldspar	66.81	18.95	0.05	0.01	0.23	3.47	11.56	0.11	101.20	31.0	67.9	1.1
94-30 fe12.5	feldspar	66.92	19.01	0.08	0.01	0.23	3.47	11.36	0.04	101.12	31.4	67.5	1.1
94-31 fe1.1	feldspar	61.98	23.24	0.16	0.00	4.70	7.94	1.13	0.08	99.23	70.4	6.6	23.0
94-31 fe1.4	feldspar	58.88	25.15	0.22	0.01	6.93	6.97	0.71	0.09	98.95	61.9	4.1	34.0
94-31 fe1.6	feldspar	58.88	25.46	0.25	0.03	6.93	7.02	0.72	0.06	99.34	62.0	4.2	33.8
94-31 fe1.7	feldspar	59.34	25.97	0.22	0.00	6.39	7.08	0.73	0.09	99.82	63.9	4.3	31.8
94-31 fe1.9	feldspar	60.20	23.63	0.20	0.01	5.14	7.68	1.05	0.05	97.96	68.5	6.2	25.4
94-31 fe1.8	feldspar	59.55	24.82	0.25	0.00	6.44	7.10	0.76	0.06	98.99	63.6	4.5	31.9
94-31 fe2.1	feldspar	56.07	27.96	0.22	0.00	9.94	5.66	0.57	0.02	100.43	49.1	3.3	47.6
94-31 fe2.2	feldspar	54.51	27.86	0.26	0.03	9.61	5.57	0.58	0.04	98.46	49.5	3.4	47.1
94-31 fe2.3	feldspar	54.79	27.50	0.24	0.01	9.34	5.75	0.66	0.04	98.33	50.7	3.8	45.5
94-31 fe2.4	feldspar	56.43	27.07	0.21	0.00	8.69	6.14	0.72	0.08	99.32	53.8	4.1	42.1
94-31 fe3.3	feldspar	58.08	24.92	0.37	0.01	7.03	6.82	1.07	0.17	98.48	59.8	6.2	34.1
94-31 fe3.4	feldspar	54.64	27.74	0.35	0.04	10.42	5.21	0.54	0.06	99.00	46.0	3.2	50.8
94-31 fe3.6	feldspar	52.75	28.37	0.45	0.02	10.72	5.31	0.49	0.07	98.18	45.9	2.8	51.3
94-31 fe3.7	feldspar	54.27	28.03	0.40	0.01	10.40	5.18	0.51	0.03	98.83	46.0	3.0	51.0
94-31 fe4.1	feldspar	65.31	22.08	0.15	0.01	2.81	9.19	1.44	0.00	100.99	78.6	8.1	13.3
94-31 fe4.2	feldspar	65.25	21.85	0.05	0.00	2.66	9.22	1.35	0.00	100.38	79.6	7.7	12.7
94-31 fe4.3	feldspar	65.13	22.08	0.14	0.00	2.93	9.23	1.25	0.00	100.76	79.1	7.1	13.9
94-31 fe4.4	feldspar	63.60	21.96	0.11	0.00	2.74	9.16	1.32	0.00	98.90	79.3	7.5	13.1
94-31 fe4.5	feldspar	65.21	21.97	0.14	0.00	2.71	9.14	1.30	0.00	100.47	79.5	7.4	13.0
94-31 fe4.6	feldspar	63.88	22.08	0.13	0.00	2.84	9.04	1.39	0.00	99.37	78.4	7.9	13.6
94-31 fe5.1	feldspar	64.66	22.28	0.18	0.01	3.04	8.93	1.25	0.01	100.36	78.1	7.2	14.7
94-31 fe5.2	feldspar	64.91	22.11	0.10	0.01	3.06	9.01	1.22	0.01	100.43	78.3	7.0	14.7
94-31 fe5.3	feldspar	64.55	22.31	0.15	0.00	3.17	8.97	1.19	0.00	100.36	77.9	6.8	15.2
94-31 fe6.1	feldspar	53.53	29.50	0.48	0.07	11.90	4.62	0.41	0.09	100.61	40.3	2.4	57.3
94-31 fe6.2	feldspar	53.06	29.05	0.99	0.03	11.65	4.62	0.41	0.07	99.87	40.8	2.4	56.8
94-31 fe6.3	feldspar	51.30	30.12	0.54	0.03	12.80	4.24	0.34	0.05	99.41	36.8	1.9	61.3
94-31 fe6.4	feldspar	51.17	29.48	0.47	0.03	12.25	4.41	0.35	0.06	98.23	38.7	2.0	59.3
94-31 fe6.5	feldspar	52.85	29.74	0.46	0.02	12.27	4.29	0.38	0.04	100.04	37.9	2.2	59.9
94-31 fe16.3	feldspar	57.65	26.05	0.29	0.00	7.90	6.51	0.53	0.15	99.07	58.0	3.1	38.9
94-31 fe16.5	feldspar	61.07	24.55	0.26	0.01	5.84	7.64	0.93	0.08	100.36	66.6	5.3	28.1
94-31 fe17.1	feldspar	59.24	24.45	0.23	0.03	5.72	7.55	0.91	0.18	98.30	66.7	5.3	28.0
94-31 fe17.2	feldspar	57.18	26.89	0.20	0.00	8.63	6.34	0.47	0.13	99.86	55.5	2.7	41.8

Appendix C: Continued.

<u>Sample</u>	<u>Mineral</u>	<u>SiO2</u>	<u>Al2O3</u>	<u>FeO*</u>	<u>MgO</u>	<u>CaO</u>	<u>Na2O</u>	<u>K2O</u>	<u>BaO</u>	<u>Total</u>	<u>Ab</u>	<u>Or</u>	<u>An</u>
94-31 fe17.3	feldspar	53.35	28.45	0.31	0.00	10.28	5.40	0.37	0.11	98.27	47.7	2.1	50.1
94-31 fe7.1	feldspar	65.01	19.03	0.09	0.01	0.21	4.10	10.44	0.01	98.90	37.0	62.0	1.0
94-31 fe7.2	feldspar	64.14	19.24	0.07	0.00	0.24	4.24	10.52	0.00	98.46	37.5	61.3	1.2
94-31 fe7.3	feldspar	63.95	19.28	0.10	0.02	0.23	4.22	10.34	0.03	98.17	37.8	61.0	1.2
94-31 fe7.4	feldspar	63.81	19.30	0.11	0.00	0.22	4.06	10.60	0.01	98.09	36.4	62.5	1.1
94-31 fe7.5	feldspar	63.89	19.24	0.11	0.01	0.23	4.12	10.77	0.02	98.38	36.4	62.5	1.1
94-31 fe7.6	feldspar	65.15	19.11	0.11	0.00	0.17	4.14	10.62	0.32	99.62	36.9	62.3	0.8
94-31 fe8.2	feldspar	65.56	18.86	0.12	0.00	0.13	4.08	10.88	0.02	99.65	36.1	63.3	0.6
94-31 fe9.2	feldspar	65.54	19.27	0.11	0.00	0.22	3.83	11.13	0.02	100.13	34.0	65.0	1.1
94-31 fe9.3	feldspar	64.00	19.16	0.05	0.00	0.22	3.81	11.17	0.00	98.41	33.8	65.2	1.1
94-31 fe9.4	feldspar	63.76	19.18	0.06	0.01	0.21	3.75	11.37	0.03	98.38	33.0	65.9	1.0
94-31 fe10.1	feldspar	65.71	19.12	0.13	0.00	0.25	4.29	10.26	0.01	99.77	38.4	60.4	1.2
94-31 fe10.3	feldspar	65.08	18.97	0.11	0.00	0.18	3.80	11.11	0.01	99.26	33.9	65.2	0.9
94-31 fe11.1	feldspar	65.62	19.22	0.14	0.00	0.24	4.00	10.78	0.03	100.04	35.7	63.2	1.2
94-31 fe12.1	feldspar	65.76	19.19	0.11	0.00	0.20	4.23	10.69	0.00	100.18	37.2	61.8	1.0
94-31 fe12.4	feldspar	63.92	19.11	0.08	0.00	0.18	4.31	10.52	0.01	98.13	38.1	61.1	0.9
94-31 fe13.3	feldspar	63.67	19.05	0.07	0.01	0.21	4.21	10.73	0.01	97.95	37.0	62.0	1.0
94-31 fe13.4	feldspar	64.30	19.03	0.04	0.00	0.18	4.25	10.49	0.11	98.39	37.8	61.4	0.9
94-31 fe13.5	feldspar	65.83	19.31	0.12	0.02	0.24	4.31	10.41	0.17	100.41	38.2	60.6	1.2
94-31 fe14.2	feldspar	64.71	18.95	0.07	0.01	0.17	3.56	11.39	0.13	98.99	31.9	67.2	0.8
94-31 fe14.3	feldspar	65.46	19.30	0.13	0.00	0.29	3.69	11.21	0.25	100.34	32.9	65.7	1.4
94-31 fe14.5	feldspar	64.41	18.96	0.14	0.00	0.26	3.59	10.98	0.30	98.65	32.8	65.9	1.3
94-31 fe14.5	feldspar	64.96	19.11	0.07	0.00	0.27	4.07	10.39	0.39	99.26	36.8	61.9	1.4
94-31 fe15.1	feldspar	63.91	19.14	0.09	0.00	0.17	3.97	10.98	0.01	98.28	35.1	64.0	0.8
94-31 fe15.2	feldspar	65.80	19.18	0.11	0.00	0.14	4.02	10.78	0.00	100.04	35.9	63.3	0.7
94-31 fe15.3	feldspar	63.79	19.10	0.03	0.00	0.12	3.87	11.21	0.00	98.12	34.2	65.2	0.6
94-31 fe18.1	feldspar	65.59	18.94	0.10	0.00	0.20	3.73	11.35	0.09	99.99	33.0	66.0	1.0
94-31 fe18.2	feldspar	65.12	18.94	0.13	0.00	0.25	3.77	11.28	0.08	99.56	33.3	65.5	1.2
94-28D fe2.1	feldspar	60.43	24.16	0.17	0.01	5.28	7.16	0.89	0.07	98.16	67.1	5.5	27.4
94-28D fe2.2	feldspar	56.58	26.45	0.10	0.01	7.88	6.53	0.47	0.07	98.08	58.3	2.8	38.9
94-28D fe2.3	feldspar	55.49	27.27	0.19	0.00	8.90	6.25	0.39	0.07	98.56	54.7	2.3	43.1
94-28D fe2.4	feldspar	59.40	24.32	0.15	0.00	5.61	7.23	1.31	0.06	98.08	64.6	7.7	27.7
94-28D fe2.5	feldspar	62.78	23.79	0.18	0.02	5.17	7.65	0.92	0.05	100.56	68.8	5.5	25.7
94-28D fe3.1	feldspar	62.20	22.62	0.15	0.01	4.26	8.42	1.04	0.00	98.70	73.5	6.0	20.5
94-28D fe3.2	feldspar	62.93	23.06	0.15	0.00	4.22	8.28	1.06	0.01	99.71	73.2	6.2	20.6
94-28D fe3.3	feldspar	60.51	24.28	0.17	0.01	5.99	7.50	0.68	0.00	99.14	66.6	4.0	29.4
94-28D fe3.4	feldspar	60.76	23.72	0.17	0.00	5.56	6.89	1.73	0.02	98.85	62.0	10.3	27.7
94-28D fe3.5	feldspar	62.17	22.59	0.14	0.01	4.16	7.86	1.41	0.00	98.33	70.9	8.4	20.7
94-28D fe3.6	feldspar	63.36	22.80	0.15	0.00	4.07	8.25	1.12	0.00	99.75	73.4	6.6	20.0
94-28D fe3.7	feldspar	61.64	24.12	0.26	0.00	5.79	7.05	1.12	0.09	100.07	64.2	6.7	29.1

Appendix C: Continued.

Sample	Mineral	SiO ₂	Al ₂ O ₃	FeO*	MgO	CaO	Na ₂ O	K ₂ O	BaO	Total	Ab	Or	An
94-28D fe3.8	feldspar	56.65	27.72	0.29	0.02	9.75	5.40	0.48	0.10	100.42	48.6	2.9	48.5
94-28D fe3.9	feldspar	57.09	27.76	0.26	0.00	9.75	5.33	0.49	0.08	100.76	48.3	2.9	48.8
94-28D fe3.10	feldspar	56.43	27.19	0.25	0.00	8.98	5.66	0.53	0.06	99.12	51.6	3.2	45.2
94-28D fe4.1	feldspar	64.56	23.03	0.15	0.00	4.02	8.09	1.16	0.01	101.02	73.0	6.9	20.1
94-28D fe4.2	feldspar	63.17	23.14	0.16	0.01	4.00	8.13	1.12	0.02	99.76	73.4	6.6	20.0
94-28D fe4.3	feldspar	62.81	23.23	0.15	0.00	4.07	8.35	1.15	0.03	99.80	73.6	6.7	19.8
94-28D fe4.4	feldspar	62.89	23.14	0.18	0.01	4.07	8.31	1.15	0.03	99.78	73.5	6.7	19.9
94-28D fe4.5	feldspar	65.95	22.66	0.12	0.01	3.71	8.04	1.27	0.00	101.76	73.6	7.6	18.8
94-28D fe4.6	feldspar	64.67	22.92	0.10	0.00	4.14	8.36	1.17	0.01	101.38	73.2	6.8	20.0
94-28D fe4.7	feldspar	62.86	22.77	0.15	0.00	3.81	8.14	1.26	0.00	98.99	73.5	7.5	19.0
94-28D fe5.3	feldspar	62.15	22.99	0.12	0.00	4.71	7.72	1.17	0.00	98.85	69.6	6.9	23.5
94-28D fe5.4	feldspar	62.24	23.40	0.18	0.00	4.79	7.65	1.13	0.00	99.38	69.3	6.7	24.0
94-28D fe7.3	feldspar	63.77	22.67	0.11	0.00	3.84	8.08	1.11	0.01	99.59	73.9	6.7	19.4
94-28D fe7.6	feldspar	61.44	23.74	0.19	0.00	5.10	7.92	0.86	0.05	99.29	70.1	5.0	24.9
94-28D fe7.7	feldspar	62.12	23.82	0.21	0.00	5.06	7.94	0.84	0.10	100.09	70.3	4.9	24.8
94-28D fe8.2	feldspar	62.10	22.60	0.11	0.00	3.79	8.49	1.23	0.00	98.32	74.5	7.1	18.4
94-28D fe16.5	feldspar	61.83	23.12	0.14	0.00	4.30	8.16	1.11	0.00	98.67	72.4	6.5	21.1
94-28D fe16.6	feldspar	62.12	22.93	0.15	0.00	4.08	8.18	1.10	0.00	98.56	73.3	6.5	20.2
94-28D fe16.7	feldspar	63.02	22.70	0.19	0.00	3.77	8.17	1.16	0.00	99.02	74.1	7.0	18.9
94-28D fe18.1	feldspar	61.78	23.13	0.20	0.00	4.28	8.13	1.10	0.00	98.62	72.5	6.4	21.1
94-28D fe18.2	feldspar	61.90	23.09	0.19	0.01	4.12	8.24	1.11	0.01	98.68	73.2	6.5	20.2
94-28D fe18.3	feldspar	64.85	22.56	0.15	0.00	3.79	8.28	1.30	0.00	100.95	73.7	7.6	18.6
94-28D fe1.3	feldspar	64.24	19.13	0.10	0.01	0.18	3.46	11.38	0.18	98.69	31.3	67.7	0.9
94-28D fe1.4	feldspar	64.98	19.25	0.10	0.01	0.19	3.51	11.40	0.18	99.61	31.6	67.5	0.9
94-28D fe1.5	feldspar	63.55	19.10	0.10	0.00	0.19	3.06	12.14	0.16	98.29	27.5	71.6	0.9
94-28D fe1.8	feldspar	65.42	18.97	0.07	0.00	0.18	3.42	11.43	0.18	99.66	31.0	68.1	0.9
94-28D fe1.12	feldspar	65.64	19.07	0.11	0.00	0.18	3.45	11.54	0.19	100.17	30.9	68.2	0.9
94-28D fe6.1	feldspar	66.24	18.97	0.09	0.00	0.21	3.42	11.43	0.25	100.62	30.9	68.0	1.1
94-28D fe6.2	feldspar	65.62	18.96	0.18	0.00	0.22	3.43	11.60	0.35	100.36	30.7	68.2	1.1
94-28D fe6.5	feldspar	65.61	19.22	0.11	0.00	0.25	3.36	11.49	0.54	100.57	30.3	68.4	1.3
94-28D fe6.9	feldspar	65.54	18.98	0.07	0.00	0.19	3.41	11.62	0.26	100.07	30.6	68.5	0.9
94-28D fe6.10	feldspar	65.47	18.89	0.11	0.00	0.20	3.21	11.53	0.32	99.72	29.5	69.6	1.0
94-28D fe9.2	feldspar	65.78	19.04	0.07	0.00	0.18	3.43	11.39	0.11	100.00	31.1	68.0	0.9
94-28D fe10.1	feldspar	64.76	19.12	0.07	0.00	0.18	3.69	11.41	0.00	99.24	32.7	66.5	0.9
94-28D fe10.2	feldspar	66.48	19.09	0.05	0.00	0.16	3.56	11.41	0.03	100.79	31.9	67.3	0.8
94-28D fe10.3	feldspar	66.49	18.99	0.06	0.01	0.15	3.47	11.51	0.04	100.72	31.2	68.1	0.7
94-28D fe10.4	feldspar	64.13	19.16	0.08	0.00	0.16	3.52	11.42	0.06	98.53	31.7	67.5	0.8
94-28D fe10.5	feldspar	64.47	19.04	0.09	0.00	0.14	3.53	11.40	0.07	98.74	31.8	67.5	0.7
94-28D fe12.2	feldspar	65.66	19.06	0.07	0.00	0.20	3.43	11.20	0.09	99.71	31.5	67.5	1.0
94-28D fe13.1	feldspar	63.75	19.22	0.08	0.00	0.18	3.51	11.49	0.00	98.23	31.4	67.7	0.9

Appendix C: Continued.

<u>Sample</u>	<u>Mineral</u>	<u>SiO2</u>	<u>Al2O3</u>	<u>FeO*</u>	<u>MgO</u>	<u>CaO</u>	<u>Na2O</u>	<u>K2O</u>	<u>BaO</u>	<u>Total</u>	<u>Ab</u>	<u>Or</u>	<u>An</u>
94-28D fe13.2	feldspar	63.99	19.07	0.05	0.00	0.23	3.48	11.30	0.00	98.13	31.5	67.3	1.2
94-28D fe13.3	feldspar	66.39	19.03	0.05	0.00	0.18	3.50	11.58	0.02	100.76	31.2	67.9	0.9
94-28D fe13.4	feldspar	64.14	19.12	0.03	0.00	0.16	3.51	11.59	0.00	98.55	31.3	67.9	0.8
94-28D fe13.5	feldspar	66.52	19.15	0.10	0.00	0.16	3.58	11.46	0.01	100.97	31.9	67.3	0.8
94-28D fe13.6	feldspar	64.63	19.04	0.07	0.00	0.13	3.51	11.54	0.00	98.93	31.4	68.0	0.6
94-28D fe14.1	feldspar	65.88	19.03	0.12	0.01	0.22	4.02	10.59	0.03	99.90	36.2	62.7	1.1
94-28D fe14.3	feldspar	66.16	19.00	0.04	0.00	0.22	3.56	11.27	0.05	100.31	32.1	66.8	1.1
94-28D fe14.4	feldspar	65.87	18.92	0.07	0.00	0.19	3.44	11.39	0.07	99.95	31.2	67.9	0.9
94-28D fe14.6	feldspar	63.67	19.01	0.10	0.00	0.22	3.58	11.55	0.09	98.21	31.7	67.2	1.1
94-28D fe15.2	feldspar	65.06	18.68	0.09	0.04	0.13	3.51	11.45	0.09	99.04	31.6	67.8	0.7
94-28D fe16.2	feldspar	66.02	19.08	0.05	0.00	0.20	3.28	11.71	0.16	100.50	29.6	69.4	1.0
94-28D fe16.3	feldspar	65.94	18.91	0.13	0.00	0.17	3.45	11.61	0.15	100.35	30.8	68.3	0.8
94-28D fe16.4	feldspar	63.87	19.01	0.10	0.02	0.19	3.35	11.77	0.13	98.42	29.9	69.2	0.9
94-28D fe17.1	feldspar	63.09	19.16	0.11	0.01	0.20	3.46	11.14	0.84	98.02	31.8	67.2	1.0
94-28D fe17.2	feldspar	63.35	19.09	0.07	0.01	0.19	3.46	11.28	0.60	98.06	31.5	67.5	1.0
94-28D fe17.3	feldspar	63.56	19.14	0.08	0.00	0.22	3.53	11.29	0.57	98.40	31.9	67.0	1.1
94-28D fe17.4	feldspar	63.77	19.16	0.08	0.00	0.17	3.46	11.15	0.43	98.23	31.7	67.4	0.9
94-28D fe17.5	feldspar	65.65	19.17	0.09	0.01	0.22	3.49	11.30	0.55	100.47	31.6	67.3	1.1
94-28D fe17.6	feldspar	63.33	19.20	0.09	0.00	0.23	3.52	11.16	0.49	98.02	32.1	66.8	1.1
94-28D fe17.7	feldspar	63.95	19.23	0.07	0.02	0.23	3.34	11.27	0.34	98.45	30.7	68.2	1.2
94-28D fe17.8	feldspar	66.99	19.14	0.13	0.00	0.20	3.43	11.54	0.01	101.46	30.8	68.2	1.0
94-28D fe17.9	feldspar	66.96	18.98	0.09	0.00	0.18	3.51	11.47	0.04	101.24	31.5	67.6	0.9
94-28D fe17.10	feldspar	67.07	19.14	0.07	0.02	0.18	4.43	9.94	0.04	100.88	40.0	59.1	0.9
94-28D fe17.11	feldspar	64.46	19.06	0.09	0.00	0.20	3.53	11.49	0.05	98.89	31.5	67.5	1.0
94-28D fe17.12	feldspar	66.87	19.04	0.11	0.00	0.25	3.52	11.43	0.04	101.26	31.5	67.3	1.2
94-9B fe1.1	feldspar	58.86	25.21	0.36	0.00	6.72	6.96	1.17	0.20	99.48	60.8	6.7	32.4
94-9B fe1.2	feldspar	53.77	28.83	0.37	0.02	10.84	5.00	0.51	0.09	99.44	44.1	3.0	52.9
94-9B fe1.3	feldspar	51.88	30.06	0.28	0.01	12.40	4.36	0.38	0.09	99.44	38.0	2.2	59.8
94-9B fe1.4	feldspar	50.78	30.73	0.36	0.00	13.10	3.93	0.30	0.06	99.26	34.6	1.7	63.7
94-9B fe1.5	feldspar	54.57	27.62	0.34	0.04	9.51	5.76	0.65	0.13	98.62	50.3	3.7	46.0
94-9B fe2.1	feldspar	57.14	27.04	0.28	0.02	8.64	6.55	0.53	0.12	100.31	56.1	3.0	40.9
94-9B fe2.2	feldspar	57.02	26.84	0.29	0.01	8.13	6.66	0.53	0.11	99.58	57.9	3.0	39.1
94-9B fe2.3	feldspar	61.32	23.65	0.26	0.00	4.82	8.19	1.18	0.02	99.45	70.4	6.7	22.9
94-9B fe3.1	feldspar	51.50	30.43	0.55	0.06	12.98	4.16	0.36	0.06	100.09	36.0	2.0	62.0
94-9B fe3.2	feldspar	53.22	29.70	0.49	0.07	12.06	4.63	0.41	0.07	100.63	40.0	2.3	57.6
94-9B fe3.3	feldspar	56.63	27.06	0.41	0.03	9.02	6.08	0.80	0.07	100.09	52.5	4.5	43.0
94-9B fe5.1	feldspar	55.88	27.76	0.24	0.02	9.51	6.14	0.46	0.10	100.10	52.5	2.6	44.9
94-9B fe5.2	feldspar	54.06	28.65	0.27	0.03	10.42	5.57	0.35	0.07	99.40	48.2	2.0	49.8
94-9B fe5.3	feldspar	58.35	25.42	0.27	0.00	6.84	7.37	0.70	0.11	99.06	63.5	3.9	32.6
94-9B fe5.4	feldspar	58.64	25.25	0.20	0.01	6.61	7.39	0.76	0.12	98.97	64.0	4.3	31.6

Appendix C: Continued.

<u>Sample</u>	<u>Mineral</u>	<u>SiO2</u>	<u>Al2O3</u>	<u>FeO*</u>	<u>MgO</u>	<u>CaO</u>	<u>Na2O</u>	<u>K2O</u>	<u>BaO</u>	<u>Total</u>	<u>Ab</u>	<u>Or</u>	<u>An</u>
94-9B fe11.3	feldspar	64.51	21.72	0.14	0.00	2.63	8.97	1.72	0.00	99.69	77.6	9.8	12.6
94-9B fe11.4	feldspar	63.35	22.49	0.17	0.02	3.29	8.84	1.52	0.00	99.68	75.8	8.6	15.6
94-9B fe14.1	feldspar	54.79	27.86	0.26	0.00	9.25	6.12	0.44	0.10	98.82	53.1	2.5	44.4
94-9B fe14.2	feldspar	56.66	27.61	0.30	0.00	9.36	6.12	0.44	0.07	100.56	52.9	2.5	44.7
94-9B fe7.1	feldspar	64.84	19.18	0.12	0.00	0.15	3.88	11.23	0.05	99.46	34.2	65.1	0.8
94-9B fe7.2	feldspar	64.69	19.17	0.08	0.00	0.18	3.88	11.17	0.03	99.20	34.2	64.9	0.9
94-9B fe7.3	feldspar	63.96	19.21	0.14	0.00	0.21	3.87	11.30	0.03	98.72	33.9	65.1	1.0
94-9B fe8.1	feldspar	65.40	19.27	0.11	0.00	0.18	3.80	11.06	0.01	99.83	34.0	65.1	0.9
94-9B fe8.2	feldspar	64.89	19.06	0.13	0.00	0.17	3.90	11.37	0.05	99.56	34.0	65.2	0.8
94-9B fe8.3	feldspar	64.95	19.16	0.10	0.00	0.19	3.88	11.24	0.03	99.55	34.1	65.0	0.9
94-9B fe11.1	feldspar	64.82	19.29	0.09	0.00	0.21	3.94	10.98	0.05	99.38	34.9	64.0	1.0
94-9B fe11.2	feldspar	65.17	19.22	0.08	0.00	0.17	3.85	11.34	0.02	99.86	33.8	65.4	0.8
94-9B fe12.1	feldspar	64.94	19.18	0.05	0.00	0.20	3.86	11.15	0.02	99.40	34.1	64.9	1.0
94-9B fe12.2	feldspar	65.08	19.28	0.09	0.01	0.21	3.87	11.11	0.08	99.72	34.3	64.7	1.0

<u>Sample</u>	<u>Mineral</u>	<u>SiO2</u>	<u>Al2O3</u>	<u>TiO2</u>	<u>FeO</u>	<u>Fe2O3</u>	<u>MgO</u>	<u>MnO</u>	<u>CaO</u>	<u>Na2O</u>	<u>K2O</u>	<u>Cr2O3</u>	<u>F</u>	<u>Cl</u>	<u>Total</u>	<u>O=F,Cl</u>
94-5B ma1.2	amphibole	41.91	13.21	1.46	11.71	1.38	13.21	0.18	11.13	1.92	0.80	0.00	0.24	0.06	97.20	0.12
94-5B ma3.1	amphibole	43.33	11.01	2.04	10.93	0.75	14.89	0.19	10.81	1.90	0.78	0.00	0.28	0.03	96.93	0.13
94-5B ma3.2	amphibole	43.18	10.96	2.13	11.19	0.78	14.53	0.13	10.99	1.84	0.82	0.04	0.32	0.04	96.93	0.14
94-5B ma3.3	amphibole	42.99	11.52	2.18	11.26	0.50	14.59	0.15	10.71	1.91	0.78	0.00	0.33	0.03	96.93	0.15
94-5B ma12.2	amphibole	44.29	10.16	1.86	12.07	0.04	14.55	0.18	10.94	1.83	0.94	0.03	0.33	0.03	97.24	0.15
94-5B ma12.3	amphibole	43.02	11.26	2.14	12.17	0.86	14.17	0.19	10.67	1.91	0.80	0.04	0.37	0.03	97.63	0.16
94-5B ma12.4	amphibole	43.93	10.32	2.11	11.35	0.61	14.78	0.09	10.98	1.74	0.79	0.02	0.40	0.04	97.14	0.18
94-5B ma12.5	amphibole	43.67	10.70	1.65	12.17	0.33	13.94	0.28	10.89	1.72	0.93	0.00	0.34	0.05	96.66	0.15
94-5B ma12.6	amphibole	43.85	10.31	1.74	11.73	0.54	14.32	0.17	11.01	1.71	0.91	0.03	0.27	0.03	96.61	0.12
94-5B ma15.1	amphibole	42.54	12.31	1.96	9.58	1.74	15.20	0.12	10.86	2.02	0.49	0.03	0.19	0.03	97.08	0.09
94-5B ma15.2	amphibole	42.82	12.22	1.65	9.30	1.69	15.85	0.14	10.16	2.09	0.46	0.14	0.35	0.00	96.88	0.15
94-5B ma18.1	amphibole	42.71	11.90	1.90	12.31	0.02	13.89	0.19	10.75	2.33	0.60	0.02	0.53	0.02	97.16	0.23
94-8 ma6.1	amphibole	41.87	11.56	3.59	13.80	0.01	12.27	0.24	10.67	2.24	0.99	0.01	0.45	0.03	97.74	0.20
94-8 ma6.2	amphibole	42.02	11.38	3.82	13.66	0.05	12.40	0.22	10.72	2.27	0.87	0.05	0.36	0.03	97.85	0.16
94-30 ma10.1	amphibole	47.64	5.85	1.36	15.63	0.00	13.22	0.85	10.68	1.33	0.65	0.00	0.45	0.09	97.74	0.21
94-30 ma10.2	amphibole	48.20	5.92	1.45	15.51	0.00	13.63	0.81	10.65	1.36	0.59	0.00	0.42	0.08	98.62	0.20
94-30 ma10.3	amphibole	47.67	6.21	1.54	15.26	0.04	13.79	0.77	10.62	1.42	0.70	0.04	0.43	0.08	98.57	0.20
94-30 ma11.2	amphibole	47.54	6.06	1.51	15.18	0.00	13.42	0.86	10.66	1.48	0.63	0.00	0.44	0.08	97.85	0.20
94-30 ma11.3	amphibole	47.42	6.08	1.46	14.97	0.00	13.38	0.79	10.54	1.35	0.64	0.00	0.44	0.07	97.15	0.20

Appendix C: Continued.

<u>Sample</u>	<u>Mineral</u>	<u>SiO2</u>	<u>Al2O3</u>	<u>TiO2</u>	<u>FeO</u>	<u>Fe2O3</u>	<u>MnO</u>	<u>MgO</u>	<u>CaO</u>	<u>Na2O</u>	<u>Cr2O3</u>	<u>Total</u>	<u>En</u>	<u>Wo</u>	<u>Fs</u>
94-5B ma1.1	pyroxene	51.71	2.87	0.47	7.07	0.51	0.20	15.96	19.96	0.26	0.06	99.06	46.1	41.4	12.5
94-5B ma8.1	pyroxene	51.96	0.97	0.15	12.30	0.05	0.58	12.43	20.05	0.34	0.01	98.83	36.5	42.3	21.3
94-5B ma8.2	pyroxene	51.02	3.02	0.68	9.86	0.33	0.25	14.84	18.52	0.32	0.04	98.88	43.7	39.2	17.2
94-5B ma8.3	pyroxene	51.18	2.92	0.67	8.50	0.59	0.27	14.56	20.15	0.33	0.00	99.17	42.5	42.3	15.2
94-5B ma8.4	pyroxene	51.31	2.58	0.59	9.16	0.60	0.27	14.99	19.04	0.35	0.00	98.88	43.7	39.9	16.3
94-5B ma8.5	pyroxene	50.62	3.30	0.76	8.74	0.81	0.23	14.57	19.22	0.43	0.02	98.71	43.1	40.8	16.1
94-5B ma8.6	pyroxene	51.83	0.97	0.17	11.84	0.25	0.51	12.61	20.26	0.32	0.00	98.75	36.8	42.6	20.6
94-5B ma9.1	pyroxene	51.52	1.06	0.15	12.18	0.87	0.71	12.37	19.84	0.38	0.02	99.09	36.1	41.6	22.4
94-5B ma9.2	pyroxene	51.61	0.95	0.17	12.33	0.22	0.61	12.45	19.65	0.36	0.00	98.35	36.7	41.6	21.7
94-5B ma9.3	pyroxene	51.68	1.43	0.23	11.36	0.38	0.64	13.14	19.64	0.35	0.00	98.83	38.4	41.3	20.3
94-5B ma9.4	pyroxene	51.75	1.30	0.24	10.98	0.48	0.66	13.26	19.86	0.34	0.00	98.87	38.7	41.6	19.8
94-5B ma9.5	pyroxene	51.52	1.39	0.24	12.42	0.06	0.60	12.46	19.47	0.36	0.00	98.51	36.9	41.4	21.7
94-5B ma11.1	pyroxene	51.49	1.30	0.25	11.83	0.17	0.66	12.35	20.01	0.37	0.00	98.43	36.5	42.5	21.0
94-5B ma11.2	pyroxene	52.03	0.87	0.17	12.20	0.00	0.67	12.24	19.99	0.31	0.02	98.48	36.2	42.5	21.4
94-5B ma11.3	pyroxene	51.84	1.30	0.17	10.91	0.41	0.63	13.04	20.15	0.37	0.01	98.81	38.1	42.3	19.5
94-5B ma12.1	pyroxene	52.52	2.04	0.27	5.20	0.50	0.17	16.86	20.91	0.23	0.11	98.80	48.0	42.8	9.3
94-5B ma12.2	pyroxene	52.86	1.87	0.25	4.96	0.28	0.17	17.07	21.03	0.22	0.33	99.06	48.5	42.9	8.6
94-5B ma12.3	pyroxene	52.50	2.36	0.36	5.84	0.40	0.21	16.86	20.41	0.22	0.06	99.21	48.0	41.8	10.2
94-5B ma12.4	pyroxene	52.18	2.44	0.33	6.05	0.34	0.17	16.40	20.45	0.26	0.09	98.71	47.2	42.3	10.5
94-5B ma12.7	pyroxene	53.37	1.43	0.20	4.81	0.40	0.17	17.78	20.69	0.21	0.35	99.42	49.9	41.7	8.4
94-5B ma12.8	pyroxene	53.48	1.38	0.21	5.47	0.29	0.19	17.90	20.27	0.16	0.11	99.45	50.0	40.7	9.3
94-5B ma10.1	pyroxene	51.33	0.36	0.11	27.98	0.00	1.63	16.31	1.07	0.04	0.01	98.85	48.4	2.3	49.3
94-5B ma10.2	pyroxene	51.01	0.33	0.11	28.34	0.00	1.82	16.04	1.13	0.04	0.05	98.86	47.5	2.4	50.1
94-5B ma10.3	pyroxene	50.88	0.31	0.09	28.34	0.00	1.94	15.80	1.10	0.02	0.00	98.48	47.0	2.4	50.6
94-5B ma10.4	pyroxene	51.32	0.34	0.09	28.68	0.00	1.74	16.20	0.95	0.02	0.00	99.35	47.7	2.0	50.3
94-5B ma10.5	pyroxene	51.34	0.32	0.08	28.18	0.00	1.47	16.53	1.00	0.02	0.00	98.93	48.8	2.1	49.1
94-5B ma12.5	pyroxene	51.37	0.50	0.14	27.21	0.00	1.25	17.07	1.23	0.02	0.04	98.83	50.3	2.6	47.1
94-5B ma12.6	pyroxene	51.47	0.33	0.10	26.51	0.00	1.04	17.62	1.07	0.02	0.00	98.16	52.0	2.3	45.7
94-5B ma13.1	pyroxene	51.22	0.35	0.10	27.89	0.00	1.27	16.82	1.07	0.02	0.00	98.75	49.5	2.3	48.2
94-5B ma13.2	pyroxene	51.43	0.30	0.09	28.33	0.00	1.40	16.61	1.11	0.02	0.02	99.30	48.7	2.4	48.9
94-5B ma13.3	pyroxene	51.20	0.68	0.14	27.97	0.00	1.42	16.60	1.45	0.03	0.00	99.49	48.6	3.1	48.3
94-5B ma13.4	pyroxene	51.26	0.36	0.10	27.49	0.00	1.38	17.00	1.31	0.01	0.01	98.91	49.8	2.8	47.5
94-5B ma14.1	pyroxene	50.78	0.82	0.12	28.12	0.00	1.28	16.65	1.22	0.03	0.00	99.02	48.9	2.6	48.5
94-5B ma14.2	pyroxene	50.84	0.45	0.14	27.70	0.00	1.30	16.21	1.28	0.03	0.00	97.94	48.5	2.8	48.7
94-5B ma14.3	pyroxene	50.93	0.66	0.18	27.50	0.00	1.27	16.48	1.47	0.03	0.00	98.51	48.9	3.1	47.9
94-5B ma16.2	pyroxene	50.97	0.43	0.13	27.45	0.00	1.37	16.57	1.19	0.03	0.01	98.13	49.3	2.5	48.2
94-5B ma16.3	pyroxene	50.91	0.41	0.12	27.85	0.00	1.32	16.57	1.15	0.03	0.00	98.36	49.1	2.4	48.5
94-5B ma17.1	pyroxene	50.84	0.59	0.12	27.22	0.00	1.22	16.76	1.21	0.04	0.01	97.98	49.9	2.6	47.5
94-8 ma2.1	pyroxene	51.66	1.26	0.19	13.11	0.00	0.67	11.87	19.71	0.35	0.01	98.82	35.1	41.9	22.9
94-8 ma2.2	pyroxene	51.95	1.35	0.20	12.91	0.11	0.67	12.33	19.59	0.36	0.00	99.46	36.2	41.3	22.5

Appendix C: Continued.

<u>Sample</u>	<u>Mineral</u>	<u>SiO2</u>	<u>Al2O3</u>	<u>TiO2</u>	<u>FeO</u>	<u>Fe2O3</u>	<u>MnO</u>	<u>MgO</u>	<u>CaO</u>	<u>Na2O</u>	<u>Cr2O3</u>	<u>Total</u>	<u>En</u>	<u>Wo</u>	<u>Fs</u>
94-8 ma2.3	pyroxene	51.68	0.95	0.11	15.42	0.00	0.92	10.55	19.36	0.32	0.01	99.31	31.4	41.4	27.3
94-8 ma2.4	pyroxene	51.92	1.33	0.21	12.26	0.04	0.63	12.58	19.78	0.35	0.00	99.11	36.9	41.8	21.3
94-8 ma2.5	pyroxene	51.73	1.22	0.16	12.29	0.30	0.69	12.31	19.98	0.35	0.00	99.03	36.1	42.1	21.8
94-8 ma2.6	pyroxene	51.80	1.10	0.17	12.49	0.00	0.65	12.18	19.96	0.34	0.00	98.69	35.9	42.3	21.8
94-8 ma3.1	pyroxene	51.52	0.89	0.16	13.29	0.00	0.78	11.75	19.66	0.33	0.00	98.39	34.8	41.8	23.4
94-8 ma3.2	pyroxene	51.54	1.32	0.23	13.62	0.35	0.68	11.80	19.43	0.38	0.01	99.34	34.7	41.1	24.1
94-8 ma9.2	pyroxene	52.05	0.95	0.16	13.32	0.00	0.76	11.97	19.90	0.32	0.01	99.45	35.0	41.8	23.1
94-8 ma9.3	pyroxene	52.27	0.95	0.19	12.76	0.01	0.73	12.27	20.20	0.31	0.00	99.69	35.7	42.3	22.1
94-8 ma9.4	pyroxene	52.06	1.06	0.20	12.60	0.12	0.62	12.45	19.88	0.35	0.03	99.37	36.4	41.8	21.9
94-8 ma9.5	pyroxene	51.99	1.04	0.20	12.55	0.27	0.59	12.49	19.80	0.37	0.00	99.29	36.5	41.6	21.9
94-8 ma10.1	pyroxene	52.68	0.77	0.16	12.58	0.10	0.54	12.67	20.33	0.31	0.00	100.13	36.5	42.1	21.4
94-8 ma10.2	pyroxene	52.46	0.89	0.16	12.70	0.04	0.59	12.38	20.32	0.32	0.01	99.87	35.9	42.4	21.7
94-8 ma10.3	pyroxene	52.07	1.14	0.19	13.39	0.00	0.71	12.20	19.48	0.33	0.02	99.51	35.8	41.0	23.2
94-8 ma12.1	pyroxene	51.76	0.91	0.17	13.25	0.51	0.71	12.06	19.69	0.35	0.00	99.40	35.1	41.3	23.6
94-8 ma12.2	pyroxene	52.08	1.06	0.23	12.50	0.15	0.62	12.44	20.05	0.34	0.00	99.45	36.3	42.0	21.7
94-8 ma12.3	pyroxene	52.28	0.84	0.17	11.97	0.00	0.50	12.61	20.28	0.31	0.01	98.98	36.9	42.6	20.5
94-8 ma13.3	pyroxene	52.00	0.98	0.15	13.60	0.00	0.71	11.79	19.70	0.34	0.00	99.26	34.7	41.7	23.6
94-8 ma14.3	pyroxene	53.57	0.98	0.13	13.64	0.00	0.70	10.88	19.53	0.32	0.00	99.75	33.0	42.6	24.4
94-8 ma14.4	pyroxene	51.92	1.38	0.23	13.37	0.19	0.71	12.21	19.40	0.36	0.01	99.78	35.8	40.8	23.4
94-8 ma14.5	pyroxene	51.97	0.97	0.17	12.93	0.32	0.75	12.16	19.82	0.36	0.01	99.46	35.5	41.6	22.9
94-8 ma14.6	pyroxene	52.00	0.94	0.18	13.21	0.14	0.74	12.05	19.90	0.32	0.00	99.49	35.2	41.7	23.1
94-8 ma14.7	pyroxene	50.91	0.93	0.19	12.55	0.26	0.63	11.74	19.94	0.33	0.01	97.48	34.9	42.7	22.4
94-8 ma14.8	pyroxene	52.21	1.22	0.19	13.15	0.14	0.71	12.56	19.35	0.35	0.00	99.87	36.6	40.5	22.9
94-8 ma15.1	pyroxene	51.96	0.93	0.15	12.86	0.31	0.78	12.03	20.14	0.33	0.00	99.49	35.1	42.2	22.8
94-8 ma15.2	pyroxene	51.56	0.93	0.21	13.37	0.06	0.80	11.72	19.75	0.32	0.00	98.72	34.6	41.9	23.6
94-8 ma16.1	pyroxene	52.05	1.22	0.19	13.23	0.14	0.80	12.24	19.54	0.34	0.03	99.78	35.8	41.0	23.2
94-8 ma16.2	pyroxene	53.02	1.13	0.16	14.27	0.00	0.85	12.00	18.73	0.37	0.00	100.53	35.3	39.7	25.0
94-8 ma16.3	pyroxene	52.27	1.22	0.19	11.83	0.38	0.65	12.88	20.01	0.38	0.00	99.81	37.4	41.7	20.9
94-8 ma16.4	pyroxene	52.14	0.97	0.18	12.98	0.16	0.70	12.27	19.99	0.31	0.00	99.69	35.7	41.8	22.6
94-8 ma1.1	pyroxene	51.84	0.51	0.12	27.78	0.00	1.19	17.29	1.21	0.02	0.00	99.97	50.2	2.5	47.2
94-8 ma7.1	pyroxene	51.47	0.56	0.13	27.38	0.00	1.23	16.84	1.24	0.01	0.00	98.86	49.8	2.6	47.5
94-8 ma8.1	pyroxene	52.23	1.59	0.22	22.19	0.00	0.71	21.11	1.19	0.04	0.03	99.31	60.6	2.5	36.9
94-8 ma8.2	pyroxene	53.00	1.61	0.22	19.66	0.00	0.49	22.67	1.41	0.06	0.03	99.15	64.8	2.9	32.3
94-8 ma8.3	pyroxene	53.43	1.23	0.17	19.81	0.00	0.56	23.37	0.94	0.02	0.00	99.52	65.9	1.9	32.2
94-8 ma8.4	pyroxene	51.69	1.09	0.18	25.19	0.00	1.08	18.83	1.09	0.04	0.04	99.22	54.8	2.3	42.9
94-8 ma8.5	pyroxene	51.37	0.53	0.11	27.31	0.00	1.31	17.08	1.20	0.03	0.00	98.95	50.2	2.5	47.2
94-8 ma11.1	pyroxene	51.35	0.42	0.13	28.15	0.00	1.43	16.46	1.26	0.03	0.00	99.21	48.4	2.7	48.9
94-8 ma11.2	pyroxene	51.37	0.44	0.12	28.62	0.00	1.52	16.50	1.25	0.03	0.00	99.85	48.1	2.6	49.3
94-8 ma11.3	pyroxene	51.57	0.41	0.13	28.55	0.00	1.37	16.37	1.27	0.05	0.00	99.71	48.0	2.7	49.3
94-8 ma11.4	pyroxene	51.46	0.35	0.11	28.53	0.00	1.37	16.72	1.24	0.00	0.01	99.79	48.6	2.6	48.8

Appendix C: Continued.

<u>Sample</u>	<u>Mineral</u>	<u>SiO2</u>	<u>Al2O3</u>	<u>TiO2</u>	<u>FeO</u>	<u>Fe2O3</u>	<u>MnO</u>	<u>MgO</u>	<u>CaO</u>	<u>Na2O</u>	<u>Cr2O3</u>	<u>Total</u>	<u>En</u>	<u>Wo</u>	<u>Fs</u>
94-8 ma11.5	pyroxene	51.31	0.47	0.12	28.25	0.00	1.35	16.65	1.23	0.02	0.03	99.44	48.8	2.6	48.7
94-8 ma11.6	pyroxene	51.29	0.45	0.11	28.71	0.00	1.39	16.38	1.24	0.03	0.01	99.61	47.9	2.6	49.4
94-8 ma14.1	pyroxene	51.22	0.61	0.17	28.20	0.00	1.28	16.90	1.15	0.01	0.00	99.55	49.3	2.4	48.3
94-8 ma14.2	pyroxene	51.39	0.37	0.10	28.44	0.00	1.28	16.66	1.22	0.04	0.00	99.49	48.7	2.6	48.8
94-8 ma14.9	pyroxene	52.12	1.38	0.24	23.59	0.00	0.80	20.42	1.07	0.04	0.00	99.66	58.5	2.2	39.3
94-8 ma18.1	pyroxene	51.00	0.77	0.14	27.37	0.00	1.32	16.62	1.10	0.03	0.01	98.37	49.6	2.4	48.1
94-8 ma18.2	pyroxene	51.50	1.11	0.20	25.13	0.00	1.03	18.81	1.08	0.03	0.00	98.88	54.9	2.3	42.8
94-8 ma18.4	pyroxene	52.60	1.05	0.20	23.36	0.00	0.76	20.79	1.19	0.03	0.00	99.98	59.1	2.4	38.5
94-8 ma18.6	pyroxene	52.52	1.25	0.24	22.54	0.03	0.77	21.34	1.21	0.03	0.01	99.93	60.4	2.5	37.1
94-8 ma18.7	pyroxene	51.95	0.58	0.10	26.65	0.00	1.26	18.02	1.15	0.02	0.03	99.76	52.2	2.4	45.4
94-8 ma18.8	pyroxene	52.01	0.98	0.16	26.18	0.00	1.01	18.72	1.12	0.03	0.01	100.22	53.8	2.3	43.9
94-13A ma4.1	pyroxene	50.60	1.25	0.17	26.90	0.00	1.23	16.64	1.22	0.05	0.00	98.04	50.0	2.6	47.4
94-13A ma7.1	pyroxene	52.08	0.99	0.15	12.71	0.00	0.63	12.25	19.94	0.30	0.02	99.06	36.0	42.1	22.0
94-13A ma7.2	pyroxene	52.11	0.87	0.17	12.23	0.12	0.62	12.37	20.30	0.35	0.01	99.13	36.1	42.6	21.2
94-13A ma7.3	pyroxene	52.32	0.90	0.16	12.41	0.00	0.60	12.33	20.18	0.31	0.00	99.21	36.1	42.5	21.4
94-13A ma7.4	pyroxene	51.32	1.44	0.18	12.34	0.25	0.65	12.02	20.02	0.34	0.03	98.58	35.5	42.5	21.9
94-13A ma7.5	pyroxene	52.18	0.98	0.15	12.84	0.00	0.63	12.27	19.94	0.34	0.00	99.35	35.9	41.9	22.1
94-13A ma8.1	pyroxene	51.00	0.52	0.16	27.79	0.00	1.20	16.41	1.20	0.06	0.00	98.35	48.9	2.6	48.5
94-13A ma8.2	pyroxene	50.90	0.48	0.19	28.38	0.00	1.35	16.31	1.23	0.04	0.00	98.88	48.1	2.6	49.3
94-13A ma8.3	pyroxene	51.41	0.46	0.13	27.63	0.00	1.22	16.61	1.27	0.03	0.00	98.77	49.3	2.7	48.0
94-13A ma8.4	pyroxene	51.23	0.50	0.14	27.61	0.00	1.24	16.67	1.22	0.05	0.00	98.66	49.4	2.6	48.0
94-30 ma11.1	pyroxene	52.82	1.17	0.25	9.33	1.04	0.54	14.51	20.60	0.37	0.00	100.65	41.0	41.9	17.2
94-30 ma11.2	pyroxene	53.08	0.96	0.24	9.50	0.77	0.53	14.51	20.74	0.34	0.01	100.68	40.9	42.1	17.0
94-30 ma11.3	pyroxene	55.83	3.01	0.32	10.07	0.00	0.47	12.59	18.23	0.39	0.00	100.92	39.8	41.5	18.7
94-30 ma11.4	pyroxene	52.94	1.08	0.25	9.78	0.77	0.54	14.21	20.72	0.36	0.01	100.65	40.3	42.2	17.5
94-30 ma11.5	pyroxene	52.70	1.12	0.25	9.29	0.88	0.55	14.23	20.71	0.41	0.00	100.14	40.6	42.4	17.0
94-30 ma11.4.1	pyroxene	52.83	1.02	0.25	9.57	0.30	0.54	14.35	20.50	0.34	0.00	99.69	41.1	42.2	16.7
94-30 ma11.4.2	pyroxene	52.32	1.99	0.59	10.30	0.00	0.31	14.68	19.37	0.30	0.02	99.87	42.5	40.3	17.2
94-30 ma11.4.3	pyroxene	52.57	1.42	0.36	9.49	0.27	0.38	14.49	20.42	0.31	0.02	99.73	41.6	42.1	16.3
94-30 ma11.4.4	pyroxene	52.63	1.42	0.37	9.12	0.46	0.37	14.76	20.45	0.32	0.02	99.92	42.1	42.0	15.9
94-30 ma11.4.5	pyroxene	52.48	1.32	0.34	9.50	0.43	0.42	14.42	20.33	0.34	0.02	99.60	41.4	42.0	16.6
94-30 ma11.4.6	pyroxene	52.64	1.15	0.26	9.66	0.33	0.48	14.32	20.48	0.31	0.02	99.64	41.0	42.2	16.8
94-30 ma11.4.7	pyroxene	51.80	2.04	0.66	10.47	0.78	0.30	15.57	17.97	0.29	0.04	99.92	44.6	37.0	18.4
94-30 ma11.5.1	pyroxene	51.15	2.40	0.64	10.72	0.83	0.30	14.01	19.16	0.34	0.02	99.57	40.7	40.1	19.2
94-30 ma11.5.2	pyroxene	51.73	1.77	0.65	11.60	0.52	0.31	14.28	18.44	0.36	0.08	99.73	41.4	38.4	20.2
94-30 ma11.5.3	pyroxene	51.29	2.36	0.65	9.76	0.98	0.32	14.55	19.51	0.29	0.00	99.70	41.9	40.4	17.7
94-30 ma11.6.1	pyroxene	52.14	1.99	0.38	7.69	0.87	0.79	14.39	20.99	0.44	0.00	99.68	41.5	43.5	15.0
94-30 ma11.6.2	pyroxene	52.67	1.29	0.24	8.20	0.57	0.86	14.85	20.43	0.37	0.02	99.48	42.5	42.1	15.4
94-30 ma11.6.3	pyroxene	53.10	1.13	0.22	7.82	0.59	0.87	15.07	20.96	0.34	0.00	100.09	42.7	42.7	14.7
94-30 ma11.6.4	pyroxene	52.13	1.94	0.40	8.05	0.91	0.86	14.55	20.47	0.44	0.01	99.76	41.9	42.4	15.7

Appendix C: Continued.

<u>Sample</u>	<u>Mineral</u>	<u>SiO2</u>	<u>Al2O3</u>	<u>TiO2</u>	<u>FeO</u>	<u>Fe2O3</u>	<u>MnO</u>	<u>MgO</u>	<u>CaO</u>	<u>Na2O</u>	<u>Cr2O3</u>	<u>Total</u>	<u>En</u>	<u>Wo</u>	<u>Fs</u>
94-30 mal17.1	pyroxene	52.29	1.76	0.44	8.93	0.60	0.45	14.63	20.27	0.38	0.03	99.77	42.1	41.9	16.0
94-30 mal17.2	pyroxene	52.26	1.47	0.45	9.23	0.17	0.30	14.85	20.08	0.27	0.04	99.12	42.8	41.6	15.7
94-30 mal17.3	pyroxene	51.55	2.18	0.65	9.03	0.71	0.31	14.23	20.49	0.34	0.00	99.50	41.2	42.6	16.2
94-30 mal18.1	pyroxene	51.66	1.93	0.50	9.51	0.31	0.32	14.10	20.34	0.29	0.01	98.96	41.0	42.5	16.5
94-30 mal18.2	pyroxene	52.36	1.37	0.34	9.50	0.09	0.45	14.27	20.29	0.34	0.00	99.01	41.4	42.3	16.3
94-30 mal18.3	pyroxene	52.07	1.23	0.27	9.66	0.22	0.54	13.96	20.22	0.35	0.00	98.52	40.7	42.3	17.0
94-30 mal19.1	pyroxene	51.59	2.03	0.62	8.72	0.64	0.30	14.24	20.70	0.35	0.01	99.19	41.3	43.1	15.6
94-30 mal19.2	pyroxene	52.32	1.40	0.35	9.22	0.48	0.40	14.54	20.27	0.34	0.01	99.34	41.8	41.9	16.2
94-30 mal19.3	pyroxene	52.06	1.69	0.52	8.71	0.54	0.29	14.62	20.56	0.33	0.06	99.38	42.1	42.6	15.3
94-30 mal19.4	pyroxene	51.33	2.13	0.65	9.95	0.70	0.34	14.69	18.93	0.34	0.00	99.06	42.7	39.5	17.8
94-30 mal110.1	pyroxene	50.60	4.16	0.52	7.31	0.98	0.19	14.68	20.33	0.37	0.56	99.69	43.2	43.0	13.8
94-30 mal110.2	pyroxene	50.98	3.88	0.43	6.60	0.55	0.13	15.02	20.63	0.36	0.70	99.27	44.3	43.7	11.9
94-30 mal110.3	pyroxene	50.54	4.26	0.59	8.31	0.48	0.21	15.38	18.58	0.31	0.62	99.27	45.6	39.6	14.9
94-30 mal110.5	pyroxene	51.96	1.41	0.34	11.29	0.14	0.35	13.66	19.53	0.32	0.01	99.02	39.8	40.9	19.3
94-30 mal111.1	pyroxene	52.65	1.22	0.26	9.53	0.26	0.67	14.14	20.47	0.36	0.00	99.56	40.7	42.4	16.9
94-30 mal111.2	pyroxene	52.73	1.11	0.26	9.55	0.26	0.57	14.18	20.51	0.38	0.00	99.55	40.8	42.4	16.7
94-30 mal111.3	pyroxene	52.20	1.58	0.32	8.93	0.11	0.48	14.36	20.43	0.34	0.00	98.74	41.8	42.7	15.5
94-30 mal111.4	pyroxene	52.39	1.21	0.28	9.02	0.42	0.49	14.29	20.54	0.39	0.04	99.06	41.3	42.7	16.0
94-30 mal17.1	pyroxene	52.07	1.13	0.25	9.56	0.50	0.56	14.00	20.30	0.35	0.00	98.73	40.6	42.3	17.2
94-30 mal17.2	pyroxene	52.43	1.00	0.23	9.23	0.80	0.45	14.17	20.65	0.40	0.03	99.40	40.7	42.6	16.8
94-30 mal17.3	pyroxene	52.48	1.52	0.38	8.96	0.46	0.43	14.64	20.52	0.33	0.05	99.76	42.0	42.3	15.8
94-30 mal17.4	pyroxene	50.97	4.33	0.55	4.56	0.58	0.13	15.47	22.02	0.27	0.66	99.53	45.2	46.3	8.5
94-30 mal17.5	pyroxene	52.58	1.35	0.29	8.13	0.26	0.31	14.98	20.74	0.33	0.02	99.00	43.1	42.9	14.0
94-30 mal12.1	pyroxene	53.08	0.56	0.18	22.39	0.22	0.95	21.74	1.16	0.03	0.00	100.29	60.8	2.3	36.9
94-30 mal12.2	pyroxene	52.86	0.64	0.14	22.68	0.00	1.11	21.11	1.22	0.03	0.00	99.78	59.7	2.5	37.8
94-30 mal12.3	pyroxene	53.21	0.50	0.15	22.44	0.29	1.05	21.73	1.15	0.04	0.00	100.54	60.5	2.3	37.1
94-30 mal12.4	pyroxene	52.83	0.59	0.18	22.23	0.18	0.97	21.62	1.21	0.02	0.02	99.84	60.7	2.5	36.8
94-30 mal12.5	pyroxene	53.19	0.41	0.14	21.90	0.45	1.02	22.06	1.17	0.03	0.00	100.36	61.3	2.3	36.4
94-30 mal12.6	pyroxene	53.25	0.49	0.15	21.87	0.00	0.97	21.86	1.10	0.02	0.04	99.74	61.6	2.2	36.2
94-30 mal12.7	pyroxene	52.74	0.80	0.29	21.54	0.28	0.90	21.88	1.47	0.03	0.00	99.92	61.3	3.0	35.7
94-30 mal13.1	pyroxene	53.06	0.57	0.19	22.03	0.00	1.01	21.66	1.19	0.02	0.00	99.73	61.1	2.4	36.5
94-30 mal13.2	pyroxene	52.60	1.04	0.32	21.01	0.46	0.68	22.25	1.43	0.05	0.02	99.84	62.4	2.9	34.8
94-30 mal13.3	pyroxene	52.57	1.04	0.32	20.68	0.30	0.68	22.24	1.60	0.05	0.01	99.49	62.6	3.2	34.2
94-30 mal13.4	pyroxene	52.39	1.02	0.29	20.71	0.34	0.76	21.93	1.87	0.03	0.03	99.36	61.8	3.8	34.4
94-30 mal13.5	pyroxene	52.67	1.10	0.34	20.47	0.41	0.67	22.69	1.44	0.01	0.05	99.84	63.4	2.9	33.7
94-30 mal13.6	pyroxene	52.92	0.63	0.18	21.45	0.06	0.87	22.15	1.21	0.02	0.01	99.50	62.3	2.4	35.3
94-30 mal13.7	pyroxene	52.64	1.15	0.36	20.40	0.00	0.66	22.48	1.40	0.06	0.01	99.16	63.7	2.8	33.5
94-30 mal17.4	pyroxene	53.38	0.46	0.15	21.80	0.00	0.95	22.02	1.13	0.02	0.00	99.91	61.8	2.3	35.9
94-30 mal17.5	pyroxene	53.11	0.53	0.16	22.02	0.18	1.04	21.90	1.16	0.03	0.02	100.14	61.2	2.3	36.4
94-30 mal17.6	pyroxene	53.09	0.48	0.17	21.75	0.00	1.05	21.71	1.04	0.04	0.00	99.33	61.6	2.1	36.3

Appendix C: Continued.

<u>Sample</u>	<u>Mineral</u>	<u>SiO2</u>	<u>Al2O3</u>	<u>TiO2</u>	<u>FeO</u>	<u>Fe2O3</u>	<u>MnO</u>	<u>MgO</u>	<u>CaO</u>	<u>Na2O</u>	<u>Cr2O3</u>	<u>Total</u>	<u>En</u>	<u>Wo</u>	<u>Fs</u>
94-30 mal112.1	pyroxene	52.91	0.50	0.14	22.12	0.00	1.10	21.58	1.15	0.01	0.00	99.51	60.9	2.3	36.8
94-30 mal112.2	pyroxene	53.08	1.02	0.33	20.64	0.00	0.63	22.61	1.41	0.03	0.00	99.76	63.6	2.9	33.6
94-30 mal112.3	pyroxene	52.94	1.21	0.33	20.54	0.55	0.59	22.78	1.43	0.06	0.02	100.46	63.4	2.9	33.8
94-30 mal112.4	pyroxene	52.75	1.14	0.33	20.71	0.00	0.66	22.07	1.78	0.06	0.02	99.51	62.4	3.6	33.9
94-30 mal112.5	pyroxene	52.88	0.82	0.26	21.58	0.00	0.91	21.91	1.31	0.03	0.01	99.69	61.8	2.6	35.6
94-30 mal116.1	pyroxene	53.09	0.57	0.17	22.47	0.00	1.06	21.49	1.11	0.02	0.01	99.98	60.5	2.3	37.2
94-30 mal116.2	pyroxene	53.10	0.54	0.16	22.57	0.00	1.00	21.60	1.16	0.00	0.03	100.15	60.6	2.3	37.1

<u>Sample</u>	<u>Mineral</u>	<u>SiO2</u>	<u>Al2O3</u>	<u>TiO2</u>	<u>FeO*</u>	<u>MgO</u>	<u>MnO</u>	<u>CaO</u>	<u>Na2O</u>	<u>K2O</u>	<u>Rb2O</u>	<u>BaO</u>	<u>F</u>	<u>Cl</u>	<u>Total</u>	<u>O=FCI</u>	<u>Mg#</u>
94-5B mal1.1	biotite	36.08	13.47	5.93	17.97	10.61	0.20	0.06	0.46	9.05	0.07	0.92	0.56	0.15	95.53	0.27	51.3
94-5B mal1.2	biotite	35.65	13.56	5.97	18.19	10.33	0.17	0.09	0.56	8.82	0.07	0.87	0.63	0.13	95.02	0.29	50.3
94-5B ma2.1	biotite	35.15	13.33	6.00	17.93	10.36	0.12	0.00	0.46	8.98	0.08	1.33	0.54	0.15	94.44	0.26	50.7
94-5B ma2.2	biotite	37.08	13.37	5.62	17.14	9.96	0.14	0.14	0.47	8.51	0.07	1.23	0.53	0.13	94.41	0.25	50.9
94-5B ma2.3	biotite	35.84	13.38	5.91	17.70	10.61	0.13	0.01	0.53	9.10	0.09	0.83	0.52	0.12	94.78	0.25	51.6
94-5B ma2.4	biotite	35.58	13.60	5.86	17.84	10.14	0.20	0.03	0.49	8.82	0.08	1.10	0.80	0.14	94.68	0.37	50.3
94-5B ma2.5	biotite	38.84	13.44	5.12	15.65	9.63	0.17	0.02	0.44	9.92	0.08	0.61	0.51	0.13	94.55	0.24	52.3
94-5B ma3.1	biotite	35.06	13.36	5.76	17.65	10.27	0.16	0.23	0.39	8.27	0.10	0.88	0.71	0.11	92.98	0.33	50.9
94-5B ma4.1	biotite	34.29	13.62	6.21	17.80	9.86	0.19	0.11	0.48	8.22	0.08	1.68	0.66	0.14	93.41	0.31	49.7
94-5B ma4.2	biotite	34.87	13.40	5.98	17.72	10.27	0.19	0.02	0.52	8.84	0.06	1.20	0.57	0.12	93.75	0.27	50.8
94-5B ma4.3	biotite	35.56	13.38	5.91	17.76	10.34	0.19	0.02	0.51	8.88	0.07	1.13	0.60	0.12	94.47	0.28	50.9
94-5B ma5.1	biotite	35.91	13.15	5.82	17.89	10.38	0.15	0.01	0.46	8.90	0.07	1.02	0.54	0.15	94.45	0.26	50.8
94-5B ma5.2	biotite	35.73	13.35	6.05	17.82	10.14	0.17	0.01	0.46	8.93	0.07	1.03	0.67	0.12	94.54	0.31	50.4
94-5B ma5.3	biotite	35.58	13.43	5.89	17.66	10.19	0.20	0.01	0.45	8.80	0.05	1.12	0.55	0.13	94.04	0.26	50.7
94-5B ma5.4	biotite	35.71	13.40	5.92	17.28	11.10	0.21	0.09	0.49	8.92	0.06	0.65	0.67	0.12	94.62	0.31	53.4
94-5B ma5.6	biotite	35.97	13.43	5.85	17.65	10.67	0.16	0.01	0.49	9.04	0.08	0.92	0.54	0.16	94.97	0.26	51.9
94-5B ma5.7	biotite	35.09	14.04	5.78	18.15	10.25	0.20	0.00	0.48	9.11	0.08	0.82	0.52	0.13	94.66	0.25	50.2
94-5B ma6.1	biotite	36.30	13.61	4.18	15.38	12.88	0.60	0.03	0.25	9.92	0.07	0.49	0.57	0.13	94.40	0.27	59.9
94-5B ma6.2	biotite	36.17	13.35	6.04	18.00	10.29	0.14	0.01	0.49	9.01	0.05	0.80	0.53	0.15	95.05	0.26	50.5
94-5B ma6.3	biotite	35.51	13.69	6.19	18.01	10.20	0.18	0.00	0.47	8.79	0.08	1.44	0.60	0.13	95.30	0.28	50.2
94-5B ma6.4	biotite	37.99	13.38	2.98	14.87	13.90	0.57	0.00	0.23	9.83	0.11	0.02	0.90	0.28	95.08	0.44	62.5
94-5B ma6.5	biotite	37.72	13.07	3.31	14.87	13.76	0.51	0.01	0.19	9.95	0.10	0.00	0.73	0.28	94.51	0.37	62.3
94-5B ma7.1	biotite	35.78	13.12	5.89	17.65	10.44	0.20	0.03	0.51	9.09	0.07	0.70	0.53	0.14	94.14	0.25	51.3
94-5B ma7.2	biotite	35.16	13.13	5.71	17.23	10.18	0.19	0.00	0.48	8.69	0.07	0.96	0.57	0.14	92.52	0.27	51.3
94-5B ma7.3	biotite	36.03	13.17	5.91	18.07	10.48	0.16	0.02	0.46	9.01	0.07	0.96	0.59	0.14	95.07	0.28	50.8
94-5B ma7.4	biotite	35.74	13.58	6.23	16.44	11.60	0.17	0.00	0.48	8.99	0.06	1.17	0.81	0.12	95.38	0.37	55.7
94-5B mal11.1	biotite	36.00	13.26	5.77	17.68	10.61	0.15	0.03	0.42	8.85	0.05	0.71	0.50	0.12	94.15	0.24	51.7
94-5B mal11.2	biotite	35.44	13.27	5.83	17.66	10.35	0.17	0.00	0.43	8.90	0.07	1.00	0.54	0.14	93.83	0.26	51.1
94-5B mal16.1	biotite	35.54	13.53	5.98	17.89	10.24	0.22	0.00	0.50	8.87	0.08	1.19	0.57	0.10	94.72	0.26	50.5
94-5B mal16.2	biotite	36.07	13.33	5.75	17.84	10.49	0.17	0.02	0.43	9.00	0.08	0.96	0.59	0.14	94.87	0.28	51.2
94-5B mal16.3	biotite	35.88	13.19	5.79	17.77	10.47	0.17	0.01	0.47	9.01	0.07	0.87	0.54	0.15	94.39	0.26	51.2

Appendix C: Continued.

Sample	Mineral	SiO2	Al2O3	TiO2	FeO*	MgO	MnO	CaO	Na2O	K2O	Rb2O	BaO	F	Cl	Total	O=FCI	Mg#
94-5B ma18.1	biotite	36.32	13.38	5.41	17.51	10.80	0.17	0.06	0.53	8.94	0.06	0.80	0.60	0.13	94.75	0.28	52.4
94-5B ma18.2	biotite	36.35	13.45	5.60	17.57	10.57	0.18	0.01	0.49	8.95	0.07	0.84	0.58	0.15	94.82	0.28	51.8
94-5B ma18.3	biotite	36.36	13.43	5.52	17.42	10.77	0.17	0.04	0.48	8.98	0.07	0.72	0.64	0.13	94.74	0.30	52.4
94-5B fe1.1	biotite	36.25	13.24	5.99	17.73	10.64	0.20	0.05	0.56	8.97	0.08	0.93	0.57	0.13	95.31	0.27	51.7
94-5B fe1.2	biotite	37.41	13.00	5.76	17.41	10.64	0.17	0.14	0.51	8.88	0.08	0.64	0.68	0.14	95.45	0.32	52.1
94-5B fe1.3	biotite	35.67	13.19	6.02	17.73	10.23	0.15	0.05	0.53	8.87	0.09	0.93	0.56	0.12	94.13	0.26	50.7
94-5B fe1.4	biotite	36.63	13.30	6.04	17.77	10.62	0.17	0.10	0.50	9.01	0.09	0.62	0.60	0.14	95.62	0.29	51.6
94-5B fe1.5	biotite	36.84	13.09	5.85	17.72	10.78	0.15	0.04	0.52	9.22	0.08	0.57	0.57	0.14	95.55	0.27	52.0
94-5B fe1.6	biotite	35.93	13.21	5.99	17.82	10.68	0.19	0.02	0.50	9.02	0.07	0.70	0.56	0.12	94.82	0.26	51.7
94-5B fe4.1	biotite	36.16	13.01	5.99	17.21	10.49	0.17	0.14	0.51	8.48	0.08	0.52	0.70	0.10	93.58	0.32	52.1
94-5B fe12.1	biotite	35.45	13.82	5.77	17.82	10.10	0.19	0.08	0.39	8.86	0.07	1.15	0.58	0.25	94.59	0.30	50.3
94-5B fe19.1	biotite	35.63	13.33	6.12	17.89	10.21	0.14	0.00	0.50	8.91	0.06	1.18	0.53	0.13	94.59	0.25	50.4
94-8 ma1.1	biotite	36.41	13.90	5.73	17.20	11.28	0.19	0.03	0.59	8.70	0.09	1.19	0.58	0.07	95.96	0.26	53.9
94-8 ma2.1	biotite	37.57	13.10	5.87	17.66	10.49	0.19	0.05	0.53	8.69	0.06	0.91	0.55	0.15	95.83	0.27	51.4
94-8 ma2.2	biotite	36.48	13.20	5.93	17.90	10.62	0.17	0.02	0.49	9.01	0.07	0.71	0.62	0.12	95.35	0.29	51.4
94-8 ma2.3	biotite	36.31	13.44	6.08	17.81	10.57	0.13	0.03	0.53	8.90	0.10	0.88	0.61	0.13	95.52	0.29	51.4
94-8 ma2.4	biotite	37.07	13.25	5.74	17.64	10.51	0.21	0.05	0.51	8.81	0.09	0.66	0.61	0.13	95.27	0.29	51.5
94-8 ma3.1	biotite	36.71	13.28	5.90	18.20	10.61	0.23	0.07	0.45	8.93	0.07	0.81	0.69	0.15	96.09	0.32	51.0
94-8 ma3.2	biotite	36.12	13.44	6.06	18.28	10.54	0.18	0.01	0.56	9.19	0.05	0.94	0.62	0.13	96.10	0.29	50.7
94-8 ma3.3	biotite	35.87	13.41	5.92	17.83	10.53	0.19	0.00	0.48	8.94	0.05	0.98	0.63	0.16	94.97	0.30	51.3
94-8 ma3.4	biotite	36.59	13.32	6.07	18.32	10.62	0.17	0.00	0.53	9.18	0.07	0.82	0.64	0.11	96.42	0.29	50.8
94-8 ma4.1	biotite	35.88	13.48	6.06	17.75	10.46	0.22	0.00	0.43	9.06	0.07	0.95	0.61	0.15	95.11	0.29	51.2
94-8 ma4.2	biotite	35.64	13.67	6.18	17.89	10.24	0.15	0.00	0.51	8.86	0.06	1.59	0.58	0.13	95.53	0.27	50.5
94-8 ma4.3	biotite	35.03	13.70	6.18	17.95	10.02	0.16	0.00	0.58	8.63	0.07	1.72	0.57	0.15	94.76	0.27	49.9
94-8 ma4.4	biotite	35.45	13.55	6.26	18.14	10.30	0.17	0.02	0.51	8.75	0.06	1.45	0.61	0.11	95.38	0.28	50.3
94-8 ma4.5	biotite	36.42	13.47	6.14	18.11	10.59	0.14	0.01	0.47	8.89	0.06	1.28	0.58	0.11	96.26	0.27	51.0
94-8 ma4.6	biotite	36.31	13.53	6.00	17.96	10.66	0.11	0.01	0.49	9.05	0.07	0.97	0.68	0.14	95.99	0.32	51.4
94-8 ma4.7	biotite	36.80	13.48	6.00	16.52	11.84	0.15	0.00	0.52	9.26	0.07	0.74	0.59	0.14	96.11	0.28	56.1
94-8 ma4.8	biotite	36.39	13.12	5.84	17.77	10.75	0.22	0.02	0.49	9.08	0.06	0.66	0.69	0.13	95.22	0.32	51.9
94-8 ma5.1	biotite	35.91	13.67	6.07	18.20	10.73	0.22	0.02	0.48	9.11	0.07	0.97	0.64	0.11	96.18	0.29	51.3
94-8 ma5.2	biotite	35.85	13.47	5.93	17.29	10.83	0.15	0.02	0.52	9.17	0.07	0.83	0.57	0.13	94.83	0.27	52.8
94-8 ma6.1	biotite	38.65	12.25	4.69	19.98	8.70	0.43	0.07	0.47	8.99	0.10	0.00	0.78	0.23	95.33	0.38	43.7
94-8 ma7.1	biotite	36.20	13.41	5.92	18.17	10.53	0.16	0.02	0.51	8.91	0.08	1.03	0.59	0.15	95.66	0.28	50.8
94-8 ma7.2	biotite	36.21	13.31	5.85	18.13	10.48	0.22	0.05	0.51	8.72	0.04	0.90	0.70	0.15	95.27	0.33	50.7
94-8 ma7.3	biotite	35.92	13.10	5.94	18.04	10.37	0.18	0.07	0.49	8.82	0.09	1.00	1.47	0.16	95.64	0.65	50.6
94-8 ma8.1	biotite	38.89	13.77	4.21	11.52	16.20	0.02	0.07	0.55	9.34	0.08	0.25	0.97	0.09	95.95	0.43	71.5
94-8 ma9.1	biotite	35.53	13.80	5.84	17.54	10.67	0.22	0.00	0.51	8.89	0.07	1.14	0.57	0.11	94.92	0.26	52.0
94-8 ma14.1	biotite	36.63	13.35	6.00	18.13	10.54	0.13	0.00	0.49	9.13	0.05	0.87	0.64	0.12	96.12	0.30	50.9
94-8 ma14.2	biotite	36.49	13.65	6.03	17.84	10.49	0.14	0.03	0.45	9.05	0.06	0.98	0.79	0.13	96.16	0.36	51.2
94-8 ma14.3	biotite	36.46	13.55	5.91	18.28	10.83	0.10	0.00	0.48	9.29	0.07	0.55	0.59	0.12	96.23	0.28	51.4

Appendix C: Continued.

<u>Sample</u>	<u>Mineral</u>	<u>SiO2</u>	<u>Al2O3</u>	<u>TiO2</u>	<u>FeO*</u>	<u>MgO</u>	<u>MnO</u>	<u>CaO</u>	<u>Na2O</u>	<u>K2O</u>	<u>Rb2O</u>	<u>BaO</u>	<u>F</u>	<u>Cl</u>	<u>Total</u>	<u>O=FCI</u>	<u>Mg#</u>
94-8 ma14.4	biotite	36.32	13.48	5.92	18.02	10.75	0.19	0.00	0.48	9.09	0.07	1.00	0.61	0.11	96.08	0.28	51.5
94-8 ma16.1	biotite	36.34	13.43	6.01	17.80	10.55	0.18	0.05	0.49	8.90	0.10	0.81	0.66	0.15	95.46	0.31	51.4
94-8 ma16.2	biotite	36.31	13.68	5.92	18.22	10.51	0.26	0.05	0.56	9.10	0.06	0.89	1.08	0.16	96.83	0.49	50.7
94-8 ma16.3	biotite	36.45	13.45	6.02	18.15	10.50	0.18	0.05	0.47	9.12	0.07	0.74	0.71	0.13	96.02	0.33	50.8
94-8 ma17.1	biotite	35.83	13.73	6.14	17.83	10.53	0.17	0.00	0.50	8.98	0.06	1.22	0.59	0.13	95.72	0.28	51.3
94-8 ma17.2	biotite	36.44	13.39	6.00	17.75	10.72	0.21	0.00	0.54	9.17	0.11	0.79	0.57	0.15	95.83	0.27	51.8
94-8 fe6.1	biotite	37.32	13.72	4.73	18.00	10.40	0.18	0.10	0.56	8.80	0.05	0.90	0.80	0.10	95.65	0.36	50.7
94-8 fe8.1	biotite	36.25	13.34	6.70	17.18	10.89	0.11	0.06	0.49	8.99	0.07	1.16	0.93	0.17	96.34	0.43	53.0
94-8 fe8.2	biotite	36.64	13.10	6.52	17.31	10.80	0.11	0.04	0.53	8.91	0.06	0.91	1.40	0.15	96.51	0.63	52.7
94-8 fe17.1	biotite	36.64	13.40	5.91	18.08	10.51	0.14	0.03	0.48	8.92	0.04	0.91	0.78	0.16	96.01	0.37	50.9
94-8 fe17.2	biotite	36.19	13.58	5.88	18.01	10.61	0.18	0.14	0.52	8.92	0.06	0.91	0.71	0.15	95.85	0.33	51.2
94-8 fe18.4	biotite	37.00	13.35	5.97	18.37	10.42	0.21	0.05	0.48	8.89	0.06	0.97	0.59	0.14	96.49	0.28	50.3
94-13a ma1.1	biotite	35.25	13.51	6.12	18.15	9.98	0.20	0.01	0.51	8.82	0.06	1.41	0.60	0.13	94.76	0.28	49.5
94-13a ma1.2	biotite	35.69	13.16	6.01	17.67	10.19	0.19	0.00	0.51	9.04	0.05	0.89	0.64	0.13	94.18	0.30	50.7
94-13a ma2.1	biotite	35.70	12.73	5.02	20.83	8.88	0.54	0.00	0.47	9.11	0.06	0.81	0.80	0.27	95.23	0.40	43.2
94-13a ma3.1	biotite	35.65	13.58	5.93	17.82	10.14	0.20	0.03	0.51	8.74	0.05	1.23	0.61	0.11	94.59	0.28	50.4
94-13a ma3.2	biotite	36.36	12.57	4.79	20.61	8.97	0.43	0.09	0.44	9.31	0.09	0.00	0.77	0.21	94.67	0.37	43.7
94-13a ma3.3	biotite	35.93	13.24	5.84	17.16	10.54	0.23	0.01	0.56	9.01	0.09	0.85	0.62	0.11	94.19	0.29	52.3
94-13a ma3.4	biotite	35.58	13.21	5.89	17.91	10.49	0.17	0.03	0.56	9.00	0.07	0.92	0.72	0.15	94.70	0.34	51.1
94-13a ma3.5	biotite	36.08	13.48	5.88	17.76	10.61	0.18	0.00	0.50	8.98	0.09	0.88	0.64	0.14	95.23	0.30	51.6
94-13a ma4.1	biotite	36.50	12.57	5.06	20.48	8.74	0.33	0.05	0.44	9.16	0.08	0.01	0.79	0.20	94.43	0.38	43.2
94-13a ma4.2	biotite	36.08	12.66	5.11	19.21	9.89	0.26	0.00	0.46	9.33	0.08	0.20	0.76	0.19	94.23	0.36	47.8
94-13a ma6.1	biotite	37.26	12.89	4.96	19.37	9.27	0.35	0.00	0.45	9.29	0.10	0.00	1.08	0.19	95.23	0.50	46.0
94-13a ma6.2	biotite	36.68	12.38	5.02	20.14	9.12	0.33	0.02	0.47	9.43	0.09	0.00	0.90	0.19	94.76	0.42	44.7
94-13a ma6.3	biotite	36.07	12.99	5.77	18.08	10.00	0.19	0.05	0.54	8.99	0.08	0.67	1.24	0.17	94.84	0.56	49.6
94-13a ma7.1	biotite	36.66	12.56	4.78	19.90	8.60	0.34	0.04	0.49	9.18	0.09	0.04	0.75	0.20	93.66	0.36	43.5
94-13a ma7.2	biotite	35.82	12.50	4.63	21.62	8.29	0.48	0.08	0.46	9.02	0.09	0.00	0.83	0.25	94.10	0.41	40.6
94-13a ma9.1	biotite	35.71	13.50	5.91	17.65	9.72	0.21	0.04	0.54	8.70	0.05	1.34	1.30	0.13	94.79	0.58	49.5
94-13a ma9.2	biotite	36.14	12.58	4.75	19.83	8.84	0.46	0.02	0.48	9.46	0.08	0.00	0.83	0.15	93.61	0.38	44.3
94-13a ma9.3	biotite	35.82	12.40	4.78	19.97	9.09	0.53	0.03	0.46	9.43	0.08	0.00	0.81	0.20	93.58	0.39	44.8
94-13a fe7.1	biotite	36.46	12.85	4.77	19.94	9.26	0.48	0.05	0.48	9.37	0.07	0.00	0.81	0.21	94.79	0.39	45.3
94-13a fe7.2	biotite	37.63	12.61	4.60	19.46	9.25	0.40	0.03	0.50	9.36	0.10	0.00	0.81	0.19	94.96	0.38	45.9
94-15 ma1.1	biotite	34.82	13.45	5.26	21.13	8.41	0.44	0.02	0.43	8.77	0.07	1.44	0.75	0.22	95.19	0.37	41.5
94-15 ma1.2	biotite	37.10	12.69	4.83	20.89	9.31	0.47	0.05	0.45	9.24	0.06	0.00	0.85	0.15	96.10	0.39	44.3
94-15 ma1.3	biotite	37.03	12.73	4.82	20.38	9.23	0.50	0.06	0.44	9.13	0.07	0.00	1.64	0.20	96.26	0.74	44.7
94-15 ma2.1	biotite	36.30	12.68	4.63	21.54	8.35	0.48	0.07	0.46	8.92	0.10	0.00	0.79	0.23	94.56	0.38	40.9
94-15 ma2.2	biotite	36.27	12.93	4.90	22.06	8.45	0.57	0.08	0.45	9.15	0.09	0.09	0.82	0.25	96.12	0.40	40.6
94-15 ma2.3	biotite	35.46	12.81	4.64	22.76	7.93	0.48	0.10	0.40	8.85	0.09	0.00	1.75	0.24	95.50	0.79	38.3
94-15 ma3.2	biotite	36.54	12.68	4.78	22.50	8.41	0.58	0.00	0.43	9.29	0.08	0.00	1.36	0.26	96.92	0.63	40.0
94-15 ma4.1	biotite	36.72	12.77	4.80	21.40	8.23	0.50	0.04	0.40	9.26	0.09	0.03	1.50	0.22	95.97	0.68	40.7

Appendix C: Continued.

Sample	Mineral	SiO2	Al2O3	TiO2	FeO*	MgO	MnO	CaO	Na2O	K2O	Rb2O	BaO	F	Cl	Total	O=FeCl	Mg#
94-15 ma6.1	biotite	36.47	12.61	4.86	21.82	8.26	0.45	0.00	0.41	9.49	0.09	0.00	0.87	0.23	95.60	0.42	40.3
94-15 ma7.1	biotite	36.00	12.62	4.77	22.02	8.32	0.57	0.00	0.43	9.43	0.09	0.03	0.82	0.22	95.35	0.39	40.2
94-15 ma17.1	biotite	35.39	13.17	5.20	21.50	7.52	0.54	0.02	0.43	8.61	0.06	1.57	1.81	0.27	96.18	0.83	38.4
94-15 ma18.1	biotite	36.10	13.07	5.00	22.08	8.24	0.53	0.00	0.46	9.29	0.08	0.63	0.86	0.22	96.56	0.41	40.0
94-15 ma18.2	biotite	35.02	13.08	5.14	21.46	8.08	0.48	0.01	0.48	8.86	0.06	1.16	1.93	0.24	96.00	0.87	40.2
94-15 ma19.1	biotite	36.36	12.80	4.89	21.86	8.45	0.49	0.01	0.47	9.26	0.07	0.27	0.83	0.23	96.01	0.40	40.8
94-15 fe5.1	biotite	36.60	12.93	4.86	22.01	8.36	0.59	0.08	0.43	9.20	0.10	0.00	1.30	0.26	96.71	0.61	40.4
94-15 fe13.1	biotite	36.30	12.93	4.77	22.56	8.12	0.54	0.01	0.42	9.52	0.07	0.00	1.76	0.27	97.28	0.80	39.1
92-22 12.2	biotite	35.67	13.35	5.89	18.84	10.28	0.15	0.03	0.50	8.87	0.06	0.94	1.29	0.13	96.01	0.57	49.3
94-30 ma12.1	biotite	36.71	13.71	6.26	14.01	13.60	0.13	0.02	0.63	8.93	0.08	1.12	1.08	0.10	96.38	0.48	63.4
94-30 ma12.2	biotite	37.30	13.26	6.33	13.80	12.33	0.11	0.05	0.56	8.49	0.07	1.64	1.02	0.10	95.05	0.45	61.4
94-30 ma12.3	biotite	36.94	13.43	6.34	13.86	13.60	0.11	0.04	0.63	9.00	0.08	0.96	1.12	0.10	96.21	0.50	63.6
94-30 ma12.4	biotite	35.35	13.71	6.45	13.95	12.83	0.13	0.02	0.57	8.62	0.06	1.75	1.07	0.12	94.67	0.48	62.1
94-30 ma12.5	biotite	37.25	13.63	6.40	13.97	13.27	0.14	0.03	0.58	8.70	0.09	1.40	1.11	0.12	96.68	0.49	62.9
94-30 ma13.1	biotite	36.71	13.61	5.30	15.83	11.89	0.33	0.01	0.54	8.89	0.07	0.96	0.67	0.15	94.94	0.32	57.2
94-30 ma13.2	biotite	36.23	13.40	5.18	15.85	12.11	0.27	0.04	0.54	9.19	0.07	1.07	0.68	0.13	94.75	0.32	57.7
94-30 ma14.1	biotite	40.23	12.63	4.87	14.91	12.26	0.31	0.07	0.54	9.09	0.09	0.00	0.87	0.14	96.01	0.40	59.5
94-30 ma14.2	biotite	40.92	12.80	4.96	13.25	12.15	0.23	0.14	0.19	8.19	0.16	0.00	0.62	0.12	93.73	0.29	62.0
94-30 ma15.2	biotite	37.60	13.20	4.99	15.18	12.80	0.30	0.04	0.54	9.44	0.07	0.12	0.64	0.11	95.09	0.29	60.1
94-30 ma15.4	biotite	38.88	13.04	4.96	15.52	12.74	0.34	0.05	0.49	9.16	0.12	0.03	0.66	0.15	96.16	0.31	59.4
94-30 ma15.5	biotite	37.22	13.55	5.08	15.47	12.19	0.29	0.02	0.51	9.38	0.08	0.02	0.84	0.11	94.80	0.38	58.4
94-30 ma16.1	biotite	38.13	13.07	4.97	15.70	12.77	0.30	0.05	0.55	9.18	0.12	0.00	0.68	0.13	95.66	0.31	59.2
94-30 ma17.1	biotite	35.84	13.57	6.38	13.60	13.40	0.12	0.01	0.63	8.76	0.07	1.96	1.06	0.12	95.52	0.48	63.7
94-30 ma18.1	biotite	36.85	13.36	5.13	16.02	12.74	0.38	0.00	0.57	9.12	0.10	0.72	0.67	0.13	95.78	0.31	58.6
94-30 ma18.2	biotite	39.02	13.02	4.85	15.36	12.35	0.32	0.04	0.57	9.09	0.07	0.57	0.63	0.09	95.98	0.29	58.9
94-30 ma19.1	biotite	36.95	13.12	5.11	16.14	11.73	0.37	0.04	0.53	9.05	0.08	0.66	0.64	0.14	94.55	0.30	56.4
94-30 ma19.2	biotite	40.35	12.38	4.64	15.07	12.33	0.35	0.06	0.52	9.01	0.13	0.00	0.64	0.12	95.65	0.30	59.3
94-31 ma8.1	biotite	36.94	13.42	5.12	16.75	12.17	0.44	0.00	0.54	9.19	0.07	0.93	1.49	0.09	97.16	0.65	56.4
94-31 ma10.1	biotite	38.08	12.96	4.88	15.68	12.75	0.42	0.02	0.51	9.45	0.09	0.00	0.84	0.15	95.86	0.39	59.2
94-31 ma10.2	biotite	37.90	13.04	4.81	15.92	12.90	0.38	0.02	0.61	9.14	0.10	0.00	0.77	0.16	95.75	0.36	59.1
94-31 ma12.1	biotite	37.67	13.31	5.86	14.20	14.11	0.12	0.00	0.60	9.26	0.07	0.79	1.72	0.08	97.78	0.74	63.9
94-9B 2.1	biotite	36.43	14.19	5.16	15.37	12.54	0.25	0.07	0.50	8.98	0.06	1.35	0.64	0.12	95.71	0.30	59.3
94-9B 6.1	biotite	36.85	13.56	5.17	16.00	12.58	0.34	0.04	0.53	9.23	0.06	0.81	0.61	0.11	95.91	0.29	58.4
94-9B 13.1	biotite	37.69	12.88	5.50	15.05	11.45	0.26	0.43	0.39	8.38	0.26	0.79	0.80	0.13	94.14	0.37	57.6
94-9B 13.2	biotite	37.04	13.37	5.17	15.85	11.97	0.34	0.17	0.41	8.16	0.09	0.96	0.59	0.08	94.19	0.27	57.4
94-9B 13.3	biotite	36.15	13.63	5.30	16.38	12.24	0.36	0.06	0.47	8.84	0.06	1.50	0.65	0.14	95.78	0.30	57.1
94-9B 14.1	biotite	37.58	12.83	4.87	16.13	12.12	0.35	0.03	0.39	9.21	0.13	0.00	0.63	0.10	94.37	0.29	57.3
94-9B 15.1	biotite	38.79	12.62	5.25	14.35	11.69	0.24	0.13	0.33	8.21	0.37	0.08	0.70	0.09	93.08	0.31	59.2
94-9B 15.2	biotite	36.96	13.58	5.14	15.85	12.51	0.44	0.04	0.49	9.22	0.09	0.45	0.60	0.12	95.51	0.28	58.5
94-9B 15.3	biotite	37.01	13.38	5.03	15.99	12.56	0.35	0.02	0.47	9.25	0.07	0.42	0.67	0.14	95.37	0.31	58.3

Appendix C: Continued.

Sample	Mineral	SiO2	Al2O3	TiO2	FeO*	MgO	MnO	CaO	Na2O	K2O	Rb2O	BaO	F	Cl	Total	O=FCI	Mg#
94-9B 16.1	biotite	36.44	13.41	5.19	17.13	12.07	0.42	0.00	0.48	9.00	0.08	1.13	0.63	0.14	96.14	0.30	55.7
94-9B 16.2	biotite	36.69	13.34	5.34	16.03	12.40	0.33	0.02	0.47	9.02	0.09	1.01	0.59	0.11	95.43	0.27	58.0
94-9B 16.3	biotite	37.44	13.19	5.13	15.63	12.06	0.26	0.09	0.47	8.63	0.12	0.84	0.64	0.12	94.65	0.30	57.9
94-9B 17.1	biotite	36.87	13.73	5.30	14.22	13.50	0.12	0.01	0.57	8.98	0.10	1.13	0.65	0.10	95.28	0.30	62.9
94-9B 17.2	biotite	38.30	13.58	4.68	13.85	14.21	0.20	0.02	0.49	9.05	0.17	0.76	0.69	0.09	96.12	0.31	64.7
94-9B 17.3	biotite	37.24	13.62	4.97	14.29	13.56	0.15	0.02	0.52	8.99	0.09	0.99	0.59	0.10	95.12	0.27	62.8

Sample	Mineral	SiO2	TiO2	Al2O3	Cr2O3	FeO*	V2O5	MnO	MgO	ZnO	NiO	ZrO2	Nb2O5	Total*	Fe2O3	FeO	Total
94-5B ox5.1	ilmenite	0.02	49.36	0.10	0.00	46.75	0.28	1.04	1.72	0.00	0.00	0.00	0.00	99.28	7.18	40.29	100.00
94-5B ox5.2	ilmenite	0.05	48.93	0.09	0.01	47.13	0.28	1.08	1.70	0.00	0.00	0.00	0.00	99.26	7.98	39.94	100.05
94-5B ox5.3	ilmenite	0.01	49.14	0.12	0.00	47.23	0.27	0.98	1.71	0.12	0.01	0.00	0.00	99.60	8.01	40.03	100.40
94-5B ox1.1	magnetite	0.10	11.86	1.81	0.04	79.50	0.38	0.56	0.75	0.10	0.03	0.00	0.00	95.12	43.32	40.52	99.45
94-5B ox1.2	magnetite	0.13	8.32	1.86	0.05	80.40	0.37	0.56	0.75	0.09	0.00	0.00	0.00	92.53	48.60	36.66	97.39
94-5B ox1.3	magnetite	0.11	13.27	1.79	0.01	78.06	0.37	0.75	1.00	0.14	0.02	0.00	0.00	95.51	40.86	41.29	99.60
94-5B ox1.4	magnetite	0.11	3.71	2.22	0.05	85.92	0.39	0.39	0.52	0.04	0.02	0.00	0.00	93.36	58.21	33.54	99.20
94-5B ox2.3	magnetite	0.06	10.12	1.88	0.04	81.30	0.43	0.61	0.84	0.16	0.04	0.00	0.00	95.48	47.19	38.84	100.20
94-5B ox3.1	magnetite	0.14	9.42	1.38	0.12	79.21	0.34	0.51	1.39	0.04	0.00	0.00	0.00	92.54	47.26	36.68	97.27
94-5B ox3.2	magnetite	0.60	15.09	1.49	0.06	73.79	0.42	0.91	1.62	0.17	0.03	0.00	0.00	94.18	35.50	41.85	97.73
94-5B ox3.3	magnetite	0.11	14.19	1.31	0.05	75.90	0.34	0.72	0.92	0.06	0.00	0.00	0.00	93.61	38.11	41.61	97.42
94-5B ox4.1	magnetite	0.26	4.99	2.25	0.04	83.43	0.43	0.48	0.64	0.18	0.00	0.00	0.00	92.70	54.70	34.21	98.17
94-5B ox4.2	magnetite	0.26	9.93	2.08	0.00	78.38	0.41	0.61	0.82	0.13	0.02	0.00	0.00	92.65	44.79	38.08	97.13
94-5B ox4.3	magnetite	0.20	5.35	2.38	0.06	83.79	0.41	0.38	0.62	0.24	0.01	0.00	0.00	93.44	54.46	34.78	98.89
94-5B ox5.4	magnetite	0.09	15.56	1.99	0.03	75.93	0.33	0.66	1.09	0.25	0.04	0.00	0.00	95.98	36.32	43.25	99.61
94-5B ox5.5	magnetite	0.10	11.63	2.07	0.03	79.66	0.31	0.54	0.90	0.27	0.01	0.00	0.00	95.51	43.94	40.12	99.90
94-5B ox6.1	magnetite	0.16	15.93	1.80	0.05	74.87	0.32	0.82	1.13	0.25	0.10	0.00	0.00	95.43	35.23	43.17	98.96
94-5B ox6.2	magnetite	0.07	26.94	1.17	0.02	65.04	0.30	1.13	1.79	0.23	0.04	0.00	0.00	96.74	50.36	19.73	101.79
94-5B ox6.3	magnetite	0.12	20.53	1.47	0.00	68.62	0.30	1.05	1.43	0.12	0.02	0.00	0.00	93.66	59.73	14.88	99.65
94-5B ox6.4	magnetite	2.29	5.34	2.22	0.01	81.44	0.32	0.46	0.71	0.25	0.06	0.00	0.00	93.08	49.39	37.00	98.03
94-5B ox8.1	magnetite	0.08	18.25	1.50	0.05	72.77	0.36	0.85	1.17	0.15	0.04	0.00	0.00	95.23	30.82	45.03	98.31
94-5B ox8.2	magnetite	0.09	10.76	1.90	0.04	80.31	0.36	0.60	0.87	0.21	0.06	0.00	0.00	95.18	45.67	39.22	99.76
94-5B ox8.3	magnetite	0.11	4.23	2.30	0.05	85.52	0.39	0.46	0.53	0.21	0.03	0.00	0.00	93.84	57.38	33.89	99.58
94-5B ox8.4	magnetite	0.22	5.28	2.12	0.01	84.50	0.41	0.50	0.62	0.23	0.02	0.00	0.00	93.93	55.28	34.76	99.46
94-5B ox8.5	magnetite	0.15	14.55	1.77	0.02	75.83	0.36	0.66	0.99	0.22	0.00	0.00	0.00	94.55	37.44	42.15	98.31
94-5B ox8.6	magnetite	0.10	4.41	2.28	0.05	84.89	0.40	0.41	0.60	0.21	0.00	0.00	0.00	93.33	56.72	33.85	99.02
94-5B ox9.1	magnetite	0.08	8.69	1.95	0.03	82.60	0.39	0.62	1.54	0.32	0.00	0.00	0.00	96.21	51.02	36.69	101.32
94-5B ox9.2	magnetite	0.08	22.10	1.36	0.03	69.19	0.35	0.82	2.54	0.19	0.00	0.00	0.00	96.66	24.94	46.75	99.16
94-5B ox9.3	magnetite	0.07	7.18	2.03	0.04	83.53	0.38	0.50	1.32	0.16	0.03	0.00	0.00	95.23	53.22	35.64	100.56
94-5B ox10.1	magnetite	0.07	5.97	2.08	0.05	83.94	0.43	0.47	0.75	0.17	0.00	0.00	0.00	93.92	54.32	35.06	99.36
94-5B ox10.2	magnetite	0.10	12.45	1.69	0.01	77.98	0.35	0.58	1.00	0.11	0.00	0.00	0.00	94.25	41.82	40.35	98.44

Appendix C: Continued.

Sample	Mineral	SiO2	TiO2	Al2O3	Cr2O3	FeO*	V2O5	MnO	MgO	ZnO	NiO	ZrO2	Nb2O5	Total*	Fe2O3	FeO	Total
94-5B ox10.3	magnetite	0.07	6.04	2.18	0.06	81.49	0.48	0.55	0.73	0.18	0.00	0.00	0.00	91.77	52.37	34.37	97.02
94-5B ox10.4	magnetite	0.08	9.53	1.58	0.03	81.16	0.48	0.60	0.93	0.00	0.03	0.00	0.03	94.45	47.97	38.00	99.22
94-5B ox10.5	magnetite	0.08	4.51	2.33	0.05	84.99	0.47	0.46	0.55	0.17	0.03	0.02	0.00	93.66	56.61	34.04	99.30
94-5B ma13.1	magnetite	0.09	7.48	2.17	0.04	83.06	0.43	0.54	0.76	0.09	0.01	0.00	0.00	94.69	51.59	36.63	99.85
94-5B ma9.1	magnetite	0.10	16.74	1.65	0.04	72.83	0.42	0.88	1.16	0.08	0.00	0.00	0.00	93.91	32.71	43.40	97.19
94-5B fe7.1	magnetite	0.10	18.86	1.45	0.02	71.56	0.42	1.29	1.38	0.06	0.00	0.00	0.02	95.16	29.61	44.91	98.10
94-5B fe12.1	magnetite	0.13	11.32	1.74	0.01	79.26	0.32	0.79	0.78	0.15	0.00	0.00	0.04	94.54	44.11	39.57	98.91
94-5B fe19.1	magnetite	0.11	11.02	1.32	0.10	79.83	0.50	0.46	1.37	0.05	0.02	0.00	0.04	94.81	45.56	38.83	99.34
94-8 ox8.1	ilmenite	0.04	49.93	0.11	0.00	48.12	0.29	1.02	1.66	0.04	0.00	0.02	0.08	101.31	8.02	40.90	102.01
94-8 ox8.2	ilmenite	0.02	49.68	0.10	0.00	47.79	0.35	0.98	1.64	0.00	0.00	0.08	0.10	100.73	7.80	40.77	101.34
94-8 ox8.3	ilmenite	0.00	50.45	0.11	0.02	47.08	0.26	0.97	1.69	0.06	0.00	0.08	0.03	100.74	6.39	41.33	101.28
94-8 ox1.1	magnetite	0.07	9.22	2.08	0.03	81.50	0.46	0.55	0.75	0.14	0.04	0.03	0.05	94.91	48.23	38.10	99.66
94-8 ox1.2	magnetite	0.10	11.32	1.73	0.03	81.22	0.50	0.63	0.77	0.24	0.00	0.00	0.08	96.61	45.47	40.30	101.08
94-8 ox1.3	magnetite	0.19	11.42	1.79	0.01	80.04	0.48	0.60	0.81	0.15	0.00	0.00	0.00	95.48	44.27	40.21	99.91
94-8 ox1.4	magnetite	0.17	9.40	1.96	0.02	80.65	0.51	0.52	0.76	0.17	0.00	0.00	0.00	94.16	47.22	38.16	98.88
94-8 ox1.5	magnetite	0.44	9.62	1.92	0.00	81.50	0.44	0.61	0.69	0.10	0.00	0.00	0.00	95.33	47.06	39.15	100.04
94-8 ox3.1	magnetite	0.98	9.43	1.89	0.10	80.60	0.47	0.64	1.42	0.12	0.00	0.04	0.00	95.69	46.66	38.61	100.32
94-8 ox3.2	magnetite	0.16	9.98	1.98	0.16	80.10	0.42	0.70	1.57	0.05	0.03	0.02	0.00	95.16	47.17	37.66	99.88
94-8 ox3.3	magnetite	0.10	10.19	1.74	0.09	81.61	0.43	0.67	1.46	0.17	0.02	0.00	0.01	96.50	48.17	38.26	101.31
94-8 ox3.4	magnetite	0.08	5.80	2.07	0.13	83.58	0.44	0.48	0.56	0.18	0.05	0.03	0.02	93.39	54.03	34.96	98.76
94-8 ox3.5	magnetite	0.63	7.88	1.97	0.09	81.37	0.42	0.59	1.00	0.18	0.02	0.00	0.00	94.15	49.36	36.95	99.08
94-8 ox4.1	magnetite	0.09	9.20	1.97	0.04	81.28	0.48	0.54	0.64	0.21	0.03	0.05	0.01	94.52	48.00	38.08	99.27
94-8 ox4.2	magnetite	0.12	11.68	1.75	0.00	80.31	0.40	0.63	0.84	0.27	0.02	0.02	0.01	96.05	44.45	40.32	100.48
94-8 ox4.3	magnetite	0.09	10.87	1.77	0.00	80.73	0.44	0.56	0.78	0.17	0.00	0.00	0.00	95.42	45.64	39.66	99.99
94-8 ox5.1	magnetite	0.11	11.88	1.27	0.04	79.66	0.16	0.90	0.50	0.23	0.02	0.00	0.00	94.77	43.75	40.29	99.15
94-8 ox5.2	magnetite	0.17	7.20	2.13	0.03	81.71	0.51	0.58	0.63	0.22	0.01	0.00	0.01	93.20	50.77	36.03	98.27
94-8 ox6.1	magnetite	0.09	10.08	2.14	0.06	81.40	0.53	0.59	0.99	0.14	0.00	0.02	0.03	96.05	47.22	38.91	100.74
94-8 ox6.2	magnetite	0.09	9.38	2.10	0.00	81.76	0.48	0.56	0.90	0.18	0.05	0.01	0.08	95.57	48.41	38.20	100.33
94-8 ox6.3	magnetite	0.11	9.71	2.11	0.03	80.99	0.48	0.61	0.86	0.23	0.00	0.09	0.05	95.27	47.34	38.40	99.87
94-8 ox7.1	magnetite	2.65	12.14	2.21	0.05	76.14	0.44	0.56	0.70	0.20	0.00	0.00	0.05	95.14	35.69	44.02	98.66
94-8 ox7.2	magnetite	0.11	12.01	1.78	0.06	80.08	0.46	0.58	0.85	0.27	0.00	0.00	0.04	96.24	43.76	40.71	100.58
94-8 fe1.1	magnetite	0.42	8.04	1.30	0.02	81.42	0.14	1.06	0.37	0.23	0.00	0.07	0.00	93.06	49.58	36.81	97.95
94-8 fe19.1	magnetite	1.22	17.78	1.66	0.03	71.66	0.49	0.75	1.00	0.21	0.02	0.08	0.00	94.88	28.23	46.25	97.63
94-13A ox4.1	ilmenite	0.02	48.27	0.13	0.00	47.47	0.30	1.21	1.41	0.01	0.00	0.08	0.07	98.96	8.64	39.69	99.68
94-13A ox4.2	ilmenite	0.01	48.50	0.33	0.00	46.69	0.30	1.06	1.55	0.05	0.00	0.05	0.04	98.58	7.74	39.73	99.28
94-13A ox4.3	ilmenite	0.02	48.62	0.12	0.02	47.00	0.25	1.17	1.55	0.01	0.00	0.08	0.02	98.86	8.01	39.79	99.58
94-13A ox4.4	ilmenite	0.01	49.02	0.20	0.01	46.12	0.31	1.08	1.53	0.04	0.02	0.03	0.00	98.38	6.55	40.22	99.00
94-13A ox1.1	magnetite	0.06	10.19	1.16	0.00	77.74	0.12	1.42	0.43	0.21	0.00	0.00	0.00	91.32	45.03	37.22	95.83
94-13A ox1.2	magnetite	0.12	10.34	1.27	0.00	77.50	0.14	1.43	0.39	0.26	0.02	0.00	0.00	91.49	44.49	37.46	95.94
94-13A ox2.2	magnetite	0.64	8.61	1.18	0.02	79.76	0.11	1.49	0.29	0.30	0.00	0.00	0.00	92.39	47.53	36.99	97.15

Appendix C: Continued.

<u>Sample</u>	<u>Mineral</u>	<u>SiO2</u>	<u>TiO2</u>	<u>Al2O3</u>	<u>Cr2O3</u>	<u>FeO*</u>	<u>V2O5</u>	<u>MnO</u>	<u>MgO</u>	<u>ZnO</u>	<u>NiO</u>	<u>ZrO2</u>	<u>Nb2O5</u>	<u>Total*</u>	<u>Fe2O3</u>	<u>FeO</u>	<u>Total</u>
94-13A ox3.1	magnetite	0.82	10.30	1.16	0.02	77.20	0.15	0.84	0.31	0.25	0.02	0.00	0.00	91.06	42.58	38.88	95.32
94-13A ox3.2	magnetite	0.77	12.17	1.10	0.05	75.54	0.17	0.76	0.33	0.21	0.00	0.01	0.00	91.09	38.90	40.54	94.98
94-13A ox5.1	magnetite	0.08	7.64	1.38	0.02	79.91	0.13	1.02	0.32	0.34	0.01	0.00	0.00	90.86	49.53	35.34	95.81
94-13A ox6.1	magnetite	0.07	8.57	1.43	0.02	80.94	0.12	1.00	0.37	0.44	0.00	0.00	0.00	92.96	49.15	36.72	97.89
94-13A fe9.1	magnetite	0.08	10.21	1.29	0.01	77.26	0.09	1.49	0.42	0.36	0.03	0.00	0.00	91.24	44.71	37.03	95.72
94-13A fe12.1	magnetite	0.11	5.84	1.39	0.00	81.86	0.17	1.11	0.29	0.36	0.06	0.00	0.00	91.20	53.39	33.83	96.55
94-13A fe14.1	magnetite	1.23	11.88	1.11	0.00	76.00	0.11	1.04	0.17	0.25	0.01	0.00	0.06	91.86	38.87	41.03	95.70
94-13A fe14.2	magnetite	0.32	13.91	0.97	0.01	75.67	0.11	1.90	0.30	0.22	0.02	0.01	0.05	93.49	38.39	41.13	97.27
94-13A fe14.3	magnetite	0.13	10.17	1.47	0.05	78.47	0.41	0.70	0.73	0.21	0.00	0.02	0.05	92.40	45.06	37.93	96.85
94-15 ox1.2	magnetite	0.08	11.51	1.11	0.00	80.04	0.14	1.80	0.03	0.24	0.03	0.00	0.00	94.98	44.77	39.75	99.45
94-15 ox1.3	magnetite	0.05	10.89	1.13	0.00	80.54	0.10	1.74	0.08	0.34	0.01	0.00	0.04	94.93	46.08	39.07	99.50
94-15 ox1.4	magnetite	0.09	11.31	1.03	0.02	79.76	0.11	1.55	0.16	0.20	0.00	0.00	0.07	94.29	44.79	39.46	98.71
94-15 ox2.1	magnetite	0.28	11.42	0.96	0.03	77.04	0.09	1.00	0.05	0.14	0.00	0.00	0.06	91.05	41.74	39.48	95.17
94-15 ox2.2	magnetite	0.20	11.05	0.96	0.01	78.19	0.19	0.43	0.02	0.28	0.00	0.01	0.04	91.37	42.81	39.67	95.61
94-15 ox2.4	magnetite	0.06	10.76	1.22	0.02	77.83	0.13	0.86	0.04	0.07	0.00	0.00	0.03	91.02	43.26	38.90	95.32
94-15 ox2.5	magnetite	0.28	10.95	0.65	0.03	79.36	0.13	0.93	0.05	0.08	0.00	0.00	0.06	92.52	44.13	39.65	96.87
94-15 ox2.6	magnetite	0.06	11.63	1.32	0.01	76.85	0.11	1.69	0.10	0.33	0.02	0.00	0.04	92.16	42.24	38.84	96.35
94-15 ox3.1	magnetite	0.63	11.94	0.60	0.00	77.91	0.12	0.27	0.01	0.09	0.00	0.03	0.09	91.69	40.62	41.36	95.64
94-15 ox3.2	magnetite	0.14	11.52	1.11	0.00	76.42	0.14	1.38	0.07	0.11	0.02	0.03	0.06	91.01	41.60	38.99	95.09
94-15 ox3.3	magnetite	0.69	12.24	0.61	0.02	78.05	0.12	0.33	0.02	0.03	0.00	0.03	0.18	92.31	40.23	41.85	96.13
94-15 ox3.4	magnetite	0.16	10.97	1.12	0.00	77.93	0.08	1.03	0.10	0.17	0.00	0.02	0.08	91.65	43.23	39.03	95.89
94-15 ox4.2	magnetite	0.13	12.61	1.17	0.00	75.44	0.12	1.18	0.14	0.28	0.02	0.00	0.02	91.08	39.48	39.91	95.01
94-15 ox4.3	magnetite	0.15	10.86	1.10	0.01	77.30	0.12	1.24	0.16	0.20	0.00	0.00	0.02	91.16	43.19	38.44	95.47
94-15 ox6.1	magnetite	0.19	11.50	0.91	0.02	76.08	0.09	1.98	0.05	0.03	0.00	0.00	0.03	90.86	41.77	38.49	95.01
94-15 fe4.2	magnetite	0.09	11.16	1.60	0.00	76.12	0.10	1.95	0.21	0.21	0.02	0.05	0.00	91.52	42.39	37.97	95.71
94-15 fe5.1	magnetite	0.11	11.07	1.10	0.00	77.69	0.08	1.18	0.09	0.14	0.00	0.00	0.00	91.47	43.12	38.89	95.78
94-9B ox4.1	ilmenite	0.00	44.63	0.19	0.00	52.02	0.36	0.65	2.34	0.00	0.01	0.08	0.10	100.37	18.57	35.31	102.06
94-9B ox4.2	ilmenite	0.00	44.33	0.21	0.01	51.80	0.41	0.60	2.29	0.06	0.05	0.11	0.07	99.94	18.58	35.09	101.62
94-9B ox4.3	ilmenite	0.00	44.09	0.22	0.03	51.35	0.40	1.82	1.80	0.00	0.05	0.00	0.09	99.85	18.66	34.56	101.63
94-9B ox4.4	ilmenite	0.01	44.71	0.22	0.00	52.11	0.40	0.57	2.30	0.03	0.00	0.02	0.08	100.44	18.45	35.51	102.19
94-9B ox4.5	ilmenite	0.00	44.54	0.22	0.01	51.73	0.41	0.70	2.30	0.06	0.02	0.03	0.07	100.09	18.41	35.17	101.85
94-9B ox5.1	ilmenite	0.01	44.75	0.20	0.02	51.95	0.42	0.63	2.36	0.00	0.03	0.00	0.10	100.47	18.43	35.37	102.22
94-9B ox5.2	ilmenite	0.00	44.85	0.22	0.02	51.49	0.42	0.68	2.40	0.04	0.00	0.05	0.09	100.25	17.95	35.34	101.91
94-9B ox5.3	ilmenite	0.02	44.60	0.23	0.04	51.61	0.42	0.61	2.35	0.13	0.00	0.03	0.00	100.05	18.23	35.21	101.84
94-9B ox5.5	ilmenite	0.00	44.73	0.24	0.00	51.76	0.39	0.65	2.32	0.11	0.04	0.14	0.02	100.39	18.29	35.30	102.07
94-9B ox5.6	ilmenite	0.02	44.47	0.21	0.02	51.88	0.39	0.72	2.31	0.02	0.00	0.08	0.00	100.13	18.59	35.15	101.91
94-9B ox6.1	magnetite	2.23	3.10	0.61	0.06	83.45	0.14	0.96	0.03	0.26	0.05	0.02	0.03	90.93	54.31	34.58	96.32

Appendix C: Continued.

Sample	Mineral	SiO2	TiO2	Al2O3	Cr2O3	FeO*	V2O5	MnO	MgO	ZnO	NiO	ZrO2	Nb2O5	Total*	Fe2O3	FeO	Total
94-30 ox5.1	ilmenite	0.02	44.81	0.22	0.05	51.79	0.45	0.64	2.29	0.05	0.01	0.09	0.08	100.50	18.04	35.56	102.13
94-30 ox5.2	ilmenite	0.00	44.85	0.21	0.00	52.31	0.43	0.64	2.11	0.01	0.00	0.12	0.08	100.76	18.21	35.92	102.38
94-30 ox5.3	ilmenite	0.05	45.85	0.18	0.01	50.67	0.37	0.65	2.28	0.09	0.00	0.09	0.08	100.33	15.75	36.49	101.73
94-30 ox5.4	ilmenite	0.02	46.02	0.21	0.01	50.82	0.42	0.67	2.54	0.04	0.00	0.03	0.06	100.83	16.28	36.17	102.37
94-30 ox7.1	ilmenite	0.04	46.06	0.18	0.02	50.66	0.40	0.66	2.45	0.03	0.00	0.04	0.07	100.60	15.86	36.39	102.08
94-30 ox7.2	ilmenite	0.02	45.61	0.18	0.01	50.96	0.38	0.67	2.46	0.02	0.01	0.04	0.10	100.45	16.68	35.95	101.99
94-30 ox9.1	ilmenite	0.02	45.39	0.17	0.03	50.80	0.42	0.60	2.43	0.00	0.01	0.11	0.07	100.05	16.57	35.89	101.53
94-30 ox9.2	ilmenite	0.03	45.26	0.19	0.01	50.29	0.37	0.67	2.39	0.03	0.02	0.14	0.03	99.42	16.15	35.75	100.86
94-30 ox9.3	ilmenite	0.00	45.21	0.18	0.00	51.10	0.39	0.65	2.51	0.09	0.02	0.12	0.08	100.35	17.41	35.43	101.89
94-30 ox9.4	ilmenite	0.03	45.62	0.19	0.00	51.09	0.41	0.69	2.21	0.00	0.00	0.11	0.04	100.39	16.30	36.42	101.87
94-30 ox9.5	ilmenite	0.01	45.61	0.19	0.03	50.83	0.38	0.60	2.46	0.08	0.00	0.09	0.07	100.34	16.51	35.97	101.84
94-30 fe15.2	ilmenite	0.25	43.61	0.73	0.02	49.88	0.18	0.43	1.01	0.19	0.07	0.12	0.06	96.54	14.26	37.05	97.79
94-30 mal11.1	ilmenite	0.05	45.39	0.22	0.00	51.12	0.39	0.71	2.31	0.20	0.06	0.03	0.08	100.54	17.01	35.81	102.13
94-30 mal11.2	ilmenite	0.00	45.62	0.21	0.04	51.27	0.37	0.70	2.49	0.16	0.03	0.02	0.10	101.02	17.29	35.72	102.63
94-30 mal12.1	ilmenite	0.00	45.11	0.22	0.03	52.30	0.42	0.64	2.31	0.08	0.00	0.07	0.04	101.21	18.41	35.73	102.94
94-30 mal12.2	ilmenite	0.00	44.81	0.24	0.03	52.11	0.45	0.62	2.29	0.02	0.00	0.07	0.03	100.67	18.38	35.57	102.42
94-30 mal14.1	ilmenite	3.60	43.56	1.15	0.03	45.49	0.43	0.30	1.24	0.01	0.00	0.05	0.00	95.85	5.05	40.95	96.31
94-30 mal14.2	ilmenite	0.22	45.15	0.24	0.03	50.66	0.39	0.52	1.83	0.06	0.03	0.04	0.12	99.27	15.20	36.99	100.65
94-30 mal111.1	ilmenite	0.01	45.40	0.18	0.00	50.99	0.37	0.68	2.45	0.09	0.02	0.03	0.09	100.30	17.01	35.68	101.88
94-30 ma10.2	ilmenite	0.04	44.77	0.25	0.00	52.07	0.42	0.63	2.43	0.05	0.00	0.05	0.04	100.75	18.64	35.29	102.52
94-30 ma10.3	ilmenite	0.02	44.47	0.23	0.00	51.53	0.41	0.56	2.41	0.13	0.02	0.00	0.01	99.80	18.35	35.01	101.62
94-30 ox2.1	magnetite	4.55	11.23	2.22	0.12	71.56	0.61	0.42	1.28	0.23	0.00	0.02	0.00	92.24	30.72	43.91	95.29
94-30 ox2.2	magnetite	0.77	11.05	2.06	0.08	74.81	0.66	0.52	1.40	0.35	0.00	0.00	0.01	91.70	40.46	38.40	95.74
94-30 ox3.1	magnetite	2.32	11.73	2.14	0.22	72.49	0.60	0.54	1.39	0.40	0.00	0.05	0.00	91.86	35.05	40.95	95.32
94-30 fe15.1	magnetite	0.11	5.94	2.16	0.01	84.45	0.25	0.45	1.21	0.24	0.07	0.02	0.07	94.97	55.39	34.60	100.42
94-31 ox1.1	magnetite	0.18	10.25	0.95	0.00	75.28	0.09	3.90	0.01	0.67	0.04	0.02	0.00	91.39	44.67	35.08	95.83
94-31 ox1.2	magnetite	0.06	10.49	0.88	0.00	77.05	0.06	3.28	0.00	0.36	0.06	0.00	0.00	92.25	45.27	36.32	96.78
94-31 ox2.1	magnetite	0.11	10.16	1.47	0.10	75.59	0.58	3.29	0.03	0.27	0.04	0.00	0.01	91.66	43.97	36.02	96.05
94-31 ox3.1	magnetite	0.08	10.95	1.19	0.06	73.34	0.66	3.92	0.03	0.47	0.00	0.11	0.07	90.88	42.03	35.52	94.91
94-31 ox7.1	magnetite	0.18	11.12	1.63	0.10	73.12	0.59	4.30	0.00	0.51	0.02	0.09	0.09	91.75	41.53	35.75	95.73
94-31 ox7.2	magnetite	0.28	11.00	1.75	0.14	73.12	0.56	4.15	0.01	0.63	0.00	0.04	0.01	91.68	41.39	35.87	95.77
94-31 ox8.1	magnetite	0.23	10.40	1.74	0.16	74.99	0.61	3.61	0.04	0.31	0.03	0.07	0.09	92.27	43.11	36.20	96.44
94-31 ox8.2	magnetite	0.15	10.28	1.54	0.22	74.30	0.53	3.51	0.02	0.32	0.01	0.05	0.01	90.95	42.90	35.70	95.19

Appendix C: Continued.

<u>Sample</u>	<u>Phase</u>	<u>SiO2</u>	<u>Al2O3</u>	<u>TiO2</u>	<u>FeO*</u>	<u>MnO</u>	<u>CaO</u>	<u>MgO</u>	<u>K2O</u>	<u>Na2O</u>	<u>P2O5</u>	<u>Total</u>
94-5B gl1.1	glass	70.72	13.02	0.15	0.50	0.03	0.85	0.11	5.08	3.89	0.02	94.37
94-5B gl1.2	glass	70.43	12.92	0.20	1.15	0.08	0.95	0.14	4.64	4.15	0.03	94.69
94-5B gl1.3	glass	72.40	13.27	0.14	0.41	0.04	0.89	0.10	5.15	3.68	0.00	96.09
94-5B gl2.1	glass	71.68	13.06	0.17	0.77	0.04	0.89	0.15	5.08	3.77	0.02	95.63
94-5B gl2.2	glass	70.72	13.07	0.16	0.94	0.04	0.96	0.15	5.02	3.87	0.01	94.94
94-5B gl3.1	glass	71.81	12.79	0.17	0.54	0.04	0.88	0.15	4.64	4.01	0.00	95.03
94-5B gl4.1	glass	70.48	12.74	0.16	0.91	0.04	0.94	0.16	4.45	4.01	0.06	93.94
94-5B gl5.1	glass	71.78	12.76	0.17	0.54	0.04	0.93	0.11	5.41	3.39	0.00	95.14
94-5B gl5.2	glass	71.99	12.63	0.16	0.65	0.00	0.84	0.12	4.53	3.86	0.00	94.78
94-5B gl6.1	glass	71.61	12.88	0.17	0.70	0.01	0.81	0.13	4.56	3.92	0.01	94.80
94-5B gl7.1	glass	72.14	12.88	0.17	0.55	0.03	0.87	0.13	4.50	3.80	0.05	95.12
94-5B gl7.2	glass	71.16	13.16	0.14	0.62	0.04	0.87	0.11	4.50	3.79	0.06	94.47
94-5B gl8.1	glass	72.28	13.08	0.19	0.68	0.02	0.88	0.13	4.62	3.90	0.00	95.78
94-5B gl9.1	glass	71.44	13.00	0.17	1.87	0.07	0.90	0.14	4.70	3.79	0.04	96.13
94-5B gl10.1	glass	72.11	13.09	0.18	0.46	0.02	0.87	0.12	4.47	3.77	0.02	95.12
94-5B gl11.1	glass	73.05	12.48	0.16	0.54	0.09	0.76	0.12	4.42	3.80	0.00	95.44
94-5B gl11.2	glass	73.45	12.18	0.16	0.84	0.06	0.77	0.11	4.50	3.78	0.03	95.88
94-5B gl11.3	glass	71.65	12.30	0.20	1.24	0.00	0.80	0.15	4.48	3.57	0.03	94.43
94-5B gl12.1	glass	72.76	13.22	0.18	0.74	0.07	0.90	0.13	4.50	4.05	0.00	96.56
94-5B gl13.1	glass	71.44	12.97	0.19	0.81	0.03	0.90	0.13	4.63	3.99	0.03	95.11
94-5B gl15.1	glass	70.31	13.21	0.16	0.72	0.03	0.82	0.11	4.85	3.73	0.07	94.00
94-5B gl15.2	glass	72.07	13.19	0.13	0.77	0.05	0.85	0.11	4.52	3.80	0.05	95.53
94-5B gl15.3	glass	72.47	13.28	0.17	0.55	0.00	0.85	0.10	4.94	3.84	0.00	96.20
94-5B gl15.4	glass	72.15	13.24	0.15	0.49	0.02	0.83	0.10	4.40	4.11	0.07	95.57
94-5B gl15.5	glass	67.79	14.36	0.23	1.38	0.08	1.53	0.37	4.46	4.06	0.12	94.36
94-5B gl15.6	glass	68.71	14.21	0.24	0.88	0.03	1.41	0.26	4.86	3.85	0.06	94.50
94-5B gl15.7	glass	70.63	13.73	0.18	1.37	0.03	1.25	0.27	4.57	3.96	0.00	95.98
94-5B ox2.1	glass	71.96	13.41	0.16	0.52	0.00	0.90	0.14	4.64	3.93	0.03	95.68
94-5B ox9.1	glass	72.44	12.42	0.19	1.57	0.06	0.84	0.18	4.41	3.61	0.00	95.74
94-8 gl3.1	glass	71.81	12.82	0.14	1.13	0.03	0.71	0.04	4.94	3.40	0.05	95.08
94-8 gl3.2	glass	72.70	12.89	0.14	0.84	0.04	0.85	0.13	4.66	3.64	0.03	95.94
94-8 gl5.1	glass	73.66	11.90	0.11	0.73	0.08	0.55	0.04	4.77	3.61	0.02	95.48
94-8 gl5.2	glass	74.67	12.04	0.12	0.91	0.04	0.52	0.03	4.63	3.55	0.00	96.50
94-8 gl6.1	glass	73.92	12.22	0.13	0.96	0.00	0.61	0.12	4.58	3.62	0.00	96.16
94-8 gl8.1	glass	74.01	11.95	0.14	0.44	0.02	0.51	0.05	4.71	3.35	0.00	95.19
94-8 gl9.1	glass	69.95	13.18	0.14	1.13	0.07	0.92	0.19	4.70	3.98	0.05	94.31
94-8 gl9.2	glass	70.29	13.04	0.20	1.42	0.01	0.96	0.18	4.72	3.65	0.01	94.48
94-8 gl10.1	glass	75.55	12.20	0.09	0.49	0.05	0.57	0.03	4.68	3.62	0.00	97.29
94-8 gl10.4	glass	73.77	11.95	0.08	0.37	0.04	0.54	0.05	4.68	3.56	0.00	95.04
94-8 ox1.1	glass	71.49	12.98	0.16	1.28	0.00	0.83	0.15	4.92	3.58	0.05	95.44

Appendix C: Continued.

<u>Sample</u>	<u>Phase</u>	<u>SiO2</u>	<u>Al2O3</u>	<u>TiO2</u>	<u>FeO*</u>	<u>MnO</u>	<u>CaO</u>	<u>MgO</u>	<u>K2O</u>	<u>Na2O</u>	<u>P2O5</u>	<u>Total</u>
94-8 ox1.2	glass	72.68	12.89	0.17	1.24	0.00	0.81	0.13	4.74	3.85	0.03	96.57
94-8 ox6.1	glass	71.13	13.26	0.20	0.97	0.05	0.89	0.13	4.67	3.93	0.00	95.22
94-8 ox6.2	glass	74.09	11.98	0.09	0.75	0.02	0.53	0.05	4.69	3.78	0.05	96.04
94-13A gl1.1	glass	75.29	12.23	0.09	0.30	0.04	0.43	0.02	4.80	3.51	0.01	96.72
94-13A gl1.2	glass	72.98	13.02	0.16	0.82	0.10	0.70	0.11	4.86	3.72	0.03	96.50
94-13A gl2.1	glass	74.34	11.99	0.05	0.77	0.03	0.50	0.04	4.21	3.89	0.02	95.84
94-13A gl2.2	glass	73.94	11.87	0.11	0.73	0.05	0.47	0.03	4.40	3.51	0.00	95.12
94-13A gl2.3	glass	74.19	11.92	0.09	0.85	0.06	0.49	0.02	4.23	3.71	0.03	95.60
94-13A gl2.6	glass	73.20	11.81	0.15	0.88	0.06	0.44	0.08	4.22	3.50	0.00	94.35
94-13A gl3.1	glass	75.12	12.07	0.06	0.79	0.03	0.52	0.02	4.20	3.75	0.00	96.57
94-13A gl4.1	glass	73.33	11.89	0.06	0.78	0.04	0.53	0.06	4.28	3.73	0.00	94.71
94-13A gl5.1	glass	73.55	11.75	0.08	0.91	0.06	0.45	0.05	4.20	3.78	0.01	94.84
94-13A gl5.2	glass	74.01	11.61	0.06	0.80	0.07	0.52	0.03	4.25	3.74	0.02	95.12
94-13A gl5.3	glass	74.67	11.80	0.08	0.81	0.05	0.52	0.04	4.12	3.80	0.02	95.89
94-13A gl7.1	glass	74.34	11.99	0.10	0.82	0.01	0.54	0.04	4.12	3.66	0.00	95.62
94-13A gl9.1	glass	74.54	11.99	0.07	0.81	0.05	0.54	0.04	4.37	3.84	0.01	96.28
94-13A gl9.2	glass	74.27	12.03	0.07	0.73	0.04	0.52	0.03	4.30	3.87	0.00	95.87
94-13A gl9.3	glass	72.89	11.62	0.07	0.77	0.06	0.50	0.06	4.21	3.66	0.00	93.85
94-13A gl10.1	glass	75.00	11.88	0.14	0.61	0.07	0.54	0.08	4.16	3.73	0.03	96.25
94-13A gl10.2	glass	74.96	12.00	0.17	0.47	0.05	0.47	0.04	4.54	3.41	0.00	96.10
94-13A gl11.1	glass	74.85	12.10	0.06	0.84	0.06	0.52	0.04	4.27	3.78	0.06	96.58
94-13A gl11.2	glass	75.05	12.09	0.08	0.70	0.05	0.56	0.05	4.32	3.77	0.05	96.74
94-13A gl12.1	glass	75.02	11.95	0.08	0.82	0.04	0.50	0.06	4.24	3.67	0.04	96.42
94-13A gl12.3	glass	75.10	12.03	0.08	0.78	0.04	0.53	0.04	4.26	3.76	0.00	96.62
94-30 gl1.1	glass	74.46	11.73	0.13	0.71	0.07	0.51	0.06	4.57	3.57	0.00	95.81
94-30 gl1.2	glass	74.04	11.62	0.12	0.67	0.07	0.54	0.07	4.54	3.36	0.06	95.08
94-30 gl1.3	glass	74.80	11.88	0.12	0.69	0.07	0.51	0.06	4.94	3.60	0.02	96.70
94-30 gl1.4	glass	75.03	11.88	0.13	0.63	0.05	0.50	0.09	4.41	3.73	0.00	96.45
94-30 gl2.1	glass	70.52	12.92	0.25	0.60	0.03	0.67	0.08	4.59	4.00	0.05	93.70
94-30 gl2.2	glass	71.87	12.83	0.24	0.70	0.03	0.67	0.06	4.86	4.05	0.04	95.34
94-30 gl2.3	glass	74.91	11.89	0.08	0.43	0.01	0.42	0.03	4.41	3.52	0.01	95.71
94-30 gl2.4	glass	72.46	13.03	0.27	0.50	0.02	0.67	0.08	4.41	3.87	0.05	95.35
94-30 gl2.5	glass	74.77	11.83	0.11	0.56	0.01	0.47	0.06	4.22	3.52	0.00	95.57
94-30 mal11.1	glass	71.30	12.85	0.26	1.26	0.04	0.75	0.18	4.50	3.81	0.01	94.95
94-30 mal11.2	glass	72.44	12.83	0.26	1.03	0.03	0.75	0.14	4.38	3.93	0.03	95.82
94-30 mal11.3	glass	72.19	12.78	0.26	1.15	0.05	0.75	0.14	4.80	3.58	0.03	95.73
94-30 gl3.1	glass	72.34	12.86	0.23	0.98	0.02	0.72	0.17	4.35	3.95	0.02	95.65
94-30 gl3.2	glass	71.80	12.88	0.25	1.15	0.04	0.78	0.17	4.30	3.84	0.02	95.22
94-30 gl3.3	glass	72.63	12.79	0.26	1.04	0.04	0.73	0.12	4.36	4.07	0.01	96.05
94-30 gl3.5	glass	72.44	13.05	0.25	1.12	0.05	0.69	0.15	4.59	4.04	0.01	96.40

Appendix C: Continued.

<u>Sample</u>	<u>Phase</u>	<u>SiO2</u>	<u>Al2O3</u>	<u>TiO2</u>	<u>FeO*</u>	<u>MnO</u>	<u>CaO</u>	<u>MgO</u>	<u>K2O</u>	<u>Na2O</u>	<u>P2O5</u>	<u>Total</u>
94-30 gl4.1	glass	71.77	12.99	0.26	0.87	0.00	0.72	0.13	4.69	3.60	0.00	95.03
94-30 gl4.2	glass	72.61	13.09	0.21	1.01	0.03	0.77	0.14	4.58	3.85	0.08	96.37
94-30 gl4.3	glass	72.51	13.21	0.27	0.65	0.00	0.61	0.09	4.45	4.03	0.00	95.84
94-30 gl5.1	glass	71.89	12.87	0.27	1.03	0.05	0.78	0.14	4.81	3.59	0.04	95.48
94-30 gl5.2	glass	72.11	12.74	0.25	1.08	0.03	0.68	0.12	4.47	3.75	0.04	95.27
94-30 gl5.3	glass	71.34	12.85	0.25	0.98	0.01	0.69	0.16	4.41	4.01	0.07	94.77
94-30 gl6.1	glass	74.91	12.17	0.11	0.79	0.07	0.59	0.09	4.22	3.50	0.03	96.49
94-30 gl6.2	glass	75.28	11.85	0.14	0.72	0.00	0.48	0.05	4.28	3.65	0.02	96.49
94-30 gl6.3	glass	74.19	12.11	0.16	0.98	0.03	0.62	0.12	4.17	3.73	0.02	96.13
94-30 gl7.1	glass	75.04	11.90	0.13	0.57	0.00	0.52	0.03	4.71	3.13	0.06	96.10
94-30 gl7.2	glass	74.24	11.86	0.11	0.51	0.06	0.45	0.05	4.44	3.47	0.00	95.19
94-30 gl8.1	glass	74.63	11.78	0.14	0.39	0.02	0.49	0.04	4.40	3.60	0.02	95.51
94-30 gl9.1	glass	74.53	11.79	0.14	0.58	0.06	0.56	0.05	4.16	3.54	0.00	95.41
94-30 gl9.4	glass	74.26	11.80	0.11	0.53	0.05	0.49	0.04	4.33	3.51	0.00	95.12
94-30 gl9.5	glass	74.26	11.72	0.10	0.60	0.04	0.52	0.04	4.24	3.45	0.00	94.98
94-30 gl9.6	glass	74.19	11.89	0.09	0.64	0.03	0.54	0.05	4.69	3.47	0.00	95.58
94-30 gl9.7	glass	74.77	11.74	0.11	0.53	0.05	0.47	0.01	4.80	3.43	0.05	95.96
94-30 gl9.8	glass	75.03	11.71	0.13	0.55	0.05	0.49	0.03	4.49	3.49	0.03	95.99
94-30 gl11.1	glass	73.09	11.83	0.09	0.72	0.02	0.53	0.07	4.30	3.38	0.05	94.07
94-30 gl11.2	glass	74.71	11.94	0.10	0.65	0.02	0.51	0.07	4.19	3.26	0.00	95.45
94-30 gl12.1	glass	73.58	11.97	0.11	0.67	0.04	0.52	0.05	4.38	3.75	0.01	95.07
94-30 gl12.2	glass	75.17	11.94	0.14	0.53	0.02	0.47	0.10	4.37	3.54	0.01	96.28
94-30 gl12.3	glass	75.39	11.89	0.12	0.67	0.02	0.51	0.07	4.26	3.73	0.00	96.66
94-30 gl12.4	glass	74.44	11.96	0.10	0.79	0.10	0.49	0.11	4.31	3.60	0.04	95.94
94-30 gl12.5	glass	75.20	11.86	0.08	0.69	0.00	0.50	0.06	4.16	3.73	0.02	96.30
94-30 gl12.6	glass	75.05	11.85	0.13	0.57	0.05	0.50	0.05	4.03	3.47	0.03	95.72
94-30 gl12.7	glass	74.65	11.91	0.11	0.60	0.08	0.52	0.06	4.30	3.40	0.00	95.62
94-30 gl13.1	glass	72.13	13.26	0.18	0.79	0.03	0.84	0.07	4.39	3.66	0.00	95.36
94-30 gl13.2	glass	72.18	13.31	0.20	0.73	0.03	0.82	0.05	4.51	3.90	0.05	95.78
94-30 gl13.3	glass	72.44	13.17	0.16	0.98	0.01	0.92	0.13	4.28	3.98	0.04	96.11
94-30 ox2.1	glass	74.30	11.65	0.11	0.70	0.06	0.46	0.06	4.23	3.44	0.00	95.02
94-30 ox4.1	glass	72.41	12.98	0.28	0.59	0.00	0.67	0.08	4.38	3.99	0.03	95.43
94-30 ox4.2	glass	72.34	13.04	0.27	0.51	0.01	0.57	0.03	4.48	3.97	0.02	95.25
94-30 ox4.3	glass	71.54	12.86	0.28	0.95	0.04	0.76	0.14	4.48	3.94	0.04	95.04
94-30 ox4.4	glass	71.77	12.97	0.28	1.04	0.05	0.86	0.17	4.57	3.81	0.08	95.60
94-30 ox7.1	glass	74.41	11.82	0.12	0.69	0.08	0.50	0.06	4.17	3.57	0.02	95.43